The Roles of Pars Flaccida in Middle Ear Acoustic Transmission

by

Su Wooi Teoh

B.S., Electrical Engineering
University of Texas at Austin, 1993

Submitted to the Department of Electrical Engineering and Computer Science
in partial fulfillment of the requirements for the degree of

Master of Science in Electrical Engineering and Computer Science

at the

MASSACHUSETTS INSTITUTE OF TECHNOLOGY

January 1996

Author .....
Department of Electrical Engineering and Computer Science
November 13, 1995

Certified by .....
John J. Rosowski
Associate Professor of Otology and Laryngology, Harvard Medical School
Thesis Supervisor

Accepted by .....
F.R. Morgenthaler
Chairman, Departmental Committee on Graduate Students

The Roles of Pars Flaccida in Middle Ear Acoustic Transmission

by

Su Wooi Teoh

Submitted to the Department of Electrical Engineering and Computer Science
on November 13, 1995, in partial fulfillment of the
requirements for the degree of
Master of Science in Electrical Engineering and Computer Science

Abstract

This thesis investigates the effect of *pars flaccida* on the signal transmission properties of the middle ear through acoustic and electro-physiological measurements. Toward this goal, the middle-ear input admittance, ear-canal to middle-ear sound pressure ratio, and round-window cochlear potential were measured in the ears of twelve gerbils. Measurements were made before and after various middle ear and tympanic membrane manipulations, including stiffening or removing the *pars flaccida*. The results are compared to the predictions of the middle-ear model proposed by Kohlloffel (1984). The input-admittance measurements show that the *pars flaccida* can be accurately modeled by a simple RLC circuit with a resonance at approximately 500 Hz. With the exception of a small frequency range from 300-600 Hz, our cochlear potential measurements support the assumption that the *pars flaccida* and *pars tensa* are independent. Within this range, the *pars flaccida* acts as a shunt path around the main ossicular transmission pathway. At frequencies below the *pars flaccida* resonance, this extra pathway reduces the ossicular transmission to the inner ear by increasing the middle-ear pressure. These results suggest that *pars flaccida* reduces low frequency hearing sensitivity, consistent with the model prediction. Between 300-600 Hz, significant deviation between the cochlear potential measurements and the model predictions was observed. The cause of this deviation is unclear and requires further investigations.

Thesis Supervisor: John J. Rosowski
Title: Associate Professor of Otology and Laryngology, Harvard Medical School

Acknowledgments

First and foremost, I would like to extend my most sincere thanks to Dr. John J. Rosowski, my thesis advisor. John has consistently been the driving force behind this work. He has patiently provided intellectual and technical guidance throughout the project, and has tolerated all the mistakes that I have committed along the way. Through numerous discussions and meetings, John has patiently corrected my often naive notion of research and has been an example of a careful and rigorous scientist. Any errors in this thesis must have been committed in spite of his teaching. I am also greatly indebted to Professor William T. Peake for introducing me to and teaching me the science of acoustics and hearing. Without him, this thesis would not have been possible.

Special thanks must go to Deborah Flandermeyer for her help in performing animal surgeries, proofreading this thesis, and especially for her encouragement in all aspects of my work. Sunil Puria, Mike Ravicz, and Susan Voss have provided valuable advice throughout the past year. I thank all members of the Eaton-Peabody Laboratory for providing such a conducive and comfortable atmosphere for conducting research.

Last but certainly not least, my deepest appreciations go to my sisters and my parents. It is their selfless sacrifice over the years that has made my higher education a reality.

This work was supported by the MIT Vinton Hayes Fellowship and NIH grant R01 DC 00194.

Contents

List of Figures

List of Tables

Chapter 1

Introduction

1.1 Brief overview of the hearing process

The hearing process in most higher vertebrates begins in the peripheral auditory organs — the external and the middle ear. These two structures are responsible for transferring acoustical vibrations in the external environment to the inner ear, where sensory hair cells convert the vibrations into neural action potentials. These neural signals are then conveyed via the auditory nerve and midbrain to the auditory cortex, where the nerve impulses can be perceived as meaningful sound.

Comprehension of this enormously complex transduction process has been made more manageable by the divide and conquer approach, where structures along the pathway are broken down into cascading systems that can be analyzed independently. In this approach, the analysis of a single stage needs only take into account the overall pre-filtering characteristics of the earlier systems and the loading effects of the following stages, freeing us from many unnecessary secondary details. At the most peripheral level, it is common to analyze the external and the middle ear as a single system, with

the inner ear acting as a load. The primary function of the external and middle ear is to collect and channel sound energy to the inner ear, and in the process filter the frequency contents of the incoming acoustic signals via passive mechano-acoustic processes[1]. The inner ear, on the other hand, uses an active mechanical feedback system, producing hair cell responses that exhibit sharp frequency sensitivity (Zwicker, 1986; Neely and Kim, 1986; Diependaal et al. , 1987; Pickles, 1988). In addition, the inner ear acts as a nonlinear mechano-chemical transducer, converting the mechanical vibration of hair cells into chemical signals that initiate all-or-none neural action potentials.

This thesis is primarily concerned with the modeling of the middle ear. In particular, it concentrates on the effects of *pars flaccida*[2] in this complex transduction process. Before we proceed further into the methodology and details of this study, a brief overview of anatomy and acoustics is in order.

1.2 Overview of the anatomy and functions of the ear

The peripheral auditory system of all mammals can be divided into three regions — external, middle, and inner ear. Despite the great variations in size and shape of the auditory system among different species, several noticeable and important structures common to all species can be identified in each of the three regions.

Figure 1-1 shows the anatomy of the human auditory system, which illustrates the important structures observed in most mammals. The outermost portion of the external ear usually consists of a protruding cartilaginous pinna that functions as a sound collector. The pinna is connected on the medial surface to a funnel-like structure called the

[1]The stapedius muscle and the tensor tympani muscle may be considered as active elements of the middle ear, but their effects are mainly felt when subjected to high intensity sound, and they work by modifying the stiffness of the middle ear, which is a passive mechanical property.

[2] *Pars flaccida* is a flaccid region of the tympanic membrane. See Section 1.2 for more details.

concha. The narrower end of the concha leads directly to the cartilaginous and bony ear canal (also called external auditory meatus), which terminates at the tympanic membrane on its medial end. The function of the external ear structures is like that of a horn, amplifying the gathered sound in a frequency-dependent manner. This amplification is directionally dependent, and this phenomenon provides cues for directional judgment (Shaw, 1974).

The tympanic membrane forms the boundary between the middle and the external ear. Attached to the medial side of the tympanic membrane is the malleus. Together with incus and stapes, they form the ossicular bones of the middle ear. These three bones are suspended by ossicular ligaments in the middle ear and act as a connecting bridge, conducting mechanical vibrations of the tympanic membrane to the fluid-filled cochlea of the inner ear. One feature of the coupling between malleus and tympanic membrane deserves further elaboration. In some mammals, such as cat and guinea pig, the entire tympanic membrane is stiff and firm. The tensa and the tightly coupled malleus form an efficient pressure transformer (Tonndorf and Khanna, 1970), such that a large part of the acoustic power received by the tympanic membrane is converted into mechanical vibrations of the ossicular bones, which then act as the inner ear input (Rosowski et al. , 1986). While this has been the conventional thought about the function of tympanic membrane and ossicular bones, it is not entirely accurate for many mammals, including gerbil, mouse, rat, deer, pig, and goat. In these mammals, the tympanic membrane consists of two distinct parts: the *pars tensa* and the *pars flaccida* (also called Shrapnell's membrane). Figure 1-2b shows the inferior lateral view of a gerbil tympanic membrane, which illustrates the clear geometrical differences between the *pars flaccida* and the *pars tensa*. The firm pars tensa is the site of attachment for the malleus, similar to the

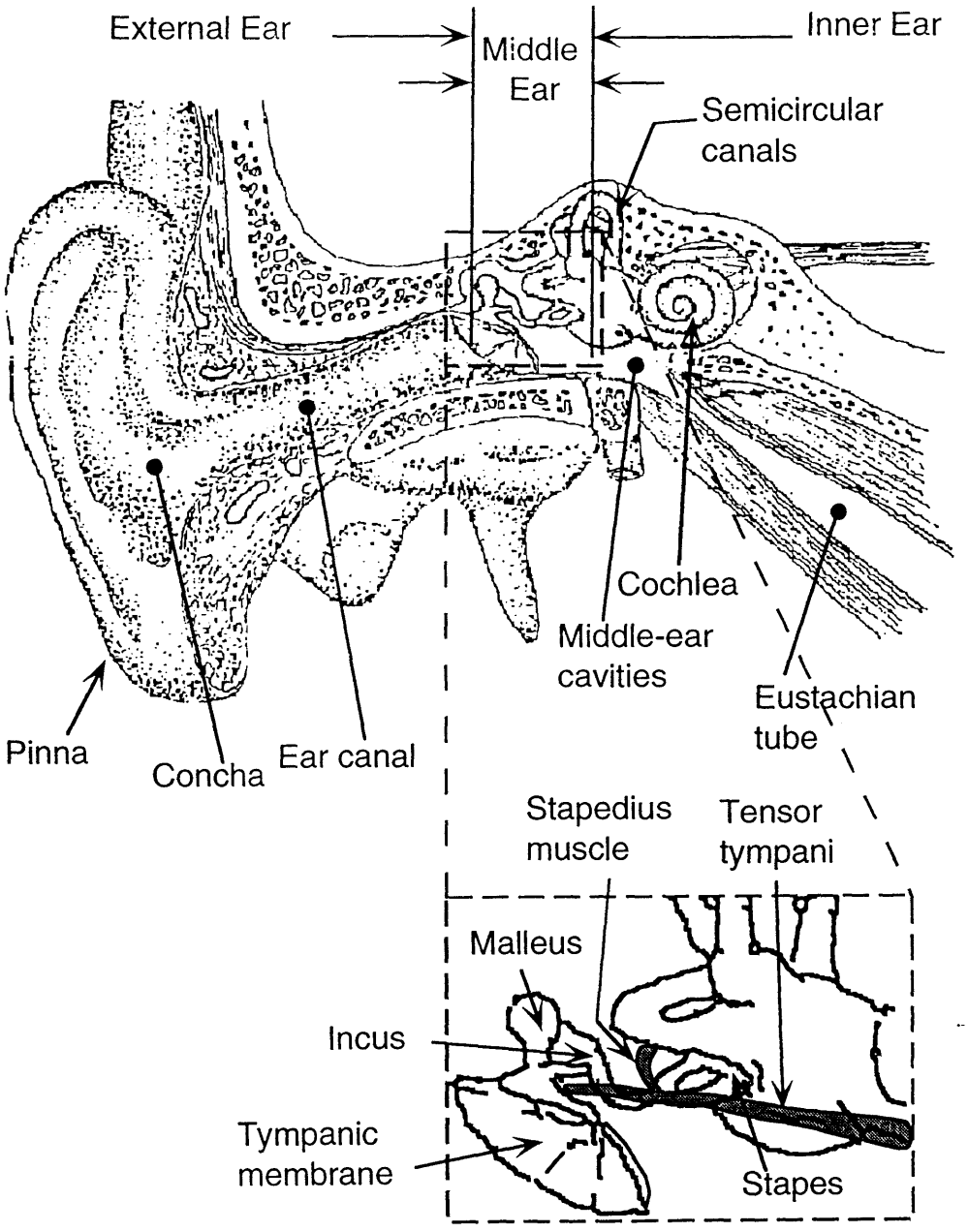

Figure 1-1: Anatomy of the ear. Sketch of the external, middle, and inner ear of human. The boxed region shows the detailed middle ear structures. From *Atlas of the Ear by Scanning Electron Microscopy*, by Y. Harada, 1983.

tympanic membrane of the cat and human discussed above. The soft *pars flaccida*, however, is loosely coupled to the tympanic ring and the *pars tensa*; thus, motion of the *flaccida* does not elicit any significant mallear movement and transfers little power to the inner ear. The exact function of *pars flaccida* is unclear, and is the subject of this thesis.

All the middle ear structures are housed in an air-filled middle-ear cavity. The cavity is connected by the Eustachian tube to the nasal-pharyngeal air space. Opening the tube eliminates any static pressure difference between the middle ear and the external environment. Other important structures in the middle ear are the two middle ear muscles. The stapedius muscle is the smallest striated muscle of the body. It arises within the posterior wall of the middle ear cavities and inserts onto the neck of the stapes (Figure 1-1). The other muscle, the tensor tympani, is attached to the malleus near the tympanic membrane. Contraction of these muscles can alter the stiffness of the ossicular chain, thus affecting the transmission properties of the middle ear (Pang and Peake, 1985).

The last component of the peripheral auditory system is the fluid-filled cochlea of the inner ear. The cochlea is the mechano-chemical transducer of the ear that initiates neural responses. However, from the viewpoint of acoustic transmission, the cochlea simply serves as a load on the middle ear, acting to limit the movements of the ossicular chain (Møller, 1965; Lynch et al. , 1982). At the oval window, where the stapes is attached to the cochlea, the annular ligament holds the footplate of the stapes in place. This ligament, together with the fluid inside the cochlea, serves as the main load of the ossicles.

The anatomical description presented in this section applies to all mammalian ears,

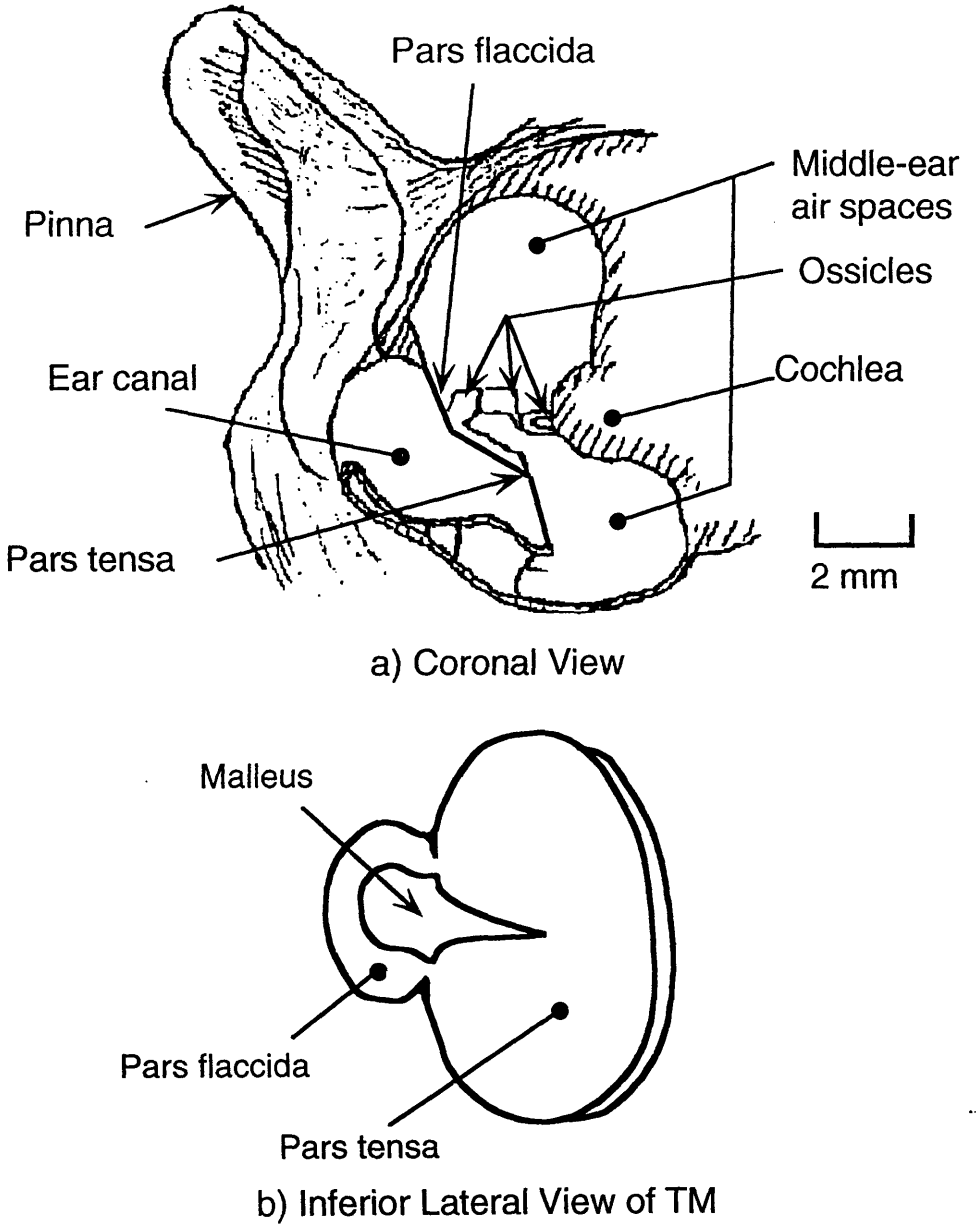

Figure 1-2: Illustrations of a gerbil ear. *a*) Coronal view of a gerbil ear viewed caudally. While it is not obvious in the figure, the middle-ear cavity of gerbil consists of several chambers of complex geometry. These chambers are formed and incompletely separated by several thin bony septa. Note that the two regions of the tympanic membrane reside in different planes. *b*) View of tympanic membrane from the inferior-lateral aspect. The geometrical differences between the *pars flaccida* and *pars tensa* are clearly visible. The *pars flaccida/pars tensa* area ratio is approximately 0.11 (Kohllöffel, 1984). Drawings from Ravicz (1990).

including our experimental subject — the gerbil. Figure 1-2 shows coronal and inferior lateral views of a gerbil ear. Note that all structures discussed so far can be identified in the figures. We also label the eggshell-like bony inferior wall of the middle-ear air spaces as the bulla, a term generally used to describe the protruding middle ear cavity wall observed in many mammals, such as gerbil, cat, chinchilla and guinea pig. Note the large extant of the middle ear air spaces and bulla in gerbil (Figure 1-3); the acoustic implication of such a hypertrophied bulla will be discussed in Chapters 3 and 4 along with the experimental results.

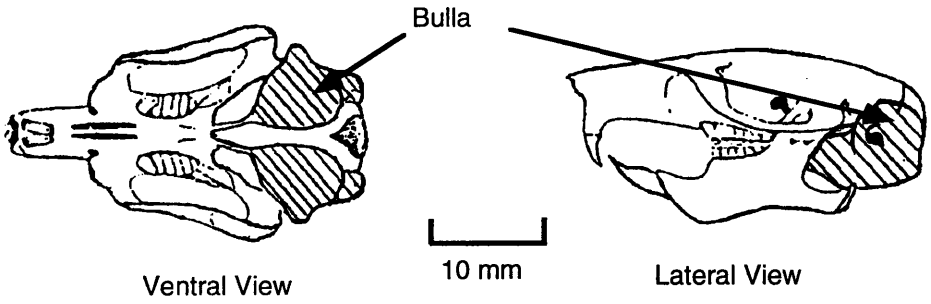

Figure 1-3: Lateral and ventral views of gerbil skull. The hatched area indicates the bulla. Note the relatively large size of the bulla with respect to the skull.

1.3 Modeling of acoustic systems

Before we proceed with a discussion of middle ear modeling, it would be beneficial to briefly review the basics of acoustics, in particular the modeling of simple acoustic elements in the low frequency region. The general study of acoustics concerns the understanding of sound, and to a more refined level, the vibrations of molecules. The physics underlying the principles of sound and vibrations has been greatly advanced in the last 100 years by such investigators as Rayleigh, Stokes, Thomson, Helmholtz, Sabine and others. The work of these pioneers provides us with a great mathematical repertoire

for the general analysis of acoustical and vibratory signals. The majority of these techniques are in the form of differential equations describing the physical phenomena of vibrations, mostly in the form of general wave theory (Beranek, 1954; Fletcher, 1992). These mathematical tools have been used in the acoustical analysis of many areas, such as speaker and microphone designs, architectural acoustics, environmental noise control, and in biological systems.

1.3.1 Low frequency circuit analogs

In cases where the system under study is small in dimension compared with the sound wavelength[3], we can greatly simplify acoustical analyses. In these cases, spatial variations of sound pressure and volume velocity[4] in the system can be ignored, and we can represent the whole structure as a lumped unit fully described by these two quantities. For those familiar with electrical circuits, the acoustical structures can be defined as circuit analogs, for which quantitative solutions can be obtained using well established analytical techniques. As we will see, the first order mathematical relationships describing the acoustical properties (pressure $\mathbf{p}$ and volume velocity $\mathbf{U}$)[5] of simple systems such as tubes, small cavities, membranes, and small apertures are the same as the three passive lumped elements commonly used in electrical circuits: inductor, capacitor, and resistor.

[3] In this case, small means that the dimension of the system is less than one-tenth of a wavelength.

[4] Sound pressure and volume velocity are the two variables that fully describe the sound wave. Volume velocity refers to the collective movements of a *unit volume* of medium molecules per second, and sound pressure refers to the amount of alternating increase and decrease in atmospheric pressure as a result of this motion. These two quantities are the preferred variables in acoustic circuits. When two acoustic elements are interconnected, the volume velocity at the adjoining node is always conserved (analogous to the conservation of electrical current at an electrical node). As a result of this analogy, acoustic structures can be modeled as electrical circuits.

[5] All acoustical variables used in this thesis are expressed in the complex frequency domain, and they are printed in bold (*e.g.* $\mathbf{p}, \mathbf{U}$). In occasional instances where time domain analysis is needed, the variables are italicized and their dependence on time are explicitly noted (*e.g.* $p(t), U(t)$). Details on frequency analysis and complex variables can be found in most general circuit texts, such as Desoer and Kuh (1969), Nilsson (1990).

In this paradigm, sound pressure is analogous to electrical voltage and sound volume velocity is analogous to electrical current. Since most biological systems, including the mammalian middle ear, consist of interconnected tubes, cavities, and membranes, we can solve the acoustical problem by simply observing the behaviors of the corresponding circuit analogs. This method has proven to be more convenient and insightful than solving systems of simultaneous differential equations.

Since the sound pressure $\mathbf{p}$ and volume velocity $\mathbf{U}$ fully describe the sound wave in a structure, it follows that the complex acoustic impedance $\mathbf{Z} = \mathbf{p}/\mathbf{U}$ fully describes the characteristics of the structure itself. Equivalently, acoustic structure is often defined in terms of its admittance $\mathbf{Y} = \mathbf{1}/\mathbf{Z} = \mathbf{U}/\mathbf{P}$. For a wide and short open tube with radius r and length l, the application of alternating pressure $p(t)$ between its two ends generates a force of $p(t)\pi r^2$. This alternating force causes the air molecules in the tube to accelerate back and forth like a simple mass. Since the enclosed air mass is $\rho_o l \pi r^2$ ($\rho_o = 1.19 kg/m^3$ is the density of air at standard temperature and pressure), it follows from simple Newtonian physics that

$$p(t) = \frac{\rho_o l}{\pi r^2} \frac{dU(t)}{dt} \tag{1.1}$$

Taking the Fourier transform of Eqn. 1.1 yields

$$\mathbf{p} = j\omega \frac{\rho_o l}{\pi r^2} \mathbf{U} \tag{1.2}$$

where j is the imaginary number $\sqrt{-1}$, $\omega = 2\pi f$ is radian frequency, and $\mathbf{p}$ and $\mathbf{U}$ are the complex amplitudes of sound pressure and volume velocity. Comparing Eqn. 1.1

with the constitutive equation of an inductor:

$$v(t) = L\frac{di(t)}{dt} \tag{1.3}$$

shows that the wide open pipe behaves like an inductor, with inductance $\rho_o l/\pi r^2$, as shown in Figure 1-4a. This information can also be obtained from Eqn. 1.2, where the complex acoustic impedance $\mathbf{Z} = \mathbf{p}/\mathbf{U}$ can be found to be $j\omega\rho_o l/\pi r^2$, which is the frequency domain representation of an inductance $\rho_o l/\pi r^2$.

If the cross sectional area of the pipe is small, its large internal surface provides significant friction to the movements of air molecules. In this case, the acoustic impedance has a resistive component in addition to the inductance. In a resistive environment, the force (or pressure) needed to displace a unit mass is directly proportional to the velocity of particles:

$$p(t) = R^A U(t) \tag{1.4}$$

where R^A is the acoustic resistance of the structure. Generally R^A is frequency-dependent and is difficult to describe with a simple analytical equation. However, for small enough apertures and with a low-viscosity fluid like air, we can approximate the resistance (Fletcher, 1992):

$$R^A \approx 1.2 \times 10^{-5}(\frac{\rho_o c}{\pi r^2})\frac{\omega^{1/2} l}{r} \approx 2 \times 10^{-3}\frac{\omega^{1/2} l}{r^3} \tag{1.5}$$

where $c = 345 m/sec$ is the propagation velocity of sound under normal atmospheric conditions. For a tube of *very* small diameter ($r < 0.002/\sqrt{f}$), the acoustic resistance approaches an asymptote that is independent of frequency (Beranek, 1954). The complex

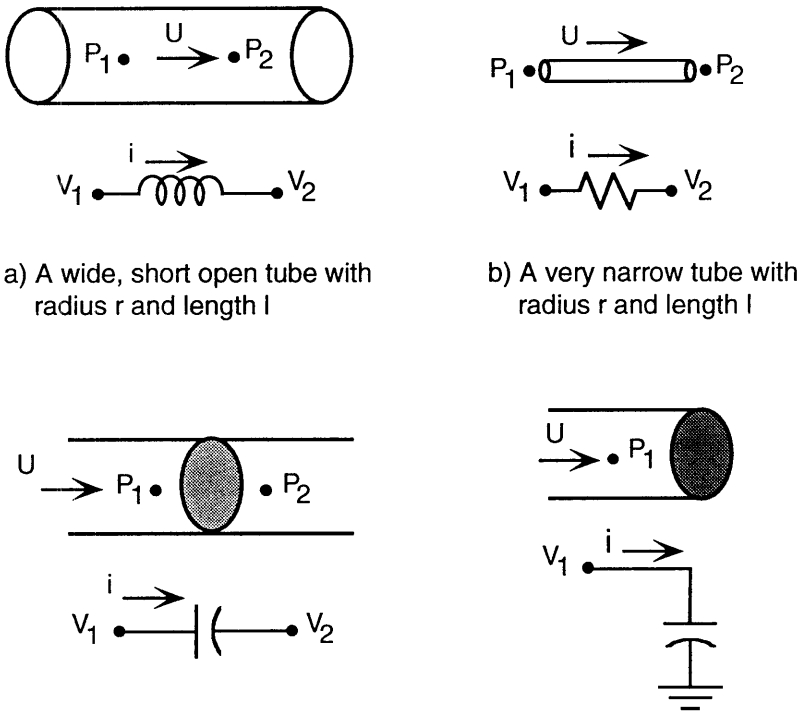

Figure 1-4: Circuit representations of lumped acoustic elements. In these four lumped circuit analogs, pressures ($\mathbf{P_1}$ and $\mathbf{P_2}$) are represented by voltages ($\mathbf{V_1}$ and $\mathbf{V_2}$), while volume velocity (U) is characterized as current (i). a) A wide, short open tube can be modeled as an inductor, with inductance $\rho_o l/\pi r^2$. b) For a very narrow tube, the impedance is dominated by the resistance (Eqn. 1.6). At higher frequency, the inductance could become significant and must be included in the model. c) For a membrane with average stiffness k and area A, the model capacitance (or compliance) is simply A/k. This model is only valid for frequency range below the membrane's lowest resonance frequency. Above that frequency, a series inductor and resistor must also be included. d) An enclosed cavity can be modeled as a grounded capacitor. The capacitance (or compliance) of the capacitor is inversely proportional to the volume of the cavity: $C^A = V/\rho_o c^2$.

acoustic impedance of such a tube is

$$\mathbf{Z^A} = \frac{8\eta l}{\pi r^4} + j\frac{4}{3}\omega\frac{\rho_o l}{\pi r^2} \tag{1.6}$$

where η is the viscosity coefficient, $\eta = 1.86 \times 10^{-5} N sec/m^2$ at $20°C$ and 0.76mHg. Note that even though the inductance of a very thin tube is 1.3 times bigger than a larger diameter tube, its impedance is greatly dominated by the resistive component (due to the contribution of $1/r^4$ in the resistive term). Therefore, it is sufficiently accurate to model a very thin tube as a simple resistor, as illustrated in Figure 1-4b.

Another simple acoustic element is a small enclosed cavity of volume V with a single inlet. If the cavity is small compared to the wavelength of the applied pressure (*i.e.* the applied ac pressure $p(t)$ is uniform throughout the volume) and the motion of air particles is small compared to the dimensions of the enclosed volume, then the adiabatic law[6] dictates that

$$p(t) = \frac{\rho_o c^2}{V}\int U(t)\,dt \tag{1.7}$$

or in frequency domain:

$$\mathbf{p} = \frac{\rho_o c^2}{j\omega V}\mathbf{U} \tag{1.8}$$

Comparing Eqn. 1.7 with the constitutive equation of a capacitor:

$$v(t) = \frac{1}{C}\int i(t)\,dt \tag{1.9}$$

clearly illustrates the capacitive (or compliance) behavior of an enclosed cavity. One

[6]Adiabatic law applies to situation where heat transfer from the air medium to the cavity wall is negligible. This condition holds true for sound waves in all but the very lowest audible frequency range.

important consideration in modeling a cavity as a capacitor is the topological position of this two-terminal electrical device. Since the applied pressure $p(t)$ is defined as the change from equilibrium pressure (which is modeled as a ground node or voltage reference), one of the capacitor terminals must always be at *ground potential* (Figure 1-4d). This restriction thus eliminates the possibility of inserting a "cavity capacitor" in series with other acoustic elements.

To achieve a series-capacitance configuration, it is necessary to utilize a stiffness controlled diaphragm or membrane (Figure 1-4c). However, besides the stiffness property, all membranes possess to a varying degree certain mass like behavior due to the inertia of their membranal fibers. As a result of the interactions between these two components, all membranes resonate at certain preset frequencies. Only at frequencies lower than the lowest resonance frequency can we model a membrane as a series capacitor. A more accurate and general representation of membrane consists of series capacitor, inductor, and resistor — the inductor accounts for the mass like property and the resistor represents the damping and frictional losses due to the membranal movements.

1.3.2 High frequency representations of acoustic systems

The maximum linear dimension of the entire gerbil middle ear (the bulla cavities) is on the order of 10mm. To model such a system with the low-frequency circuit analogs developed in the previous section would entail a frequency limit of approximately 3.5 kHz[7]. For frequencies significantly above 3.5 kHz, the pressure in the middle ear is no longer uniform at any given time. As a result, a lumped quantity such as a voltage can no

[7]In developing the lumped parameter system, we assume that the wavelength of the sound wave is at least ten times larger than the dimension of the structure. In this case, the frequency limit is $f_c = c/\lambda \approx 3.5\ kHz$, assuming $c = 345\ m/sec$ is the propagation velocity of sound, and $\lambda = 0.1\ m$ is ten times the typical gerbil middle ear dimension.

longer accurately represent the spatially distributed pressure wave. Since the audible range of gerbils extends beyond 20 kHz (Ryan, 1976), other modeling techniques will be needed to cover the entire functional frequency range.

One general approach is to model the acoustic structures as systems of distributed parameters. A straightforward implementation of such a system is to use the finite element modeling technique. Such implementation provides a large degree of freedom, thus increasing the flexibility of modeling a complex system. However, such capability is achieved at the expense of increasing computational cost and the loss of physical correlations between model parameters and acoustic structures. Fortunately, for structures with well defined geometry, there exist special techniques that would provide accurate high frequency modeling, while utilizing only a limited number of parameters. For instances, tubes and horns can be modeled as transmission lines, and membranes emulated as shells. The mathematical constructions of such models can often be formulated in terms of two-port networks. This two-port modeling technique is used in Section 3.1.1 to represent the bony ear canal of the gerbil.

1.4 Middle ear models

As pointed out in Section 1.1, there is no active element present in the middle ear; therefore, it is justifiable to treat the middle ear in the framework of passive mechano-acoustical structures. Since the main focus of this thesis is on the effects of *pars flaccida* in middle ear transmission, and the effects of the *flaccida* appear mainly in the low frequency region[8], the acoustical structures can be accurately modeled as circuit analogs.

[8] As will be shown in Chapter 3, the effect of *pars flaccida* is observed primary at frequencies below 2 kHz.

Figure 1-5 depicts the key structures and the relevant acoustical variables of the gerbil middle ear. As discussed on page 19, the gerbil tympanic membrane consists of two regions of distinct physical characteristics. As a result, application of sound pressure in the ear canal, $\mathbf{P_{EC}}$, is likely to induce different vibratory patterns on the *pars flaccida* and the *pars tensa.* To better describe this phenomenon, it is necessary to represent the volume velocities of these two regions as two separate acoustic variables, $\mathbf{U_{PF}}$ and $\mathbf{U_{PT}}$. The sum of these two variables is $\mathbf{U_T}$, the volume velocity of the entire tympanic membrane. The movement of the *pars tensa* causes the subsequent vibration of the malleus, incus, and stapes. The ossicular bones, however, are not the only load on the tympanic membrane. The movement of the *pars flaccida* and *pars tensa* must also compresses the air in the bulla cavity, generating sound pressure in the middle-ear cavity, $\mathbf{P_{MEC}}$. In this reasoning scheme, the volume velocity entering the middle-ear cavity must necessarily be the same as the volume velocity of the tympanic membrane, $\mathbf{U_T}$, as they all involve the displacement of the same membrane. This observation has important implication in middle ear modeling, as it dictates a series configuration between the bulla cavity and the tympanic membrane-ossicular complex. At the end of the ossicular chain, the motion of the stapes produces volume velocity $\mathbf{U_S}$ at the oval window, which serves as the input to the inner ear.

Several quantitative models have been proposed to represent the acoustical behavior of the middle ear. The simplest models share the simple network topology shown in Figure 1-6. One central feature of this model is the presence of the series admittance $\mathbf{Y_{CAV}}$ representing the middle-ear cavity. The middle ear input impedance $\mathbf{Y_T} = \mathbf{U_T}/\mathbf{P_{EC}}$ is thus the series combination of $\mathbf{Y_{CAV}}$ and the total admittance contribution from tympanic membranes, ossicular bones, and cochlea, $\mathbf{Y_{TOC}}$.

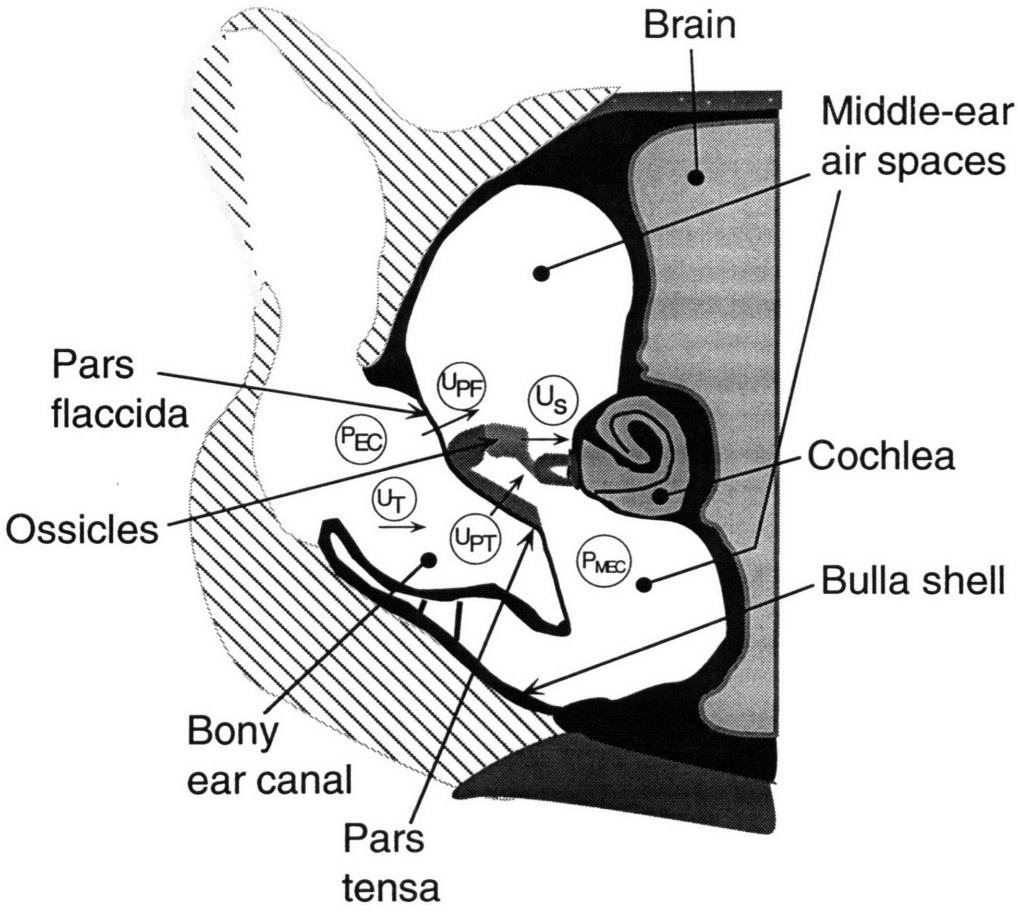

Figure 1-5: A schematic representation of the gerbil middle ear. The acoustic variables used in middle ear modeling are shown circled in this diagram. $\mathbf{P_{EC}}$ = sound pressure in the external ear canal; $\mathbf{U_T}$ = volume velocity of the ear canal (which equals the volume velocity of the entire tympanic membrane); $\mathbf{U_{PT}}$ = volume velocity of the *pars tensa*; $\mathbf{U_{PF}}$ = volume velocity of the *pars flaccida*; $\mathbf{U_S}$ = volume velocity of the stapes — a measure of the input to the inner ear; and $\mathbf{P_{MEC}}$ = sound pressure in the bulla cavity.

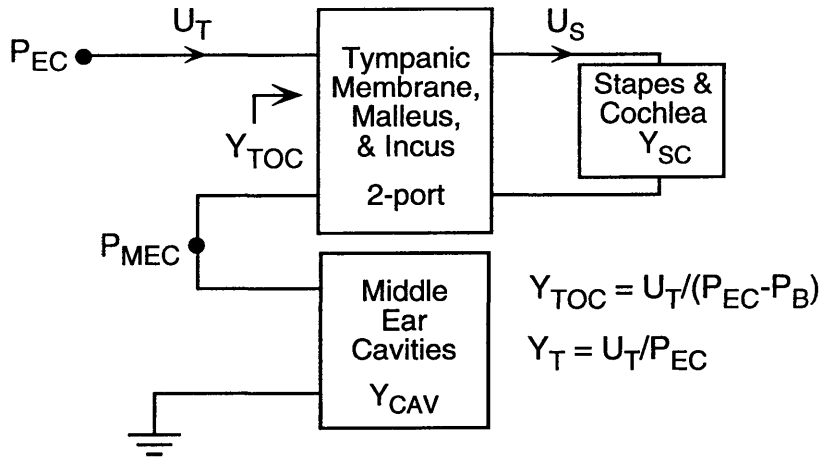

Figure 1-6: The simple middle ear series model. In this representation, all bulla cavities are lumped as a one-port admittance, $\mathbf{Y_{CAV}}$. The total input admittance of tympanic membranes, ossicles, and cochlea are represented by a two-port input admittance $\mathbf{Y_{TOC}}$. The loading effects of stapes and cochlea are modeled as a one-port, $\mathbf{Y_{SC}}$, with $\mathbf{U_S}$, the volume velocity of the footplate, as its sole input. The other model variables are: $\mathbf{P_{EC}}$, sound pressure at the ear canal; $\mathbf{P_{MEC}}$, sound pressure at the middle-ear cavity; and $\mathbf{U_T}$, volume velocity of the tympanic membrane.

One important corollary of this series model is that all volume velocity entering the middle ear cavities is used to compress the tympanic membrane and ossicles, and consequently contributes to the inner ear input. As described in Section 1.2, this assumption may not be entirely accurate. The presence of *pars flaccida* (and to some lesser extent a small uncoupled portion of *pars tensa*) may provide a potential shunt path for the sound volume velocity entering the ear canal. As a result, the middle-ear model for animals with significant *pars flaccida* needs to be revised to include its effect[9].

The function of *pars flaccida* was first described by English surgeon Henry Jones Shrapnell in 1832. He suggested that the compliance of *pars flaccida* is mainly responsible for protecting the stiffer pars tensa from loud noises and large pressure fluctuations by

[9]Zwislocki (1962), Møller (1965), and Kringlebotn (1988) all provided a shunt path in their model for the uncoupled portion of the tympanic membrane. However, they made no provision for the physical correlation of such a path to *pars flaccida*, nor did they quantify the effect of the shunt path on middle ear acoustic transmission.

reducing the quasi-static pressure build up across the tympanic membrane. A similar conclusion was reached by Stenfors *et al.*(1979). However, Hellström *et al.*(1983) found that in rats, which have one of the largest *pars flaccida-pars tensa* ratio among mammals, the volume involved in the *pars flaccida* movements is only 0.5 percent of the middle ear volume, not significant enough to equilibrate the large changes in pressure that can occur within the middle ear.

Thus far, no experimental studies have been done to investigate the role of *pars flaccida* in sound transmission through the middle ear. As a result, the role of *pars flaccida* in middle-ear mechanics is largely unknown; consequently it is often omitted from most middle ear models. In a note published in 1984, Kohllöffel proposed that *pars flaccida* may act as a shunt route for acoustic volume velocity at the tympanic membrane, thus reducing the power available to the inner ear. Such a middle ear model is represented in Figure 1-7.

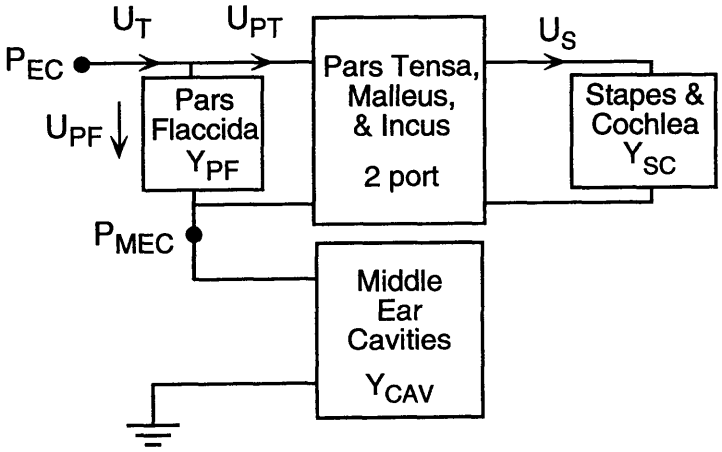

Figure 1-7: Series model that includes the effect of *pars flaccida*. The *pars flaccida* is represented as a one-port complex admittance acting across the input of the *pars tensa*-ossicular complex. The variables of the model are: $\mathbf{P_{EC}}$, sound pressure at the ear canal; $\mathbf{P_{MEC}}$, sound pressure in the middle-ear cavity; $\mathbf{U_T}$, volume velocity of the tympanic membrane; $\mathbf{U_{PT}}$, volume velocity of the *pars tensa*; and $\mathbf{U_{PF}}$, volume velocity of the *pars flaccida*.

In this model, the complex admittance of *pars flaccida* ($\mathbf{Y_{PF}}$) is acting in parallel with the input admittance of the *pars tensa*-ossicular-cochlear complex ($\mathbf{Y_{TOC}}$). As a result, if the input admittance of $\mathbf{Y_{TOC}}$ and $\mathbf{Y_{PF}}$ are in phase (*e.g.* both are compliance dominated), then the addition of the *pars flaccida* could serve to reduce the flow of acoustic volume velocity into the ossicular chain and the inner ear.

The four model blocks can be represented explicitly as circuit elements discussed in Section 1.3 (Figure 1-8). The advantage of such a model is to allow direct quantification of the auditory effect introduced by each modeled component, such as cavity compliance, membrane damping, and ossicular mass. (1) The air spaces of the middle ear cavities are lumped as a single capacitor. This representation should be accurate in the low

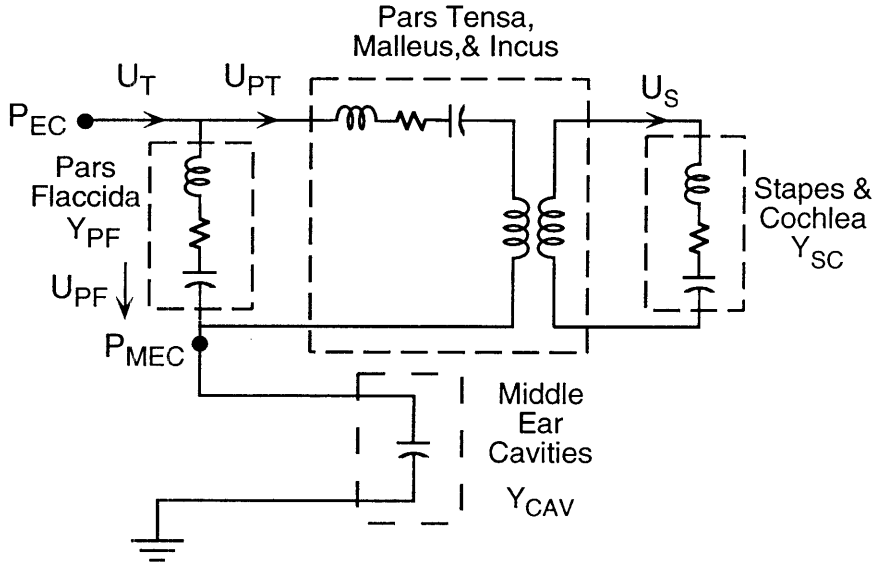

Figure 1-8: Low frequency circuit analog of the middle ear. This model represents the compliance, mass and resistive properties of the middle ear as circuit elements discussed in Section 1.3.

frequency region, where the acoustic effects of the foramina created by the middle ear bony septa are negligible. Experimentally measured cavity admittance (see Chapter 3) shows that this assumption is accurate up to 3 kHz. (2) The *pars flaccida* of the tym-

panic membrane is modeled as a series inductor, capacitor, and resistor as discussed on page 27 to account for its compliance, mass-like and heat dissipative properties. (3) The *pars tensa*, malleus, and incus are similarly modeled by an RLC circuit. In this case, the addition of the malleus, incus, and their associated ligaments are assumed to add additional mass, compliance, and damping to the tympanic membrane. Their effects can therefore be lumped into the series inductor, capacitor, and resistor used to represent the *pars tensa*[10]. An electrical transformer is added to this box to account for the impedance transforming effect of the middle ear. This transformer takes into account the area ratio between the tympanic membrane and the stapes footplate, the lever action of the middle ear ossicles, and the buckling effect of the tympanic membrane. (4) The circuit analog for stapes and cochlea admittance $\mathbf{Y_{SC}}$ follows the work of Lynch *et al.* (1982). According to this report, $\mathbf{Y_{SC}}$ in cat is compliance dominated in the low frequency region, mostly due to the stiffness of the annular ligament. As frequency increases, resistive properties become significant; and at even higher frequencies, the mass-like properties of the stapes and the inner ear fluid predominate. Similar results were obtained by Puria *et al.* (1995) in human. The simplest circuit analog that is capable of achieving such frequency dependent behavior is a simple series RLC circuit, as shown in Figure 1-8.

Most of the element values in this circuit representation, with the exception of *pars flaccida* components, can be obtained by fitting the model to various measurement data available in existing literature. However, since no reported experiments were aimed at studying the effect of *pars flaccida* in middle ear transmission, we have no way of quantifying the *flaccida*'s component values, and hence their impact on sound conduction.

[10]We assume that the malleus and the incus are tightly coupled, such that there is no slippage in the incudo-mallear joint. Therefore, no shunt branch is included to account for the loss of volume velocity through such slippage.

Unge *et al.* (1991) reported that manipulation of the *pars flaccida* in the gerbil ear, in an in vitro preparation, has no effect on the input admittance of the middle ear. In their experiment, the *pars flaccida* was immobilized by either a) covering its external surface with epoxy glue, b) covering the surface with elastic enamel in place of glue, or c) filling the epitympanum with water, which covered the internal surface of the *pars flaccida* but not the *pars tensa*. The tympanogram (essentially the input admittance) of the middle ears was measured at 220 Hz and 660 Hz before and after the manipulations, and they found little or no changes in their measurements. They consequently concluded that the admittance of the gerbil middle ear is dominated by the *pars tensa* and the ossicles, with very little contribution from the *pars flaccida*. Such a result is inconsistent with other available experimental observations. Our preliminary data in rat and gerbil showed that the middle-ear input impedance magnitude at low frequency (<1kHz) greatly increased after the *pars flaccida* was immobilized by dental acrylic, suggesting that *pars flaccida* is either as compliant or more compliant than the *pars tensa*. This finding contradicts the findings of Unge *et al.* (1991).

It is the purpose of this thesis to determine the relative importance of the *pars flaccida* on the signal transmission properties of the middle ear, to test the validity of the circuit model presented in Figure 1-8, and to measure the extent of its influence on the eventual excitation of the cochlea. To accomplish these goals, the middle-ear input impedance, bulla-cavity pressure, and round window cochlear potential are measured under various middle ear conditions. Several sets of experiments are conducted: 1) with the *pars flaccida* and bulla wall intact; 2) with the *pars flaccida* intact, but the bulla cavities widely opened; 3) with the *pars flaccida* replaced by a thin sheet of dental acrylic — thus greatly increasing its stiffness, and leaving the bulla wall intact; 4) with

the *pars flaccida* replaced by dental acrylic, and with the bulla cavities widely opened; and finally 5) with the *pars flaccida* removed, but the bulla wall intact. The results of these measurements are used to compute the *pars flaccida* parameters of the circuit model, verify the linearity assumption in the model, and quantify the amount of inner ear excitation which results from the acoustic properties of the *pars flaccida.*

Chapter 2

Methods

2.1 Experimental subjects

The anatomy of the gerbil middle ear has the attractive features of large cavities and significant *pars flaccida*. These anatomical features make the manipulation of these structures possible, thus allowing us to investigate their acoustic properties and their effect on the animal's hearing. A total of twelve gerbils were used for acoustic and electro-physiological measurements. Two out of the twelve gerbils were used to develop the experimental methodology and to learn about gerbil anatomy. Descriptions of measurements made on these gerbils are documented in Appendix A.

2.2 Acoustic sources and their characteristics

2.2.1 Calibration theory

The configuration of the stimulus delivery system is shown schematically in Figure 2-1. The acoustic source consists of an earphone for sound generation and a microphone for sound measurement. The microphone readings are used as both an indication of sound

level in the ear canal and for the computation of middle ear input-admittance.

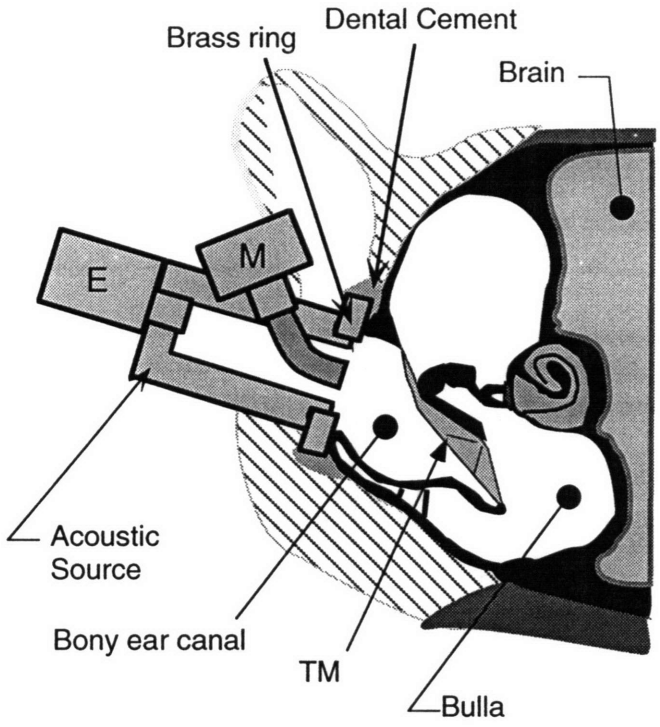

Figure 2-1: Schematic drawing of the acoustic source in a gerbil ear. The acoustic source assembly consists of an earphone (marked E in the diagram) and a microphone (M). The source is coupled to the gerbil ear canal via a cemented brass ring.

The "Comparison Method" is used to retrieve admittance information from the pressure measurements. This method has been described in detail in the research literature (Lynch, 1981; Rosowski et al. , 1984; Dear, 1987; Ravicz et al. , 1992; Lynch et al. , 1994). Simply put, the sound source is modeled as a linear system, with its terminal behaviors completely described by an equivalent volume velocity source $\mathbf{U_S}$ and internal source admittance $\mathbf{Y_S}$. This Norton-equivalent circuit model is shown diagrammatically in Figure 2-2. If $\mathbf{U_S}$ and $\mathbf{Y_S}$ are known, measurements of sound pressures generated by the acoustic source in an unknown load, $\mathbf{P_L}$, can be used to compute the unknown

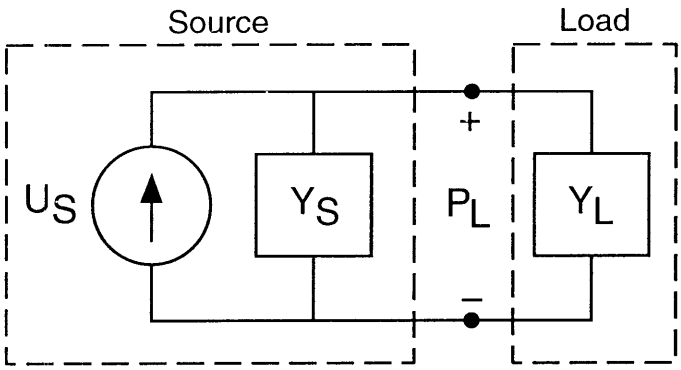

Figure 2-2: Norton-equivalent model of an acoustic source with load. In this circuit analog, the sound source is represented by an ideal current source. The loading of the internal admittance $\mathbf{Y_S}$ and load admittance $\mathbf{Y_L}$ determine the resulting pressure output $\mathbf{P_L}$.

admittance:

$$\mathbf{Y_L} = \frac{\mathbf{U_S}}{\mathbf{P_L}} - \mathbf{Y_S} \tag{2.1}$$

The calibration process of the acoustic source thus includes the determination of the complex amplitudes $\mathbf{U_S}$ and $\mathbf{Y_S}$. These two quantities can be obtained by measuring the sound pressure produced by the acoustic source in two reference loads whose admittances are known theoretically. From Eqn 2.1, it follows that

$$\mathbf{Y_S} = \frac{\mathbf{P_{L1}Y_{L1}} - \mathbf{P_{L2}Y_{L2}}}{\mathbf{P_{L2}} - \mathbf{P_{L1}}} \tag{2.2}$$

where $\mathbf{P_{L1}}$ and $\mathbf{P_{L2}}$ are the pressures measured in the reference loads with known admittances $\mathbf{Y_{L1}}$ and $\mathbf{Y_{L2}}$. $\mathbf{U_S}$ can then be calculated from Eqn 2.1 using either one of the measurements.

In practice, we do not measure $\mathbf{P_L}$ directly, rather, we measure the amplified voltage

output of the microphone, $\mathbf{V_L}$, which is directly proportional to $\mathbf{P_L}$:

$$\mathbf{V_L} = \mathbf{k_s P_L} \tag{2.3}$$

where $\mathbf{k_s}$ is a complex proportionality constant that includes the sensitivity of the microphone and the gain of the amplifier. It has units of $volt/Pa$.

Due to the proportionality relationship between $\mathbf{V_L}$ and $\mathbf{P_L}$, substituting Eqn 2.3 into Eqn 2.2 allows us to cancel $\mathbf{k_s}$ from the equation, and thus we have:

$$\mathbf{Y_S} = \frac{\mathbf{V_{L1}Y_{L1} - V_{L2}Y_{L2}}}{\mathbf{V_{L2} - V_{L1}}} \tag{2.4}$$

We cannot, however, eliminate $\mathbf{k_s}$ from the expression of $\mathbf{U_S}$. As a result, a scaled version of the source volume velocity is obtained:

$$\mathbf{k_s U_S} = \mathbf{V_{L1}(Y_S + Y_{L1}) = V_{L2}(Y_S + Y_{L2})} \tag{2.5}$$

This is not a problem, however, as we are still able to compute the unknown load admittance from $\mathbf{k_s U_S}$, $\mathbf{Y_S}$, and $\mathbf{V_L}$:

$$\mathbf{Y_L} = \frac{\mathbf{U_S}}{\mathbf{P_L}} - \mathbf{Y_S} = \frac{\mathbf{k_s U_S}}{\mathbf{k_s P_L}} - \mathbf{Y_S} = \frac{\mathbf{k_s U_S}}{\mathbf{V_L}} - \mathbf{Y_S} \tag{2.6}$$

Since Eqn 2.6 is the actual equation used to determine the experimental input admittance, I will report the scaled volume velocity as the source volume velocity $\mathbf{U_S}$ throughout this thesis. $\mathbf{U_S}$ thus has the units of $volt - m^3/Pa - sec$.

2.2.2 Source description and characteristics

Theoretically, the paradigm described in the previous section can be used to measure admittance of any unknown load. In practice, the experimental inaccuracies of $\mathbf{U_S}$, $\mathbf{Y_S}$, and $\mathbf{P_L}$ limit the admittance and frequency range of our measurements.

One possible source of error can be explained in terms of the Norton-equivalent model of the acoustic source. Judging from Figure 2-2, it is clear that if $|\mathbf{Y_L}|$ is significantly smaller than the $|\mathbf{Y_S}|$, the resulting pressure $\mathbf{P_L}$ will be controlled primarily by the internal source admittance, not the acoustic load. Thus, the resulting admittance measurements are highly dependent on the accuracy of $|\mathbf{Y_S}|$, whereby a small experimental error in source specification can result in erroneous admittance measurements. Consequently, if we can only specify $|\mathbf{Y_S}|$ with 10% accuracy, we will not be able to accurately measures admittances which are smaller than $0.1|\mathbf{Y_S}|$.

The experimental uncertainty of the measured admittance is also directly dependent on the uncertainty of the pressure measurements. We would therefore expect the strength of the volume velocity source to be an important consideration in determining the signal-to-noise ratio of the resulting sound pressure, and consequently the accuracy of the measured admittance.

In order to produce reasonably accurate and consistent gerbil middle-ear input-impedance measurements, two acoustic sources were used in our study. The combination of these two sources enabled us to measure sound pressure and acoustic admittance over approximately three decades of frequency and four decades of admittance magnitude. Details concerning the construction of these two sources are described in Ravicz *et al.* (1992)[1]. Briefly, one source uses a Knowles ED-1913 hearing aid receiver (Knowles Elec-

[1] A slight modification has been made to the high frequency source, where the sound-delivery tube has

tronics, Elk Grove, IL) as an earphone and a Knowles EK-3027 microphone for sound pressure measurement (Figure 2-3). The relatively small size of this source allows it to

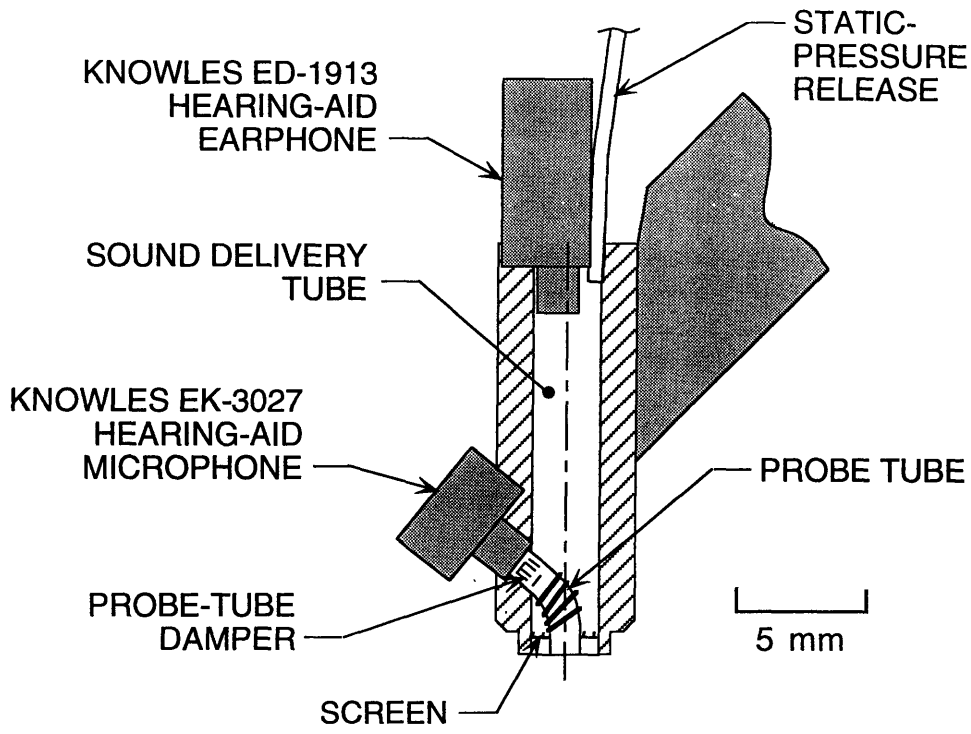

Figure 2-3: Cross-sectional diagram of the low frequency source. The sound delivery tube is packed with cotton to decrease the internal admittance of the source. A small tube is also inserted into this space to prevent static-pressure buildup in the source. The screen is there to prevent fluids from entering the source and changing its internal admittance.

have low admittance, especially at lower frequencies. This desirable feature is achieved at the expense of lower source strength, particularly at frequencies above 3 kHz. Consequently, this source is used primarily for low frequency measurements, and will be termed "low frequency source" or "lfs" in this thesis. The other acoustic source uses a Beyer DT48 dynamic earphone (Beyerdynamic, Germany) as the sound source, while retaining the same Knowles microphone (Figure 2-4). This larger source has higher internal

been lengthened. This has some small effects on the source characteristics, as manifested in the slight differences in U_S and Y_S estimated in this study and Ravicz *et al.* (1992). The source construction

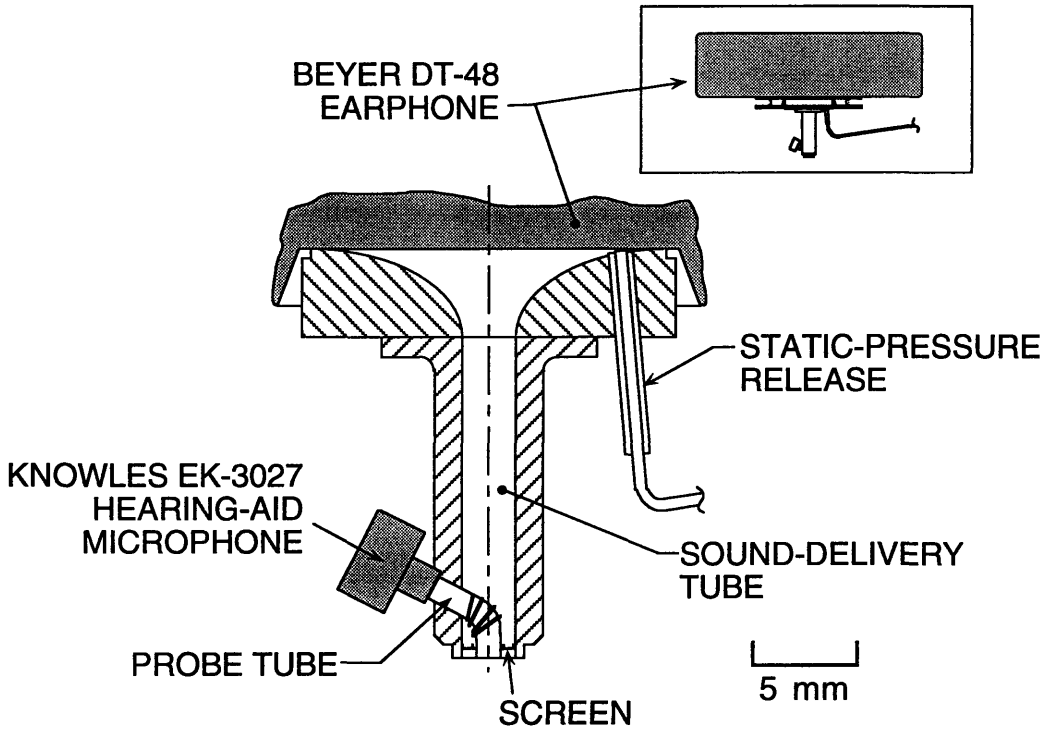

Figure 2-4: Cross-sectional diagram of the high frequency source. This source is similar to the low frequency source, but with the Beyer DT-48 earphone in place of the Knowles ED-1913 receiver.

admittance than the lfs, especially at the lower frequencies. This limitation makes this source unsuitable for measuring loads with low acoustic admittance. However, the Beyer earphone is capable of generating larger sound volume velocity per unit driver voltage, compensating for the shortcoming of the lfs. This source was therefore primarily used for measuring acoustic loads with high admittances, in which large volume velocities are needed to produce a good signal-to-noise ratio, as well as for high frequency measurements in all loads. This source will be referred to as "high frequency source" or "hfs" in this thesis.

Figure 2-5 shows the internal input admittances and source volume velocities of the high and low frequency sources, along with their 95% confidence intervals (which is statistically equivalent to $\pm$ 2 standard errors). The confidence intervals were calculated from fourteen measurements made over a period of seven months. The consistency of the source characteristics are evident from the tight error bounds shown in the figures. The input admittance of the lfs shows compliant behavior over most of the frequency range, resulting in low admittance at the low-frequency region. On the other hand, the source admittance of the hfs is primarily resistive-dominated, with a small peak near 2 kHz, due mostly to the resonance in the sound delivery tube. Note that at frequencies above 7 kHz, the lfs admittance increases dramatically. This is an intrinsic artifact of the lfs, a result of cross-talks between the earphone and the microphone that do not depend on the actual measured sound pressure level. This crosstalk phenomenon is clearly demonstrated in Figure 2-6a, where the blocked microphone registered non-random baseline readings that were independent of the real sound pressure levels. At frequencies above 7 kHz, this artifact recording dominates the microphone output of the tygon tube measurement, thus

method, however, remains the same.

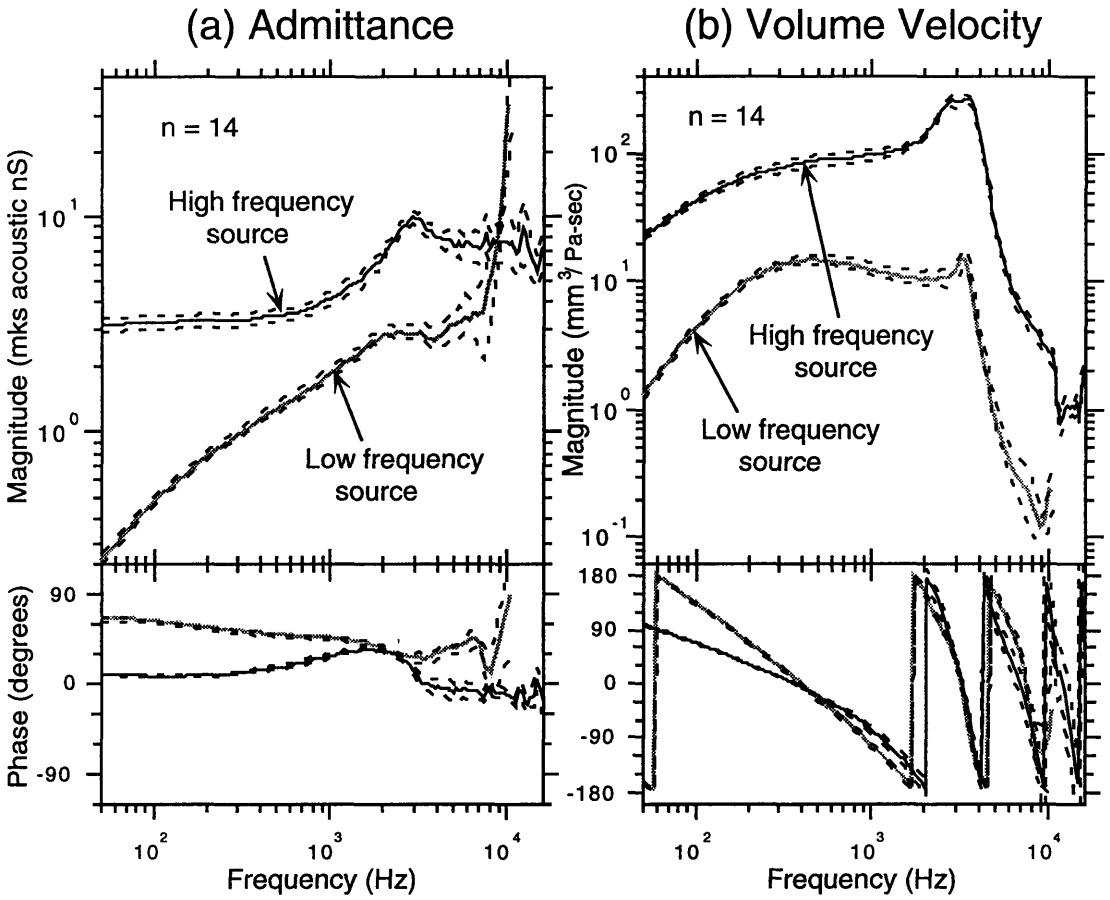

Figure 2-5: Internal admittances and normalized volume velocities of the acoustic sources. (a) Internal admittance of acoustic sources. 14 measurements over a 7 month period are used to calculate the 95% confidence intervals of these plots. The measurements include several pre and post-experiment calibration results. The error bounds are small over most of the low frequency region. They increase slowly for both sources at frequencies above 3 kHz, where the impedances are primarily resistive. These variations are most likely due to the different conditions of cotton packing in the sound delivery tubes, where the presence of fluid or other materials could affect their damping property. The reference loads used to obtain the source admittances are described in Section 2.2.3. (b) Normalized source volume velocities of the acoustic sources. The substantially higher volume velocity output of the hfs shows the greater efficiency of the Beyer earphone as compared to the Knowles earphone. Both sources exhibit bandpass behavior that could decrease the accuracy of pressure and admittance measurements in the very low and very high frequency region, especially in high admittance acoustic loads.

causing the gross inaccuracy in the admittance calculation. This phenomenon renders the lfs unusable at frequencies above 7 kHz. The volume velocity plots in Figure 2-5b are normalized quantities. They represent the volume velocity outputs per unit driver voltage[2]. The high frequency source shows approximately 20dB greater output than the lfs, thus making it more suitable for measurements of high admittance acoustic loads. In addition, the crosstalk artifact that plagued the lfs does not affect the hfs except at frequencies above 10 kHz (see Figure 2-6b). Both sources show dramatic decrease in volume velocity output at high frequencies. This could affect the signal-to-noise ratio of measurements made in this region. The low frequency rolloffs are not as severe, but they do pose a limitation for measurements at very low frequencies.

2.2.3 Acoustic loads for source calibration

Lynch *et al.* (1994) described the considerations involved in choosing suitable calibration loads to minimize the experimental errors in determining $\mathbf{U_S}$ and $\mathbf{Y_S}$. The analysis indicates that most error-magnifying conditions can be avoided if one of the reference load admittances is larger, and the other is smaller than the source admittance:

$$|\mathbf{Y_{L1}}| < |\mathbf{Y_S}| < |\mathbf{Y_{L2}}| \tag{2.7}$$

Two types of reference loads were designed to satisfy this requirement. A long Tygon tube terminated by an acoustic resistor that matches the characteristic impedance of the tube was used as the high admittance load, while a small stiffness-dominated cavity

[2]The stimulus used in this study is a linear chirp rather than tone sweep, the voltage unit is therefore not defined as the customary rms voltage. Instead, the amplitude of the uniform frequency spectrum (which incidentally is equal to the amplitude of the chirp signal) is used as the reference unit. More information on this topic is discussed in Section 2.4 concerning stimulus paradigms.

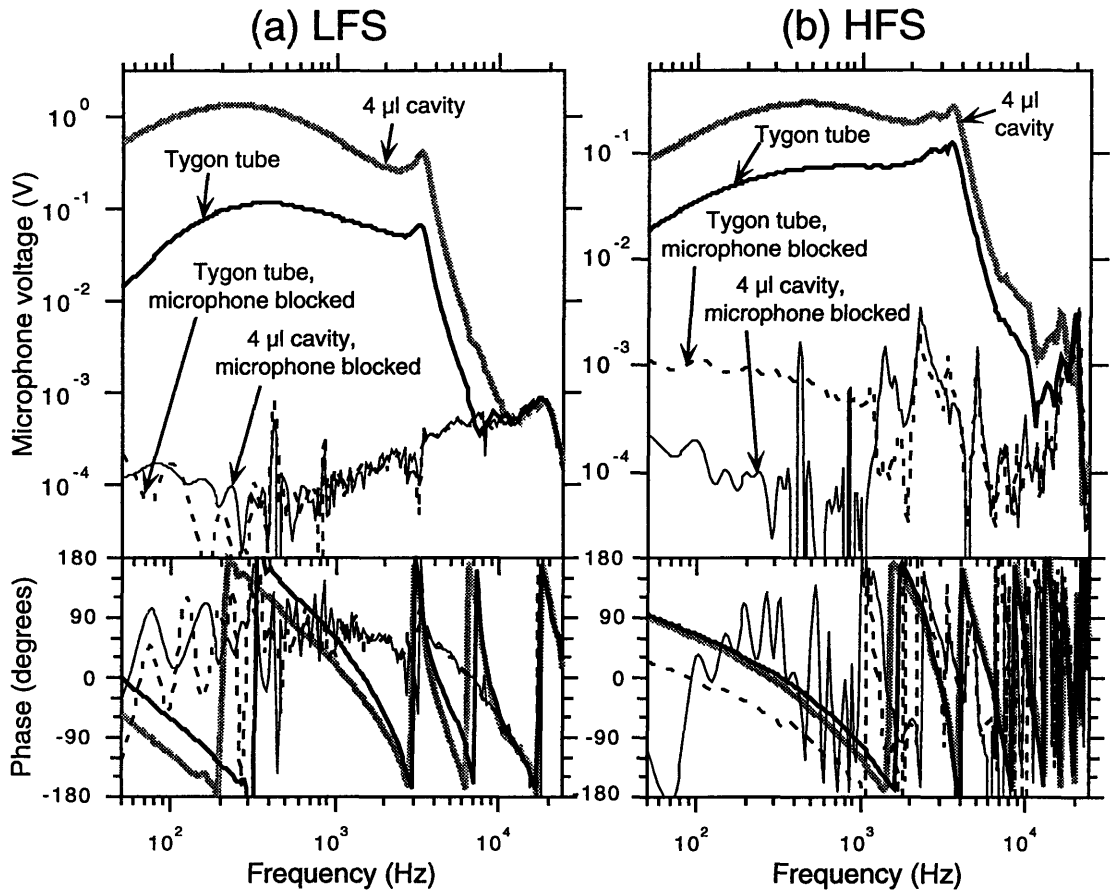

Figure 2-6: Sound pressure recordings that illustrate the crosstalk artifact in the acoustic sources. The pressure measurements were made with (a) low-frequency source and (b) high-frequency source. Four pressure measurements are shown in this figure: two were made in the 4 μl cavity and two were measured in the long Tygon tube. For one measurement in each load, the microphone opening was completely blocked with clay. The earphone driver voltage was set to either 0.1V (LFS) or 0.01V (HFS).

was used as its low admittance counterpart. The accuracy of the source calibration was verified by measuring acoustic admittances of other known reference loads using the computed $\mathbf{Y_S}$ and $\mathbf{U_S}$, and comparing them with their theoretical values. All reference loads were designed such that their physical characteristics, including volumes, lengths, and diameters, could be measured accurately for use in theoretical computations (Ravicz, 1990). Figure 2-7 illustrates how a reference load can be coupled to the acoustic source. Table 2.1 lists the physical characteristics of all the reference loads used in this study,

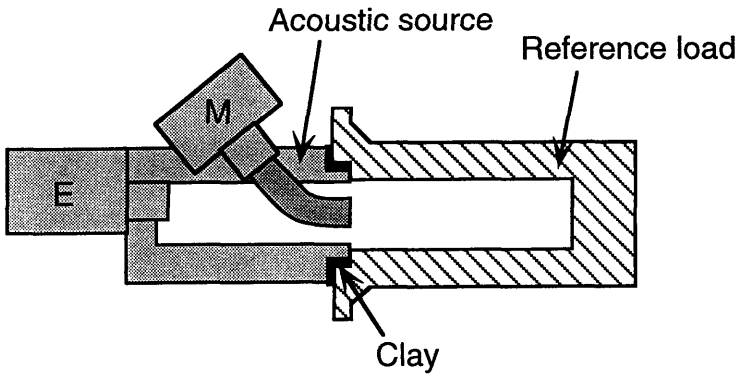

Figure 2-7: Coupling of reference load to the acoustic source. To ensure airtight sealing, clay is used to fill the spaces between the contacting surfaces.

and Figure 2-8 shows the cross sectional diagrams of their physical constructions.

The reference loads were modeled according to the two-port transmission line equations proposed by Egolf (1977). This two-port model takes into account thermal losses due to viscous friction and heat conduction through the cavity walls. The model uses equations originally developed for application to transient fluid flow in pipes, and requires as input arguments the length, diameter, and the termination load of the cavity. Figure 2-9 shows how the two-port model can be combined with the appropriate terminating conditions to model the reference loads. The computed load admittances are shown in Figure 2-10.

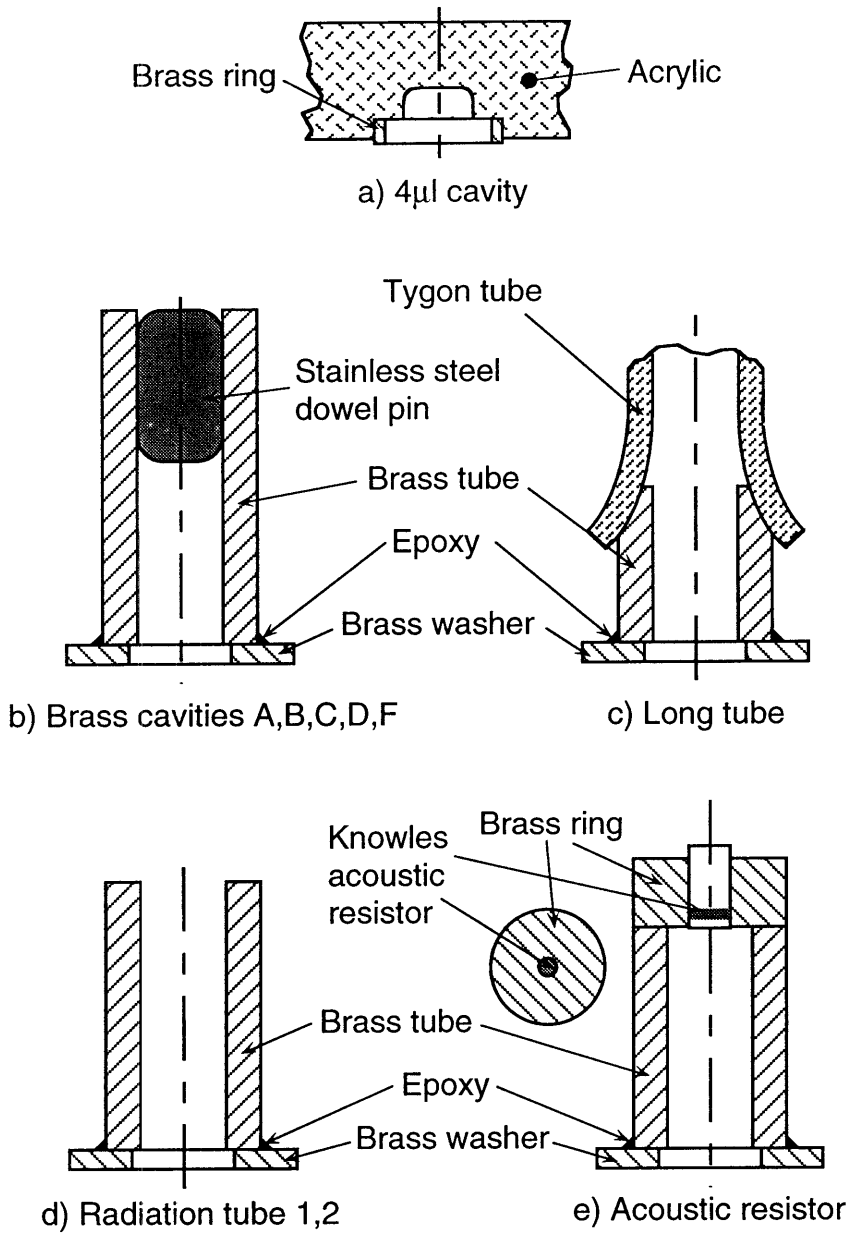

Figure 2-8: Cross-sectional diagram of reference loads. All these reference loads contain either a brass ring or washer that allows easy coupling to the acoustic source. a) The $4\mu l$ cavity, along with the long tube, are used to calibrate $\mathbf{U_S}$ and $\mathbf{Y_S}$. Its small volume gives it the highest stiffness among all the acoustic loads. b) Brass cavities A, B, C, D, and F all have the same constructions. The cavities are made of brass tubes with a stainless steel dowel pin pressed in at one end. c) The long tube consists of a Tygon tube inserted into a tapered brass tube to minimize any abrupt change in diameter. The end of the tube is terminated by an acoustic resistor that matches the characteristic impedance of the Tygon tube. d) The radiation tubes have the same construction as the enclosed cavities except that the dowel pins are omitted. e) The acoustic resistor is constructed by attaching a brass ring to one end of a radiation tube. The inner diameter of the brass ring is approximately equal to the outer diameter of a Knowles acoustic resistor, such that the Knowles resistor can fit snugly in the bored hole.

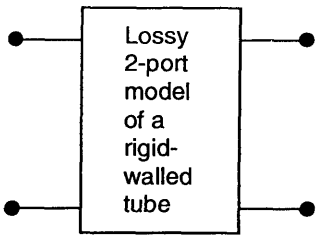

a) Mathematical model of all rigidly terminated cavities

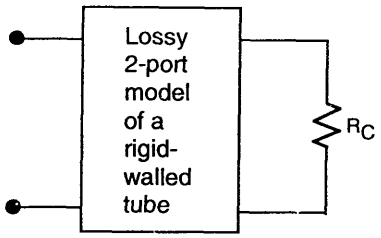

b) Mathematical model of the long Tygon tube

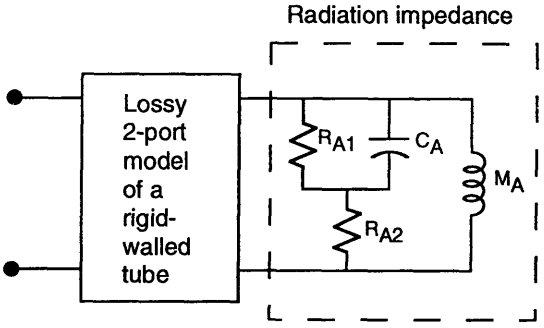

c) Mathematical model of radiation tube 1 and 2

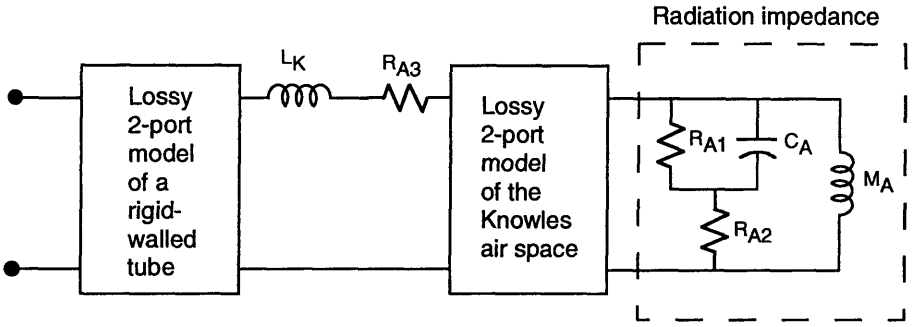

d) Mathematical model of the acoustic resistor

Figure 2-9: Mathematical models of the acoustic loads. All acoustic cavities are modeled as lossy two-port transmission-line models. a) For all enclosed cavities, the rigid termination is modeled as a load of infinite impedance (*i.e.* an open circuit). b) For the long Tygon tube, the tube characteristic impedance $R_C = \rho_o c/A$ is used as the terminating impedance, where A is the cross-sectional area of the tube. c) The radiation tube is terminated by the radiation impedance, which was modeled after the circuit analog by Beranek (1986). The circuit variables are defined as: $R_{A1} = 0.1404\rho_o c/a^2$ mks acoustic Ω, $R_{A2} = 0.318/a^2\rho_o c$ mks acoustic Ω, $C_A = 5.94a^3/\rho_o c^2\ m^5/newton$, and $M_A = 0.27\rho_o/a\ kg/m^4$, where a is the inner radius of the tube. d) Both the spaces in the Knowles resistor and the brass tube are modeled as transmission-line two-ports. The radiation impedance is considered the load of the smaller Knowles cavity. The input impedance of this Knowles two-port, plus the Knowles resistance R_{A3} and Karal inertance L_K, act as the cascading load on the second two-port. $R_{A3} = 100$ mks MΩ is the specification of the Knowles resistor. The Karal correction factor L_K (Karal, 1953) is used to model the sudden change in cross-sectional area from the brass tube to the Knowles cavity. Its value was determined from fitting experimental data to the model, and was found to be 0.02 Henry.

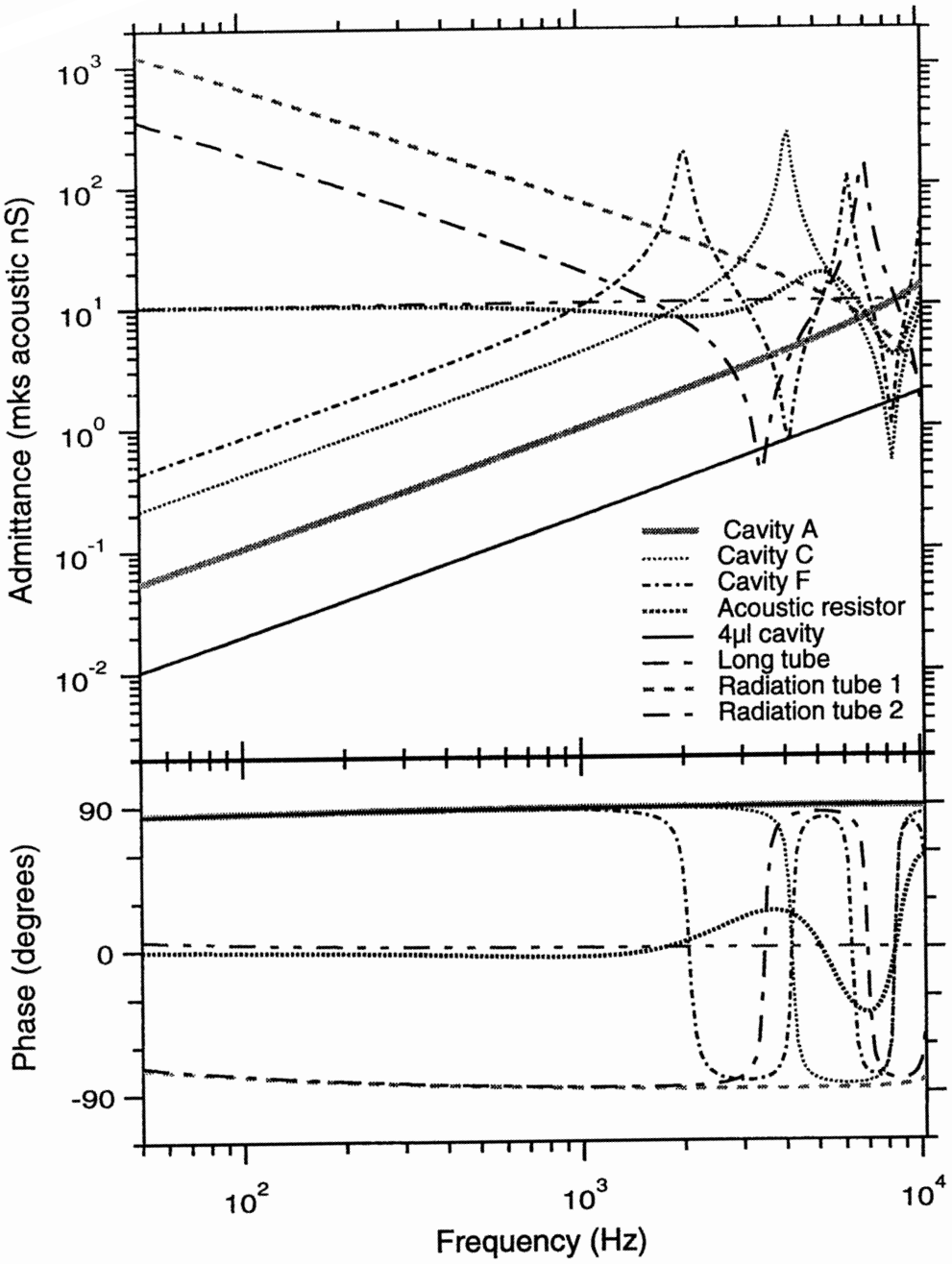

Figure 2-10: Admittances of reference loads. Below 1 kHz, the $4\mu l$ cavity and cavities A, C, and F all exhibit compliance behavior, with slope of 20 dB/decade, consistent with the circuit analog characteristics described in Chapter 1. In this frequency range, the radiation tubes show mass-like characteristics, with 20 dB/decade drop in admittances; while the acoustic resistor and the long tube are mostly resistive, with their admittances independent of the frequency. Above 1 kHz, damped poles-and-zeros oscillations are observed in all loads except the long tube. These phenomena are the results of quarter-wave resonances occurring in these cavities. The matched impedance at the end of the long tube prevents the occurance of such resonance in that load. The impedances were computed at frequencies that were separated by 25 Hz. Finer frequency resolution could enhance the sharp minima and maxima.

Load	Diameter (mm)	Length (mm)	Volume (μl)	Acoustic characteristics
4 μl cavity	2.34	1.02	4	compliance
Cavity A	2.30	5.07	21	compliance
Cavity B	2.30	10.28	43	compliance
Cavity C	2.30	20.32	84	compliance
Cavity D	2.30	29.95	125	compliance
Cavity F	2.30	40.61	170	compliance
Acoustic resistor	2.30	23.5	-	resistive
	1.96	4.00	-	
Long tube	2.37	30 m	-	resistive
Radiation tube 1	2.30	6.45	-	mass-like
Radiation tube 2	2.30	23.70	-	mass-like

Table 2.1: Specifications of the reference loads. This table lists the dimensions and primary acoustic characteristics of the reference loads used in this thesis. Note that there are two spaces associated with the acoustic resistor (see Figure 2-8), thus two rows are needed to specify its dimension. The characteristics of the larger brass tube is shown on the first row, while the second row shows the dimensions of the Knowles acoustic resistor inserted into the brass ring at the top of the load.

For the hfs, the source volume velocities and admittances (Figure 2-5) were obtained using the $4\mu l$ cavity and long Tygon tube as the calibration loads. Theoretically, these two cavities can also be used to accurately calibrate the low-frequency source, as their admittance magnitudes satisfy the constraint of Eqn. 2.7 (all these admittances are shown in Figure 2-11). In practice, the low power output of the lfs and the high admittance of the Tygon tube in low frequency regions caused the pressure response in the reference load to be near the noise floor. Consequently, cavity F is used to calibrate the lfs for frequencies below 900 Hz. At frequencies above 1500 Hz, the resonances of the cavity F admittance adversely affected the accuracy of the calibration computation, thus the long Tygon tube is used in this range instead. For frequency between 900 and 1500 Hz, a linearly weighted average of the two measurements was used.

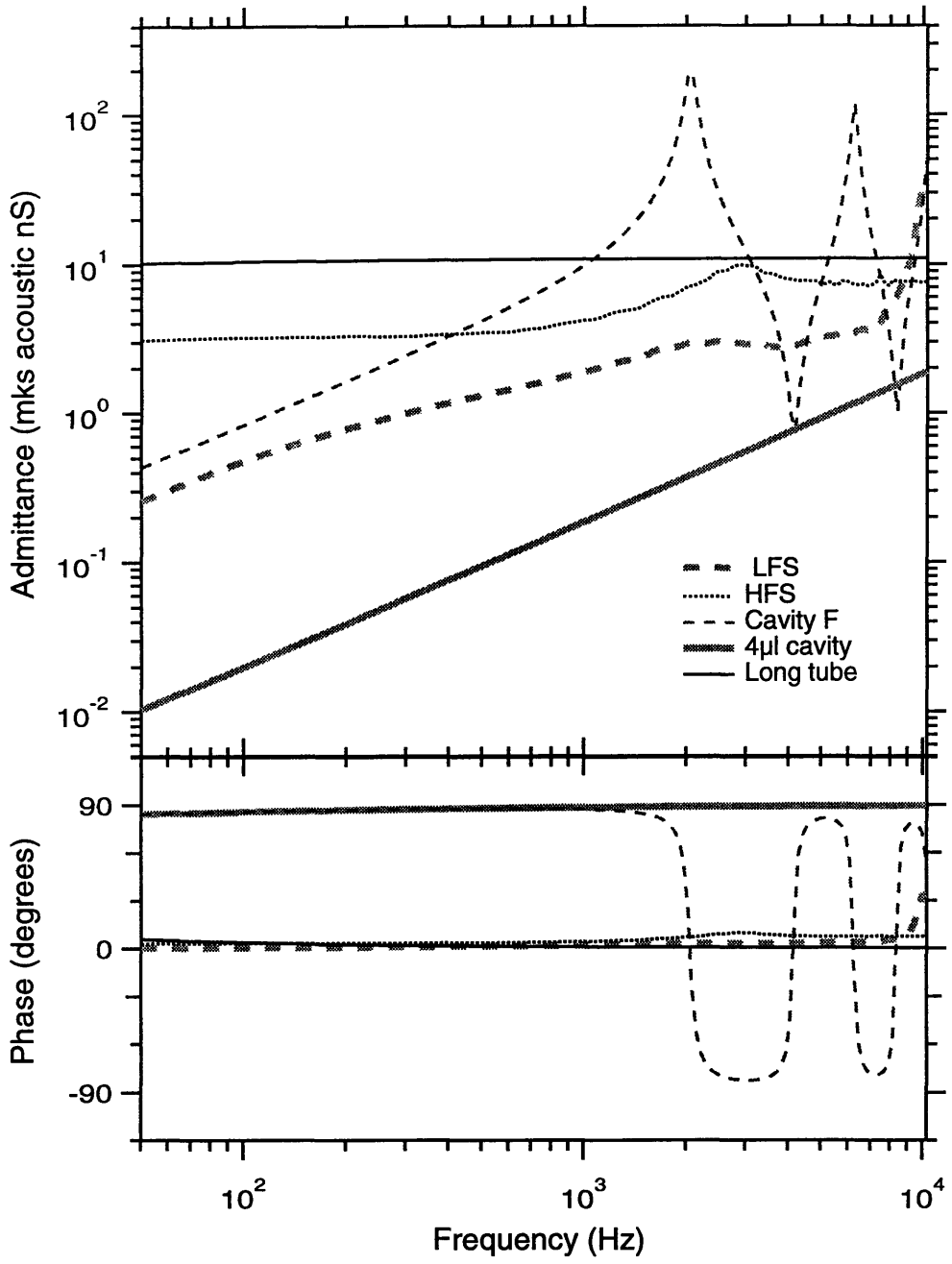

Figure 2-11: Admittances involved in the calibrations of acoustic sources. Consistent with Eqn. 2.7, the admittance magnitudes of the high and low frequency sources are intermediate to the admittances of the two reference loads: the long Tygon tube and the $4\mu l$ cavity. To overcome the problem of lfs's low pressure output in the Tygon tube at low frequency, cavity F is used at frequencies below 900 Hz.

2.2.4 Accuracy and limits of acoustic calibration

To verify the accuracy of the calibration results, admittance measurements in other reference loads were made. Figure 2-12a shows the theoretical admittance of cavity D, along with the measured results using the low frequency source. Consistent with the discussions in the previous section, the lfs measurement agrees well with the expected value for frequencies up to approximately 6 kHz. Beyond that region, the high source admittance and the low pressure output combine to cause the measurement to be grossly inaccurate. The high frequency source measurement of cavity D admittance is shown in Figure 2-12b. The accuracy of this source at high frequency is substantially improved, while large errors are evident at frequencies below 200 Hz.

This verification process was performed on all the reference loads shown in Figure 2-8. In order to determine the volume velocity limits of the acoustic sources, measurements were repeated at various pressure levels. The errors[3] computed from these measurements were used to determine the range of impedance magnitude and frequency that can be measured accurately. Appendix B contains the accuracy charts determined in this fashion. The levels of the earphone driver voltage were varied over a 30 dB range: from 0.32 V to 0.01 V for the lfs (*i.e.* set the computer output to 1 V and varied the attenuator setting from 10 dB to 40 dB), and from 0.032 V to 0.001 V for the hfs.

Results in Appendix B show that the usable range of the lfs was limited to frequencies below 6 kHz for all voltage levels. This limitation on high frequency measurements was the result of the low volume-velocity output of the earphone and the cross-talk artifact between the earphone and the microphone. The low earphone output at the low frequency region also restricted the measurement accuracy, especially at admittance above

[3]Error is defined as the difference between the measured and the theoretical values.

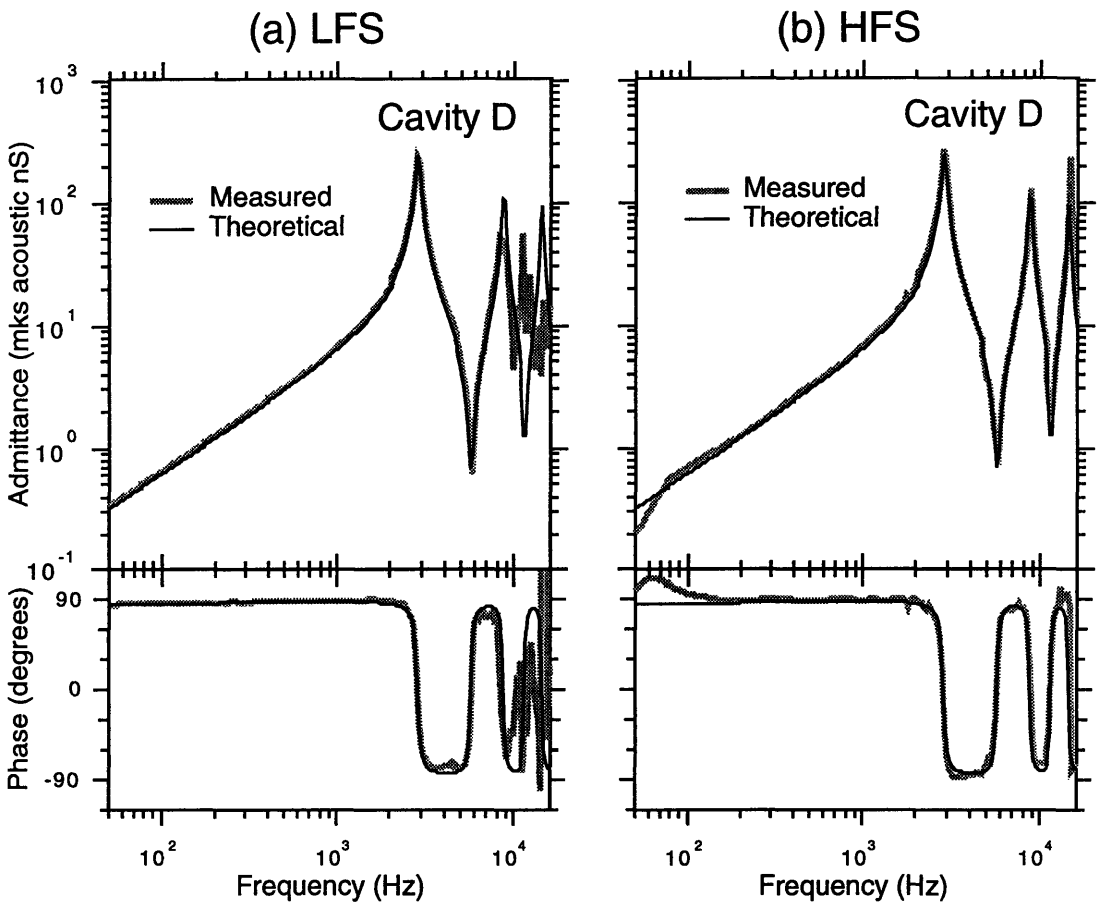

Figure 2-12: Comparison of theoretical and measured cavity admittance. (a) The lfs measurement result clearly shows that the lfs is more suitable for measurements at frequencies lower than 5 kHz, as predicted from its source characteristics. (b) The hfs produced substantially more accurate admittance measurements in the high frequency region. Due to its large source admittance at low frequencies, significant errors can be observed at frequencies below 200 Hz.

20 nS. Aside from these two regions, the lfs showed great accuracy, with errors smaller than 1 dB in magnitude and 5° in phase, over region that extend from 50 Hz to 6 kHz in frequency and 0.1 nS to 20 nS in admittance (except when the driving voltage was set to 0.32 V). This measurement region encompasses the gerbil middle-ear input admittance and middle-ear cavity admittance, as well as the internal admittances of both acoustic sources. With the driving voltage set to 0.32 V, the generated sound pressures levels in low admittance loads were beyond the measurable range of the microphone amplifier. The clipped signals thus resulted in gross inaccuracy when measuring admittances below 0.5 nS.

The charts of the hfs show improved accuracy at frequencies up to approximately 10 kHz. No signal clipping occurred in any of the four voltage settings; thus, the accuracy patterns were similar in all four cases. The lower limit of the measurable admittance was restricted by the high internal admittance of the hfs (as discussed in Section 2.2.2). As a result, the accuracy of the admittance measurements below 0.3 nS was substantially inferior to that of the lfs. The volume velocity output of the hfs earphone determined the upper limit of the admittance measurements. With high admittance loads, the generated sound pressure is reduced. This, along with the lower source output at low frequency, caused the decrease in signal-to-noise ratio and increase in measurement errors in the high-admittance, low-frequency region. At the high frequency end, the cross-talk artifact was present only at frequencies above 10 kHz, making it more suitable for high frequency measurements. Overall, the hfs provided accurate admittance measurements from 200 Hz to 10 kHz in frequency, and from 0.3 nS to 200 nS in admittance amplitude.

2.2.5 Level dependency of source characteristics

The acoustic sources used in this study were assumed to be linear devices. This assumption required that source admittances and normalized source volume velocities measured at different pressure levels be identical. To test the validity of this linearity assumption, $\mathbf{U_S}$ and $\mathbf{Y_S}$ were measured at several pressure levels. Figure 2-13 shows the admittances and the normalized volume velocities of the hfs obtained with the driver voltages 20 dB apart (the corresponding sound-pressure levels were approximately 70 dB SPL and 90 dB SPL, respectively). Most physiological measurements were made within this 20 dB range. The results show that in both cases, the 95% confidence intervals have significant overlaps over all frequencies (measurements were also made at three intermediate pressure levels between these two cases, and the results are similar). We can therefore conclude that the linearity assumption is valid for the hfs, at least in the sound-pressure range of interest.

The corresponding lfs measurements are plotted in Figure 2-14. Both $\mathbf{U_S}$ and $\mathbf{Y_S}$ show good consistency with very small error bounds. However, the 95% confidence intervals of the two $\mathbf{Y_S}$ show some small but noticeable differences for frequencies below 300 Hz. For $\mathbf{U_S}$, the disagreements occur only at frequencies below 100 Hz. This nonlinearity, while noticeable, is less than 2% over a 20 dB pressure range. This is significantly lower than the experimental uncertainty of most physiological measurements, and therefore can be considered negligible. As a matter of consistency, all impedance measurements shown in this thesis were computed from the source characteristics obtained at the same stimulus voltage level.

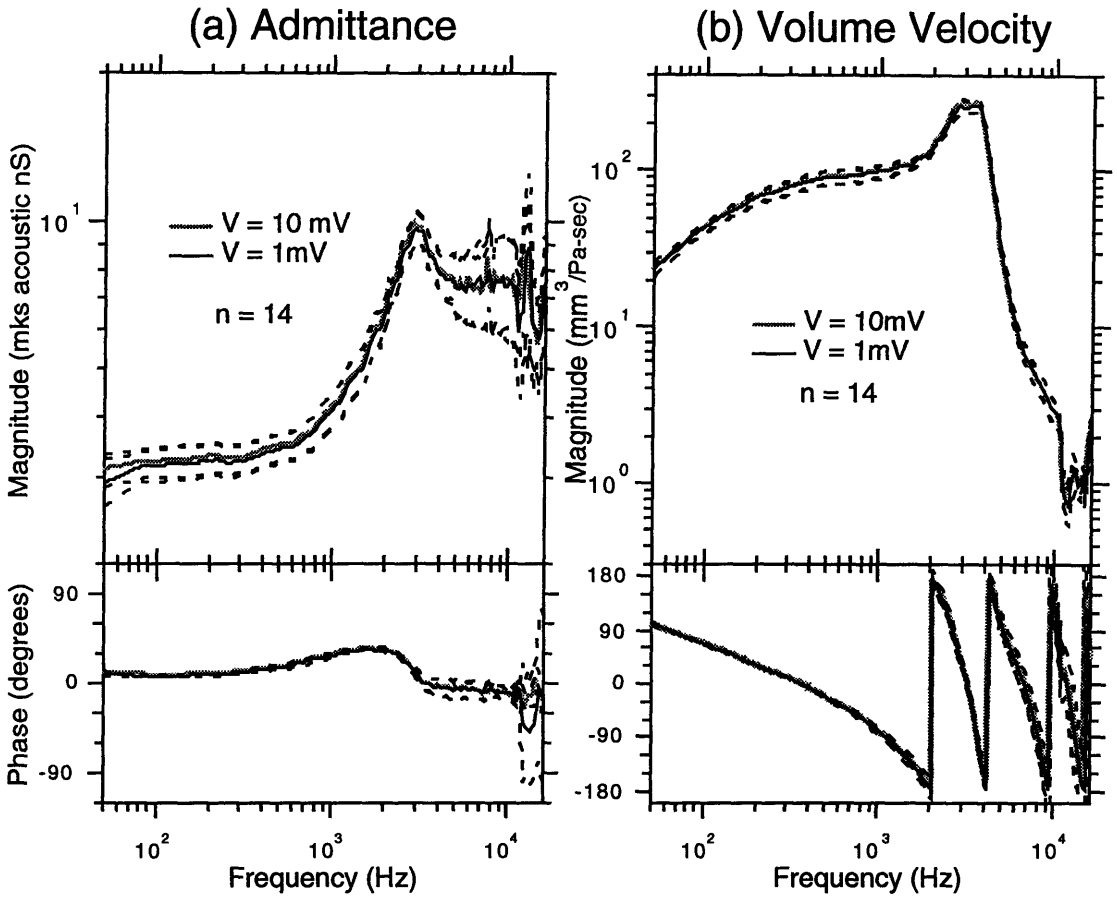

Figure 2-13: Source admittance and volume velocity measurements of hfs at two pressure levels. The two pressure levels were generated with the source driving voltages set to 1 and 10mV (The voltage values correspond to the amplitude of the chirp spectra). The 95% confidence intervals are shown along with the means calculated for 14 different measurements.

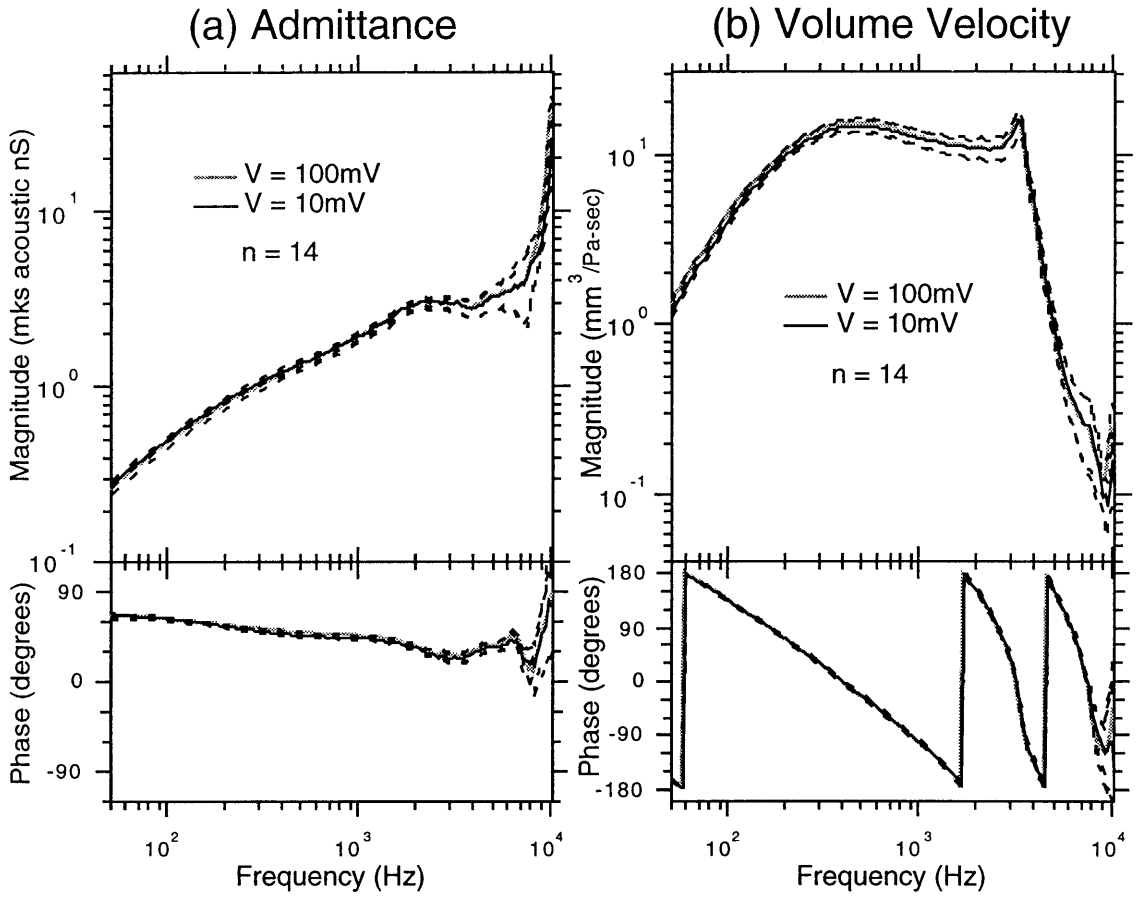

Figure 2-14: Source admittance and volume velocity measurements of lfs at two pressure levels. The two pressure levels were generated with the source driving voltages set to 10 and 100mV (The voltage values correspond to the amplitude of the chirp spectra). The 95% confidence intervals are shown along with the means calculated for 14 different measurements.

2.3 Acoustic calibration

2.3.1 Absolute calibration

Most measurements of interest in this thesis, such as middle-ear input admittances, ear-canal-to-middle-ear pressure ratios, and middle-ear transfer functions, do not require the knowledge of actual sound pressure levels in either the ear canal or the middle ear. However, to ensure that the applied sound-pressure level was in the linear region of middle-ear mechanics (Guinan and Peake, 1967; Nedzelnitsky, 1980), it was necessary to determine the exact sound pressure level applied at the ear canal.

The absolute calibration of the sound sources required the use of a third microphone. This reference microphone (a Larson Davis 1/4 inch microphone model 910B) was pre-calibrated with a Larson Davis piston phone that was known to generate 114 dB SPL at 250 Hz. Since the reference microphone has a flat frequency response across the frequency range of interest, the piston phone measurement at a single frequency allowed us to fully characterize the sensitivity of the reference microphone (in terms of $\frac{Pa}{|\mathbf{V_{ref}}|}$).

Each sound source was coupled to the reference microphone in a small brass cavity. The tonal stimulus generated by the earphone was then measured simultaneously with both the sound source and the reference microphones. Assuming that the pressure measurements of the two microphones were the same[4], their ratio allowed us to determine the absolute calibration of the sound source for tonal stimulus:

$$\frac{Pa}{|\mathbf{V_S}|} = \frac{Pa}{|\mathbf{V_{ref}}|}\frac{|\mathbf{V_{ref}}|}{|\mathbf{V_S}|}. \tag{2.8}$$

[4]Using the 1/10th wavelength criterion of Chapter 1, this assumption is valid at frequencies up 10 kHz if the distance between the the two microphones is less than 3mm. Most of the calibration measurements were made with the two microphones less than 1mm apart.

The calibration with the chirp stimulus required further computations. In SYSid (the data acquisition software used in this study), the frequency spectra of chirp and tone are scaled such that their spectral amplitudes are the same as the amplitudes of their time domain counterparts. For example, a sine wave of unit amplitude and a linear chirp of unit amplitude are both scaled by SYSID to have unit spectral amplitudes, even though the spectrum of the sine wave has only a single component while the chirp spectrum represents $nfft/2$ different sinusoidal components ($nfft$ is the size of the discrete-time spectrum). This convention is useful for the visual comparison of signal levels in both time and frequency domains; however, it is mathematically incorrect. Since both the chirp and the sine waves contain the same amount of power in the time domain, their frequency spectra must also contain equal amount of power. The power of the chirp spectrum (which is the square of the pressure amplitude) must therefore be rescaled by a factor of $1/(nfft/2)$ to correct for this power discrepancy. if x is the amplitude of the tonal spectrum, and y is the corrected amplitude of the chirp spectrum, the power consideration thus requires that:

$$y = \frac{x}{\sqrt{nfft/2}} \tag{2.9}$$

where $1/\sqrt{nfft/2}$ is the correction factor. With the tonal calibration factor determined above, we can compute the new chirp calibration factor as:

$$\left.\frac{Pa}{|\mathbf{V_S}|}\right|_{chirp} = \left.\frac{Pa}{|\mathbf{V_S}|}\right|_{tone} \frac{1}{\sqrt{nfft/2}}. \tag{2.10}$$

Multiplication of this calibration factor with the source microphone output $\mathbf{V_S}$ thus generates the sound pressure level in Pa.

2.3.2 Probe-tube microphone calibration

In the experiment, a probe-tube microphone was used to measure the gerbil middle-ear pressure. The complex proportionality constant of the probe-tube microphone $\mathbf{k_{pt}}$ was most often different from that of the acoustic source $\mathbf{k_s}$ (see Section 2.2.1). As a result, we must determine the relationship between these two constants in order to meaningfully compare the pressure levels in the ear canal and the middle ear cavity.

To calibrate their relative sensitivities, the acoustic source and the probe-tube microphones were coupled in a small cavity, such that the pressure measured by the two microphones were considered equal. Consequently, the ratio of the two microphone output voltages was also the ratio of their proportionality constants:

$$\frac{\mathbf{V_S}}{\mathbf{V_{PT}}} = \frac{\mathbf{k_s}}{\mathbf{k_{pt}}} = \mathbf{m} \tag{2.11}$$

where $\mathbf{m}$ is a new normalization constant. Figure 2-15 shows the experimentally obtained $\mathbf{m}$. The 95% confidence intervals were obtained from 14 measurements over a seven month period.

When the probe-tube microphone is placed in the bulla cavity and the acoustic source in the ear canal, the pressure ratio at these two locations can be obtained by simply multiplying their voltage ratio with $\mathbf{m}$:

$$\frac{\mathbf{V_{PT}}}{\mathbf{V_S}}\mathbf{m} = \frac{\mathbf{V_{PT}}}{\mathbf{V_S}}\frac{\mathbf{k_s}}{\mathbf{k_{pt}}} = \frac{\mathbf{P_B}}{\mathbf{P_{EC}}} \tag{2.12}$$

where $\mathbf{P_B}$ is the pressure in the bulla cavity, and $\mathbf{P_{EC}}$ is the pressure in the ear canal.

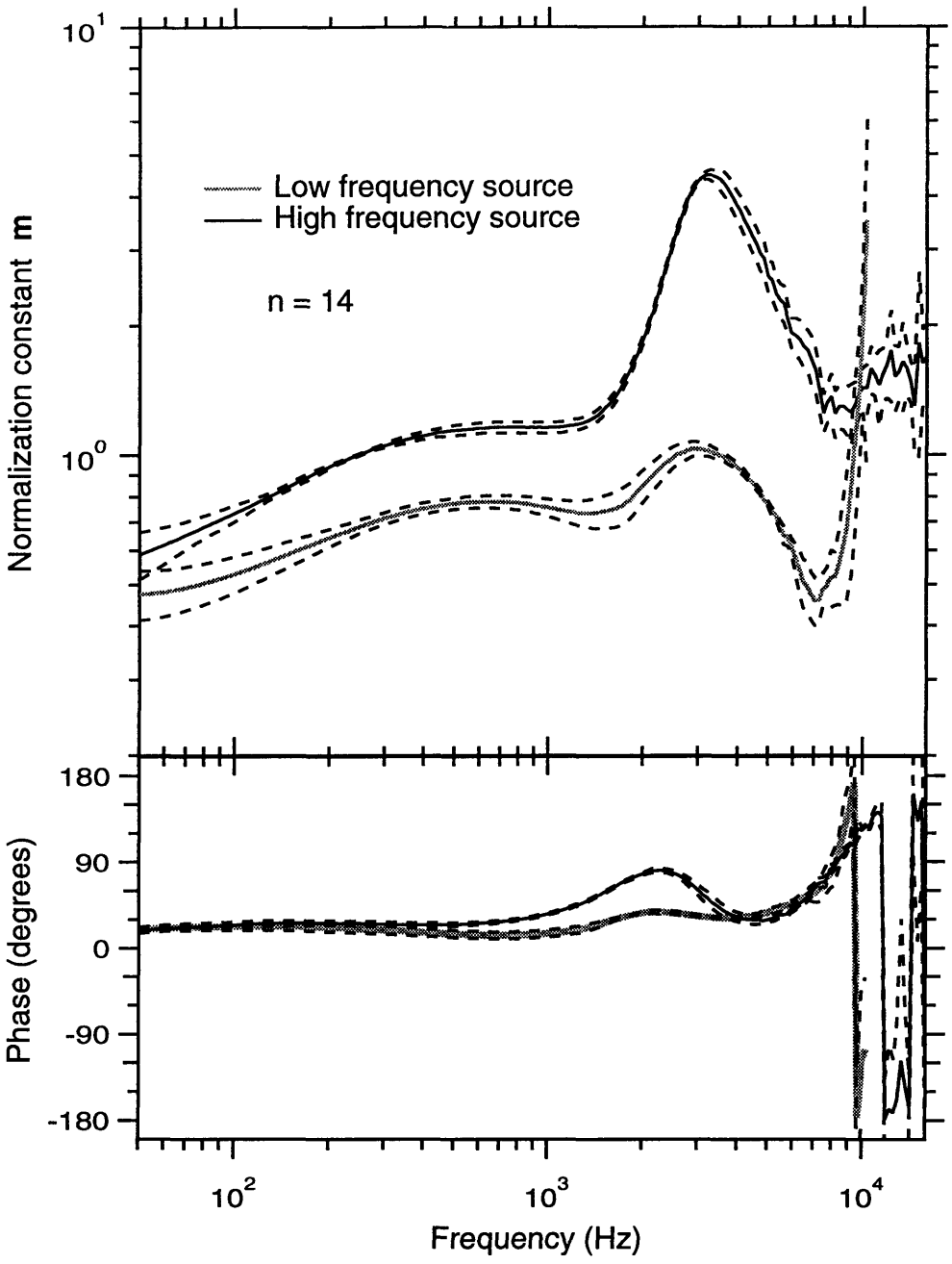

Figure 2-15: The probe tube normalization constant **m**. Except at the lowest frequencies, the normalization constant shows good consistency over the seven month measurement period. The larger variations at frequencies below 100 Hz is most likely due to leakage in some of the measurement setups. The peaks at 2 kHz are the results of resonance in the source probe tubes. The difference between the high and low frequency sources will be explained in Section 2.2

2.4 Stimulus paradigms

Two type of stimuli were employed in this study: chirp and tone sweep. The chirp stimulus was used to measure middle-ear input admittance, and ear canal and middle-ear pressures. The stimulus was synthesized digitally by performing an Inverse Fast Fourier Transform (IFFT) of a flat frequency spectrum with quadratic phase (linear group delay):

$$\mathbf{F}[k] = \begin{cases} e^{-j\frac{2\pi k^2}{nfft}} & k = 0 \ldots \frac{nfft}{2} \\ e^{j\frac{2\pi k^2}{nfft}} & k = -\frac{nfft}{2} + 1 \ldots -1 \end{cases} \tag{2.13}$$

where $nfft = 2048$ is the size of the discrete-time spectrum. The main advantage of using a chirp signal was the speed of the measurement process. With the sampling rate of our digital-to-analog converter set at 50 kHz, the duration of the whole stimuli was only 81.92 ms. This brief signal covers a frequency range from 25 Hz to 25 kHz. Each of our measurements consisted of an average of 150 chirp responses, which took approximately 13 seconds to complete. This procedure saved a considerable amount of time compared to a normal tone sweep. Depending on the frequency resolution of the measurement, the tone sweep protocols require several minutes to complete. In fact, the time saved was critical in achieving consistent measurements, as drying of the tympanic membrane and physiological stresses placed on the animal can cause deterioration in both acoustic and physiological measurements.

One major disadvantage of the chirp signal was the temporal spreading of signal energy. Since the signal had a linear group delay, the energy associated with a particular frequency only occurred for a very brief period. This would not pose any problem if a system was linear and the measurement noise was a strictly independent zero-mean random process. Such requirements are sufficient to guarantee the convergence of the

mean asymptotically to its true value. This condition held true for our acoustic measurements that included middle-ear input admittance, ear canal, and middle-ear pressure. Thus, sufficient averaging of these responses could provide results of high accuracy. Our electro-physiological measurements, however, did not satisfy this requirement. The round-window cochlear potential was not entirely linear, and the electrical artifacts of the electrode were neither independent nor a zero-mean random process. In fact, signals that contain multiple frequency components presented simultaneously or closely following each other could trigger highly nonlinear cochlea responses (Pickles, 1988). As a result, chirp signals were not suitable for cochlear potential measurements, and tonal stimulation were used instead.

Our tone sweep measurements consisted of 50 logarithmically spaced continuous tones over the range of 12 Hz to 10 kHz. In order to increase the signal-to-noise ratio of the noisy cochlear potential measurements, each tone was presented 50 times, with a total duration of 8.192 sec. The average of these 50 responses was used to calculate the magnitude and phase of the cochlear potential at that frequency. The entire tone sweep protocols consumed approximately 7 minutes.

For both chirp and tonal stimulus, measurements were made at a minimum of two different sound-pressure levels. For the lfs, measurements were usually done with the driver voltage set at 10 or 100 mV (voltage level refers to the amplitude of the chirp signal). For the hfs, driver voltage were set at 1 or 10 mV. Such voltage levels correspond to approximately 50–80 dB SPL sound-pressure level, well within the linear range of the gerbil middle ear.

2.5 Experimental configuration and procedures

Figure 2-16 shows the overall schematic diagram of the experimental setup. A computer based data acquisition system is used to control the measurement process. The following sections will describe the methods used in this study in detail.

2.5.1 Animal preparation

All gerbils were anesthetized with sodium pentobarbital (Nembutal) at 70 mg/kg of body weight. The body temperature was monitored throughout the experiment and maintained between 34 and 37°C with a heating pad. The paw pinch reflex was checked periodically during the procedure, and supplemental doses of Nembutal were administered as required. To prevent excessive secretion, Atropine at 1mg/kg of body weight was administered every two hours.

The pinna of one ear (usually the left) was removed and the ear-canal excised as necessary to allow the acoustic source to be placed against the external auditory canal. A small metal ring was cemented to the skull around the ear canal opening to allow rapid and repeatable removal and replacement of the acoustic source. The ring also served to facilitate an airtight seal between the source and the skull. Since there is evidence that anesthesia interferes with Eustachian-tube function (Guinan and Peake, 1967; Hutchings, 1987), the gerbil middle ear was vented by sealing a long thin tube to the surface of the bulla (100 mm long and 0.25 mm inner diameter). Due to the small size of the tube, it was able to prevent static pressure build up in the bulla cavity, while still acting as an acoustic open circuit[5]. The animal head was held in position by hooking the jaw around

[5]The cutoff frequency of the vent tube was determined to be approximately 70 Hz. It was computed using the modeling techniques described in Chapter 1. Specifically, the bulla cavity ($V = 220\mu l$) was modeled as a capacitor ($C = V/\rho c^2$), and the vent tube was modeled as a series inductor and resistor

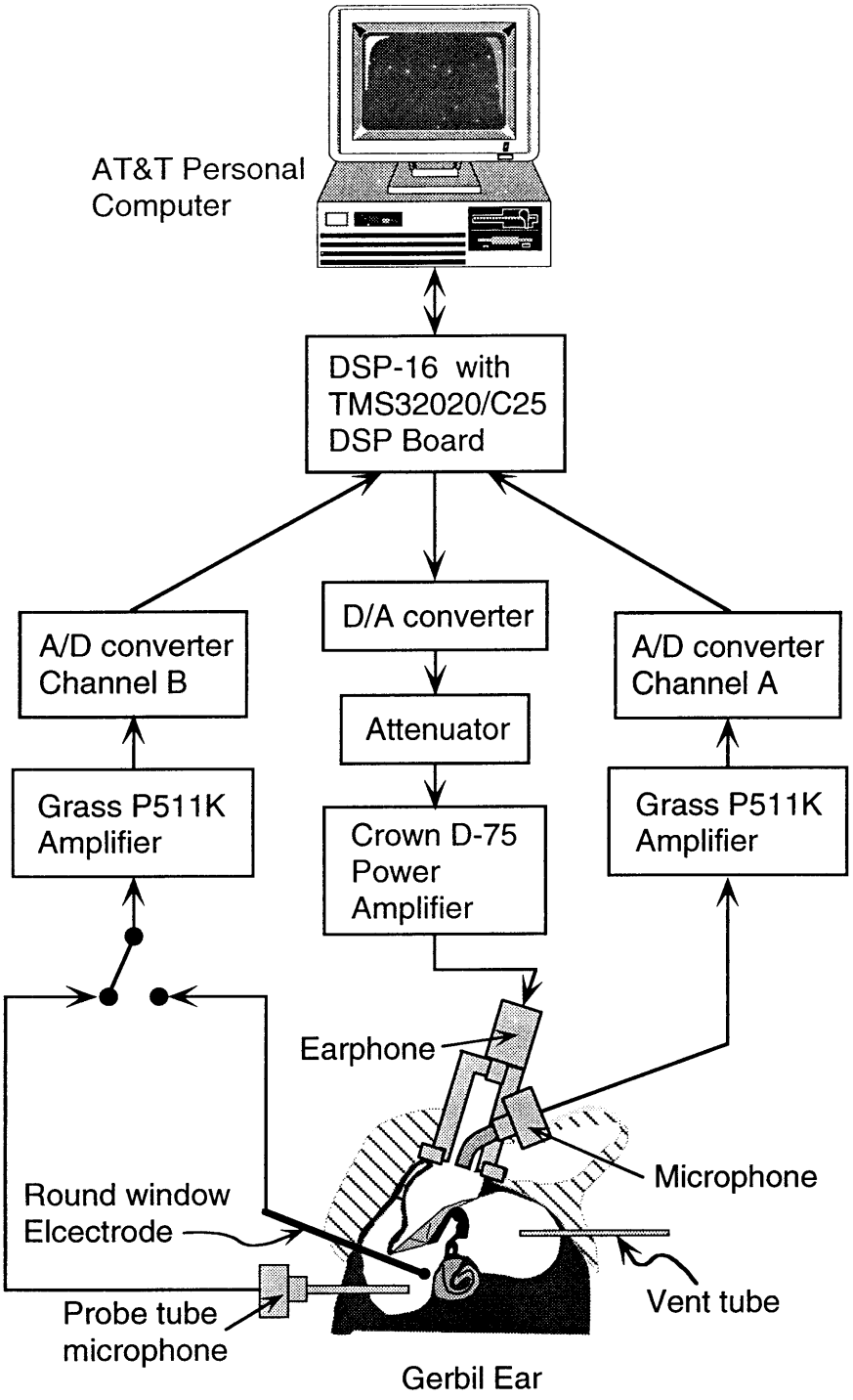

Figure 2-16: Schematic diagram of the experimental setup. An AT&T personal computer with a DSP-16 data acquisition board was used as the controller of the experimental measurements. The computer generated signal was delivered to the earphone via an attenuator and a power amplifier. The resulting acoustic and cochlear potential responses were acquired by the computer after the signals were amplified.

a vertical rod. Pressure measurements were made with the animal lying on its side and the experimental ear up. These procedures have been reviewed and approved by the MIT Committee on Animal Care–Protocol #92-003.

2.5.2 Instrumentation

The instrumentation involved in the experiments is schematically shown in Figure 2-16. A DSP-16+ data acquisition board from Ariel (Highland Park, NJ), with its on-board TMS32020/C25 DSP processor, was placed in an AT&T 486 personal computer. The DSP-16+ board had two channels of 16-bits analog-to-digital (A/D) and digital-to-analog (D/A) conversions for stimulus generation and data acquisition. In our experiments, only one channel of D/A and two channels of A/D were used. SYSid (an acronym for System Identification), an audio-band test and measurement system from Ariel, was used as the software for controlling the experiments.

The digitally synthesized stimulus (either chirp or tone) was converted by the D/A converter into analog signals according to the sampling rate and amplitude specified by SYSid. The signal was passed through an anti-aliasing filter and an adjustable attenuator to set the signal level. The resulting output was used to drive the earphone of the acoustic source through a Crown D-75 Power Amplifier set to unity voltage gain. The power amplifier was there to provide the necessary current to drive the earphone, as well as to effectively increase the input impedance of the earphone in order to prevent unwanted loading attenuation of the signal.

There were three recordable responses in the experiment: the ear-canal sound pressure, the middle-ear sound pressure, and the round-window cochlear potential. Since

(Eqn. 1.6). The cutoff frequency was then determined as the parallel resonance frequency of these two acoustic elements.

only two input channels were available, only two responses were measured simultaneously. As shown in Figure 2-16, the output from the ear-canal microphone is always connected to channel A of the DSP-16+ A/D converter. The second input channel was then used to record either from the round-window electrode or middle-ear probe tube microphone. All the input signals were amplified by Grass P511K amplifiers before being quantized by the data acquisition system. The two measured transfer functions[6] were stored by the computer in the form of time domain impulse responses for further analysis.

2.5.3 Cochlear potential measurements

One important assumption made in the middle-ear models presented in Chapter 1 is that input to the inner ear is strictly dependent on the pressure across the tympanic membrane. To uphold this assumption, it is necessary for the pressure difference to produce a proportional vibration velocity at the malleus, which in turn produces a proportional vibration in the cochlear fluid, the principle transduction mechanism of the inner ear. Over a limited frequency region, the cochlear potential near the round window is essentially a direct replica of the cochlear fluid vibration (Møller, 1963; Møller, 1965). Figure 2-17 shows the data obtained by Møller (1965), which show the proportionality relationship between the middle ear input impedance (inverse of admittance) and the inverse cochlear potential at constant sound-pressure level at the tympanic membrane.

In our experiments, we will measure changes in cochlear potential, middle-ear input admittance, and pressure difference across the tympanic membrane while manipulating *pars flaccida*. Comparisons of these data will provide a direct indication of how the

[6]Transfer function is defined as the ratio of the response to the stimulus.

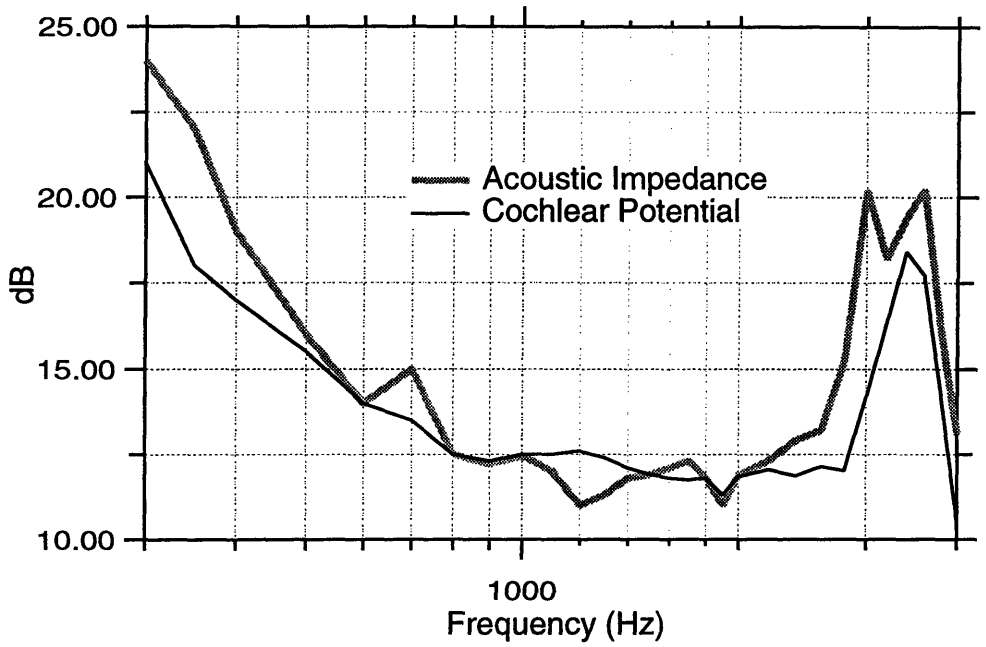

Figure 2-17: Cochlear potential and impedance measurements obtained from Møller (1965). Plots show the proportionality relationship between the middle-ear input impedance and inverse cochlear potential at constant sound pressure level at the eardrum in an anesthetized cat. Measurements were made with bulla intact. Impedance given in logarithmic measure relative to 100 cgs units. CP reference is arbitrary.

acoustic transmission through the middle ear is affected by the condition of the *pars flaccida*, and whether these effects can be explained by changes in either the input admittance or the middle-ear sound pressure level.

2.5.4 Experimental protocol

A series of experiments were performed to answer questions concerning the role of *pars flaccida* on the middle-ear pressure transmission, as well as to validate and quantify the circuit models presented in Chapter 1. To accomplish these goals, the middle-ear input impedance, ear canal and bulla-cavity pressures, and cochlear potential of gerbils were measured under various middle ear conditions.

As illustrated in Figure 2-16, calibrated microphone-and-sound-source assemblies were coupled to the ear canal through the cemented metal ring. A round-window electrode and a probe-tube microphone were placed in the bulla cavity through sealed bulla holes. The middle-ear input admittance, $\mathbf{Y_T}$, the cochlear potential, $\mathbf{CP}$, and the middle-ear cavity pressure, $\mathbf{P_{MEC}}$, were measured. Several sets of experiments were conducted: 1) with the *pars flaccida* and bulla wall intact; 2) with the *pars flaccida* intact, but the bulla cavities widely opened; 3) with the *pars flaccida* replaced by a thin sheet of dental acrylic (thus greatly increasing its stiffness), and leaving the bulla wall intact; 4) with the *pars flaccida* replaced by dental acrylic, and with the bulla cavities widely opened; and finally 5) with the *pars flaccida* removed, but the bulla wall intact. In all cases where the bulla wall was unopened, the bulla cavity was vented by a long thin tube, as explained in Section 2.5.1.

The different middle ear manipulations specified above are represented as switches in Figure 2-18. When the *pars flaccida* is rigidified by dental acrylic, its impedance is

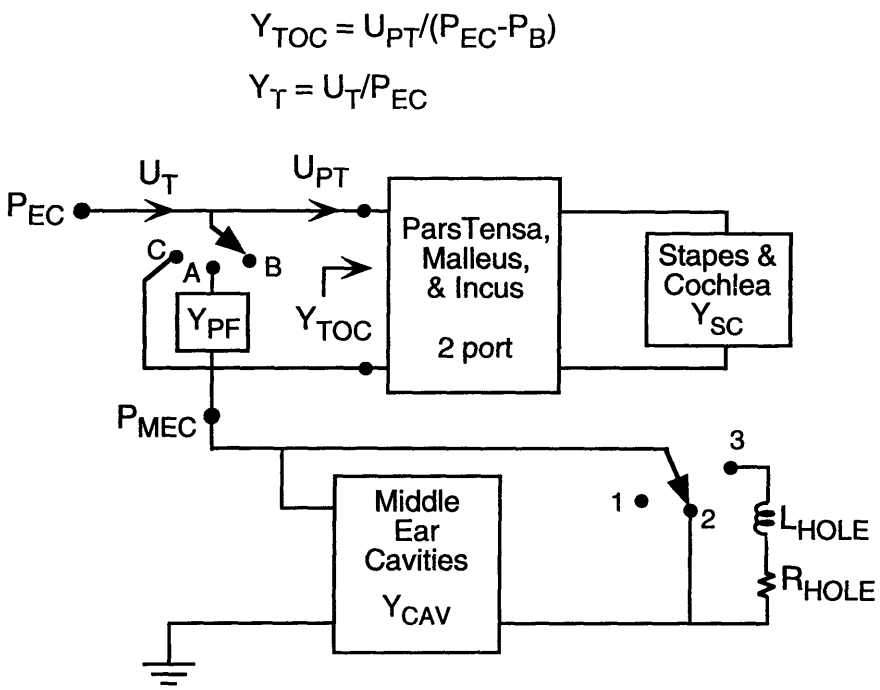

Figure 2-18: Schematic diagram showing the effects of experimental manipulations on the middle ear input admittance $\mathbf{Y_T}$. $\mathbf{Y_T}$ is defined as the ratio of $\mathbf{U_T}$ and $\mathbf{P_{EC}}$. which in the natural state is the parallel combination of $\mathbf{Y_{PF}}$ and $\mathbf{Y_{TOC}}$ ($\mathbf{Y_{TOC}}$ is defined as the input admittance of the *pars tensa* and its load) in series with $\mathbf{Y_{CAV}}$. The manipulations on *pars flaccida* is modeled as a switchable impedance with three possible settings. When the *pars flaccida* is intact, the switch is in position "A", where $\mathbf{Y_{PF}}$ acts as a shunt path across the *pars tensa*-ossicular complex. Switch position "B" models the immobilized *pars flaccida*, which causes all the tympanic-membrane volume velocity $\mathbf{U_T}$ to pass through *pars tensa*. Switch position "C" represents a removed *pars flaccida*, where it effectively shorts out the rest of the $\mathbf{Y_{TOC}}$. The second switch models the state of the middle ear cavities. Switch position "1" represents sealed middle ear cavities (with the exception of the thin vent tube); widely opening the cavity wall is represented as switch position "2", where $\mathbf{Y_{CAV}}$ is assumed to be short circuited; and position "3" represents the configuration where the probe-tube hole on the bulla wall is left open.

significantly increased due to the added stiffness. Since this impedance is in parallel with $\mathbf{Y_{TOC}}$ (which has substantially higher admittance than the rigid acrylic), the parallel combination is thus dominated by $\mathbf{Y_{TOC}}$, and the first switch should therefore be set at position "B". If at the same time, the middle ear cavity is widely open (second switch at position "2"), the measured input admittance($\mathbf{U_T/P_{EC}}$) was essentially $\mathbf{Y_{TOC}}$. To experimentally measure $\mathbf{Y_{CAV}}$, the *pars flaccida* was removed, and the middle ear cavities remained sealed (this correspond to the switches at positions "C" and "1" respectively). At low frequencies, $\mathbf{Y_{CAV}}$ can be compared with the theoretical values, which can be obtained through volumetric measurement of the middle ear cavity V_{CAV}:

$$\mathbf{Y_{CAV}} = \frac{j\omega V_{CAV}}{\rho_o c^2} \tag{2.14}$$

After $\mathbf{Y_{CAV}}$ and $\mathbf{Y_{TOC}}$ are determined, the admittance of the pars flaccida, $\mathbf{Y_{PF}}$, can be found through the input admittance measurements of the undisturbed ear, $\mathbf{Y_T}$. The spectrum of $\mathbf{Y_{PF}}$ can then be used to synthesize a circuit model of the *pars flaccida* admittance. The resulting model admittance, $\hat{\mathbf{Y}}_{\mathbf{PF}}$, can be tested against the input impedance measured in other middle ear configurations.

Chapter 3

Experimental results

3.1 Middle-ear input admittance

Measurements of middle-ear input admittance were made in fifteen healthy ears from ten gerbils. In six of these ears, measurements were made with both high and low frequency sources. The lfs results were used to compute the input admittances below 3500 Hz; while the hfs results were used for frequencies above 6000 Hz. Between these frequencies, a linearly weighted average of both admittances was used to describe the results.

The accuracy of all admittance measurements was determined from the appropriate source accuracy charts in appendix B. Only admittances that are accurate to within 2 dB in magnitude and 10° in phase are shown in this thesis. Consequently, most measurements made with the lfs alone were limited to frequencies below 6 kHz; while no hfs measurements below 200 Hz were accepted. Measurements made with both sources had a frequency range of 50 Hz to 10 kHz.

As explained in Chapter 2, chirp stimuli were used for all impedance measurements. For the low frequency source, the earphone driver voltage was set to either 100 mV or

32 mV (correspond to -20 dB and -30 dB re 1V), while the high frequency source was generally driven by 10 mV or 3.2 mV chirp signal (correspond to -40 dB and -50 dB re 1V). The actual sound pressure levels generated by these stimuli were measured using the calibrated probe-tube microphone and are shown in Figure 3-1.

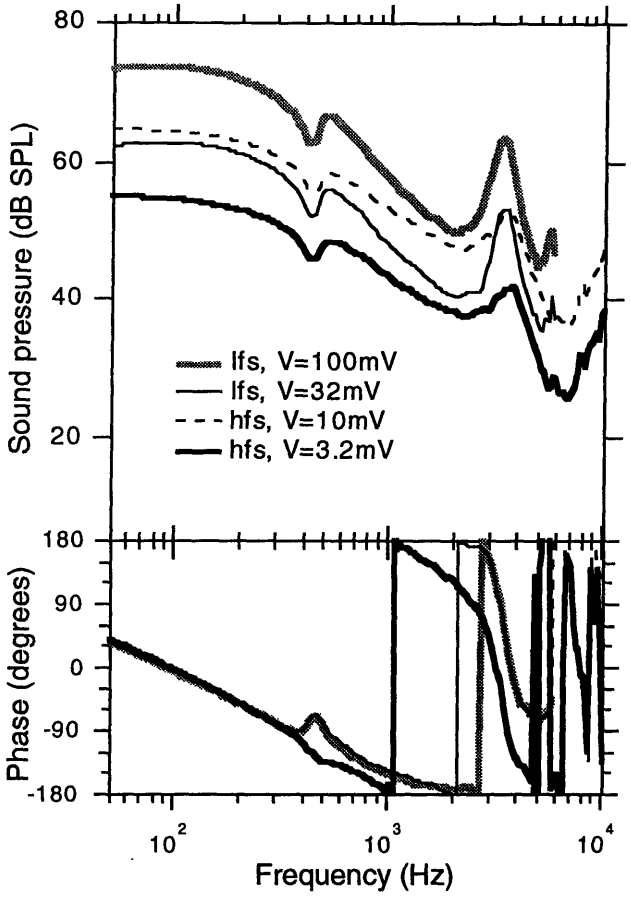

Figure 3-1: The actual sound pressure levels generated by chirp stimuli in a gerbil ear canal (B8). The sound pressure levels were computed from microphone outputs using the calibration scheme described in Section 2.3.1. The amplitudes of the earphone driver voltage are shown in the legend.

3.1.1 Correction for ear canal volume

The irregular geometry of the gerbil ear canal did not allow the microphone to be placed directly on top of the tympanic membrane—the ideal anatomical position for measuring middle-ear input admittance (see Figures 1-2 and 2-1). The actual pressure measurements in our experiments were made with the sound source coupled to the lateral opening of the bony ear canal, leaving a small ear-canal cavity between the measuring microphone and the tympanic membrane. Table 3.1 lists the volumetric measurements of this ear-canal cavity made in fourteen ears from nine gerbils. The mean volume was found to be 18.6 μl, close to the published data of Schmiedt and Zwislocki, 1977 (20 μl) and Ravicz *et al.*, 1992 (21 μl).

Animal	Ear	Weight (grams)	Ear-canal volume (μl)
B2	Left	59	17
B3	Left	51	17
B4	Left	53	18
B5	Left	65	18
B5	Right	65	19
B7	Left	66	17
B7	Right	66	23
B8	Left	57	20
B8	Right	57	19
B9	Left	54	18
B9	Right	54	19
B10	Left	60	18
B10	Right	60	17
B11	Left	59	21

Table 3.1: Body weight and ear-canal volume measurements of gerbils used in this study.

Two methods are available to remove the effects of the ear-canal cavity on the measured middle-ear input admittance. In the low frequency region, ear canal can be modeled as a capacitor in parallel with the middle-ear input impedance, such that the theoretical

contribution of the canal can be subtracted from the overall measured admittance. At higher frequencies, where the sound wavelengths are less than ten times the cavity dimension, distributed parameter models should be used instead. A commonly employed distributed system models the ear canal cavity as a cylindrical tube represented by transmission-line equations (Lynch et al. , 1994). Such a model can be further enhanced to include the effects of viscous and thermal losses, and can be fully described in terms of a two-port system (Egolf, 1977; Zuercher et al. , 1988; Ravicz, 1990; Ravicz et al. , 1992). The two-port parameters are computed using Bessel functions of the zero and the first kind, with the length and the radius of the cavity as the input arguments. The two-port parameters used in this thesis were calculated with the dimensions of 2.4 mm diameter and 4.1 mm length, consistent with our measured volume of 18.6 μl and the measurements made by Ravicz, 1990.

Figure 3-2 compares the measured and the corrected middle-ear input admittances of gerbil B8. The admittances calculated from both the distributed two-port model and the lumped parameter circuit model are shown in the figure. The magnitudes and the angles of the two corrected admittances are virtually identical from 50 Hz to 1 kHz. Major discrepancies occur only for frequencies above 3 kHz, where they differ by as much as 60% in magnitude and 30° in phase at 10 kHz. While all discussions in this thesis will be made in terms of low frequency circuit analogs, most admittance plots will be presented at frequencies up to 10 kHz; the circuit analog was thus determined to be an insufficient model for the residual ear-canal volume, and the distributed two-port model was used instead. All input admittance measurements presented in this thesis were corrected for the ear canal using the two-port method.

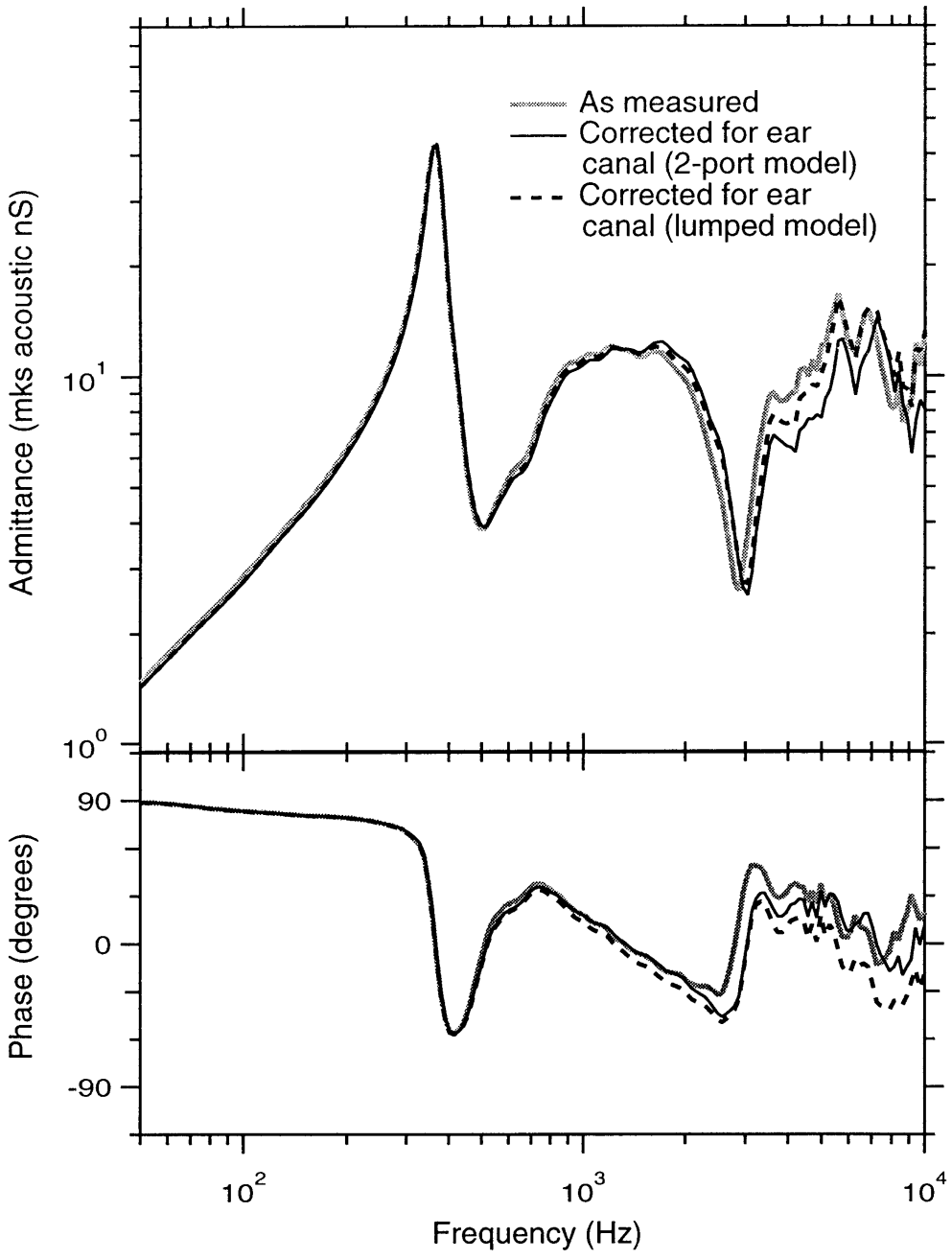

Figure 3-2: Measured and corrected gerbil middle-ear input admittances. The result of the two-port ear-canal cavity correction is compared with the correction made by the simple lumped circuit model. The two models agree in both magnitude and phase at frequencies below 1 kHz. At higher frequencies, both their magnitudes and phases show significant deviations.

3.1.2 General features of the measured middle-ear input admittance

Input admittance of intact middle ears

Measurements of the input admittance with the middle ear intact (but vented by a long thin tube) were made in eight ears (A1, A2, B1, B2, B3, B5, B8, B9), and are plotted in Figure 3-3. These measurements are denoted as $\mathbf{Y^I}$ throughout this thesis. At frequencies below 2 kHz, the admittance is clearly compliance dominated, with the admittance magnitude directly proportional to frequency for the most part, and the phase close to 90° (*i.e.* $\mathbf{Y^I} \approx j\omega C^I$, where C^I is the series combination of the compliances of tympanic membrane-ossicular-cochlear complex and bulla cavity). In this region, the measured admittances are very consistent, with the maximum variation on the order of 5 dB in magnitude — an indication of the intersubject stability of C^I. Measurements in five out of the eight ears (A1, B1, B2, B8, B9) show a small but well defined resonance peak and angle change in the 400-700 Hz region. The compliance below this resonance frequency tends to be higher than the compliance above the resonance frequency. As we shall see in the following sections, such behavior is consistent with our series model presented in Chapter 1 (Figure 1-7 and 1-8), where the compliance and mass-like properties of the *pars flaccida* interact to produce such a resonance peak. With the exception of ears A1, B1 and B9, the admittances above 2 kHz are mostly resistance dominated, where the magnitudes are approximately constant (between 6 and 20 nS), and the angles vary between ±45°.

Some of the measured admittances deviate from the general characteristics described above. The admittance angles of ears A1 and B5 (which were measured with the hfs) at frequencies below 400 Hz and the angle of B5 at approximately 6.5 kHz are all greater than 90°. Such results must be in error, since it implies that the middle-ear input

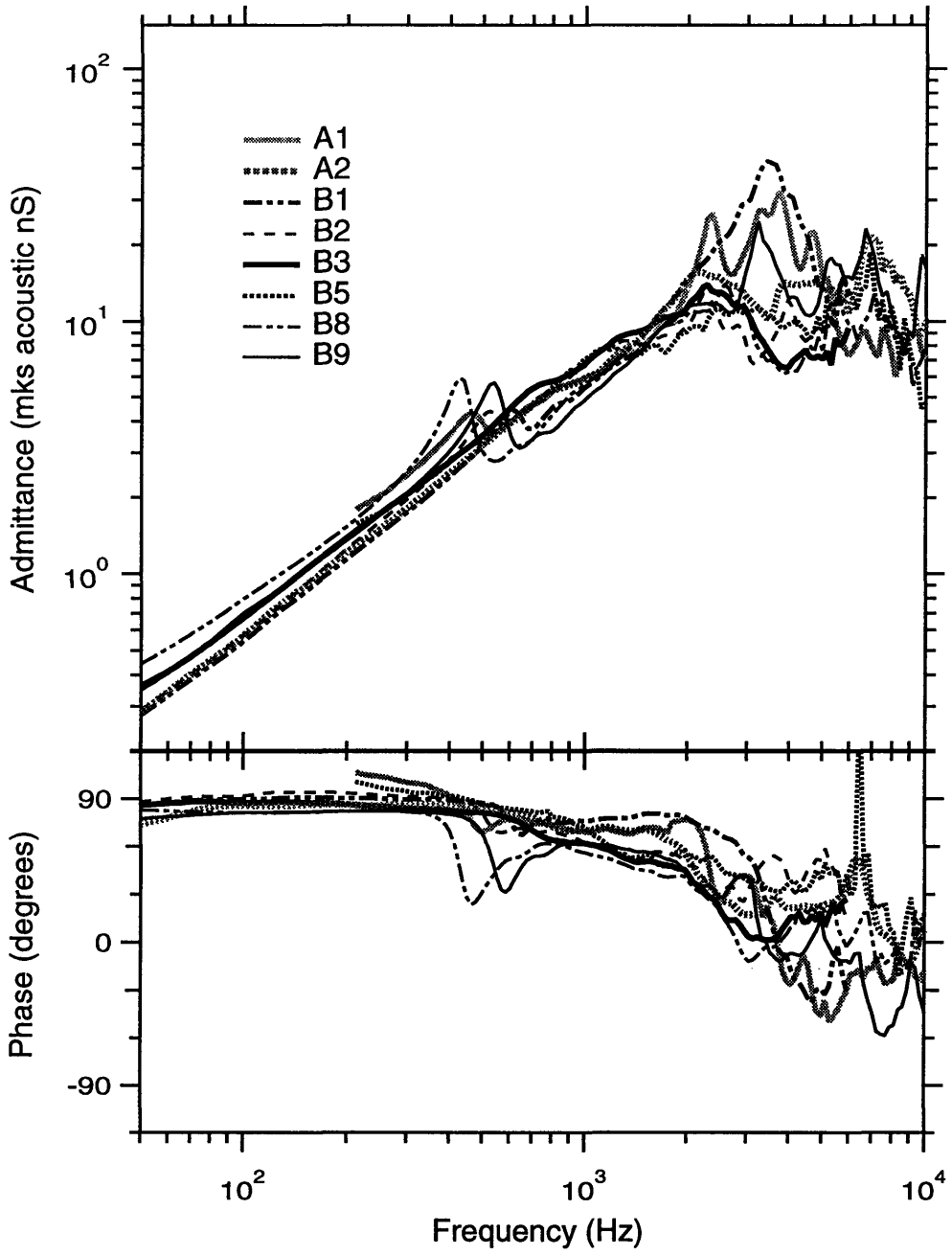

Figure 3-3: Input admittance of eight intact gerbil middle ears, $\mathbf{Y}^{\mathrm{I}}$. Among the eight ears, three (A2, B8, B9) were measured with both high and low frequency sources; these admittance measurements cover a frequency range of 50 Hz to 10 kHz. Ears A1 and B5 were measured with the hfs alone, thus their accuracy range was limited to frequencies above 200 Hz. The three remaining ears (B1, B2, B3) were measured by the lfs alone, which limited their measurements to frequencies below 6 kHz.

admittance contains negative real parts, thus making the middle ear a source of acoustic energy. For ears A1, B1, and B9, the admittance magnitudes at frequencies above 2 kHz feature several peaks and reversals in slope that are accompanied by angles significantly less than $-30°$. These admittance values suggest that these ears contain significant mass-like components at high frequencies.

Input admittance with the bulla hole open

Figure 3-4 shows the middle-ear input admittance measured in the same ears as the previous section, but with the probe-tube hole on the bulla wall left open. These admittance measurements are denoted as $\mathbf{Y^{HO}}$ in this thesis. Opening the bulla hole has two major effects on the middle-ear input admittance. First, the resistive and mass-like properties of the aperture form a parallel resonance with the compliance of the middle-ear cavity, which is manifested as a sharp valley near 3 kHz on the input admittance plot. The frequency of this resonance behavior can be predicted solely based on the volume of the middle-ear cavity and the size and length of the bulla hole[1]. Below 3 kHz, the acoustic property of this parallel combination is dominated by the hole inductance, which effectively "shorts out" the admittance of the middle-ear cavity. Consequently, the low-frequency middle-ear input admittance (*i.e.* $f < 1\ kHz$) is predominantly determined by the compliance of the *pars flaccida* and the *pars tensa*-ossicular-cochlear complex.

These two effects are clearly visible in the middle-ear input admittance plots in Fig-

[1]The interaction between the bulla hole and the middle-ear cavity can be modeled as a parallel resonance between the compliance (capacitance) of the cavity with the damping (resistance) and mass-like property (inductance) of the bulla hole. These three quantities can be fully specified in terms of the middle-ear cavity volume, V_{MEC}, bulla-hole radius, r, and bulla-hole length (the thickness of the skull), l. The resistance can be obtained from Eqn. 1.4 and the capacitance from Eqn. 1.8. The inductance can be computed by modifying Eqn. 1.2 to take into account the radiation effect of the aperture: $L = \rho_o(l + 1.75r)/\pi r^2$. With the cavity volume of 218 μl (Lay, 1972), the measured hole radius of 0.5 mm and thickness of 0.3 mm, the predicted resonance frequency is approximately 3 kHz.

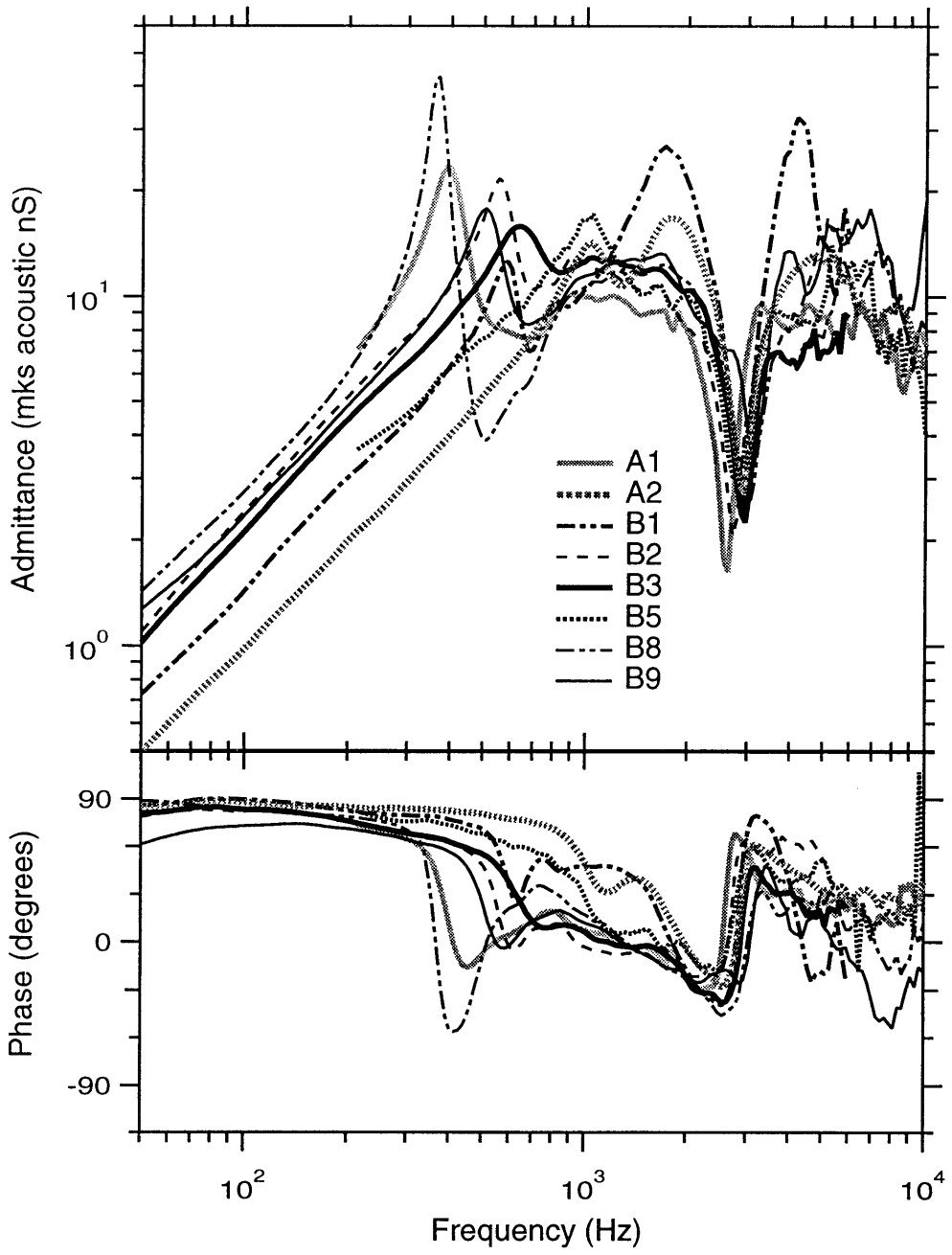

Figure 3-4: Input admittance of eight gerbil middle ears — with the bulla hole left opened, $\mathbf{Y}^{\mathbf{HO}}$. The admittance measurements were made in the same ears, and using the same sound sources as in Figure 3-3. The resonance caused by the open hole is clearly visible in this figure.

ure 3-4. Consistent with theoretical consideration, the resonance peaks can be observed at approximately 3 kHz. The lower resonance frequency observed in ear A1 may be the result of a partially covered bulla hole[2], presumably by the leftover vaseline initially used to cover the hole in the middle ear intact case. In the low frequency region, all measured ears show higher admittances with the hole open than in the intact middle ear, with the amount of increases ranging from 5 to 11 dB. Such results agree with our expectation that opening the bulla hole eliminates the series compliance of the middle-ear cavity, thus increasing the overall input admittance. Without the cavity admittance, the remaining low-frequency compliances show increased intersubject variation, where the compliance values vary by as much as 10 dB. As will be discussed in the next few sections, these compliance values are mainly determined by the acoustic properties of the *pars flaccida*, and are greatly influenced by its physical condition. Another apparent difference between Figure 3-4 and 3-3 is the increased prominence of the resonances in the 300-700 Hz frequency range. This feature is another result of the removal of the stiffer middle-ear cavity, allowing the *pars flaccida* compliance and mass to dominate the low-frequency admittance measurements. At frequencies above 4 kHz, the hole-open input admittance is very similar to the admittance of the intact middle ear.

3.1.3 Effects of membranal drying on middle-ear input admittance

In several earlier experiments, we tested the consistency of the measured input admittance by repeating the same acoustic measurements over a 2-3 hour period. The results show good consistency for frequencies above 1 kHz, but they also reveal a systematically varying trend at lower frequencies. Figure 3-5a shows three middle-ear input admit-

[2]The smaller the hole, the higher the inductance, and consequently the lower the resonance frequency.

tances measured over a two-hour period. As time progressed, the compliance-dominated low-frequency admittance was observed to shift gradually to the right (higher frequency), while the resonance near the 500 Hz region was increasingly damped. The increase in stiffness and resistance were found to be mainly a result of the drying of tympanic membrane, especially in the *pars flaccida* region[3]. Figure 3-5b shows that the increase in stiffness can be reversed by moistening the tympanic membrane on the lateral surface using 0.9% saline solution. After rehydration, however, the input admittance remained unstable, as additional drying continued to increase the membranal stiffness. The low-frequency stiffness was reverted to its original values approximately 1 hour after the TM was moistened. The reduction in damping was not restored by the simple rehydration process.

To overcome the complication of this drying effect, our experimental protocol was revised to shorten the measurement duration as much as possible. For each gerbil ear, measurements were made in only one middle-ear configuration (either with the middle ear opened widely or the middle ear intact). This change shortened the initial acoustic and cochlear potential measurement time (when the TM was undisturbed) to 15 to 30 minutes, during which the tympanic membrane was repeatedly moistened. The *pars flaccida* was then stiffened, obviating the need for further moistening. This protocol was used in animal B8, B9, B10, and B11, and the resulting measurements were found to be more consistent than the earlier experiments. Measurements obtained from these four animals will be emphasized in this chapter, while the results obtained from the earlier experiments are included in Appendix C.

[3]The admittance region that varied the most is dominated by *pars flaccida*. See the next Section for experimental evidence that support this conjecture.

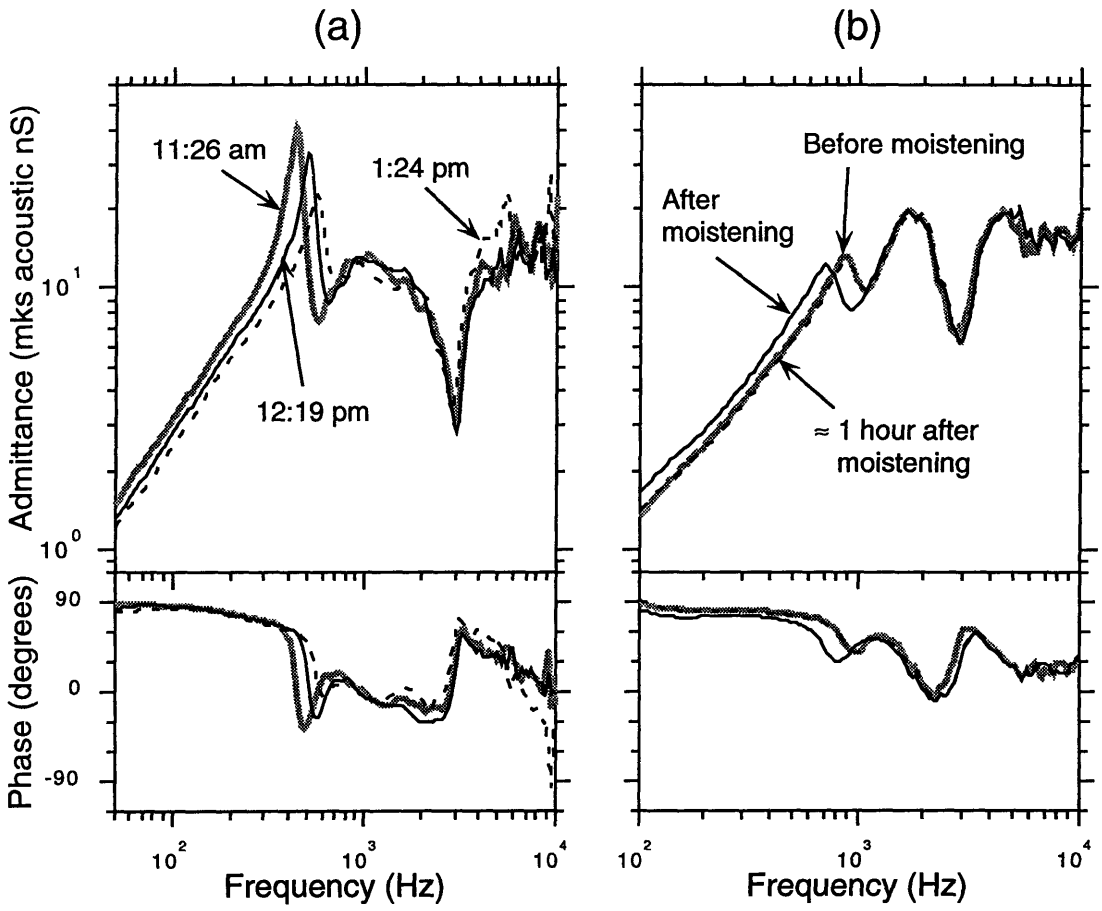

Figure 3-5: Effects of membranal drying and moistening on the gerbil middle-ear input admittance, $\mathbf{Y}^{\mathbf{HO}}$. (a) The input admittances of a gerbil middle ear (gerbil A2) with an open bulla hole were measured over a two hour period. The shift in the low frequency admittances and the reduction of resonance amplitudes around 500 Hz are clearly visible in these plots. (b) The input admittances of a gerbil middle ear (gerbil B2) with an open bulla hole were measured before and after the tympanic membrane was moistened by 0.9% saline solution. The low frequency compliance was increased by the rehydration process. Approximately one hour after the TM was moistened, the low frequency admittance shifted back to the original level, presumably due to additional drying of the tympanic membrane.

3.1.4 Input admittance before and after manipulation of *pars flaccida* — ears with intact bulla

Measurements of input impedance of the intact middle ear were made in the left ear of five gerbils (A1, A2, B1, B2, B3) and the right ear of three gerbils (B5, B8, B9). In this configuration, a long thin vent tube was also inserted into the middle-ear cavity to prevent the buildup of static pressure. Of these eight ears, only measurements made in A2, B8, and B9 included manipulation of the *pars flaccida*, where it was either stiffened or removed. Figures 3-6 shows the input admittance measurements made in gerbils B8 and B9. Three admittance plots are displayed in each figure, one was measured with the tympanic membrane intact and undisturbed ($\mathbf{Y^I}$), another one with the *pars flaccida* stiffened by dental acrylic ($\mathbf{Y^I_{FS}}$)[4], and a third one with the *pars flaccida* removed ($\mathbf{Y^I_{FR}}$).

A quick examination of these three admittance plots allows us to determine three important parameters of our middle-ear model shown in Figures 1-7 and 1-8: the compliance of the middle-ear cavity (C_{CAV}), the compliance of the *pars flaccida* (C_{PF}), and the compliance of the *pars tensa*-ossicular-cochlear complex (C_{TOC}). With the *pars flaccida* removed, the middle-ear input admittance is for the most part the admittance of the middle-ear cavity — which is primarily compliance dominated, especially in the low frequency region. Measurement of this acoustic compliance can thus be used to compute the middle-ear cavity volume. This cavity compliance, C_{CAV}, can be calculated directly

[4]The notational convention used in this thesis is to indicate the condition of the middle ear in the superscript of the admittance variable (*e.g.* **I** for intact), and to represent the manipulation to the *pars flaccida* in the subscript of the variable (*e.g.* **FS** for *pars flaccida* stiffened).

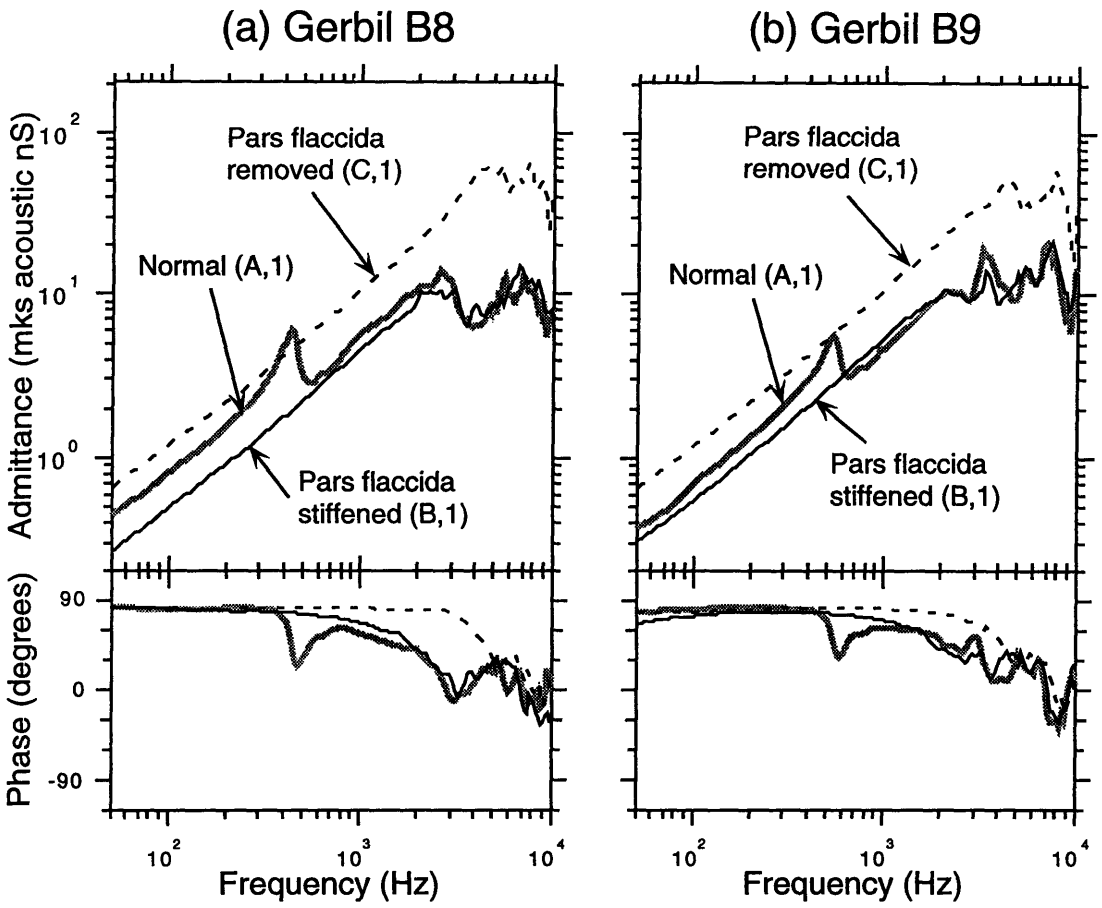

Figure 3-6: The middle-ear input admittance measured in the right ears of gerbils B8 and B9—middle ear intact. Three measurements are shown in this figure: 1) with a normal and undisturbed tympanic membrane, $\mathbf{Y^I}$, 2) with the *pars flaccida* stiffened, $\mathbf{Y^I_{FS}}$, and 3) with the *pars flaccida* removed, $\mathbf{Y^I_{FR}}$. The alphanumeric characters (which are enclosed in parenthesis) following each legend indicate the switch positions used to represent the particular experimental manipulations (see Figure 2-18).

from the low-frequency admittance magnitude plot[5]:

$$C_{CAV} = \frac{|\mathbf{Y_{FR}^I}|}{2\pi f} \tag{3.1}$$

With the mean compliance of 1.67×10^{-3} mm^3/Pa, the measured values correspond to an effective middle-ear volume of 230 μl, similar to the middle-ear air volume measured by Lay, 1977 (218 μl).

When the *pars flaccida* and middle-ear cavity are intact, the admittance of the right ears of B8 and B9 show all the features described in section 3.1.2. When the *pars flaccida* is stiffened with dental acrylic, the high-frequency input admittance $\mathbf{Y_{FS}^I}$ is similar to the admittance measured in the normal ear, while the low-frequency admittance is significantly different. These differences provide a means of determining the effects of *pars flaccida* on the middle-ear input admittance. The dental acrylic increases the stiffness of the *pars flaccida* and essentially "open circuits" the acoustic shunt path provided by the *pars flaccida* (see Figures 1-7 and 1-8); the remaining low-frequency input admittance thus consists of the series combination of $\mathbf{Y_{CAV}}$ and $\mathbf{Y_{TOC}}$. From Figure 3-6, it is evident that such modification primarily affects the input admittance at frequencies below 700 Hz, where the low-frequency resonance seen near that frequency in the *flaccida* intact ears is entirely eliminated and the acoustic compliance below the resonance frequency is decreased from a mean value of 1.13×10^{-3} mm^3/Pa to 0.79×10^{-3} mm^3/Pa, matching the acoustic compliance of $\mathbf{Y^I}$ at frequencies above the resonance (0.80×10^{-3} mm^3/Pa). These results, along with the *pars flaccida* removed measurements, are consistent with the middle ear model, with compliances of the cavity, *pars flaccida*, and *pars*

[5]This method of computing model parameter directly from admittance plot works only for the simplest case—such as $\mathbf{Y_{FR}^I}$, which has only one parameter C_{CAV}. Other parameters discussed in this chapter were computed using the least-square model fitting technique discussed in Chapter 4.

tensa-ossicular-cochlear of $1.67 \times 10^{-3}\ mm^3/Pa$, $1.99 \times 10^{-3}\ mm^3/Pa$, and $1.51 \times 10^{-3}\ mm^3/Pa$ respectively.

The location of the low-frequency resonance further allows us to compute the acoustic mass of the *pars flaccida*. Its role in generating such resonance is clearly demonstrated by the disappearance of the sharp magnitude peak and angle change in the *pars flaccida* stiffened ear. Assuming that this resonance is generated by the series interaction between the *flaccida*'s compliance and acoustic mass, the following equation governs the location of the resulting resonance:

$$f_{resonance} = \frac{1}{2\pi\sqrt{L_{PF}C_{PF}}} \tag{3.2}$$

With the mean measured resonance frequency of 480 Hz, the corresponding acoustic mass, L_{PF}, thus has a value of $0.55\ g/cm^4$. Assuming that the *pars flaccida* is circular with a radius of 0.8 mm (in agreement with our *flaccida* area measurement of $1.95\ mm^2$), the estimated mechanical mass of the *pars flaccida* is $0.55 \times Area^2$ (in cm^4) $= 2.2 \times 10^{-4} g$. Further assuming that the average density of the *pars flaccida* is that of water, $1 g/cm^3$, we can compute an estimated thickness of the *pars flaccida* of $0.11\ mm$. This estimated thickness is consistent with anatomical measurements.

3.1.5 Input admittance with and without manipulation to *pars flaccida* — bulla hole open

Measurements of the middle-ear input impedance with the bulla wall intact but with the probe tube hole open were made in the left ear of five gerbils (A1, A2, B1, B2, B3) and the right ear of three gerbils (B5, B8, B9). Out of these eight ears, only A2, B8, and B9 were measured with the TM undisturbed and with the *pars flaccida* stiffened.

Figure 3-7 shows the input admittance measurements made in the left ears of gerbils B8 and B9. Two plots are displayed in each figure; one was measured with the tympanic membrane intact and undisturbed, $\mathbf{Y^{HO}}$ and the other one was measured with the *pars flaccida* stiffened, $\mathbf{Y_{FS}^{HO}}$. Regardless of the conditions of the *pars flaccida*, the input admittances are stiffness dominated at frequencies below 300 Hz, where the admittances increase proportionally with frequency, and the angles are near 90°.

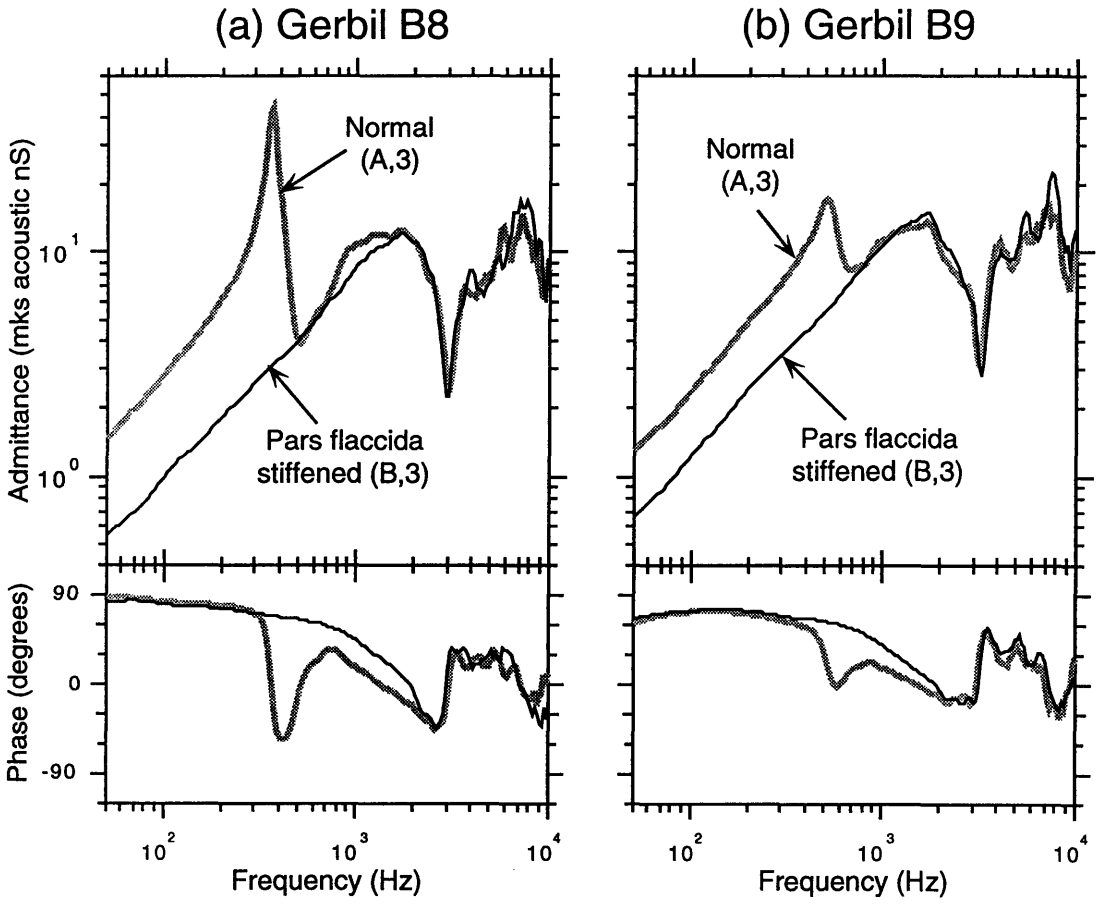

Figure 3-7: The middle-ear input admittance measured in the right ears of gerbils B8 and B9—with the bulla wall intact but the probe-tube hole open. Two measurements are shown in this figure: one was obtained with a normal and undisturbed tympanic membrane $\mathbf{Y^{HO}}$, the other one was measured with the *pars flaccida* stiffened $\mathbf{Y_{FS}^{HO}}$. The alphanumeric characters (which are enclosed in parentheses) following each legend indicate the switch positions used to represent the particular experimental manipulations (see Figure 2-18).

The changes produced by stiffening the *pars flaccida* in this configuration are very

similar to the changes produced in the intact middle ear. The low frequency compliance is decreased and the resonance near 400 Hz disappears. With the tympanic membrane undisturbed, the mean low-frequency compliance was found to be $3.69 \times 10^{-3}\ mm^3/Pa$; while the ears with the *pars flaccida* stiffened have a mean compliance of $1.71 \times 10^{-3}\ mm^3/Pa$. Stiffening *pars flaccida* had little effect at frequencies greater than 800 Hz.

According to our model, the compliance of the open-hole-flaccida-stiffened condition should be a direct measurement of the compliance of the pars tensa, while the open-hole-flaccida-intact condition should represent the sum of the flaccida and tensa compliances. This model than suggests that $C_{TOC} = 1.71 \times 10^{-3}\ mm^3/Pa$ and $C_{PF} = 1.98 \times 10^{-3}\ mm^3/Pa$, values that are nearly identical with the compliances estimated from the middle-ear intact measurements made on these same ears (Section 3.1.4).

3.1.6 Input admittance before and after manipulation of *pars flaccida* — middle ear widely opened

In the left ears of six gerbils (B1, B2, B3, B5, B8, B9), as much as possible of the bulla walls were removed. The middle-ear input admittance measurements made in the left ears of B8 and B9 are shown in Figure 3-8. Again, two measurements are displayed in each figure, one measurement with the tympanic membrane intact and undisturbed, $\mathbf{Y^{WO}}$, and the other measurement with the *pars flaccida* stiffened, $\mathbf{Y_{FS}^{WO}}$. The input admittances in these two ears share many common features with the measurements made in the hole-open configuration. In both ears, the differences in the magnitudes of $\mathbf{Y^{WO}}$ and $\mathbf{Y_{FS}^{WO}}$ are evident at frequencies below 600 Hz. The differences in phase can be seen at frequencies below 2 kHz. Changing the property of the *pars flaccida* did not

significantly affect the admittance magnitude or phase beyond those frequencies.

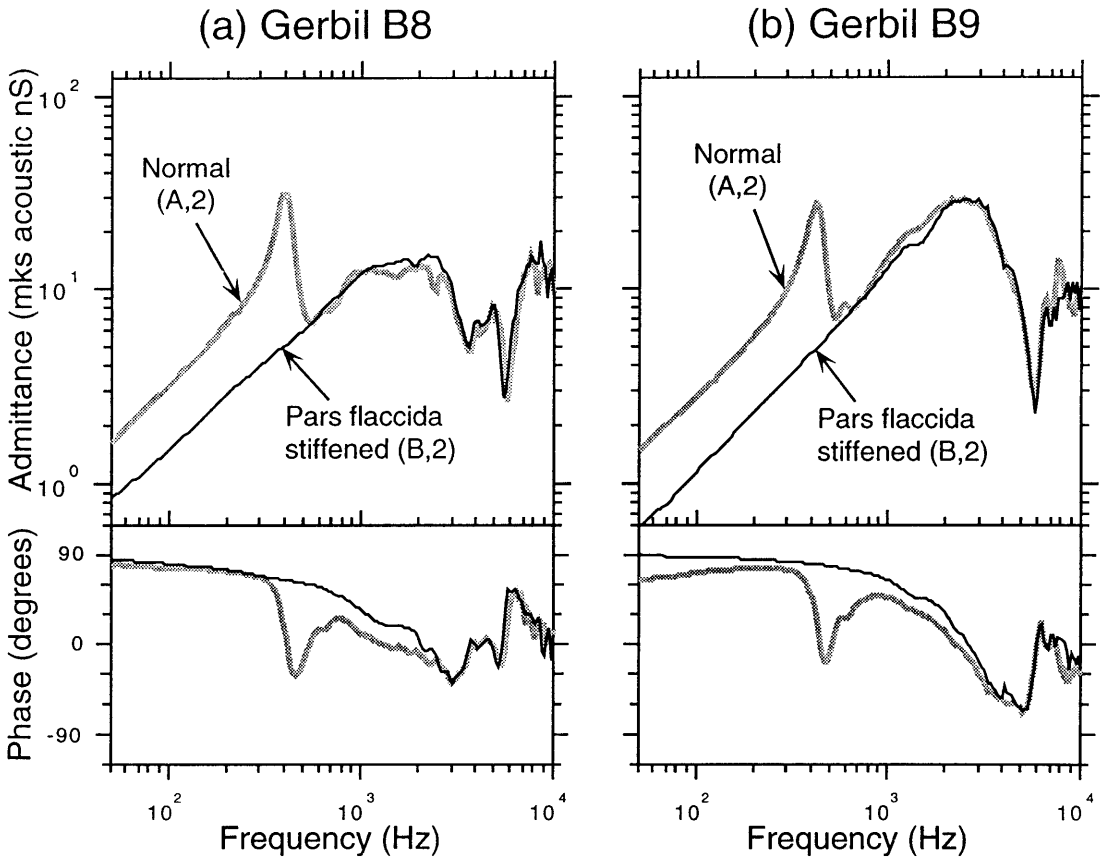

Figure 3-8: The middle-ear input admittance measured in the left ears of gerbils B8 and B9—bulla wall widely opened. Two different measurements are shown in this figure: one was obtained with the tympanic membrane intact and undisturbed $\mathbf{Y}^{\mathbf{WO}}$, the other one was measured with the *pars flaccida* stiffened $\mathbf{Y}_{\mathbf{FS}}^{\mathbf{WO}}$. The alphanumeric characters (which are enclosed in parentheses) following each legend indicate the switch positions used to represent the particular experimental manipulations (see Figure 2-18).

The major difference between this measurement configuration and the case of leaving the probe-tube hole open is the range of frequencies where the middle-ear cavity admittance can be considered "shorted out." Ideally, widely opening the bulla involves removal of all enclosing structures of the middle ear cavity, such that the effect of the cavity on the input admittance can be eliminated entirely. In practice, the presence of large blood vessels limits the removal of the bone to only the postero-lateral and ventro-lateral

surface of the bulla wall. This limitation will be demonstrated in middle-ear pressure measurements made in these ears (Section 3.1.8), where it is clear that the short-circuit assumption is not valid at frequencies above 6 kHz — the frequency at which the effective acoustic mass of the widely opened hole resonates with the middle-ear cavity compliance. Above this resonance frequency, the widely opened hole is essentially an effective open circuit (*i.e.* the cavity is acoustically closed), allowing the cavity admittance to be added serially to the input admittance in the same manner as the intact middle ear.

For the case of undisturbed tympanic membrane, the mean compliance of the two ears was found to be $4.26 \times 10^{-3}\ mm^3/Pa$. With the *pars flaccida* stiffened, the mean compliance decreased to $1.98 \times 10^{-3}\ Pa/mm^3$. Again, the *pars flaccida* resonance observed in the ears with normal TM disappears when the *pars flaccida* is stiffened, consistent with the discussion of the previous section. The input admittances remain stiffness dominated in the frequency range of 600 Hz to 1.5 kHz. The stiffness in this range is unaffected by the condition of the *pars flaccida*, and is approximately equal to the low-frequency stiffness of the ears with the *pars flaccida* stiffened, C_{TOC}. These data and model yield estimates of C_{TOC} and C_{PF} of $1.98 \times 10^{-3}\ mm^3/Pa$ and $2.28 \times 10^{-3}\ mm^3/Pa$

3.1.7 Effects of removing the *pars flaccida* "shield" on middle-ear input admittance

To confirm that the stiffening of *pars flaccida* is indeed the cause of the reduction in low-frequency admittance and the disappearance of low-frequency resonance, we measured the middle-ear input admittance following the removal of the dental acrylic shield used to stiffen the *flaccida*. Figure 3-9 shows the admittance measured in the left ear of gerbil A2, where measurements were made with tympanic membrane undisturbed $\mathbf{Y^{HO}}$, with

the *pars flaccida* stiffened $\mathbf{Y}_{\mathbf{FS}}^{\mathbf{HO}}$, and with the dental acrylic removed $\mathbf{Y}_{\mathbf{AR}}^{\mathbf{HO}}$.

In this ear, as with most of the earlier measurements, the effects of drying on the middle-ear input admittance were not fully recognized. Therefore, the tympanic membrane was not regularly moistened, and the low frequency resonance measured in this ear is of higher frequency and lower sharpness than most later measurements. Nonetheless, the effects of stiffening *pars flaccida* are clearly visible in this figure, with the expected reduction in low-frequency compliance and the elimination of low-frequency resonance clearly demonstrated in $\mathbf{Y}_{\mathbf{FS}}^{\mathbf{HO}}$. With the dental acrylic removed, the input-admittance clearly reverted to the general features of the pre-stiffened condition, with a prominent low-frequency resonance and an increase in low-frequency compliance. This result is consistent with our assumption that the addition of dental acrylic is responsible for stiffening the *pars flaccida* and the removal of this acoustic shunt path.

Several differences do exist between the undisturbed ear and the ear with the dental acrylic removed. The low-frequency admittance of $\mathbf{Y}_{\mathbf{AR}}^{\mathbf{HO}}$ is approximately 1 dB greater than $\mathbf{Y}^{\mathbf{HO}}$, indicating greater compliance of the *pars flaccida.* This phenomenon is probably due to the moistening effect of the vaseline, which was used to hold the dental acrylic in place but was mostly removed along with the acrylic. Another noticeable difference is the increase in the resonance frequency in the unstiffened ear, an indication of a decrease in the acoustic mass of *pars flaccida* — maybe a result of the dehydration process. At higher frequencies, the slight shift in the resonance near 2 kHz cannot be explained in terms of the *pars flaccida* manipulations. We can only speculate about the cause of this change; for example, this feature is consistent with a smaller probe-tube hole, presumably covered by leftover vaseline during the measurement process.

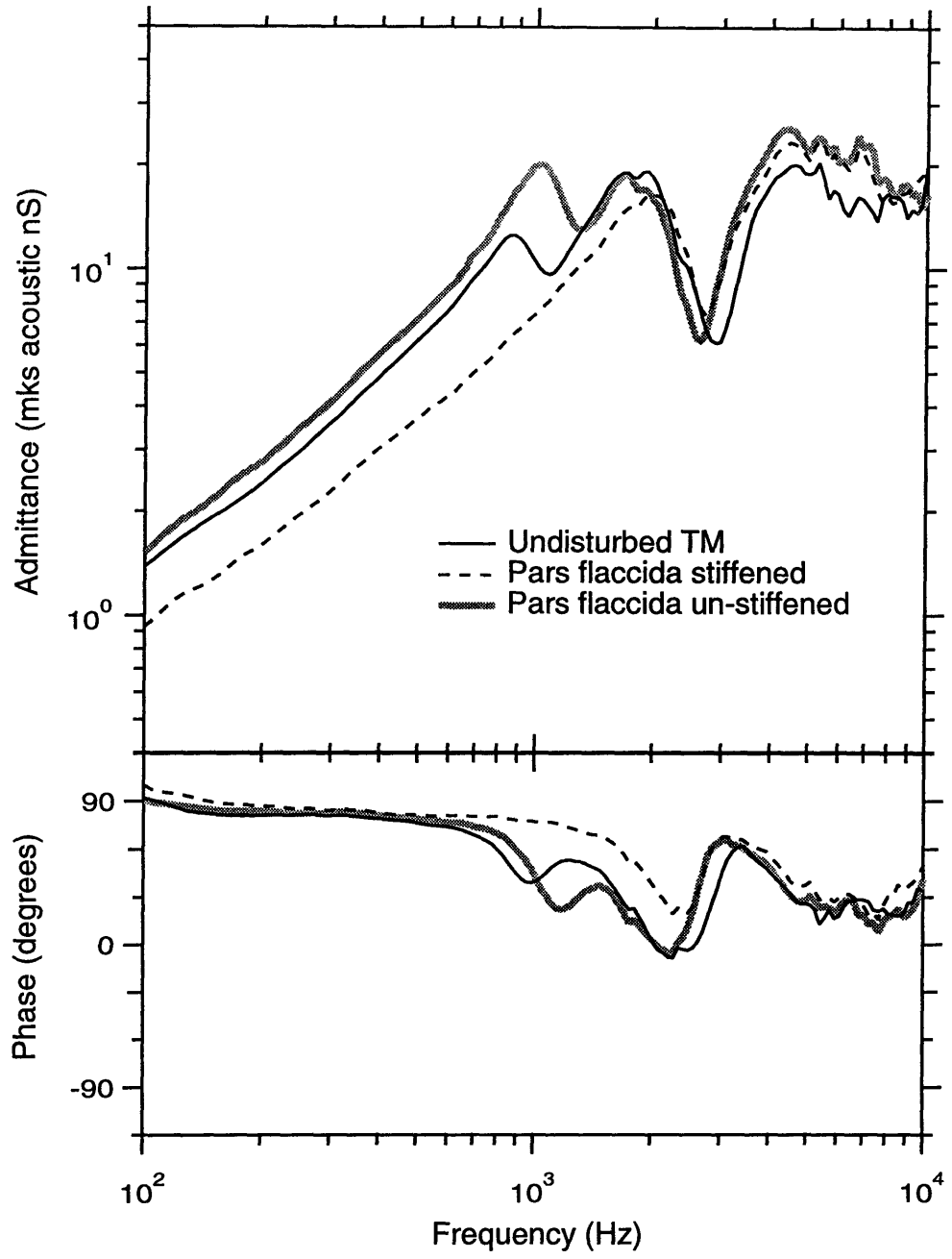

Figure 3-9: Effects of removing dental acrylic on the middle-ear input admittance. These measurements were made in the left ear of gerbil A2, with the probe-tube hole left open. Three plots are shown in this figure, one with the tympanic membrane undisturbed, one with the *pars flaccida* stiffened by dental acrylic, and a third one with the acrylic removed.

3.1.8 Pressure measurements in the ear canal and the middle-ear cavity

Our results thus far have primarily been compared with the middle-ear model shown in Figure 1-7 and 1-8. For such discussion to be meaningful, it is essential for the circuit representation to accurately depict the actual middle-ear pressure transmission. A simple but important test of the middle-ear model is to measure the sound pressures in both the ear canal and the middle-ear cavity, and compare these measurements with the predicted values based on the admittance measurements discussed in the previous sections.

Figure 3-10 shows the middle-ear to ear-canal pressure ratios measured in the right ears of gerbils B8 and B9 under three conditions: 1) with the tympanic membrane intact and undisturbed, 2) with the *pars flaccida* stiffened, and 3) with the *pars flaccida* removed. In the preparation of these figures, the measured ear-canal pressure levels have been corrected for the residual ear-canal volume using the two-port model described in Section 3.1.1. In the low-frequency region, where the pressures at both ear-canal and middle ear are in phase, the sound pressure levels are determined by a simple voltage divider between the compliance of the middle-ear cavity C_{CAV} and the compliance of the tympanic membrane-ossicular-cochlear complex (C_{TOC} or C_{PF}+C_{TOC} depending on the condition of the *pars flaccida*). The measured pressure ratios thus provide a means of determining the relative stiffness between these compliances, specifically:

$$\left.\frac{|\mathbf{P_{MEC}}|}{|\mathbf{P_{EC}}|}\right|_{PFstiffened} = \frac{C_{TOC}}{C_{TOC} + C_{CAV}} \tag{3.3}$$

and

$$\left.\frac{|\mathbf{P_{MEC}}|}{|\mathbf{P_{EC}}|}\right|_{TMundisturbed} = \frac{C_{TOC} + C_{PF}}{C_{TOC} + C_{CAV} + C_{PF}} \tag{3.4}$$

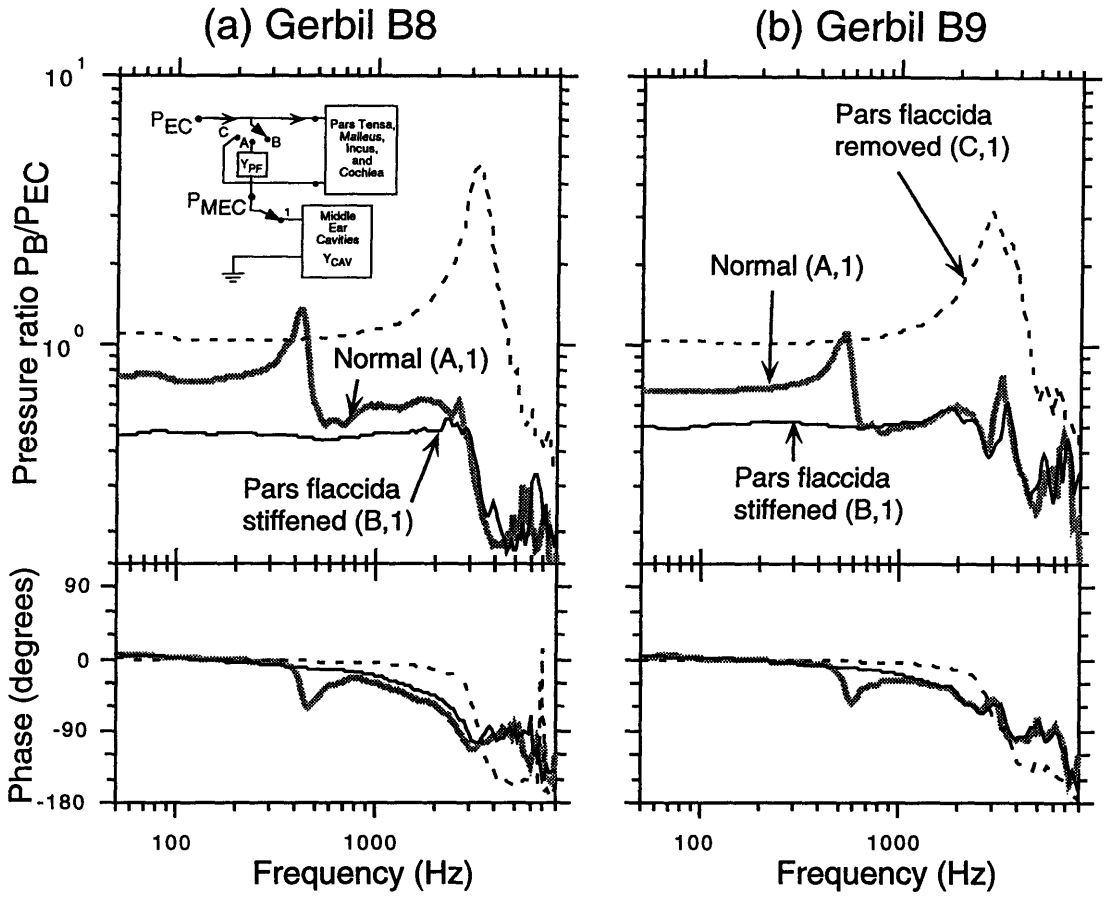

Figure 3-10: Middle-ear cavity to ear-canal pressure ratio measured in the right ears of gerbils B8 and B9—middle ear intact. The pressure ratios were measured under three conditions: 1) with the tympanic membrane intact and undisturbed, 2) with the *pars flaccida* stiffened, and 3) with the *pars flaccida* removed. The alphanumeric characters (which are enclosed in parentheses) following each legend indicate the switch positions used to represent the particular experimental manipulations (see Figure 2-18).

For measurements made in the right ear of gerbil B8, the measured pressures are in-phase at frequencies below 300 Hz. In this range, the pressure ratio measured with *pars flaccida* removed is near unity, confirming that the hole made in the *pars flaccida* was indeed acting as open circuit, and that the middle-ear and ear-canal microphones were properly calibrated. For the case where the *pars flaccida* is stiffened, the measured pressure ratio is approximately 0.46, close to the value of 0.44 calculated from Eqn. 3.3 and the data of Figure 3-6a[6]. The measured low-frequency pressure ratio when the tympanic membrane is undisturbed has a magnitude of approximately 0.73, which compares well with the model prediction of 0.69.[7] The measurements made in gerbil B9 share most of the general features observed in gerbil B8. At frequencies below 300 Hz, the measured pressure ratios for cases of *pars flaccida* removed, stiffened, and undisturbed are 0.01, 0.50, and 0.68 respectively. These measured values are very close to the model predictions of 0.00, 0.50, and 0.66.[8] The close agreement between the predicted pressure ratios and the measured values in both ears confirms the validity of the series configuration between the cavity admittance and the admittance of the tympanic membrane-ossicular-cochlear complex, at least in the low-frequency region.

The admittance and the pressure measurement results all demonstrate that the *pars flaccida*, the *pars tensa*-ossicular-cochlear complex, and the middle-ear cavity all have compliances of comparable magnitude, with the *pars flaccida* having a slightly greater value than the other two. Consequently, in the series topology, the cavity compliance is less than half the compliance of the overall tympanic membrane-ossicular-cochlear com-

[6] $C_{TOC} = 1.32 \times 10^{-3}\ mm^3/Pa$ and $C_{CAV} = 1.66 \times 10^{-3}\ mm^3/Pa$.

[7] Prediction is based on Eqn. 3.4, with $C_{PF} = 2.45 \times 10^{-3}\ mm^3/Pa$ and the same C_{TOC} and C_{CAV} as above.

[8] Model prediction values were obtained from Figure 3-6b, where $C_{TOC} = 1.68 \times 10^{-3}\ mm^3/Pa$, $C_{PF} = 1.51 \times 10^{-3}\ mm^3/Pa$ and $C_{CAV} = 1.66 \times 10^{-3}\ mm^3/Pa$.

plex. Thus, the cavity compliance tends to dominate the low-frequency input admittance of the intact middle ear, as demonstrated in Figures 3-3 and 3-4.

Figure 3-11 shows the middle-ear cavity to ear-canal pressure ratio measured in the left ears of gerbils B8 and B9, where the middle-ear cavities were widely opened. In the middle-ear model, widely opening the middle-ear cavity should "short" out the admittance of the cavity, causing the middle-ear pressure to be uniformly zero. However, the loading effect of the radiation impedance and the incomplete opening of all bulla walls resulted in the generation of finite sound pressure in the middle ear cavity. Figure 3-11 shows that at frequencies above 4 kHz, the separation between the ear-canal and the middle-ear pressures is less than 20 dB, proving that the "short circuit" assumption does not apply in this frequency range. The frequency of the pressure maxima agrees well with the frequency of middle-ear admittance minima measured with middle ear widely opened (Figure 3-8).

Consistent with the admittance measurements, the pressure ratios at frequencies above 500 Hz do not differ significantly between the case where the tympanic membrane is undisturbed and case where the *pars flaccida* is stiffened. Below 500 Hz, the ears with normal tympanic membrane show approximately 10 dB higher middle ear pressure than the ears with *pars flaccida* stiffened. Such results confirm the shunt path configuration between the *pars flaccida* and the *pars tensa*-ossicular-cochlear complex, where substantial volume velocity can be channeled through the shunt path to produce higher pressure in the middle ear.

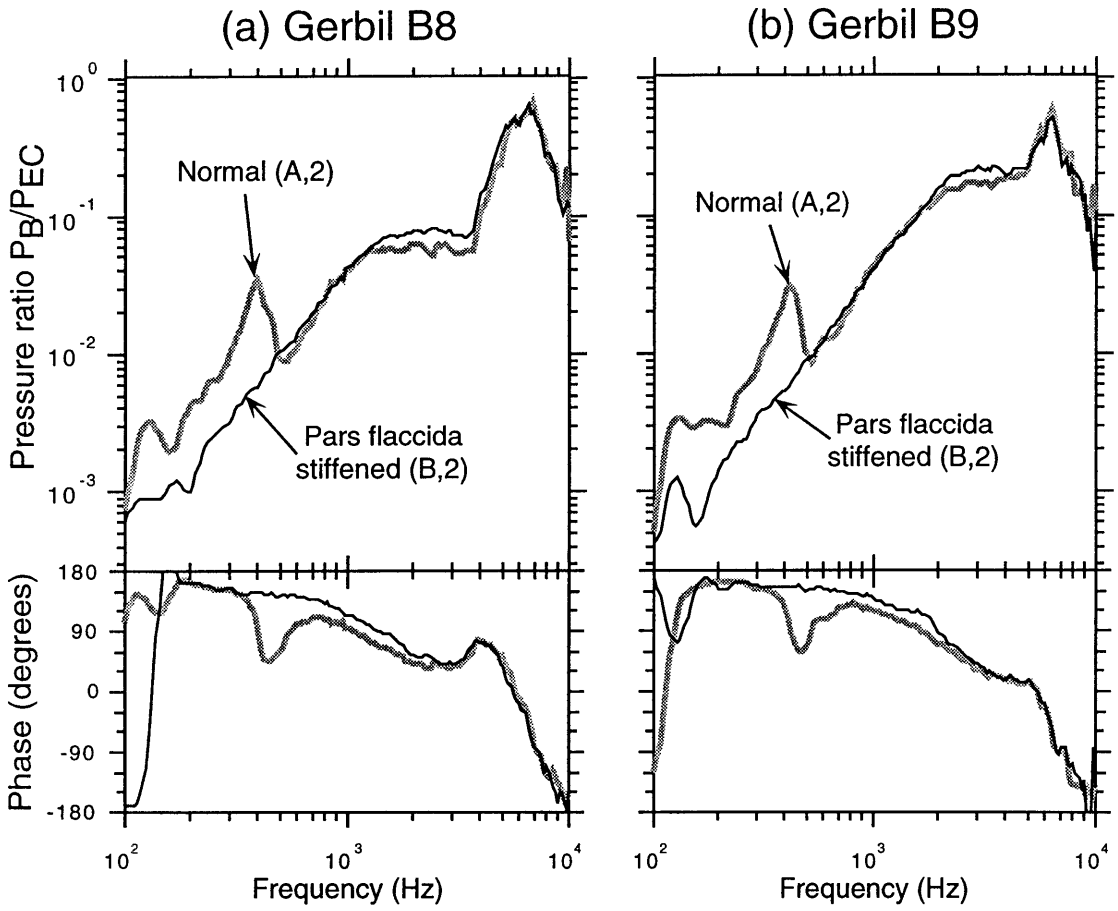

Figure 3-11: Middle-ear cavity to ear-canal pressure ratio measured in the left ears of gerbils B8 and B9—middle ear widely opened. The pressure ratios were measured under two conditions: 1) with the tympanic membrane intact and undisturbed, and 2) with the *pars flaccida* stiffened. The alphanumeric characters (which are enclosed in parentheses) following each legend indicate the switch positions used to represent the particular experimental manipulations (see Figure 2-18).

3.2 Cochlear potential measurements

One major assumption of the middle ear model of Figure 1-7 is that input to the inner ear is strictly dependent on the pressure difference across the tympanic membrane. This premise assumes that the difference in pressure produces a proportional vibration velocity of the ossicles, which induces an equally proportional vibration in the cochlear fluid — the principle stimulus that triggers the neural transduction mechanism of the inner ear. Møller (1963; 1965) showed that over a limited frequency range, the cochlear potential measured near the round window is approximately proportional to the velocity of stapes vibration. Thus CP measurements provide a means of measuring the output of the middle-ear transmission process. Two important factors must first be considered, however, before the gerbil measurement system can be used for such a purpose: 1) The appropriate stimulus paradigm, and 2) The presence of nonlinearity in the round-window cochlear potential.

3.2.1 Linearity of cochlear potential measurements

As described in Section 2.4, the non-stationary behavior of round-window cochlear potential renders the chirp stimulus unsuitable for the measurement of cochlear response. Figure 3-12 shows examples of measured cochlear potentials in response to chirp stimuli, where the resulting nonlinearities produce sharp dips in the potential measurements, mostly at frequencies below 1 kHz. Consequently, all other results presented in this section were measured with tone-sweep stimuli.

The measured AC round-window cochlear potential actually consists of two components, cochlear microphonic and neural action potential (Dallos et al. , 1974). Cochlear microphonic is derived from the ionic current flowing through the outer hair cells, and is

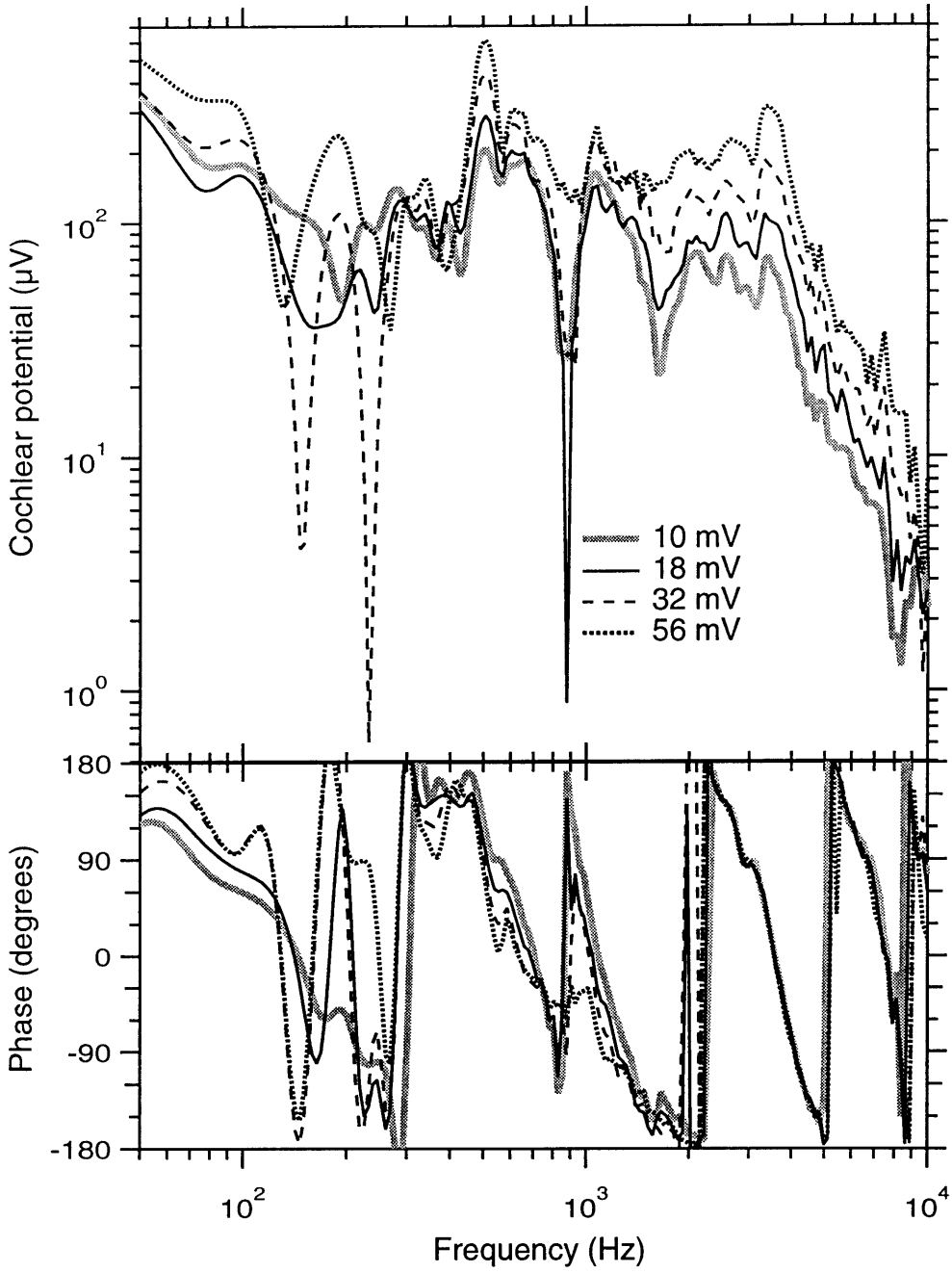

Figure 3-12: Examples of cochlear potential responses to chirp stimuli. The nonlinearity of the cochlear potential responses to chirp stimuli is evident in this figure. These particular responses were obtained from the right ear of gerbil B8, with the lfs driven by the voltage levels shown in the legend. While the applied pressure levels were evenly spaced at 5 dB apart, the responses did not follow the same linear spacing.

the component of cochlear potential that actually follows the vibration of the cochlear fluid. On the other hand, the neural action potential is due to the all-or-none firing of the auditory nerve fibers — a highly nonlinear process. Figures 3-13a and 3-14B clearly illustrate this nonlinear phenomenon. In Figure 3-13a, the low intensity cochlear potentials are dominated by neuronal firings, resulting in the observed nonlinear relationship between cochlear potentials and sound pressure levels. In 3-14B, the neural firings produced a regular distortion in the cochlear potential.

TTX (Tetrodotoxin, from Sigma Chemical Co.), a chemical that blocks neural action potentials but has no effect on the outer hair cells, was used to eliminate the neuronal component from the cochlear potential in two ears, the left ears of gerbil B10 and B11. 1 mg of TTX was mixed with 1 ml of artificial perilymph to obtain a 3.13 mM solution. 1 μl of this solution was added to the round window niche, where it diffused through the round-window membrane into the inner ear. The effects of TTX on cochlear potential are demonstrated in Figures 3-13 and 3-14. Figure 3-14A shows the sound pressure level measured in the external ear canal. Figure 3-14B shows the corresponding pre-TTX cochlear potential response, where the phase-locked neural action potential is clearly visible. The neural component was eliminated in the post-TTX measurements, as displayed in 3-14C.

Figure 3-13b shows the level functions of the growth of post-TTX cochlear potentials with increasing stimulus pressure levels. The results show great improvement in the linearity of the cochlear responses, where the neural components no longer dominate the low-stimulus cochlear potentials. Some lesser nonlinearities, however, are still visible in the measured responses. The cochlear potential level functions at 220 Hz, 244 Hz, 330 Hz, and 488 Hz all have slopes of greater than 1. Such nonlinearity is mainly limited

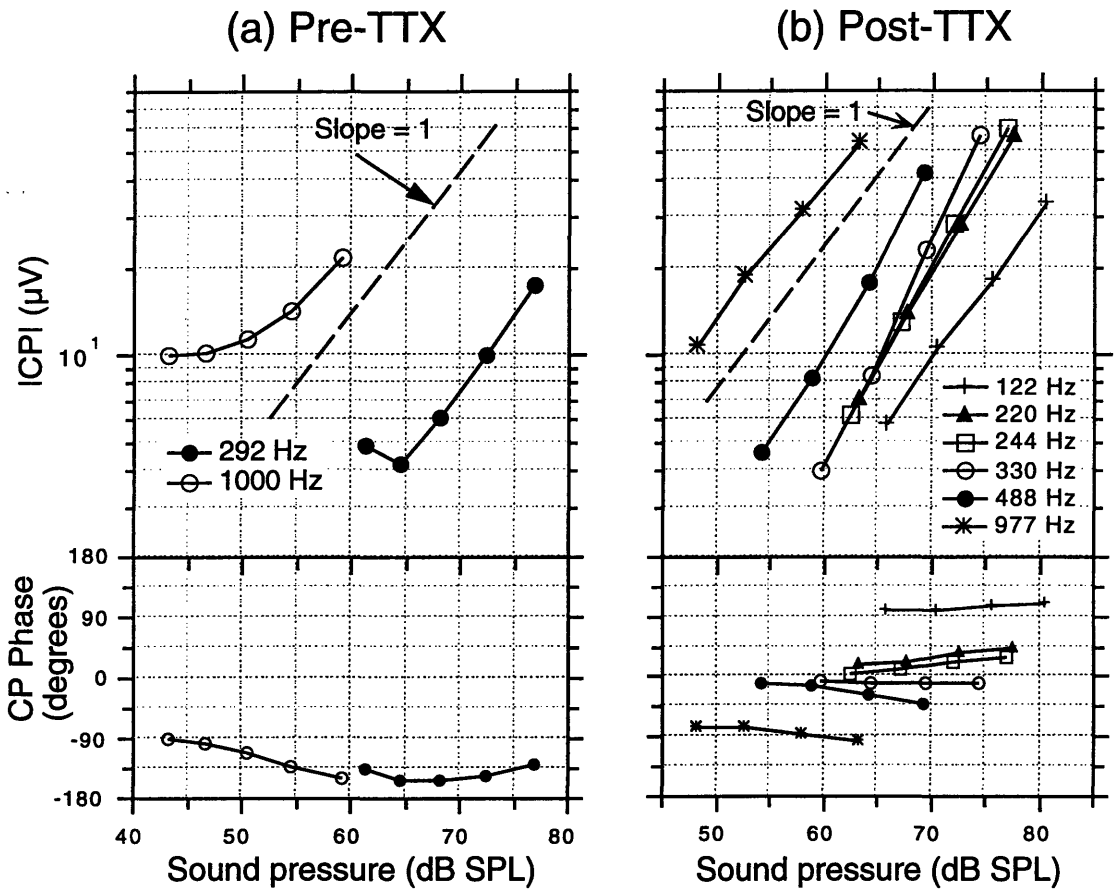

Figure 3-13: Plots of cochlear potentials versus sound pressure levels before and after the application of TTX. The measurements were made with tonal stimuli in the left ear of gerbil B11. (a) The nonlinearity, especially at low sound levels, are evident at the two measured frequencies. (b) The linearity of the cochlear potentials has been greatly improved in comparison with the pre-TTX measurements. The cochlear potentials at 220 Hz, 244 Hz, 330 Hz, and 488 Hz still exhibit some nonlinearities, where the slopes are all slightly greater than one. Figure 3-15 and 3-16 show that this type of nonlinearity is limited to frequency between 200 and 600 Hz.

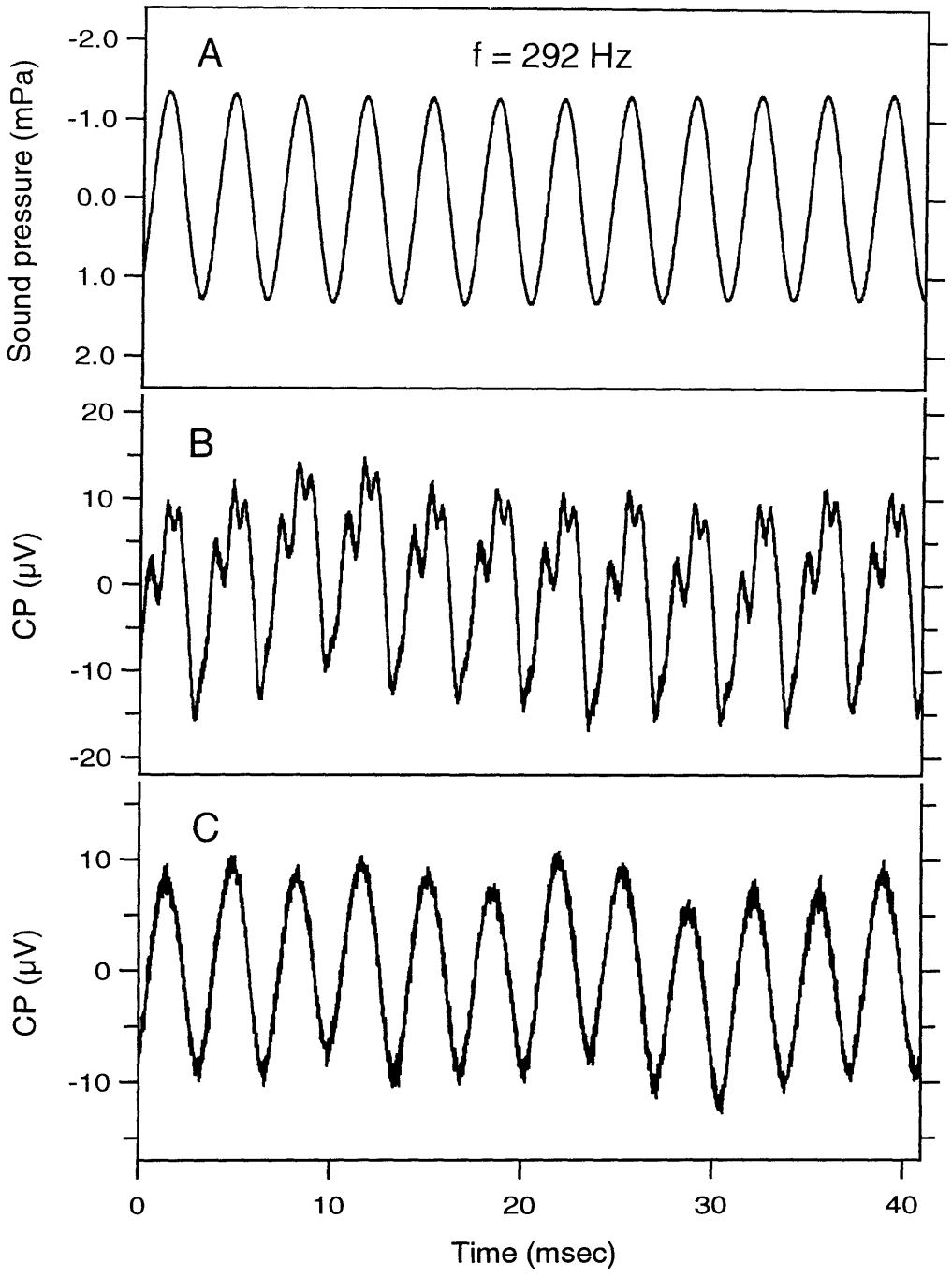

Figure 3-14: Effects of TTX on the cochlear potential recording. These measurements were obtained from the left ear of gerbil B10, where most of the bulla wall has been removed. Top (A): The tone burst stimulus applied at the gerbil ear canal. Middle (B): Cochlear potential response to the tone burst stimulus before the application of TTX. Bottom (C): Cochlear potential response after the application of TTX.

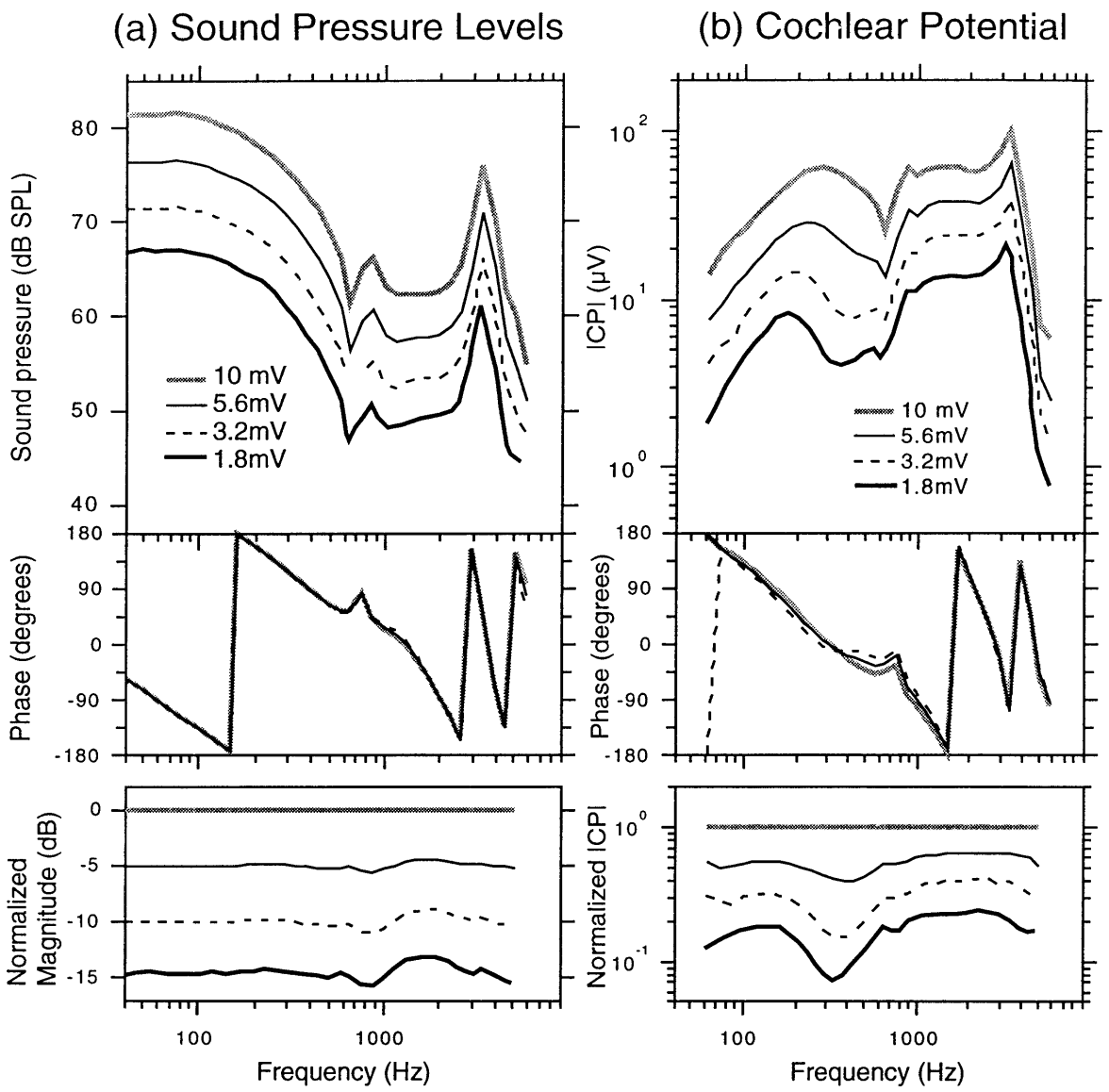

Figure 3-15: Stimulus pressure levels and post-TTX cochlear potential responses measured in the left ear of gerbil B11 (middle ear widely opened). (a) The first two plots display the sound pressure levels at the gerbil ear canal when different amplitudes of tone-sweep voltages were applied to the lfs. All measurements were made in ear with normal tympanic membrane. The bottom plot represents the pressure levels normalized by the pressure measurements made with 10 mV driver voltage. (b) The cochlear potential measurements correspond to the pressure stimuli shown in panel (a). The bottom plot represents the measured cochlear potentials normalized by the cochlear response made with 10 mV driver voltage.

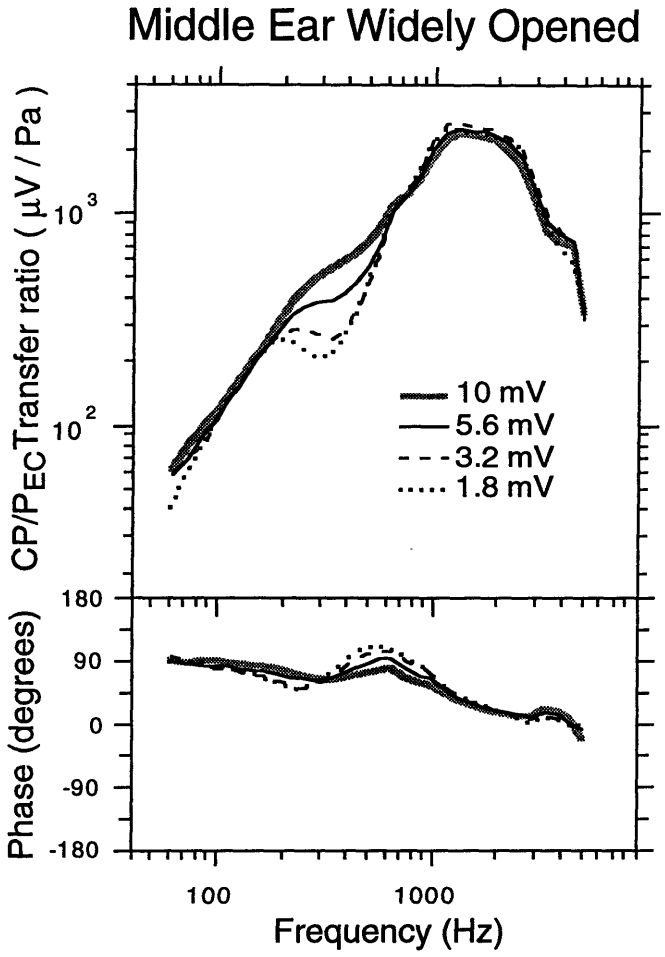

Figure 3-16: Middle-ear transfer function at various stimulus levels (gerbil B11). The transfer function is defined with the ear-canal sound pressure level as input and the round-window cochlear potential as output. They are computed by dividing the cochlear potential spectra of Figure 3-15b with the pressure spectra of Figure 3-15a.

to frequencies between 200 and 600 Hz, as illustrated in the tone-sweep measurements of Figures 3-15 and 3-16. Figure 3-15b shows the cochlear potential spectra measured with four different stimulus settings, with the corresponding ear-canal sound pressure levels shown in Figure 3-15a. In both figures, the bottom plots show the respective normalized spectra magnitudes, which allow easy identification of any nonlinearity across the whole frequency spectrum. The normalized cochlear potential spectra demonstrate the above mentioned nonlinearity between 200 and 600 Hz, with the cochlear potential apparently suppressed at low sound intensity. The stimulus pressure also shows signs of some slightly nonlinear behavior; however, this nonlinearity is most apparent in the mid to high frequencies. The origin of this nonlinearity is unknown but may be in the instrumentation.

A better way of determining the linearity of a system is to plot the system transfer function at various stimulus levels. Figure 3-16 displays such a plot for the middle-ear transfer function, defined with the ear-canal sound pressure level as input and the round-window cochlear potential as output. The transfer functions show good consistency (which is an indication of linearity) for most of the frequency range, with the exception of the frequency range from 200 to 600 Hz, where the suppressed cochlear potential phenomena at low sound intensity is manifested as deeper and deeper dips in the transfer function. The magnitude of this nonlinearity is significant. The transfer-function magnitude at 300 Hz varies by a factor of 3, while the stimulus voltage varies by a factor of 5.

3.2.2 Effects of *pars flaccida* manipulation on round-window cochlear potential

In the left ears of gerbil B10 and B11, where the middle-ear cavities were widely opened, the post-TTX cochlear potential before and after the stiffening of *pars flaccida* were measured. Figures 3-17 and 3-18 show the ear-canal sound pressure levels measured in these two ears, where the earphone driver voltage was kept constant at 10 mV during the measurement process. As expected from the admittance results of Section 3.1, at frequencies below the *pars flaccida* resonance, the measured ear-canal sound pressure levels in the stiffened ears have larger magnitude than the undisturbed ears — a direct result of the increased stiffness following the removal of the *pars flaccida* compliance. At frequencies above the resonance, the sound pressure levels are approximately equal for both measurement configurations.

Using the acoustic calibration methods described in Chapter 2, these pressure spectra can be used to compute the middle-ear input admittance of the two measured ears (Figure 3-19). Since the tone-sweep paradigm consists of only five tonal stimuli per octave, the frequency resolution of these input admittance plots is substantially lower than the admittance measured with the chirp paradigm. Nonetheless, the results do capture several important features of the effects of *pars flaccida* in the functioning of the middle ear. Figure 3-19 shares many similar features with the other admittances measured with the middle ear widely opened (Section 3.1.6), where the stiffening of *pars flaccida* suppresses the overall low frequency compliance and eliminates the low-frequency resonance. Note however that the frequency of the *pars flaccida* resonance of B11 is slightly higher than that observed in either B8, B9, or B10 (Figures 3-8 and 3-19a), and the difference in low-frequency admittance between the stiffened and the

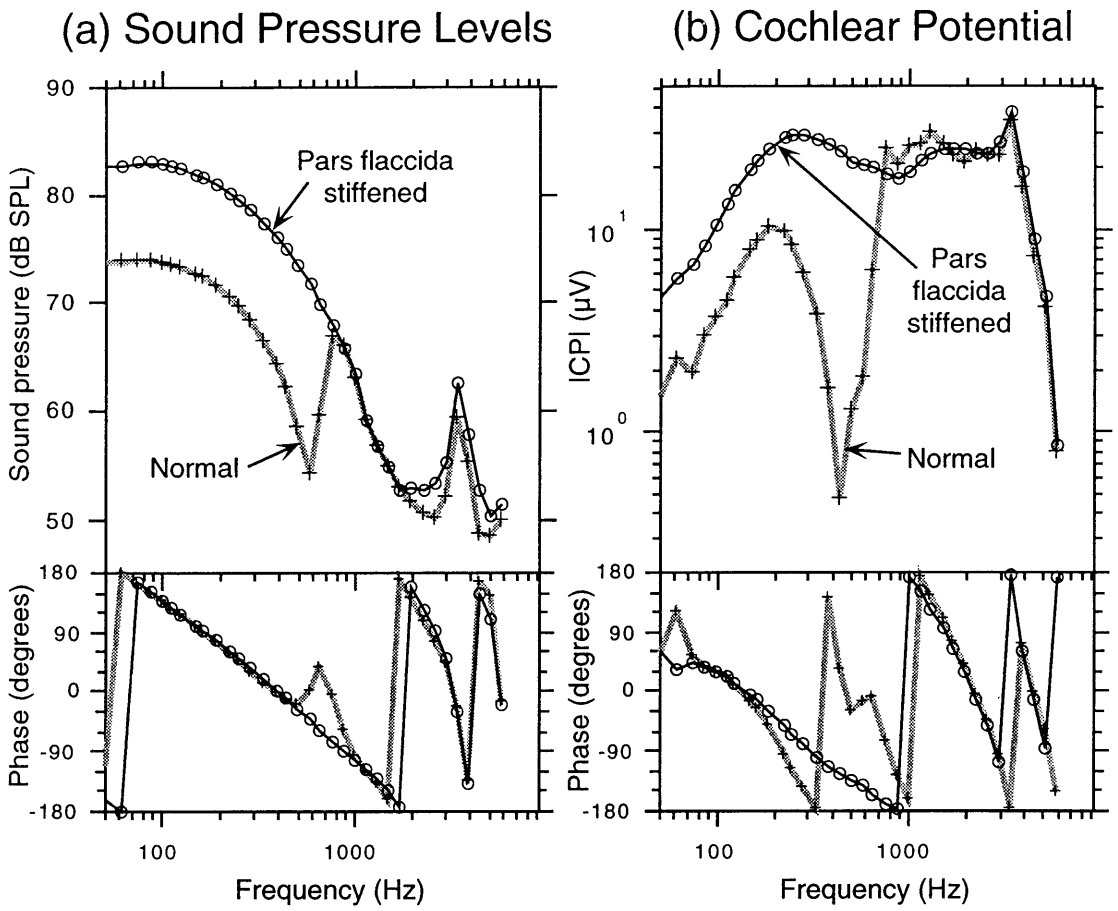

Figure 3-17: The tone-sweep stimulus spectra and cochlear potential responses measured in the left ear of gerbil B10 (middle ear widely opened). (a) This plot shows the sound pressure levels at the gerbil ear canal when voltages of constant amplitude (10 mV) were applied to the lfs. At frequencies below 600 Hz, the generated sound pressure in the *pars flaccida* stiffened ear is approximately 4 dB higher than the sound pressure generated in the normal ear — a result of the increased stiffness at that frequency region. (b) The general features of the cochlear responses are similar to that of the stimulus, where the difference in pressure levels at low frequency directly translated to a similar separation in measured cochlear response. No obvious nonlinearity is evident. The markers along the plots indicate the frequencies of the stimuli.

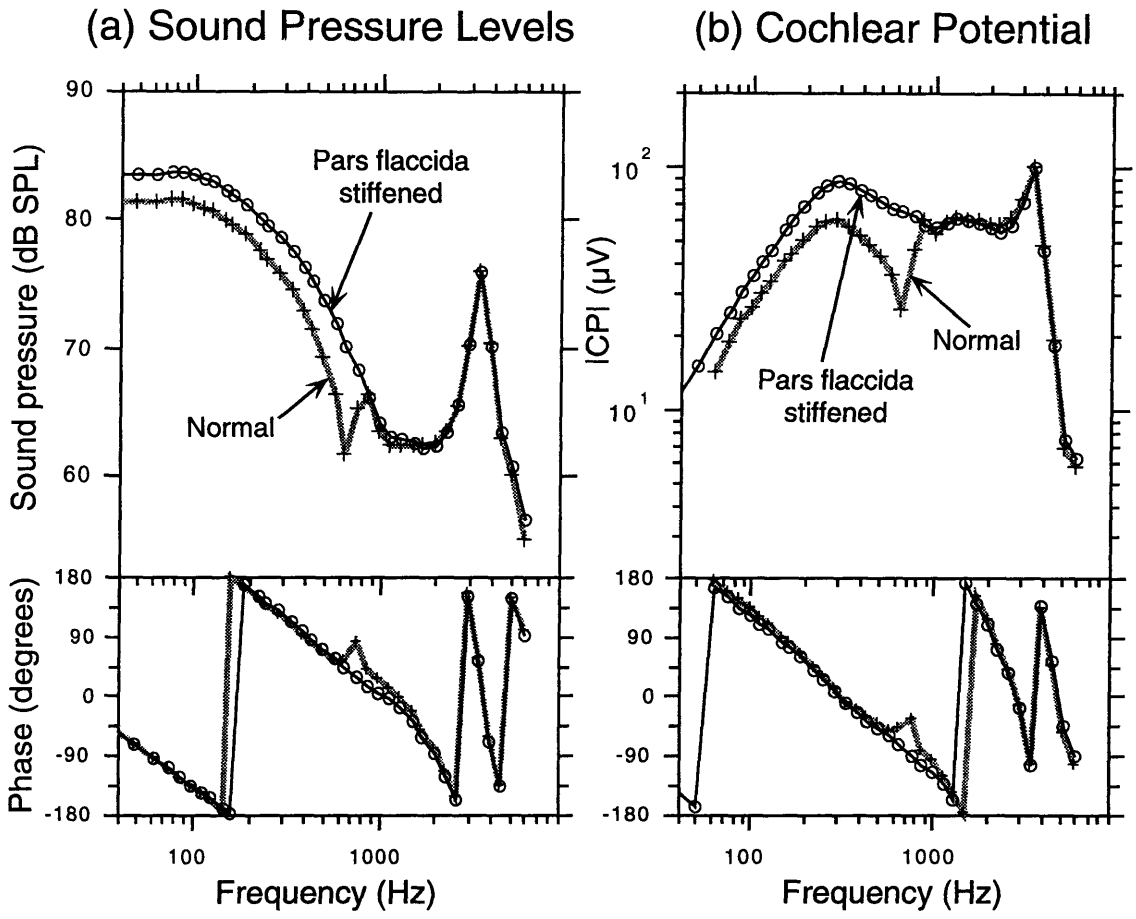

Figure 3-18: The tone-sweep stimulus spectra and cochlear potential responses measured in the left ear of gerbil B11 (middle ear widely opened). (a) This plot shows the sound pressure levels at the gerbil ear canal when voltages of constant amplitude (10 mV) were applied to the lfs. At frequencies below 600 Hz, the generated sound pressure in the *pars flaccida* stiffened ear is approximately 4 dB higher than the sound pressure generated in the normal ear — a result of the increased stiffness at that frequency region. (b) The general features of the cochlear responses are similar to that of the stimulus, where the difference in pressure levels at low frequency directly translated to a similar separation in measured cochlear response. No obvious nonlinearity is evident. The markers along the plots indicate the frequencies of the stimuli.

normal conditions is also smaller in this ear than the other three. Such phenomena indicate that the *pars flaccida* of B11 may have been slightly dehydrated during the measurement process.

Figures 3-17b and 3-18b show the cochlear potentials measured in gerbils B10 and B11 in response to the pressure stimuli of Figures 3-17a and 3-18a. At frequencies below the *pars flaccida* resonance, the difference in ear-canal pressure levels translated to a similar separation in the measured cochlear responses; at higher frequencies, where the sound pressure levels are approximately equal, the resulting cochlear potentials are also equal under the two measurement conditions. This finding is consistent with the middle ear model: when the middle ear is widely opened, the pressure difference across the tympanic membrane is approximated by $\mathbf{P_{EC}}$, which we assume to be the effective input to the inner ear. Therefore, the model predicts a proportionality between $\mathbf{P_{EC}}$ and CP. One region where CP and $\mathbf{P_{EC}}$ are not proportional is near the 400 Hz dip in CP in ear B10. This dip is much deeper that that observed in $\mathbf{P_{EC}}$ in this ear. This dip may be the result of a continuing nonlinearity in cochlear potential measurements, or it may indicate that the model separation of *pars flaccida* and *pars tensa* into separate blocks is not accurate near resonance.

A better quantitative understanding of middle-ear transmission properties can be gained from the transfer function of ear-canal pressure to cochlear potential response. Figure 3-20 shows the left ears transfer functions of gerbils B10 and B11, both before and after the stiffening of *pars flaccida.* The transfer functions were calculated from measurements made with the earphone driver voltage set at constant amplitude of 10 mV (this is the only stimulus level where the *pars flaccida* stiffened measurements were made). For frequencies below 1 kHz, the middle-ear transfer functions (with the exception of

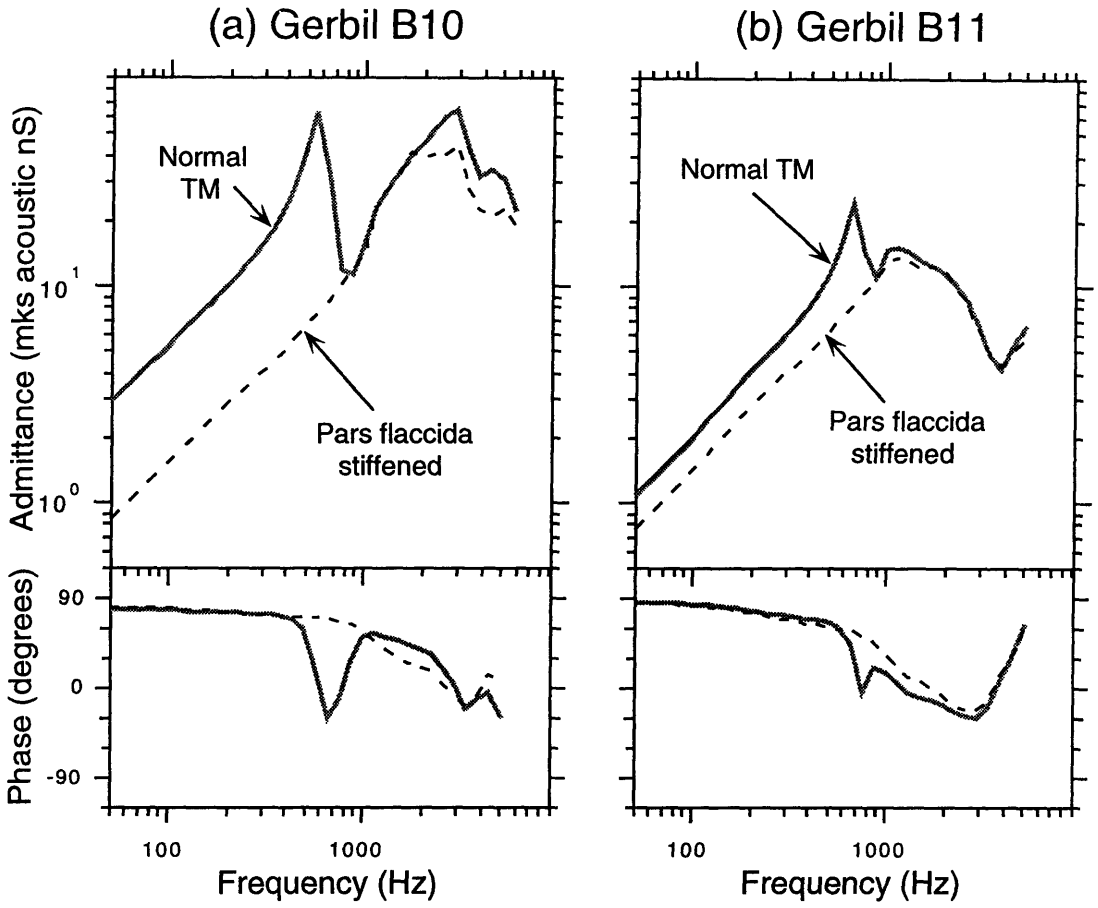

Figure 3-19: Middle-ear input admittance measured in the left ears of gerbils B10 and B11—middle ear widely opened. (a) The admittance plots of gerbil B10 were calculated from the ear-canal pressure measurement of Figure 3-17a. The effects of the stiffened *pars flaccida* on the low-frequency admittance is apparent in this figure, with the familiar *pars flaccida* resonance and compliance entirely suppressed. The markers along the plots indicate the frequencies of the stimuli. (b) The admittance plots of gerbil B11 were calculated from the ear-canal pressure measurement of Figure 3-18a. The effects of *pars flaccida* on the low-frequency admittance is again apparent in this figure. Note that the low-frequency resonance in this ear is higher than the measurements of B8, B9, and B10 (Figures 3-8 and 3-19a). The difference in low-frequency admittance between the stiffened and the normal configuration is also lower than the other three ears. All these phenomena show that the tympanic membrane may have been slightly dehydrated when the measurements were made. The markers along the plots indicate the frequencies of the stimuli.

the undisturbed ear of gerbil B10) are all stiffness dominated, where the magnitudes are generally proportional with frequency, and the angles are between 45° to 90°. For gerbil B10, the transfer function of the undisturbed ear shows a dip between 200 and 600 Hz, a result of the unexpected decrease in cochlear potential in this frequency range (see Figure 3-17b). This feature shares some similarities but also some differences with the nonlinear cochlear potential observed in gerbil B11. While all these features occur at the same frequency range, the sharp dip in cochlear response at approximately 400 Hz is noticeably absent in the B11 measurements. Also, the amount of cochlear potential decrease, after correction for the difference in ear-canal pressure levels, is substantially larger in B10 than the reduction shown in B11. Besides this peculiarity, the two transfer functions exhibit most of the characteristics predicted by the middle ear model. Recall from the pressure ratio measurements of Figure 3-11 that with the middle ear cavity widely opened, $\mathbf{P_{EC}} \gg \mathbf{P_{MEC}}$ at frequencies below 5 kHz; thus, the bulla cavity is essentially shorted out in this frequency range. As a result, the middle-ear model consists of only *pars flaccida* in parallel with the *pars tensa*-ossicular-cochlear complex. In this configuration, the volume velocity entering the inner ear is only dependent on the pressure of the ear canal, and independent of the *pars flaccida*. Such characteristics are clearly demonstrated by the measured middle-ear transfer ratio, where the pre- and post-stiffened ears show great similarity in both magnitudes and angles. This similarity suggests that any modulation of ear-canal pressure by the acoustic properties of *pars flaccida* (*i.e.* increasing the low-frequency input admittance and decreasing the sound pressure) produces a similar modulation of the input to the cochlea.

To compare the relative effects of *pars flaccida* stiffening on the middle-ear input admittance, ear-canal pressure level, and cochlear potential generation, we computed the

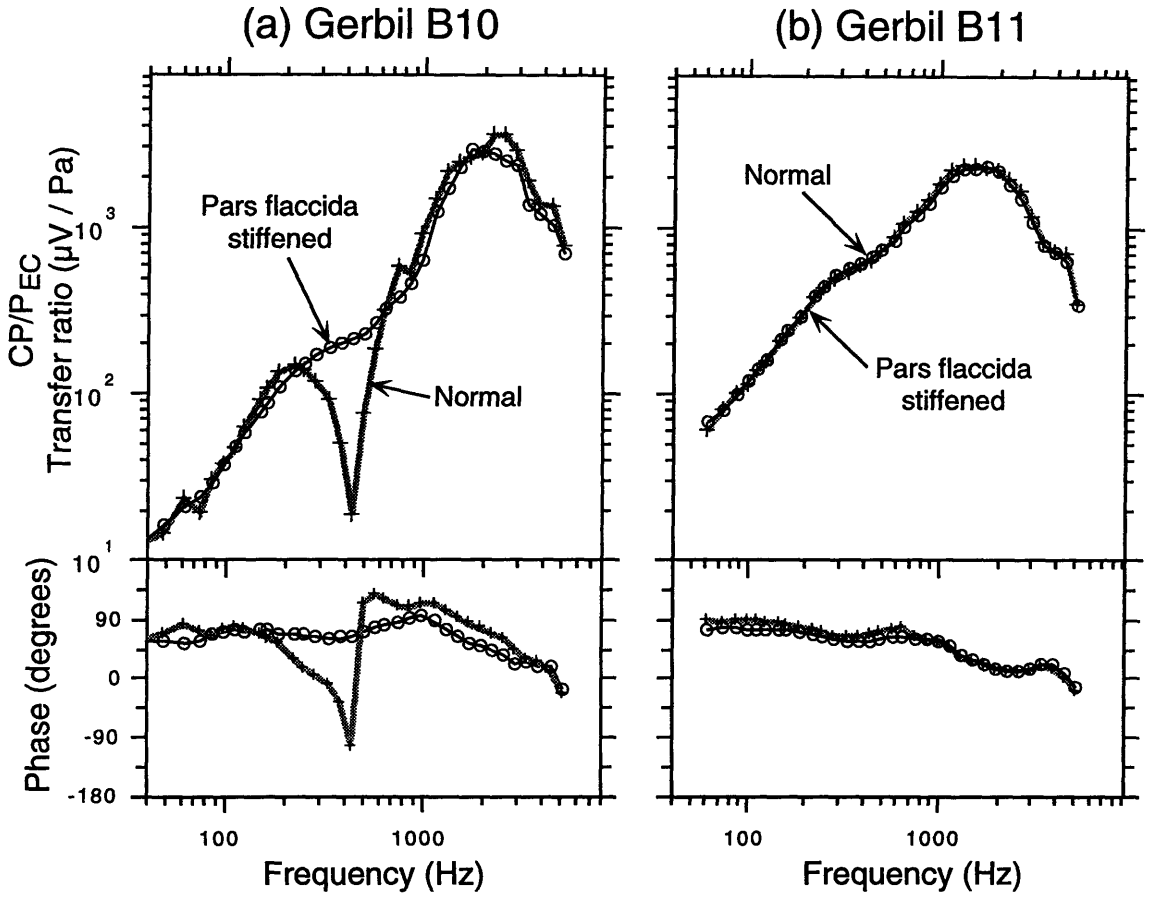

Figure 3-20: Middle-ear transfer functions of gerbils B10 and B11 (middle-ear cavity widely open). The transfer functions before and after the stiffening of *pars flaccida* are shown in this figure. The measurements were made with the earphone driver voltage set at constant amplitude of 10 mV. The markers along the plots indicate the frequencies of the tonal stimuli.

ratio between the pre- and post-stiffening results of each of these measurements. The changes in the cochlear potentials and sound pressure levels were obtained by taking the ratios (in dB) between the measurements made in the normal ear and the measurements made in the stiffened ear. It is important to realize that the measurements used for these computations were produced by applying a constant voltage to the earphone, which essentially acted as a constant volume velocity source in parallel with an internal source admittance. The results of these computation would have been different if a constant pressure source was used instead (see Section 4.5 for a more complete discussion on this topic).

$$\Delta CP|_V = 20\log\left|\frac{\mathbf{CP}|_{\mathbf{FS},constant\ V}}{\mathbf{CP}|_{constant\ V}}\right| \tag{3.5}$$

$$\Delta P_{EC}|_V = 20\log\left|\frac{\mathbf{P}|_{\mathbf{FS},constant\ V}}{\mathbf{P}|_{constant\ V}}\right| \tag{3.6}$$

$$\Delta Y = 20\log\left|\frac{\mathbf{Y}}{\mathbf{Y}|_{\mathbf{FS}}}\right| \tag{3.7}$$

The subscript V is used to indicate that constant voltage was applied to the earphone in the measurement process. Since ΔY is not sensitive to the source type, no subscript is needed. Also note that for ΔY, the order of division was reversed. This is due to the fact that increasing admittance actually decreases sound pressure level as well as cochlear potential response. Analysis based on Equations 3.5–3.7 allows us to quantitatively characterize the *pars flaccida* contributions to each of the three quantities, and to compare the relative variation among these contributions. Figure 3-21 shows the results from measurements made in gerbil B10 and B11, plotted in dBs of magnitude. Except for the noted anomaly of the cochlear potential measurement at frequencies between 200 and 600 Hz in gerbil B10, all three computed quantities are equal to within $\pm$ 2 dB. Such

results agree with the traditional view of the middle ear as a linear system (Guinan and Peake, 1967; Pickles, 1988), where a linear proportionality relationship exists between stimulus and response, and demonstrate that any of these quantities can be used as indicators of the effects of *pars flaccida* in the middle-ear mechanics when the middle ear is open. At frequencies above the *pars flaccida* resonance ($\approx$ 800 Hz), the three quantities are all uniformly close to 0, indicating that the acoustic properties of *pars flaccida* do not affect the middle ear signal transmission in this frequency range. At lower frequencies, the presence of *pars flaccida* apparently causes a uniform decrease in cochlear potential and sound pressure level, except at the resonance frequency where the amount of decrease is sharply higher. The actual amount of low-frequency change in these two ears is fairly different, with gerbil B11 showing changes of approximately 2-3 dB, while gerbil B10 shows a far greater 10 dB difference. The small differences between ΔY and $\Delta P_{EC}|_V$ can be explained in terms of the circuit models of the middle-ear and the sound source. Recall from Section 2.2 that the sound source can be represented by a Norton equivalent circuit. The pressure generated in the ear canal by the equivalent volume-velocity source is directly proportional to the impedance (inverse of admittance) of the internal *and* the measured loads, $\mathbf{P_{EC}} = \mathbf{1/(Y_S + Y_{ME})}$. Therefore the change in $\mathbf{P_{EC}}$ produced by a change in middle-ear input impedance is, $\mathbf{P_{EC} + \Delta P_{EC} = 1/(Y_S + Y_{ME} + \Delta Y_{ME})}$. Note that $\Delta P_{EC}|_V$ is not proportional to $|\mathbf{1/(\Delta Y_{ME})}|$ unless $|\mathbf{Y_S}| \ll |\mathbf{Y_{ME}}|$. This condition is generally true for measurements made at low frequencies using the lfs (see Figures 2-11 and 3-19), therefore the differences between ΔY and $\Delta P_{EC}|_V$ are expected to be small.

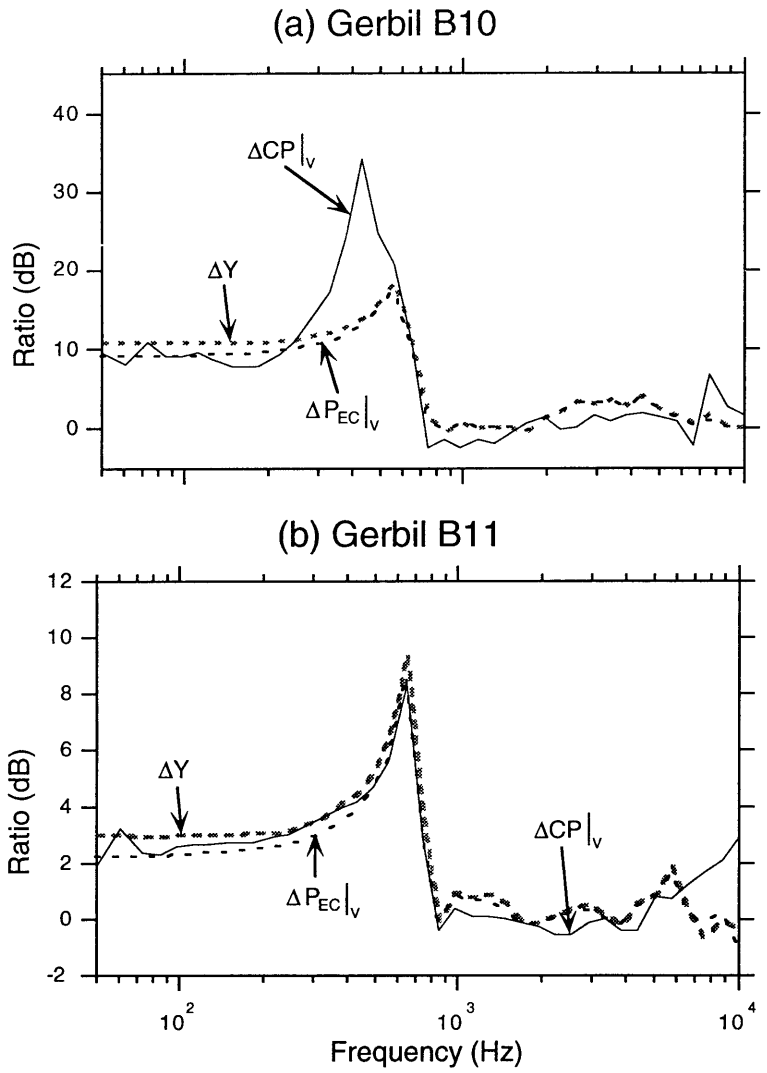

Figure 3-21: Changes in middle-ear input admittance, ear-canal sound pressure, and cochlear potential between pre- and post-stiffened measurements in gerbils B10 and B11. The plots in these figures were obtained by subtracting the measurements of cochlear potential and sound pressure level made in the normal ear from the measurements made in the stiffened ear (all in dB). The change in admittance was calculated as $20 \log \left| \frac{\mathbf{Y}^{\mathbf{WO}}}{\mathbf{Y}^{\mathbf{WO}}_{\mathbf{FS}}} \right|$. This is due to the fact that increasing admittance actually decreases sound pressure level as well as cochlear potential response.

Chapter 4

Discussion

4.1 Comparison with previously reported measurements

Middle-ear input admittance of gerbils was measured by Ravicz *et al.* (1992) using methodology similar to this study. The average $\mathbf{Y^I}$ reported by Ravicz *et al.* is shown in Figure 4-1a along with the mean of our measurements. Both admittance means are accompanied by their statistical 95% confidence intervals (*i.e.* $\pm$ 2 standard errors, with $n = 5$ for Ravicz *et al.*'s data and $n = 8$ for our measurements). Good agreement exists at frequencies below 2 kHz, where the admittance is clearly compliance dominated. The maximum variation between the two mean measurements is on the order of 5 dB in magnitude. This result, along with the small error bounds, indicates good consistency in low-frequency compliance across all measured gerbil ears. The error bounds of our measurements increase substantially in the frequency range between 3–5 kHz. This significant increase is mainly the result of measurements made in three ears — A1, B1, and B9 — which feature several peaks and reversals in slope along with significant negative phase angles. These mass-like behaviors are not evident in measurements of

other ears, which are mainly resistance dominated — similar to the data of Ravicz *et al.* At even higher frequencies, both average measurements are resistance dominated, with magnitudes of approximately 10 nS and phase angles near 0°. Figure 4-2 shows the t-test result that compares the similarity of these two means. For the middle ear intact measurements, the two means are equal at 5% significant level over most of the frequency range. Only at frequencies between 1 to 2 kHz are the two means statistically different. From Figure 4-1a, however, we see that the means are less than 2 dB apart in this frequency range. The statistical result is mainly due to the small sample size and the small standard errors of the two measurement sets.

Also shown in the amplitude plot of Figure 4-1a is an estimate of the middle-ear input admittance computed from the umbo velocity measurements of Cohen *et al.* (1993) and the *pars tensa* area measurements of Rosowski *et al.* (1995, unpublished)[area$\approx 8.3mm^2$]. The Cohen data clearly do not match the others. A possible reason for this discrepancy arises from the experimental method used by Cohen *et al.*, where a hole was drilled into the dorsomedial extent of the skull to reveal the umbo tip, thereby exposing the middle-ear cavity to the ear canal and the sound stimulus. At low frequencies, the hole would act to reduce the pressure difference across the tympanic membrane, limit the vibration velocity of the umbo, and reduce the middle-ear input admittance. Consequently, the slope of this admittance estimate at low frequencies is substantially steeper than the other measured admittances.

Ravicz *et al.* (1992) also reported the gerbil middle-ear input admittance measured with the vent tube removed and the hole in the bulla left open. Their average admittance is shown in Figure 4-1b along with our $\mathbf{Y}^{\mathbf{HO}}$ measurements. One obvious difference between the two sets of measurements is the frequency of the minimum in admittance

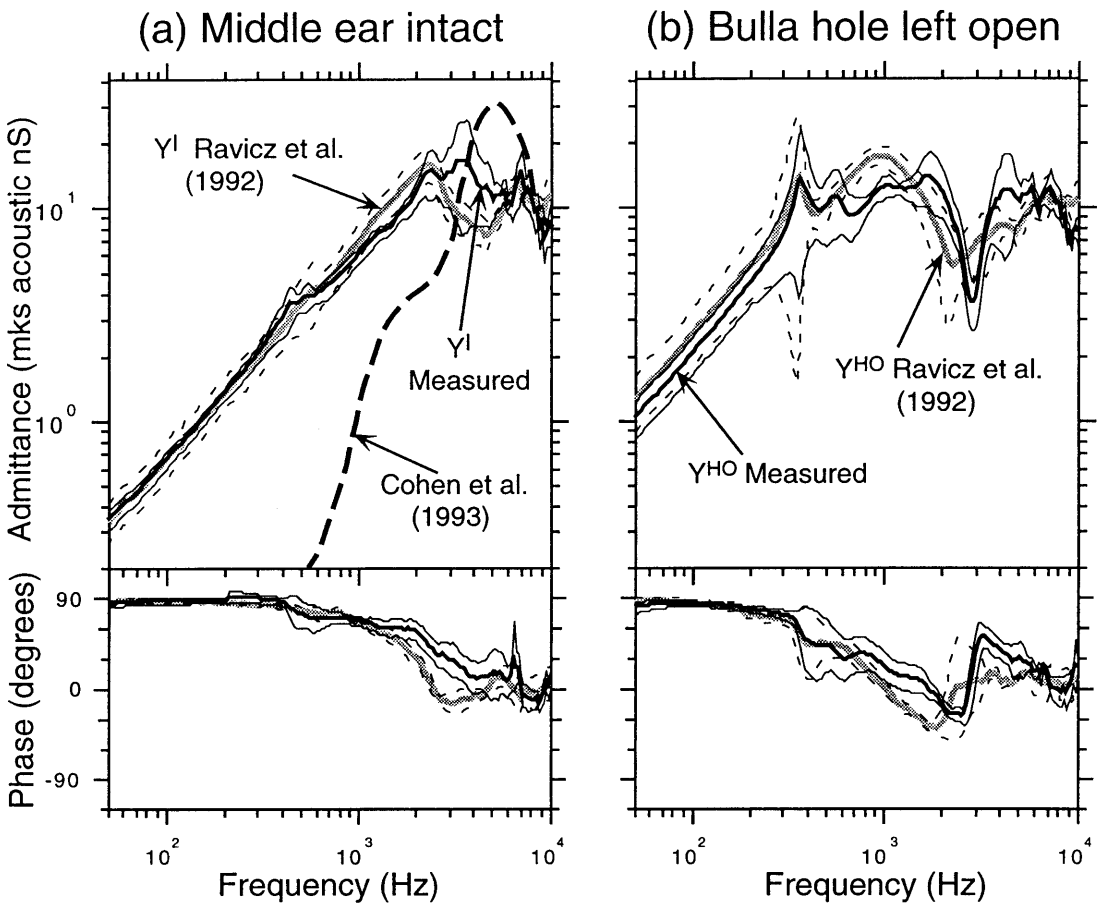

Figure 4-1: A comparison of the measured $\mathbf{Y^I}$ and $\mathbf{Y^{HO}}$ with other available admittance data. (a) The mean of all $\mathbf{Y^I}$ measurements (shown in Figure 3-3) is plotted along with the 95% confidence interval (indicated by the fine solid lines). The admittance data from Ravicz *et al.* (1992) were calculated from the measurements made in five ears, where the middle ear cavity was vented by a long thin tube (shown in Figure 9a of that paper). The fine dashed lines delineate the corresponding 95% confidence interval. The third plot shows the admittance estimate calculated from the umbo velocity measurements made by Cohen *et al.* (1993), assuming the area of the *pars tensa* is $8.3mm^2$. (b) The mean of all $\mathbf{Y^{HO}}$ measurements (shown in Figure 3-4) is plotted along with the 95% confidence interval (indicated by the fine solid lines). The admittance data from Ravicz *et al.* were calculated from the measurements made in six ears, with the middle-ear vent tube hole left open (shown in Figure 9b of that paper).

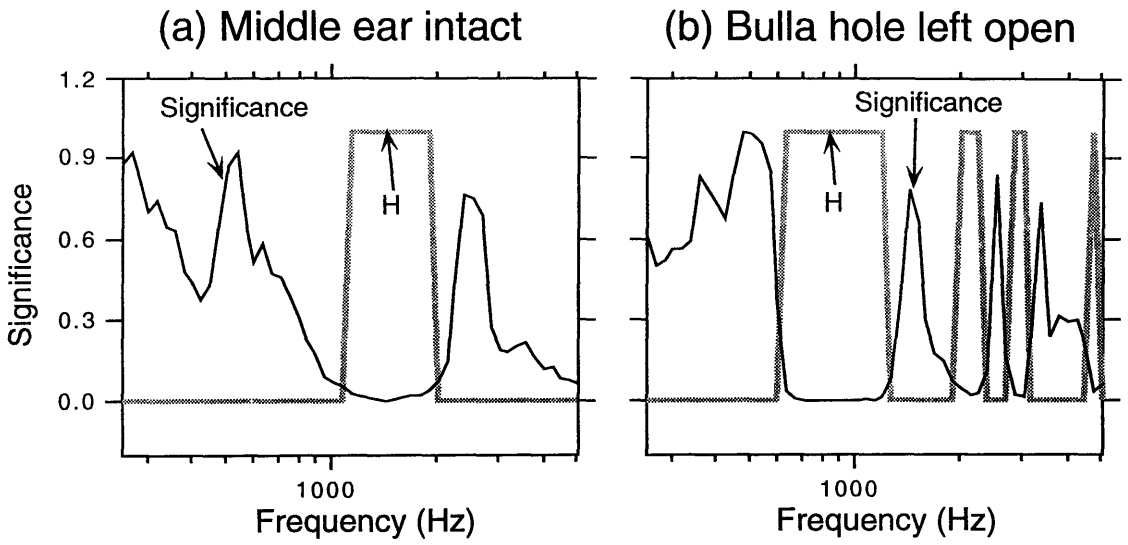

Figure 4-2: T-test comparison of the similarity between the our measured $\mathbf{Y}^{\mathbf{I}}$ and $\mathbf{Y}^{\mathbf{HO}}$ with the measurements of Ravicz *et al.* (1992). The significance curves indicate the probability of observing the given results by chance given that the measurement means are equal. The "H" curves show the acceptability of the null hypothesis that the two means are equal. "H=1" means that we can reject the null hypothesis at 0.05 significance level, whereas "H=0" means do not reject the null hypothesis at 0.05 significance level.

magnitude that occurs near 3 kHz. The Ravicz data show a minimum that occurs at lower frequencies. According to Ravicz *et al.* (1992), this minimum results from the anti-resonance produced by the parallel combination of the compliance of the air within the middle-ear cavity and the acoustic inertance of the bulla hole. The magnitude of this inertance is inversely proportional to the diameter of the bulla hole, such that a smaller hole produces larger inertance. A larger inertance should result in a larger susceptance magnitude, a lower resonance frequency, and a lower frequency for the minimum in admittance magnitude. We can thereby explain the difference between the two sets of measurements based on the size of the bulla hole. Ravicz *et al.* suggested that the holes they made were approximately 1 mm in diameter, and we estimate our holes to be 1.2 mm in diameter. Therefore, the difference in the hole size is consistent with the parallel resonance theory. One similarity observed in both sets of measurements is the increase in

the size of the error bounds, especially in the low-frequency compliance-dominated region. Consistent with the discussion in Chapter 3, such a feature is the direct result of removing the stiffer cavity admittance, thus revealing the greater variation among the compliances of the tympanic membrane-ossicular-cochlear complex. Except for the aforementioned resonance frequency, both sets of measurements have overlapping confidence intervals, and they all exhibit the general features of $\mathbf{Y}^{\mathbf{HO}}$ described in Section 3.1.2. The t-test result shown in panel B of Figure 4-2 shows the expected rejections of the "equal hypothesis" at the two anti-resonance frequencies of 2-3 kHz. The two means also differ statistically at frequencies between 600 Hz and 1 kHz (the actual difference is less than 5 dB in magnitude). At other frequencies, the two sets of measurements are equal at 5% statistical significance level. One noteworthy point in the results of Ravicz *et al.* is the absence of *pars flaccida* resonance in all but one measurement. Since the tympanic membranes in that study were not moistened periodically, such a finding is not surprising given the rapidly decaying resonance under conditions of dehydration.

4.2 Correlation of input admittance measurements with middle ear models

4.2.1 General considerations

To quantify the contributions of the middle-ear anatomical structures to the measured input admittance requires the use of a middle ear model. In chapter 3, we presented the measured admittance data along with the discussions of some simple model parameters that can be estimated directly from the admittance plots, such as the *flaccida* and the cavity compliances. In this section, a systematic approach will be employed to estimate

all middle-ear parameters deemed important to the understanding of the roles of *pars flaccida* in middle-ear acoustic transmission. Figure 4-3 shows the circuit model that was used for this purpose, which includes the modeling of the *pars flaccida*, *pars tensa*, middle-ear cavity, ossicles, and the cochlea. Variations of this model have previously been used to explain the functioning of the middle and inner ear (Zwislocki, 1962; Zwislocki, 1963; Møller, 1961; Møller, 1965; Schmiedt and Zwislocki, 1977; Lynch et al. , 1982; Kohllöffel, 1984; Rosowski et al. , 1986; Rosowski et al. , 1990; Rosowski, 1991; Rosowski and Merchant, 1995). The model appears to provide adequate approximations to most experimentally measured data.

The basic premise of this simplified series circuit model has been described in Chapter 1. Note, however, that some modifications have been made to facilitate the modeling discussion in this chapter. The circuit elements that represent the *pars tensa*, the ossicles, and the cochlea have been replaced by a simplified circuit — a series RLC network L_{TOC}, R_{TOC}, and C_{TOC}. This simplified representation of the *pars tensa*, ossicular and cochlear complex (1) requires a smaller number of model parameters, and (2) adequately represents important acoustical and mechanical features at low frequencies, such as the stiffness of the tensa and ossicles and the damping of the cochlea (Zwislocki, 1962). The use of the simplified representation forfeits our ability to represent more detailed acoustic variables. For example, the volume velocity entering the stapes footplate $\mathbf{U_S}$ (which is commonly accepted as the stimulus that directly triggers the cochlear response) can no longer be represented by any circuit variable. Consequently, the model cochlear potential is assumed to be directly proportional to the volume velocity entering the *pars tensa*-ossicular-cochlear complex, $\mathbf{U_{PT}}$. Such an assumption is justified, at least as a first order approximation: Møller (1965) [Figure 2-17] demonstrated a proportionality

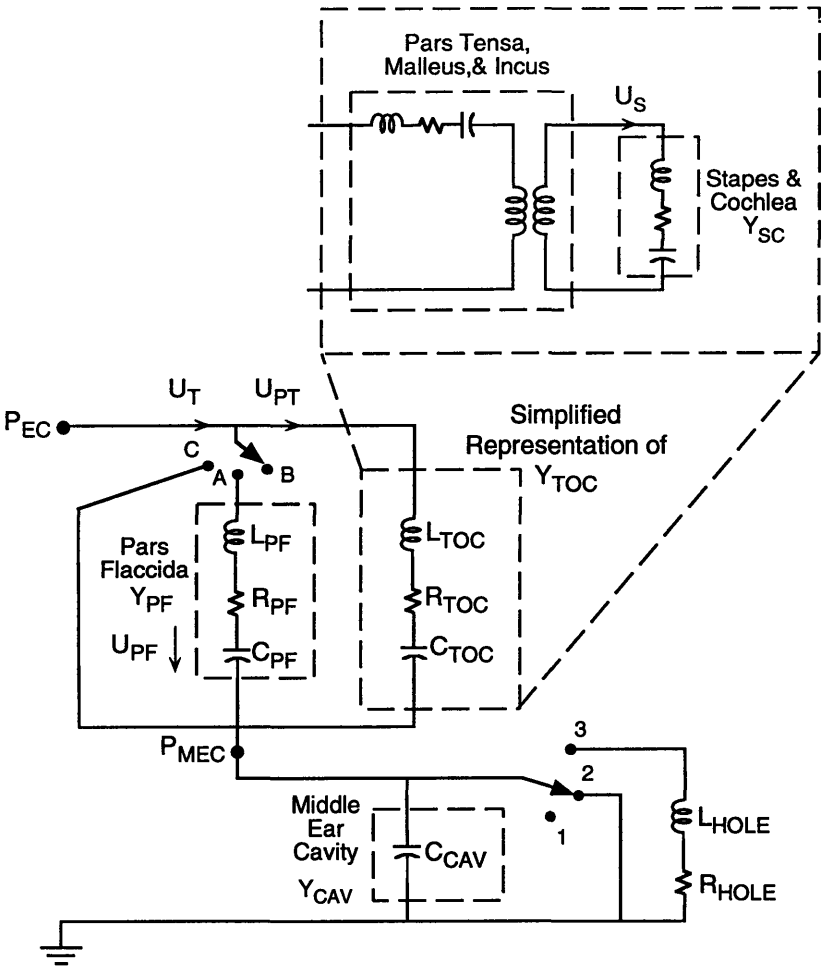

Figure 4-3: Circuit representation of the series model of the middle ear. This circuit model is a modified version of that shown in Figure 1-8. The modification is done to facilitate the modeling discussion that will be presented in this chapter. In particular, the circuit elements that represent the *pars tensa*, the ossicles, and the cochlea have been replaced by a simplified circuit (in the form of a series RLC network). The manipulations of the bulla wall are represented as switches in parallel with the cavity admittance: Position "3" represents the bulla hole open configuration; Position "2" models the widely opened cavity wall, where $\mathbf{Y_{CAV}}$ is assumed to be short circuited; and the intact middle ear is represented by switch position "1". Similarly, the manipulations of the *pars flaccida* is represented as a switchable admittance with three possible settings. When the *pars flaccida* is intact, the switch is in position "A", where $\mathbf{Y_{PF}}$ acts as a shunt path across the *pars tensa*-ossicular complex. Switch position "B" models the immobilized *pars flaccida*, which causes all the tympanic-membrane volume velocity $\mathbf{U_T}$ to pass through *pars tensa*. Switch position "C" represents a removed *pars flaccida*, where it effectively shorts out the rest of the $\mathbf{Y_{TOC}}$.

relationship between the middle-ear input admittance and the cochlear potential over a frequency range from 400 Hz to 2 kHz.

Another important assumption of the model is that *pars flaccida* and *tensa* are independent sound paths, in that the volume velocity through either path is completely determined by the pressure difference across the TM and the impedance of the path. In other words, changes in *pars tensa* which do not affect the pressure difference across TM are expected to have no effect on *pars flaccida* and vice versa. This assumption of independence underlies the traditional thinking that *pars flaccida* forms a passive shunt path around the main ossicular transmission path of the hearing process. Tests of the validity of this assumption are thus essential to our understanding of the roles of *pars flaccida* in hearing. In this chapter, specifically in Section 4.4, we will discuss tests of this assumption using the cochlear potential measurements in ears with widely opened middle-ear cavities.

By using our simple scheme to represent the complex middle-ear transmission, it is imperative to realize the possible inaccuracies and limitations in our predicted values. First, our model does not take into account any possible relative motions between the ossicular bones. Guinan and Peake (1967) reported that in cats, relative motions do occur between the malleus and incus at frequencies above 5 kHz. These motions shunt some portion of the volume velocity entering the middle ear away from the cochlea. A second possible source of error has its origin in the mechanics of the tympanic membrane vibrations. Khanna and Tonndorf (1970,1972) reported that at high frequencies ($f >$ 3 kHz), eardrum vibrations tend to break up into sectional patterns, where the higher harmonic modes of vibration reduce the transmission of high frequency power to the middle ear. Since the tympanic membrane of gerbil is smaller than cat, we might expect

these deviations to occur at higher frequencies. These possible deviations from the ideal simple model must therefore be considered when comparing the model predictions with the measured data.

4.2.2 Estimation of model parameters

In Chapter 3, we were able to calculate the compliances of the middle-ear cavity (C_{CAV}) directly from the low frequency admittance data using Equation 3.1. Such an intuitive approach cannot be directly extended to the estimations of other middle-ear model parameters, especially when the middle-ear input admittance results from the interactions of multiple acoustic components. In this section, a more systematic optimization process is used to estimate these parameters. With the computed model parameters, we will further demonstrate that only certain subsets of these model elements are necessary to accurately describe the overall input admittance results.

The admittance data presented in Section 3.1 were used to estimate the seven parameters modeled in Figure 4-3 (C_{TOC}, R_{TOC}, L_{TOC}, C_{PF}, R_{PF}, L_{PF}, C_{CAV}). For measurements made with the bulla hole left open, two additional parameters, R_{HOLE} and L_{HOLE}, were needed to describe the resonance behavior between the middle-ear cavity and the bulla hole.

The estimation procedure consists of three separate optimization processes, whereby the parameter values of each admittance block are defined separately. For measurements made with the intact middle-ear cavity, the cavity compliance (C_{CAV}) was first determined by fitting the circuit model with the two switches at positions C and 3 (which in effect eliminates $\mathbf{Y_{PF}}$ and $\mathbf{Y_{TOC}}$, leaving a single capacitor C_{CAV} in the model) to the admittance measurement made with *pars flaccida* removed and middle-ear cavity intact.

The value of C_{CAV} was varied to minimize the mean-square-errors between the measured and the model admittances. This optimization procedure was implemented in Matlab using the *fmins* function[1]. Since the circuit model can only accurately represent the input admittances at low frequencies, all of the optimization computations utilize only measurements made at frequencies below 4 kHz. The next step involved the estimation of the *pars tensa*-ossicular-cochlear complex parameters — $C_{TOC}, R_{TOC}, L_{TOC}$. With the first switch of the model at position B, these three parameters were optimized simultaneously by finding the best model fit to the measured admittance data obtained with *pars flaccida* stiffened. Once the four parameters above were known, the compliance, mass, and damping of the *pars flaccida* (C_{PF}, L_{PF}, R_{PF}) can be obtained by matching the complete model (with the first switch at position A) to the admittance measurements made in ears with normal tympanic membranes. In all cases, the second model switch was set at position "1" if the measurements were made in ears with middle ears intact, or at position "2" if the measurements were made in ears with either bulla hole open or with bulla wall removed.

Figure 4-4 compares the middle ear intact measurements made in the right ears of gerbil B8 and B9 with the best model fits. The model parameter values are tabulated in Table 4.1. At frequencies below 2 kHz, both the magnitude and phase of the model predictions closely resemble the shapes and numerical values of the measured admittances. In particular, the low-frequency resonances at approximately 400 Hz are adequately described by the simple RLC representation of the *pars flaccida.* However, several differences between the measurements and the model predictions can be observed. At

[1]The *fmins* function uses the Nelder-Meade simplex search algorithm (Nelder and Mead, 1964; Dennis and Woods, 1987). It is a direct search method that does not require gradients or other derivative information. See the Matlab manual or the two references for more details.

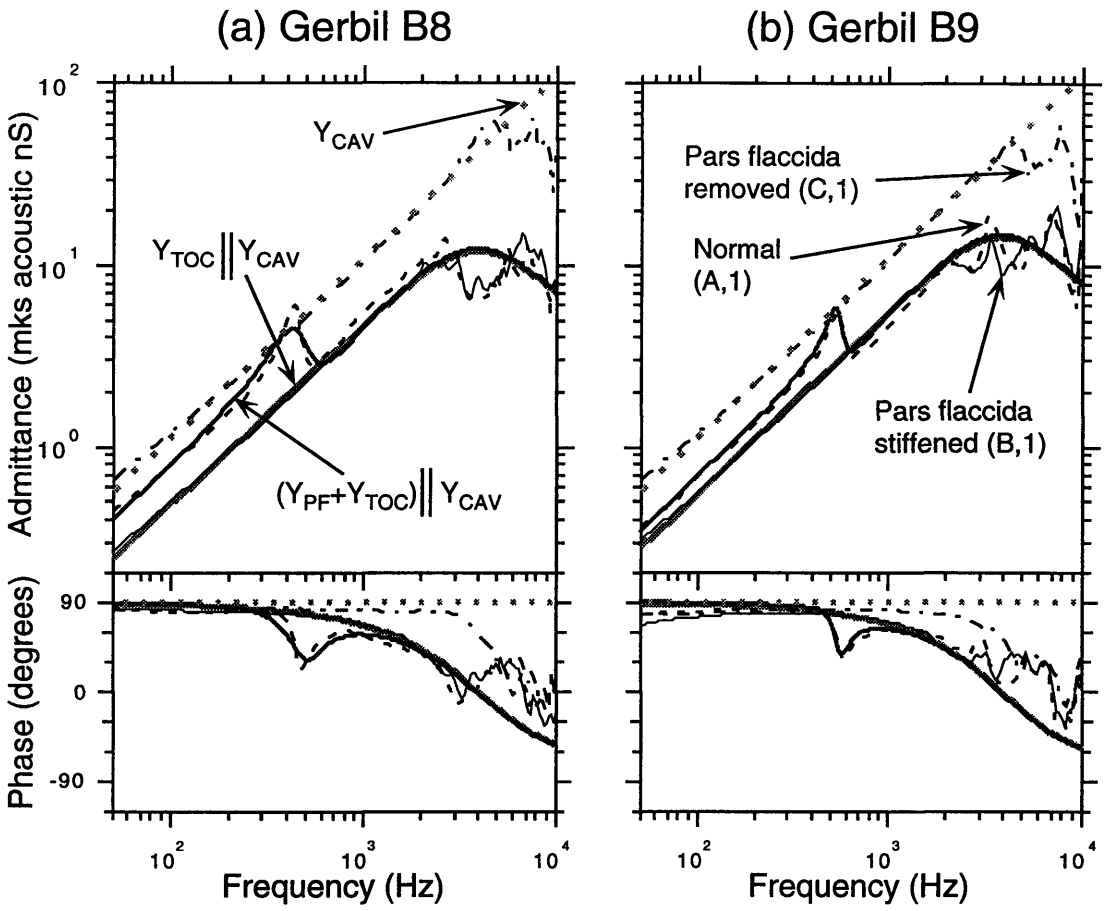

Figure 4-4: Comparison of the input admittances $\mathbf{Y^I}$, $\mathbf{Y^I_{FS}}$, and $\mathbf{Y^I_{FR}}$ measured in gerbils B8 and B9 with the input admittances of the middle-ear circuit model. Of the six curves presented in this figure, the three model prediction curves are labeled in the left panel, while the right panel shows the line type used for the measurements. For $\mathbf{Y^I_{FS}}$, a simple compliance is sufficient to represent the measured admittance at frequencies up to 2 kHz. The deviation from compliance behavior at higher frequencies was a result of the acoustic mass and resistance created by the hole in the pars flaccida. For $\mathbf{Y^I}$ and $\mathbf{Y^I_{FS}}$, the model admittances match the measured data well at frequencies below 2 kHz. At higher frequencies, the simple RLC circuit that represent the *pars tensa*-ossicular-cochlear complex is not capable of representing the fine structures observed in the actual measured admittances.

frequencies above 3 kHz, clear discrepancies between the circuit model and the measurements exist for all three admittance curves in Figure 4-4. For the admittance measured with *pars flaccida* removed, the masslike property of the *flaccida* hole is significant at high frequencies; therefore, the short circuit assumption between the ear canal and the middle ear cavity is not valid in this range. Assuming the admittance of the *pars flaccida* hole is $\mathbf{Y} = 1/j\omega L$, where $L = \rho_o(l + 0.6r)/\pi r^2$ is the acoustic mass of the hole, the predicted frequency where the admittance changes from compliance to mass-like is:

$$f = \frac{r}{2\sqrt{\pi C_{CAV}\rho_o(l + 0.6r)}} \tag{4.1}$$

Assuming that the *pars flaccida* is circular with radius $r = 0.1\ cm$, and with a thickness of $l = 0.15mm$, this equation predicts a resonance frequency of approximately 7 kHz. The measurements in Figure 4-4 show that it is indeed in this frequency range that the cavity admittance stops behaving as a compliance structure; however, there is no observable resonance is this frequency range. Instead, the measured admittance magnitudes show a gradual plateau with several minor peaks and valleys. Such behavior indicates that under this configuration, some resistive components may also be present in the middle-ear system, as indicated by angle measurements that are close to 0°. For the tympanic membrane intact measurements (*i.e. pars flaccida* is either undisturbed or stiffened), the simple circuit model is unable to follow the fine structures observed in the admittance measurements at frequencies above 3 kHz. This is not surprising considering the simplistic representation of the *pars tensa*-ossicular-cochlear complex.

A more accurate "broad-band" representation of $\mathbf{Y_{TOC}}$ can be obtained from the admittance measurements made with the middle ear intact and *pars flaccida* stiffened,

	B8 (Right Ear)	B9 (Right Ear)	B8 (Right Ear)	B9 (Right Ear)
Measurement configuration	Bulla wall intact	Bulla wall intact	Bulla hole open	Bulla hole open
C_{TOC} $(10^{-12}\ m^3/Pa)$	1.3	1.7	1.5	1.9
C_{PF} $(10^{-12}\ m^3/Pa)$	2.4	1.5	2.3	1.7
R_{TOC} $(10^7\ Pa\text{–}s/m^5)$	8.5	7.0	8.4	7.1
R_{PF} $(10^7\ Pa\text{–}s/m^5)$	10.3	6.7	3.8	10.9
L_{TOC} $(10^3\ kg/m^4)$	2.2	2.0	1.8	1.5
L_{PF} $(10^4\ kg/m^4)$	9.4	13.0	8.7	5.4
C_{CAV} $(10^{-12}\ m^3/Pa)$	1.7	1.7	-	-

Table 4.1: Middle-ear model parameters. These model parameters were calculated from the admittance measurements made either with the middle-ear cavity intact or with the bulla hole left opened. For the bulla hole open measurements, C_{CAV} cannot be estimated from the admittance data.

$\mathbf{Y_{FS}^{I}}$:

$$\mathbf{Y_{TOC}} = \frac{1}{\frac{1}{\mathbf{Y_{FS}^{I}}} - \frac{1}{j\omega C_{CAV}}} \tag{4.2}$$

Equation 4.2 is justified based on the assumption that the middle-ear cavity is in series with the tympanic membrane-ossicular-cochlear complex, which has been verified by numerous researchers [page 125], and will be further tested in Section 4.3. It is preferable to calculate $\mathbf{Y_{TOC}}$ from $\mathbf{Y_{FS}^{I}}$ rather than $\mathbf{Y_{FS}^{HO}}$ or $\mathbf{Y_{FS}^{WO}}$ because of the presence of high frequency resonance in the two later measurements — a result of the opening of the bulla wall. The circuit model for this "broad-band" representation of $\mathbf{Y_{TOC}}$ is shown in Figure 4-5.

Figure 4-6 shows the admittance predictions of this "broad-band" model. Also included in the figure are the various circuit blocks that make up the complete middle-ear input admittance $\hat{\mathbf{Y}}^{\mathbf{I}}$ — $\mathbf{Y_{TOC}}$, $\hat{\mathbf{Y}}_{\mathbf{CAV}}$, and $\hat{\mathbf{Y}}_{\mathbf{PF}}$. With the exception of $\mathbf{Y_{TOC}}$, all the circuit elements used to produce this figure are the same as that shown in Figure 4-4. Comparing these individual acoustic admittances allows us to appreciate the quantitative

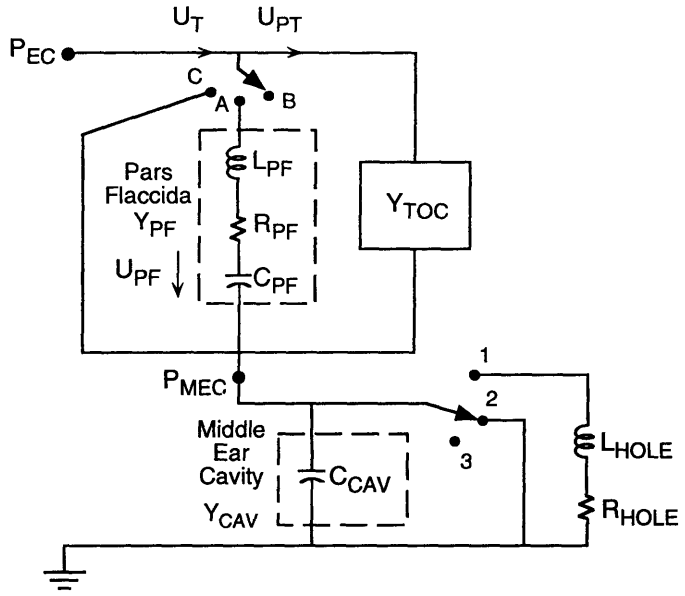

Figure 4-5: Modified "broad-band" middle ear model that allows high frequency representation of the middle-ear input admittance. This model is essentially the same as the model shown in Figure 4-3 — with the RLC network representing the *pars tensa*-ossicular-cochlear complex replaced by a single broadband admittance $\mathbf{Y_{TOC}}$ that is computed from the $\mathbf{Y^I_{FS}}$ measurements.

contribution of each of these acoustic blocks to the overall middle-ear input admittance. At frequencies below 300 Hz (below the resonance frequency of the *pars flaccida*), the input admittances of all acoustic blocks are mostly compliance dominated. In this range, the acoustic compliances of the middle-ear cavity, the *pars flaccida*, and the *pars tensa*-ossicular-cochlear complex are all comparable in magnitude ($\approx 1 - 2 \times 10^{-12} m^3/Pa$), and they combine in the parallel-series configuration of the middle-ear model to produce the overall compliance.

$$\mathbf{Y^I}\Big|_{f<300\ Hz} \approx j\omega\, C^I\Big|_{f<300\ Hz} \tag{4.3}$$

where

$$C^I\Big|_{f<300\ Hz} = \frac{(C_{PF} + C_{TOC})C_{CAV}}{C_{PF} + C_{CAV} + C_{TOC}} \tag{4.4}$$

At frequencies between 600 Hz and 2 kHz, the *pars flaccida* admittance is mass domi-

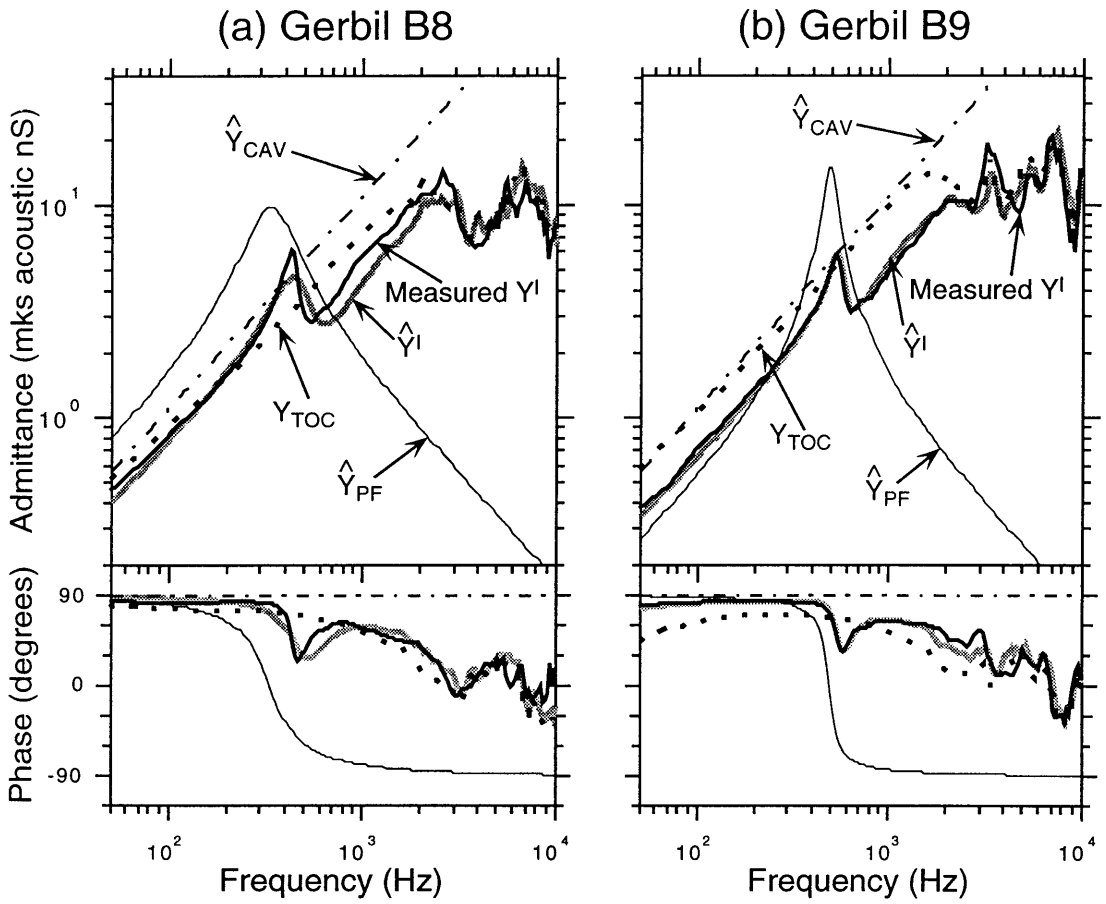

Figure 4-6: The ingredients that compose the input admittance of the broadband middle-ear model, $\hat{\mathbf{Y}}^{\mathbf{I}}$. Comparing these individual admittances allows us to appreciate the quantitative contributions of these acoustic blocks to the overall middle-ear input admittance. To achieve better match between the middle-ear model and the measured data at higher frequencies, the RLC representation of $\mathbf{Y_{TOC}}$ is replaced by a broadband admittance that was computed from $\mathbf{Y^I_{FS}}$ (Eqn. 4.2). The measured $\mathbf{Y}^{\mathbf{I}}$ is also plotted for comparison purpose.

nated, and its contribution to the overall input admittance is negligible. In this range, $\mathbf{Y^I}$ is still compliance controlled, where the overall compliance is now simply the series combination of C_{CAV} and C_{TOC}.

$$\mathbf{Y^I}\Big|_{600<f<2000\ Hz} \approx j\omega \frac{C_{CAV}C_{TOC}}{C_{CAV}+C_{TOC}} \tag{4.5}$$

Between these two frequency ranges, the middle-ear input admittance exhibits a resonance that is mainly influenced by the RLC behavior of $\mathbf{Y_{PF}}$. Together with contributions from C_{TOC} and C_{CAV}, they form the overall input admittance:

$$\mathbf{Y^I}\Big|_{300<f<600\ Hz} = \frac{(\mathbf{Y_{PF}}+j\omega C_{TOC})j\omega C_{CAV}}{\mathbf{Y_{PF}}+j\omega(C_{TOC}+C_{CAV})} \tag{4.6}$$

Not surprisingly, the "broad-band" circuit of Figure 4-5 models the measured admittance well at frequencies above 2 kHz, since this is the range where $\mathbf{Y_{TOC}}$ is the major contributor to the admittance.

We also fit the single seven-parameter model of Figure 4-3 to the data measured after opening the bulla hole. For these measurements, one additional step was needed to estimate the mass and resistance values of the probe tube hole (R_{HOLE} and L_{HOLE}). These two parameters are related to the size of the hole, and are constrained by the following equations [Beranek (1986)]:

$$R_{HOLE} = \frac{\rho_o\sqrt{2\omega\nu}}{\pi r^2}\left(\frac{l}{r}+2\right) \approx 2\times 10^{-3}\frac{\sqrt{\omega}l}{r^3} \tag{4.7}$$

$$L_{HOLE} = \frac{rho_o(l+1.75r)}{\pi r^2} \tag{4.8}$$

where $\nu = 1.56\times 10^{-5}m^2/s$ is the kinematic velocity of the air, $l = 0.3\times 10^{-3}m$ is the

thickness of the bulla wall, and r is the radius of the bulla hole. For these measurement sets, the RLC values of the *pars flaccida* and *pars tensa*-ossicular-cochlear complex were first determined without the bulla hole parameters. R_{HOLE} and L_{HOLE} were then added to the model, and their values were chosen by varying r to obtain the best model fit for frequencies between 2 and 5 kHz. The final values of r for both gerbil B8 and B9 were found to be $\approx 0.5 \times 10^{-3}m$, very similar to the physically measured hole radius of $0.6 \times 10^{-3}m$.

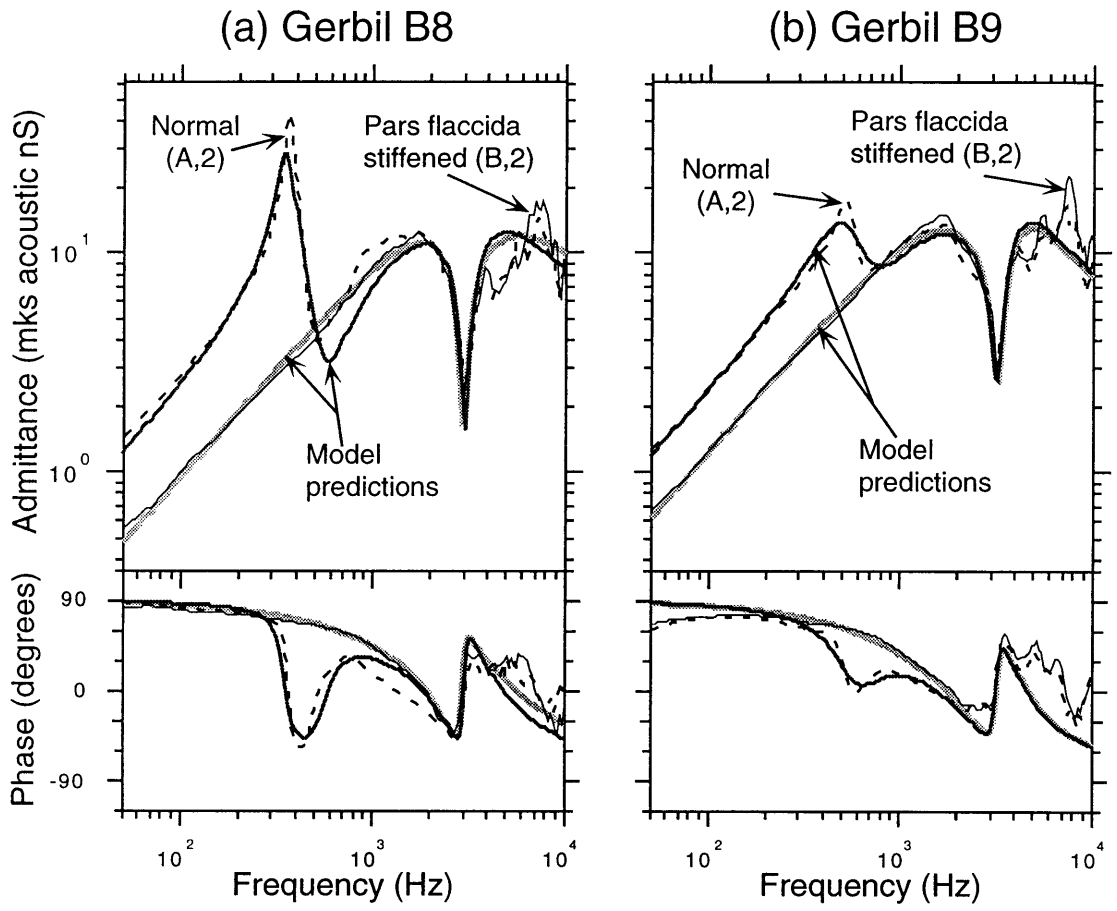

Figure 4-7: Comparison of the input admittances $\mathbf{Y^{HO}}$ and $\mathbf{Y_{FS}^{HO}}$ measured in gerbils B8 and B9 with the input admittances of the middle-ear circuit model. Again, the model admittances at frequencies lower than 4 kHz match well with the measured values, but the high frequency prediction fail to follow the measured trends.

Figure 4-7 shows the best admittance fits to the $\mathbf{Y^{HO}}$ and $\mathbf{Y_{FS}^{HO}}$ measurements made

in the right ears of gerbil B8 and B9. The corresponding model parameters are tabulated in the last two columns of Table 4.1. Since these are independent measurements made in the same ears as the middle ear intact cases, their respective parameters can be compared to test the validity and consistency of our circuit model. From Table 4.1 we see that all three parameters of the *pars tensa*-ossicular-cochlear complex are consistent across all four measurements. For the *pars flaccida*, however, only the compliance parameter displays good consistency. The damping and masslike properties of the *flaccida* (R_{PF} and L_{PF}) show changes that are as large as 60% of their original values. Note that these two parameters are the ones that are most likely to be affected by the drying and moistening of the tympanic membrane. In Section 3.1.3, we showed that moistening the tympanic membrane was able to restore some of the low frequency (presumably *pars flaccida*'s) compliance, whereas the increase in damping could not be restored. Furthermore, since drying and moistening of the tympanic membrane could affect its overall mass (especially the thicker *pars flaccida*), the revelations that L_{PF} varied moderately from measurement to measurement should not be surprising.

The same model fitting technique was used to fit the simple circuit model to measurements in B8, B9, B10, and B11 made with the middle ear widely opened. In this configuration, the model has its middle-ear cavity "shorted out" (*i.e.* second switch set at position "2"). The resulting model admittances and parameter values are shown in Figures 4-8, 4-9, and Table 4.2. As was explained in Chapter 3, widely opening the bulla wall does not eliminate entirely the acoustic effect of the middle-ear cavity. Rather, the masslike property of the bulla opening interact with the remaining cavity to provide a high frequency resonance. The size of this irregularly-shaped bulla wall opening was not measured, and its effect was not included in the model.

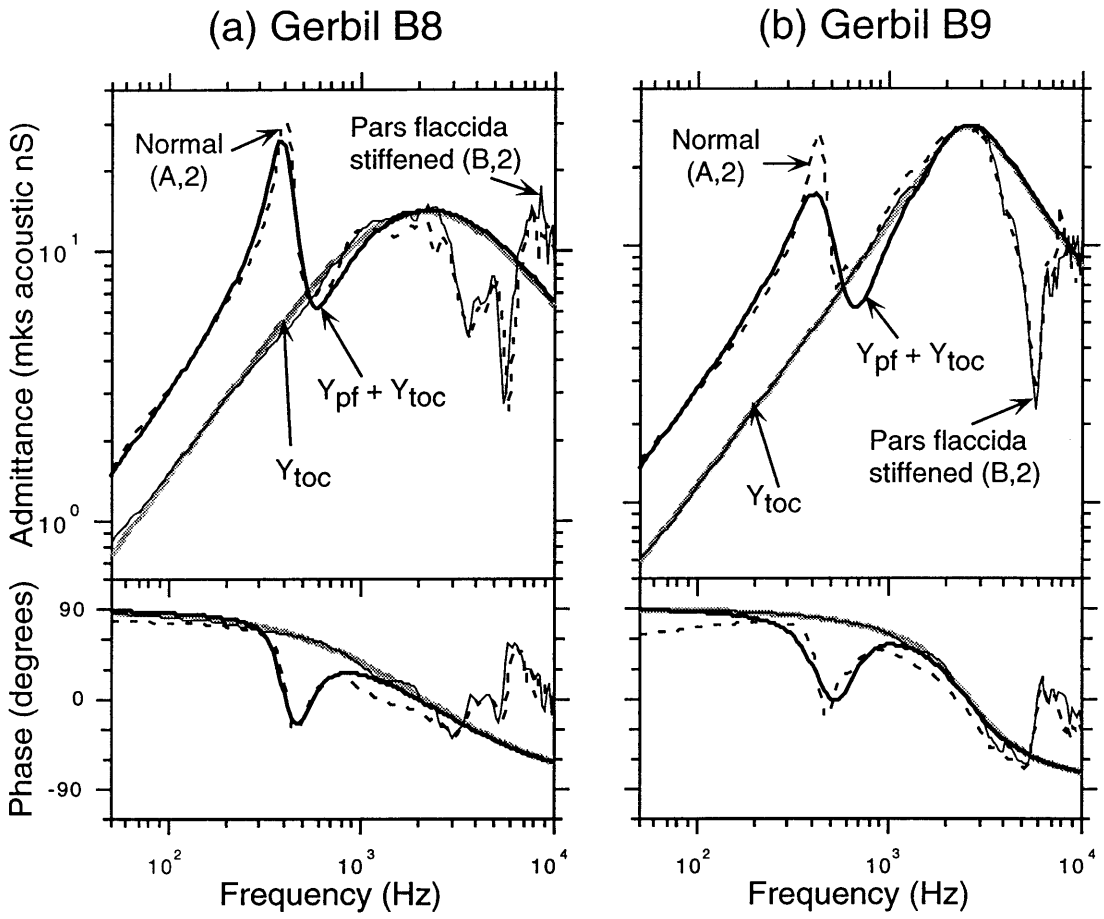

Figure 4-8: Comparison of the input admittances $\mathbf{Y^{WO}}$ and $\mathbf{Y_{FS}^{WO}}$ measured in gerbils B8 and B9 with the input admittances of the middle-ear circuit model. Note the measured impedances show a sharp dip at approximately 6 kHz that is not represented in the circuit model. Such feature is the result of the resonance between the acoustic mass of the widely-opened middle-ear hole and the compliance of the middle-ear cavity; the middle ear model assumes that such a hole is large enough that it shorts out the cavity compliance, and no resonance is predicted.

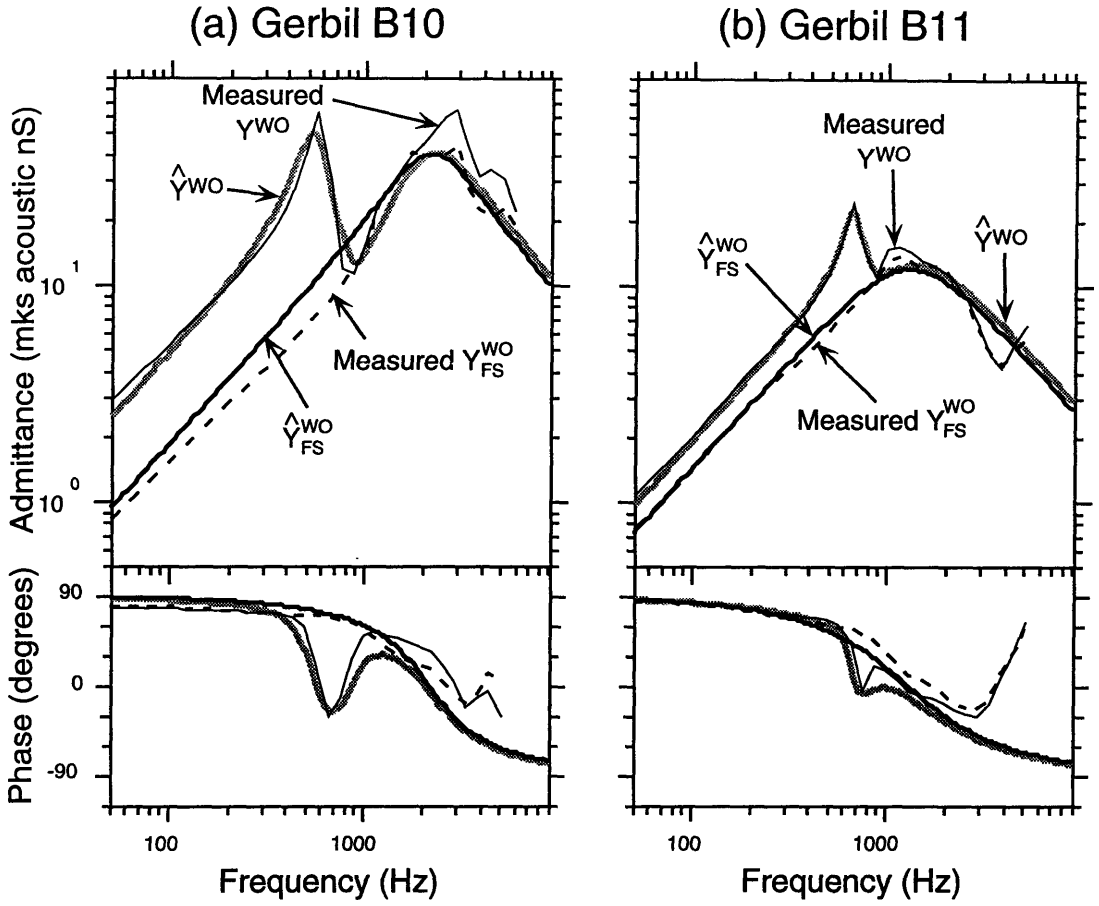

Figure 4-9: Model fit of the middle-ear input admittance of gerbils B10 and B11 — $\mathbf{Y^{WO}}$ and $\mathbf{Y_{PF}^{WO}}$. The measurements were made in the left ears of gerbil B10 and B11 with the tone-sweep paradigm designed for cochlear potential measurements (see Section 2.4). As a result, the frequency resolution of these two input admittance plots is substantially lower than the other results presented in this section.

	B8 (Left Ear)	B9 (Left Ear)	B10 (Left Ear)	B11 (Left Ear)
Measurement configuration	Middle ear wide open	Middle ear wide open	Middle ear wide open	Middle ear wide open
C_{TOC} $(10^{-12}\ m^3/Pa)$	2.1	1.8	2.9	2.3
C_{PF} $(10^{-12}\ m^3/Pa)$	2.2	2.3	4.8	0.9
R_{TOC} $(10^7\ Pa\text{–}s/m^5)$	7.2	3.5	2.5	8.5
R_{PF} $(10^7\ Pa\text{–}s/m^5)$	4.5	7.6	2.2	6.7
L_{TOC} $(10^3\ kg/m^4)$	2.4	2.1	1.9	6.8
L_{PF} $(10^4\ kg/m^4)$	7.3	5.8	1.8	7.1

Table 4.2: Middle-ear model parameters. These model parameters were calculated from the admittance measurements made with the middle-ear cavity widely opened.

Similar to the input admittance of the intact middle ear, the low-frequency admittances of $\mathbf{Y^{HO}}$ and $\mathbf{Y^{WO}}$ can be approximated using the RLC's values shown in Table 4.2. For both cases, the acoustic admittance of the middle-ear cavity is negligible at frequencies below 2 kHz. Consequently, below the *pars flaccida* resonance, we have:

$$\mathbf{Y^{HO}}\Big|_{f<300\ Hz} = \mathbf{Y^{WO}}\Big|_{f<300\ Hz} \approx j\omega(C_{PF} + C_{TOC}) \tag{4.9}$$

At frequencies above the low-frequency resonance (≈600 Hz), the *pars flaccida* admittance is mass dominated, and its contribution towards the overall input admittance is also negligible. Thus, we have:

$$\mathbf{Y^{HO}}\Big|_{600<f<2000\ Hz} = \mathbf{Y^{WO}}\Big|_{600<f<2000\ Hz} \approx j\omega C_{TOC} \tag{4.10}$$

In the frequency region where the *pars flaccida* resonates, the input admittance can be adequately described by the RLC circuit of the *pars flaccida* in parallel with C_{TOC}:

$$\mathbf{Y^{HO}}\Big|_{300<f<600\ Hz} = \mathbf{Y^{HO}}\Big|_{300<f<600\ Hz} \approx \mathbf{Y_{PF}} + j\omega C_{TOC} \tag{4.11}$$

With the use of these five simple parameters, we were able to accurately describe the low frequency behaviors (50 Hz< f <2 kHz) of the gerbil middle-ear input admittances, as illustrated in Figures 4-7-4-9. Specifically, we have quantitatively described the admittance contributions from the *pars flaccida*, the middle-ear cavity, and the *pars tensa*-ossicular-cochlear complex. Table 4.3 shows a summary of all the middle-ear model parameters discussed in this section in terms of their means and standard deviations.

Model parameter	Mean	Standard deviation
C_{TOC} $(10^{-12}\ m^3/Pa)$	1.9	0.5
C_{PF} $(10^{-12}\ m^3/Pa)$	2.3	1.2
R_{TOC} $(10^7\ Pa\text{–}s/m^5)$	6.6	2.3
R_{PF} $(10^7\ Pa\text{–}s/m^5)$	6.6	3.0
L_{TOC} $(10^3\ kg/m^4)$	2.6	1.7
L_{PF} $(10^4\ kg/m^4)$	7.3	3.3
C_{CAV} $(10^{-12}\ m^3/Pa)$	1.7	0

Table 4.3: Means and standard deviations of middle-ear model parameters. The results in this table are computed from all circuit parameter values presented in Tables 4.1 and 4.2.

4.3 Middle-ear pressure levels—model vs measurements

Having computed the parameters of the middle-ear model, we can test the validity of its implications by comparing its predictions with measurements that can be determined experimentally.

One important quantity in the middle-ear sound transmission process is the pressure ratio (dB difference) across the tympanic membrane. Since this pressure ratio is considered the effective driving force for ossicular motions, any factors that modulate this ratio can have a significant impact on the hearing process.

Figure 4-10 shows the simple circuit model predictions of the middle-ear to ear-canal pressure ratio in the middle ear intact configuration. The basic features of these measurements have been discussed in Section 3.1.8 and will not be repeated here. Suffice it to say that the close agreement between the circuit model predictions and the measurements at low frequencies confirms the voltage divider principle expressed by Equations 3.3 and 3.4.

An important corollary to such confirmation is the validity of the series model topology, which forms the basis of the voltage divider principle. Results in Figure 4-11, where

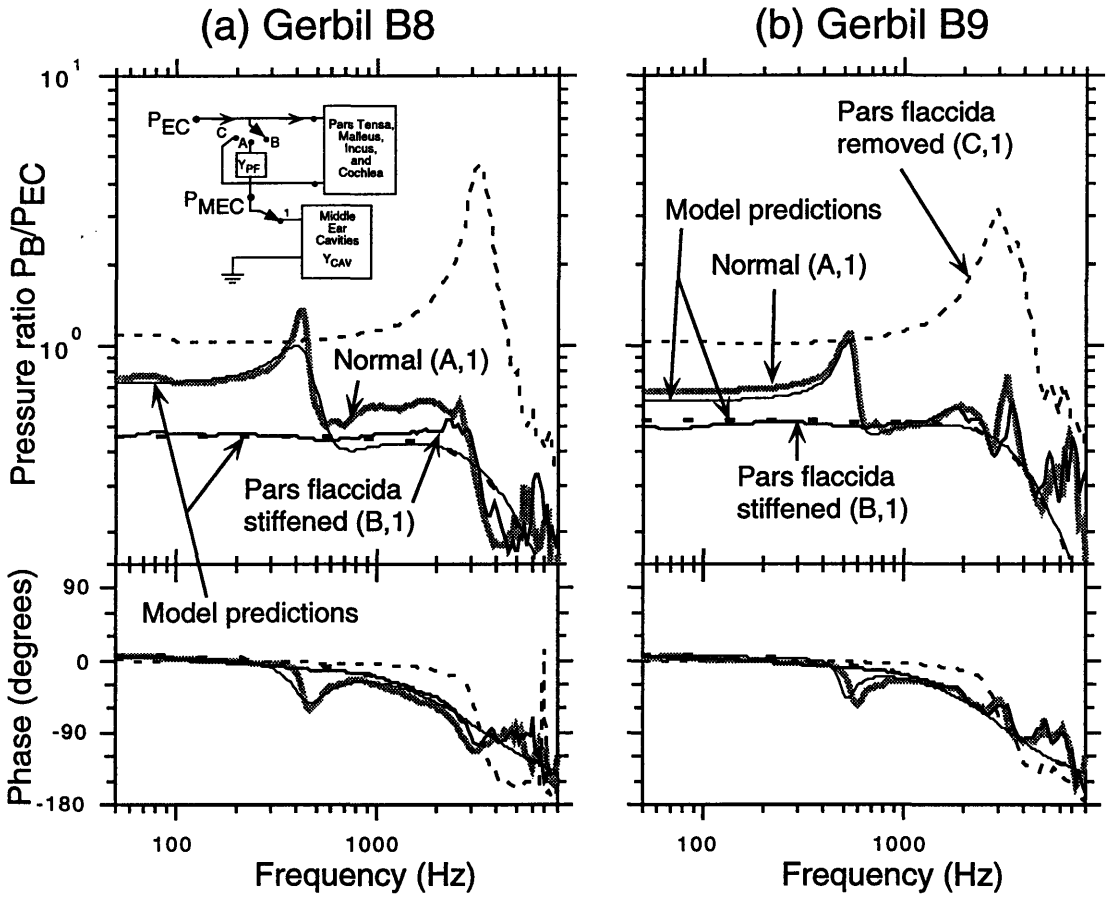

Figure 4-10: Predictions of middle-ear to ear-canal pressure ratio in the middle ear intact configuration—circuit model. The pressure ratio predicted by the low-frequency circuit model and the actual pressure ratio measurements are shown in this figure. The predictions are based on the model parameters determined in the previous section.

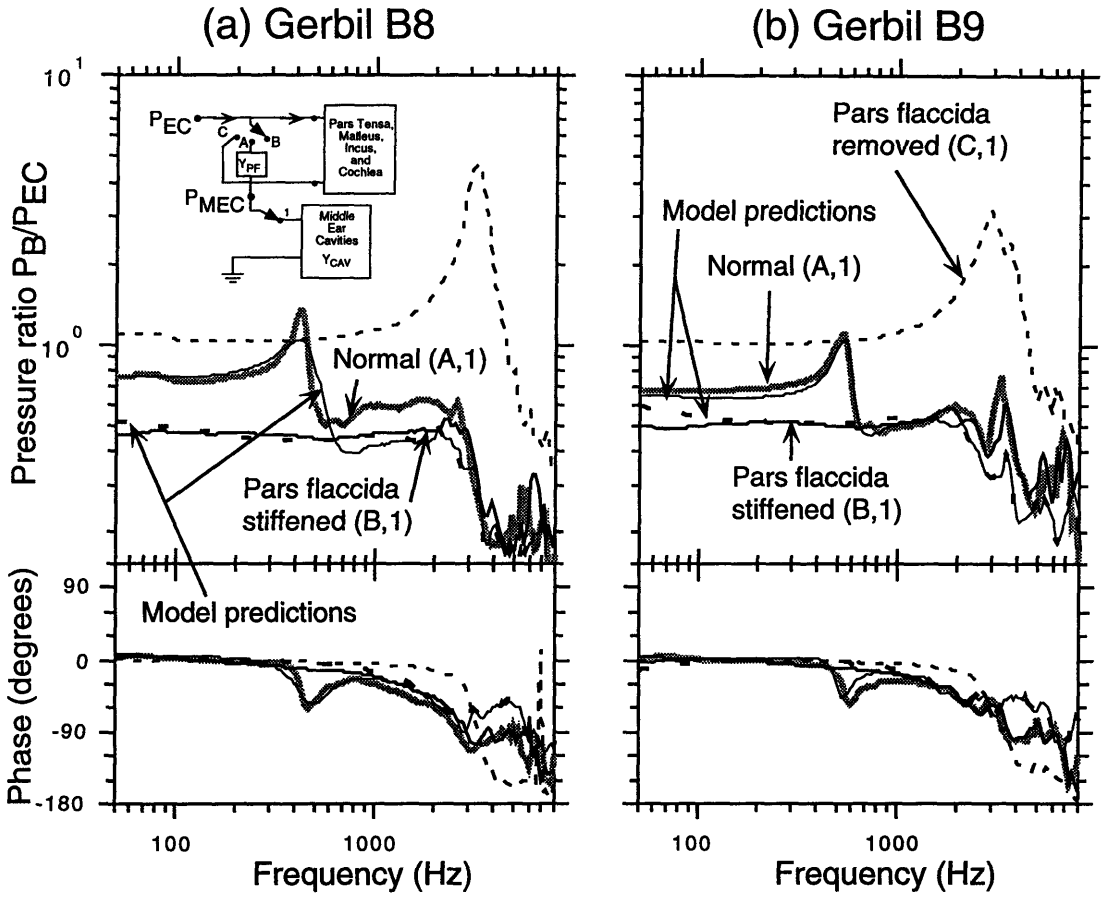

Figure 4-11: Broadband model predictions of middle-ear to ear-canal pressure ratio in the middle ear intact configuration. At frequencies below 2 kHz, both the broadband and circuit models are similar to the actual measured pressure ratio. At higher frequencies, the prediction based on the broadband model is superior to the low-frequency circuit model when compared with the measured data.

the broadband $\mathbf{Y_{TOC}}$ replaced the simplistic RLC representation, show good agreement between the broadband model predictions and the measured data at frequencies up to 8 kHz. These results suggest that the range of the series model can actually be extended to frequencies above 5 kHz, where the pressure measurements in the ear canal and the middle-ear need not be in phase. In this case, the voltage divider equations (Equations 3.3 and 3.4) should be generalized such that the division is based on the overall admittances of the acoustic blocks rather than their low-frequency compliance values:

$$\left.\frac{|\mathbf{P_{MEC}}|}{|\mathbf{P_{EC}}|}\right|_{PF\ stiffened} = \frac{\mathbf{Y_{TOC}}}{\mathbf{Y_{TOC}} + \mathbf{Y_{CAV}}} \tag{4.12}$$

and

$$\left.\frac{|\mathbf{P_{MEC}}|}{|\mathbf{P_{EC}}|}\right|_{TM\ undisturbed} = \frac{\mathbf{Y_{TOC}} + \mathbf{Y_{PF}}}{\mathbf{Y_{TOC}} + \mathbf{Y_{CAV}} + \mathbf{Y_{PF}}} \tag{4.13}$$

4.4 Effects of *Pars Flaccida* manipulations on the input to the inner ears — bulla wall widely open

Results in the last section (Figures 4-10 and 4-11) show that the decrease in middle-ear pressure of approximately 3–8 dB at frequencies below the *pars flaccida* resonance (≈500 Hz) seen after stiffening the *pars flaccida* is consistent with our model predictions. In this section, we will discuss whether this change in pressure difference across the tympanic membrane actually affects the input to the inner ear.

Based on the ear-canal pressure measurements made in the left ears of gerbil B10 and B11 (Figures 3-17 and 3-18), along with the middle-ear parameters estimated from the admittance data (Figure 4-9), we can predict the input to the inner ear based on the volume velocity entering the *pars tensa*-ossicular-cochlear complex, $\mathbf{U_{PT}}$, with the

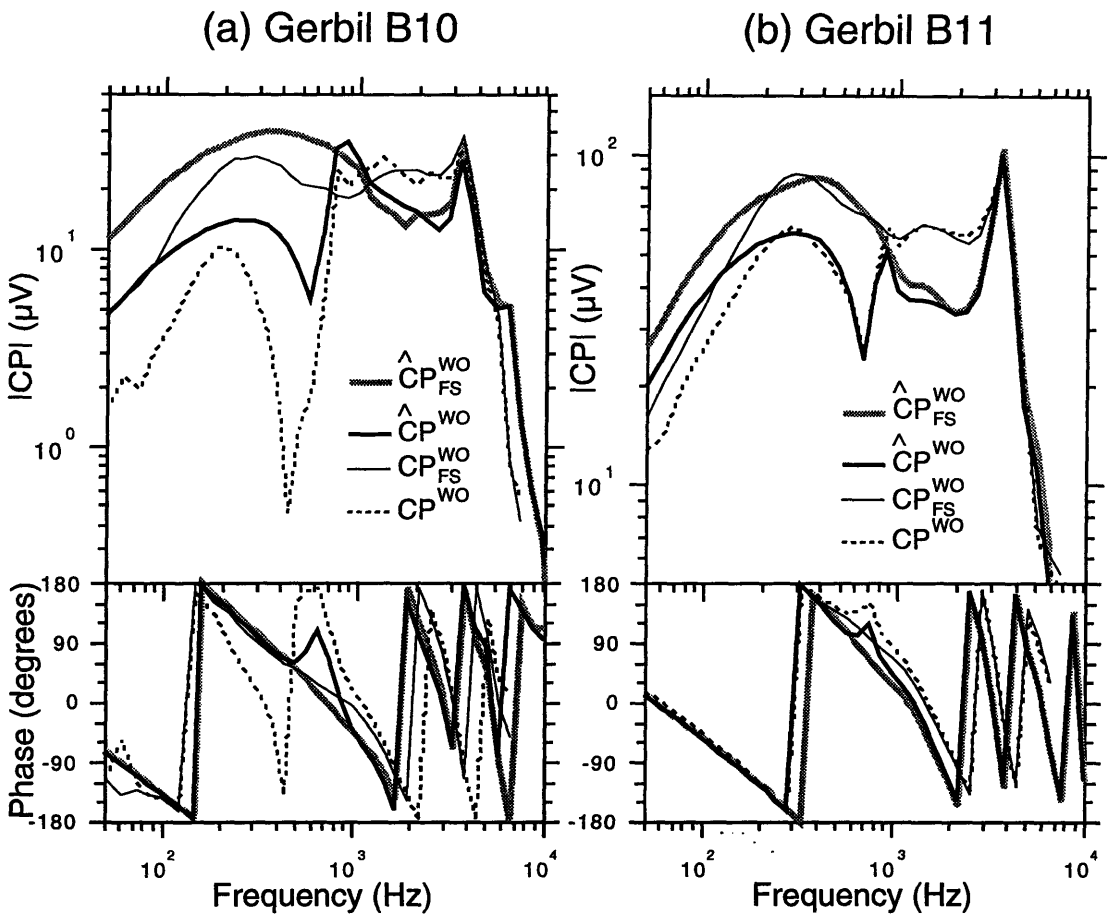

Figure 4-12: Comparison of the measured cochlear potentials in gerbils B10 and B11 with the model predictions. The model cochlear potentials shown in this figure were calculated as the scaled volume velocities entering the *pars tensa*-ossicular-cochlear complex, with measured ear-canal pressure levels as the input to the model. The scaling constant was arbitrarily chosen such that both the model and the measured cochlear potentials are approximately equal in magnitude throughout the entire spectrum.

assumption that these two quantities are proportional to each other. In practice, we used the cochlear potential recordings as a means of measuring the volume velocity entering the inner ear, as was explained in Chapter 3.

Figure 4-12 shows a comparison of the experimentally measured cochlear potentials with the model predictions. The magnitudes of the model predictions were arbitrarily scaled such that both the model and the measured cochlear potentials are approximately equal throughout the entire spectrum. Based on the middle ear model, where the *pars flaccida* is assumed to be independent from the *pars tensa*, a change in the pressure difference across the tympanic membrane should produce a proportional change in the volume velocity entering the inner ear. The proportionality constant (or transfer function), $\frac{\mathbf{U_{PT}}}{(\mathbf{P_{EC}}-\mathbf{P_{MEC}})}$, should be equal to the admittance of the *pars tensa*-ossicular-cochlear complex, $\mathbf{Y_{TOC}}$, independent of the condition of the *pars flaccida* [see Figures 3-20 and 4-16]. Since the measurements in gerbils B10 and B11 were made with the middle ear widely opened, $|\mathbf{P_{EC}}| \gg |\mathbf{P_{MEC}}|$ for all frequencies where cochlear potentials were measured ($f < 5$ kHz); therefore it is acceptable to ignore the sound pressure level in the middle ear cavity. From the ear-canal pressure level measurements in Figures 3-17 and 3-18, we would expect that at frequencies below the *pars flaccida* resonance ($\approx$ 600 Hz), the increase in sound pressure levels which result from stiffening *pars flaccida* should cause a similar increase in the input to the inner ear. The thicker curves in Figure 4-12 express this fact in the form of the modeled cochlear potentials before and after stiffening the *pars flaccida*. Comparing these predictions with the measured cochlear potentials shows some similarities but also some differences. The measurements show the expected increases in cochlear potential production at frequencies below 600 Hz, and few changes at higher frequencies. The actual shape of the measured spectra, however, are different

than the predicted values. At low frequencies ($f < 200$ Hz), the measured cochlear potentials show a steeper slope than expected, indicating a possible filtering mechanism that has sharper low-frequency cutoff than simply the transfer function based on admittance $\mathbf{Y_{TOC}}$. A possible explanation for this phenomenon is the helicotrema effect on the cochlear response, which is known to reduce low-frequency sensitivity by reducing the pressure gradient across the basilar membrane (Dallos, 1970). Another observable difference between the measured and the model responses is the rate of change of the phase angles, where the model predicted a faster rate that the actual measured cochlear potentials. Since the rate of phase angle decrease is directly proportional to the number of poles minus the number of zeros of the transfer function, this result suggests that the model circuit contains a greater number of poles with respect to zeros than the data would indicate. At other frequencies, the observed differences in magnitude are more difficult to explain because of the uncertainty in the absolute values of the model predictions. These differences, however, are due mostly to our naive RLC representation of the far more complex ossicular to cochlear transmission process. This limitation, however, does not pose any serious problem in the current study. Since our points of interest are to test the validity of the *pars flaccida* model and its topological connection in the overall middle-ear model, it is sufficient to know only the difference in cochlear potential productions in ears with normal tympanic membranes and ears with *pars flaccida* stiffened, not the actual mechanism of cochlear potential generation. We therefore quantified the effects of *pars flaccida* stiffening on the middle-ear input admittance, ear-canal sound pressure level, and cochlear potential generation in terms of the ratio between the pre- and post-stiffening results, which are denoted by $\Delta Y, \Delta P_{EC}|_V$, and $\Delta CP|_V$ respectively (The subscript V is used to indicate that constant voltage was applied to the earphone

in the measurement process).

$$\Delta CP|_V = 20\log\left|\frac{\mathbf{CP}|_{\mathbf{FS},constant\ V}}{\mathbf{CP}|_{constant\ V}}\right| \tag{4.14}$$

$$\Delta P_{EC}|_V = 20\log\left|\frac{\mathbf{P}|_{\mathbf{FS},constant\ V}}{\mathbf{P}|_{constant\ V}}\right| \tag{4.15}$$

$$\Delta Y = 20\log\left|\frac{\mathbf{Y}}{\mathbf{Y}|_{\mathbf{FS}}}\right| \tag{4.16}$$

The changes in cochlear potential and sound pressure level were obtained by taking the ratio (in dB) between the measurements made in the stiffened ear and the measurements made in the normal ear. For ΔY, the order of division was reversed. This is due to the fact that increasing admittance actually decreases sound pressure level as well as cochlear potential response. Such analysis would thus show the quantitative contributions of the *pars flaccida* to each of these quantities, making it possible to test the modeling of *pars flaccida* in the context of the circuit model, but without the complexity of the *pars tensa*, ossicles, and cochlea.

Figure 4-13 shows a comparison between the predicted and measured $\Delta Y, \Delta P_{EC}|_V$, and $\Delta CP|_V$. For gerbil B11, the model predictions and the measured responses are essentially identical from 50 Hz to 10 kHz. Such results support our assumption that the *pars flaccida* is an independent shunt path in parallel with the main transmission mechanism of the middle ear (*i.e.* the *pars tensa*-ossicular-cochlear pathway). In other words, if we assume the ear is listening to a constant volume velocity sound source (as in the case of our experimental setup), the presence of *pars flaccida* (as opposed to an ear with stiffened *pars flaccida*) provides an additional path for the sound volume velocity at frequencies below its resonance frequency — region where its admittance is comparable to that of the *pars tensa* [see Figure 4-15]. Consequently the pressure generated at the

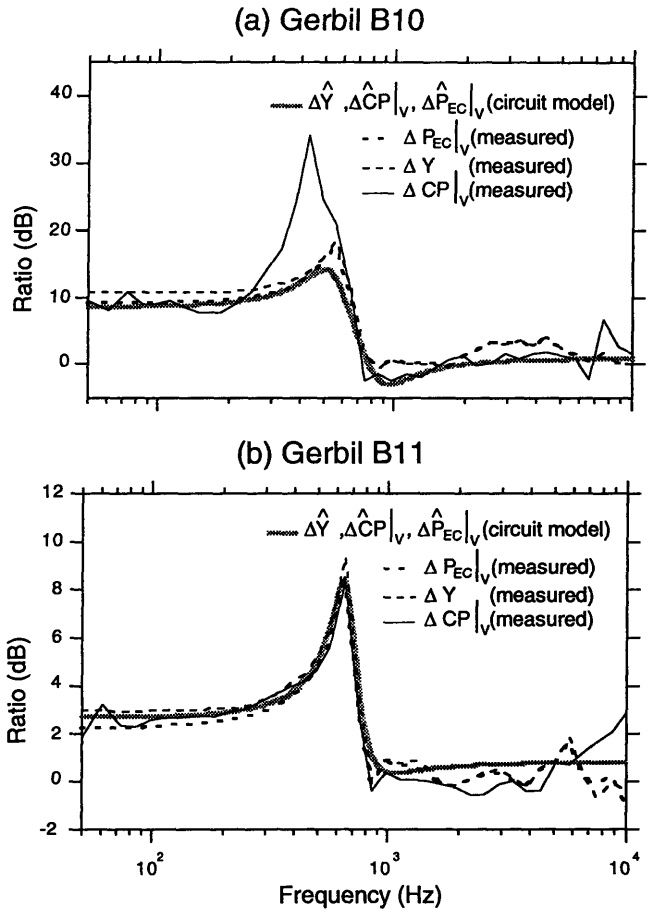

Figure 4-13: Comparison of the predicted and measured $\Delta Y, \Delta P_{EC}|_V$, and $\Delta CP|_V$ in ears with middle ear open. The model calculations do not take into account the loading effects of the source internal admittance, thereby making the assumption that $|\mathbf{Y}_{gerbil\ ear}| \gg |\mathbf{Y}_{internal}|$. As a result, all predicted changes ($\Delta\hat{Y}, \Delta\hat{C}P, and \Delta\hat{P}_{EC}$) are identical (see the discussion in Section 3.2.2).

ear canal is decreased. The amount of sound level decrease (in dB) should thus be exactly the same as the change in admittance between normal and *pars flaccida*-stiffened ears. In addition, if the assumption is correct that *pars flaccida* and *pars tensa* are independent, the decrease in the input to the inner ear (in dB) should also be identical to the change in ear-canal sound pressure level (recall that $\frac{\mathbf{U_T}}{\mathbf{P_{EC}}}$ is independent of the *pars flaccida* when the middle ear cavity is widely opened). Quantitatively, we would expect:

$$\Delta P_{EC}|_V = \Delta Y = \Delta CP|_V = 20\log\left|\frac{\mathbf{Y_{TOC}} + \mathbf{Y_{PF}}}{\mathbf{YTOC}}\right| \tag{4.17}$$

This was exactly what we measured in gerbil B11. Results in Gerbil B10 (Figure 4-13a), however, show a small frequency region where this assumption is not entirely accurate. Between 300 Hz and 600 Hz, the measurements show a significant increase (up to 20 dB) in cochlear potential that cannot be explained by our circuit model. This region incidentally also exhibits some expansive nonlinearity in cochlear potential production (see Section 3.2.1). In addition, it is also the region where *pars flaccida* resonates. Therefore, this inconsistency could possibly be a result of the interactions between the *pars tensa* and the *pars flaccida* in the acoustic transmission process. The feasibility of such an explanation required further investigation.

Figures 4-14 and 4-15 provide a test of our circuit model concerning two important points raised in the above discussions. Figure 4-14 shows the $\frac{\mathbf{CP}}{\mathbf{P_{EC}}}$ transfer functions measured in gerbils B10 and B11 after stiffening the *pars flaccida*, along with a scaled version of our model prediction, which in this case is simply the admittance $\mathbf{Y_{TOC}}$ (shown in the figure as the measured $\mathbf{Y_{FS}^{WO}}$). Figure 4-15 shows the model and measured $\frac{\mathbf{CP}}{\mathbf{U_T}}$ transfer functions for ears with normal tympanic membrane and ears with stiffened

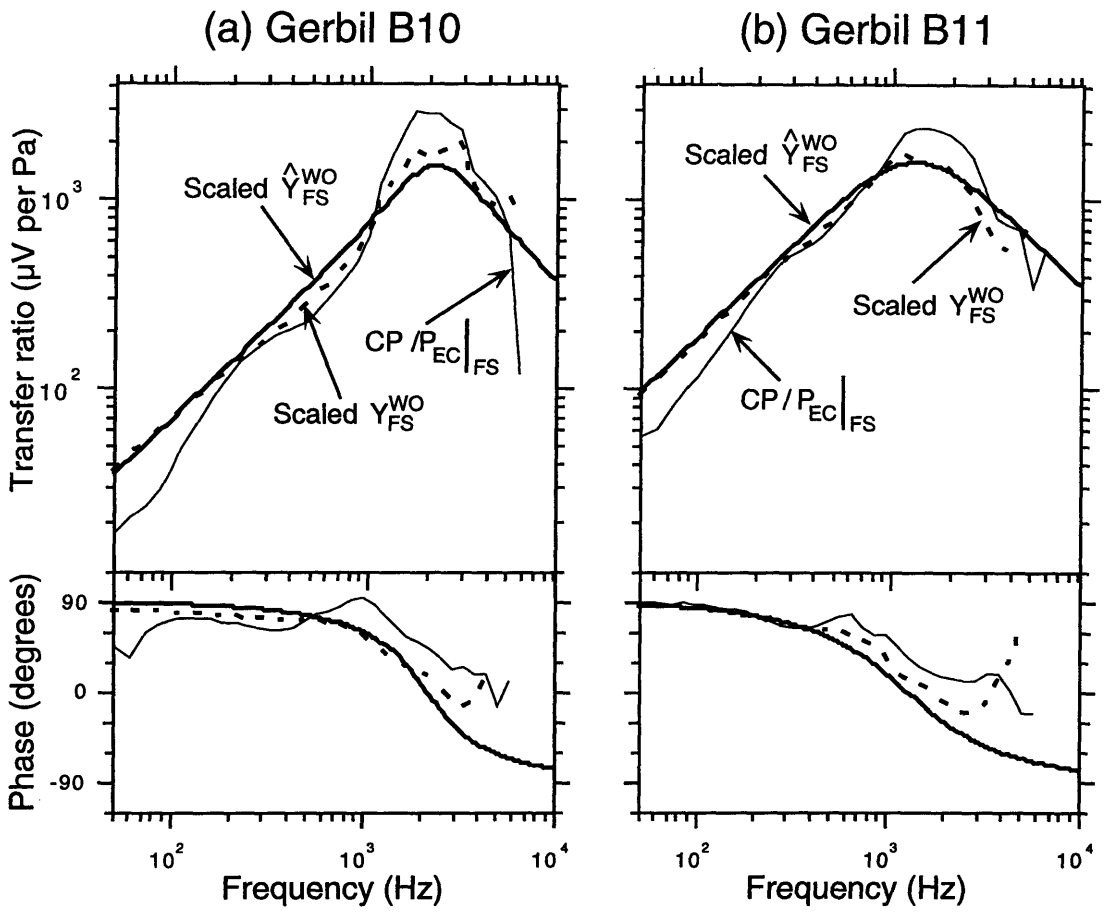

Figure 4-14: Comparison of the measured input admittances $\mathbf{Y_{FS}^{WO}}$, model input admittances $\mathbf{\hat{Y}_{FS}^{WO}}$, and the middle-ear transfer functions $\mathbf{\left.\frac{CP}{P_{EC}}\right|_{FS}}$ measured with the *flaccida* stiffened. The admittance plots are scaled relative to the transfer ratio measurements to obtain a good visual match.

pars flaccida. For both figures, it is apparent that the model is unable to represent the fine structures of the experimentally measured transfer functions. For example, the model $\frac{\mathbf{CP}}{\mathbf{U_T}}$ transfer function does not account for any ossicular slippage or non-planar vibration of the tympanic membrane (see Section 4.2.1); therefore, it predicts a constant transfer function that is frequency independent, substantially different than the actual measurements. Nonetheless, all the basic features observed in these two figures agree with the discussion presented in the previous paragraphs. In particular, both the model and the measured $\left.\frac{\mathbf{CP}}{\mathbf{P_{EC}}}\right|_{\mathbf{FS}}$ are compliance dominated at low frequencies; the magnitude increases with frequency, and the phase angle is close to +90°. Both transfer functions peak at approximately 2 kHz, and they both roll off at higher frequencies. For the $\frac{\mathbf{CP}}{\mathbf{U_T}}$ transfer function, the most important feature, at least for the purpose of determining the topology of the *pars flaccida*, is the difference between measurement made in a normal ear and measurement made in ear with *pars flaccida* stiffened. Figure 4-15 shows that in this regard, both the model and the measurements agree with each other for most of the frequency range, as is indicated in Figure 4-13.

4.5 Prediction of the effects of *Pars Flaccida* manipulations on the input to the inner ears — intact bulla wall

When the bulla wall is intact, the addition of the middle-ear cavity changes some of the behaviors described in the last section. In particular, the middle-ear sound pressure level is now a significant portion of the ear-canal sound pressure level (see Figure 4-10). The $\frac{\mathbf{CP}}{\mathbf{P_{EC}}}$ transfer function (with middle ear intact) is no longer simply proportional to $\mathbf{Y_{TOC}}$, rather it depends on all three acoustic blocks in the middle-ear model—

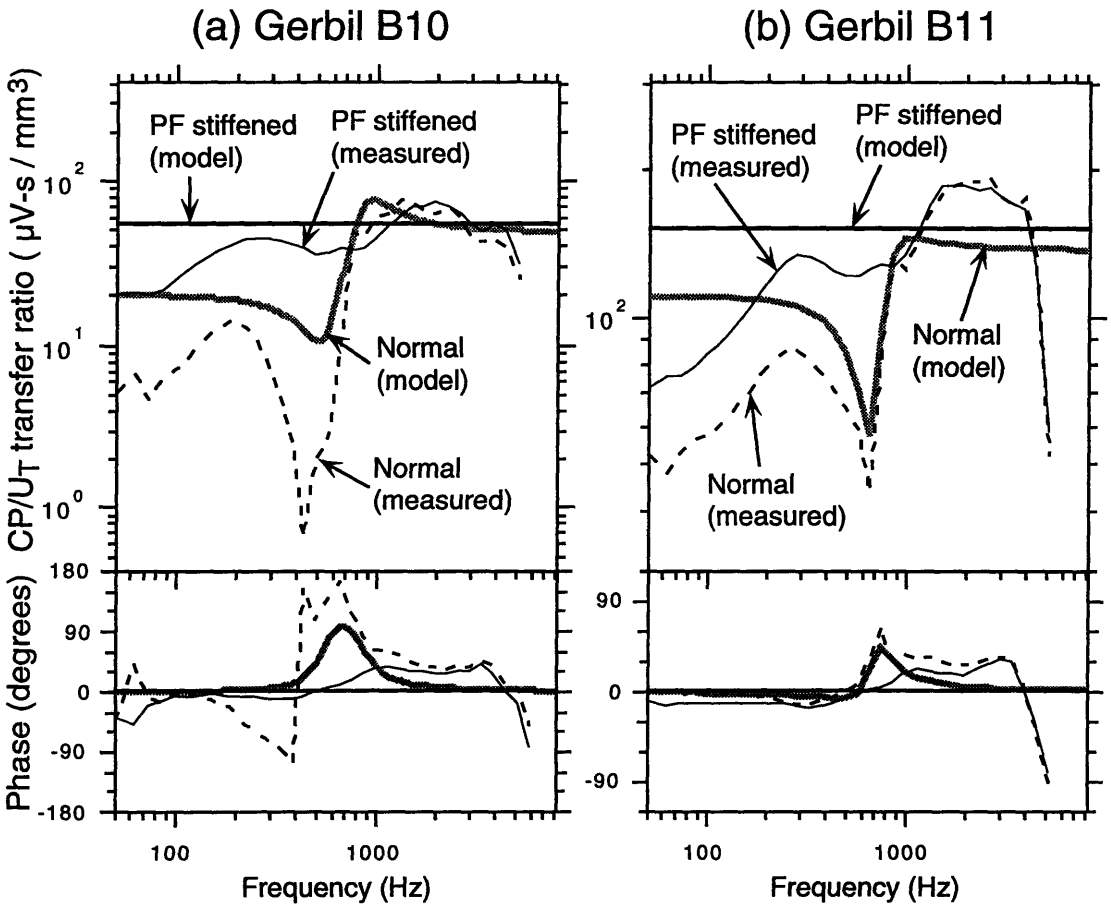

Figure 4-15: Comparison of the model and measured $\mathbf{CP/U_T}$ transfer functions in gerbils B10 and B11. The measured volume velocities of the entire tympanic membrane $\mathbf{U_T}$ were computed as the product of the measured input admittances and measured ear-canal sound pressure levels. The model transfer functions were scaled in magnitude to allow visual comparison of the predictions and the experimental data.

Y_{TOC}, Y_{CAV}, and Y_{PF}:

$$\left.\frac{CP}{P_{EC}}\right|^{I} = \frac{Y_{TOC}Y_{CAV}}{Y_{PF}+Y_{TOC}+Y_{CAV}} = \left(\left.\frac{CP}{P_{EC}}\right|^{WO}\right) \times \frac{Y_{CAV}}{Y_{PF}+Y_{TOC}+Y_{CAV}} \quad (4.18)$$

where $\left.\frac{CP}{P_{EC}}\right|^{I}$ represents the transfer admittance of sound pressure level in the ear-canal to the volume velocity entering the *pars tensa*-ossicular pathway with the middle ear intact. Stiffening the *pars flaccida* should simply remove the Y_{PF} term from the above equation.

Figure 4-16 shows the predicted $\frac{CP}{P_{EC}}$ transfer functions for gerbils B10 and B11 under various middle ear conditions. The predictions are based on the admittance measurements shown in Figure 4-9. Intuitively, the main effect of the middle ear cavity is to reduce the pressure difference across the tympanic membrane (*i.e.* by increasing the pressure in the middle ear cavity), thereby decreasing the volume velocity entering the inner ear and the production of cochlear potential. Such effect is indeed what is predicted in Figure 4-16. At frequencies below 3 kHz, the transfer function of ears with intact middle-ear cavity is substantially decreased when compared to ears with widely opened bulla walls. In addition, the presence of *pars flaccida* causes a further decrease in the transfer function at frequencies below the *pars flaccida* resonance. All these phenomena can be readily explained using Equation 4.18. At frequencies above 3 kHz, $|Y_{CAV}| \gg |Y_{TOC}| \gg |Y_{PF}|$; Equation 4.18 thus predicts that $\frac{CP}{P_{EC}}$ is the same with or without the middle ear cavity. Below 3 kHz but above the *flaccida* resonance ($\approx$500 Hz), $|Y_{CAV}|$ and $|Y_{TOC}|$ are of same order of magnitude, and they are both substantially greater than $|Y_{PF}|$. Consequently, Equation 4.18 predicts an approximately 6 dB drop in the transfer function of the intact middle ear. At even lower frequencies,

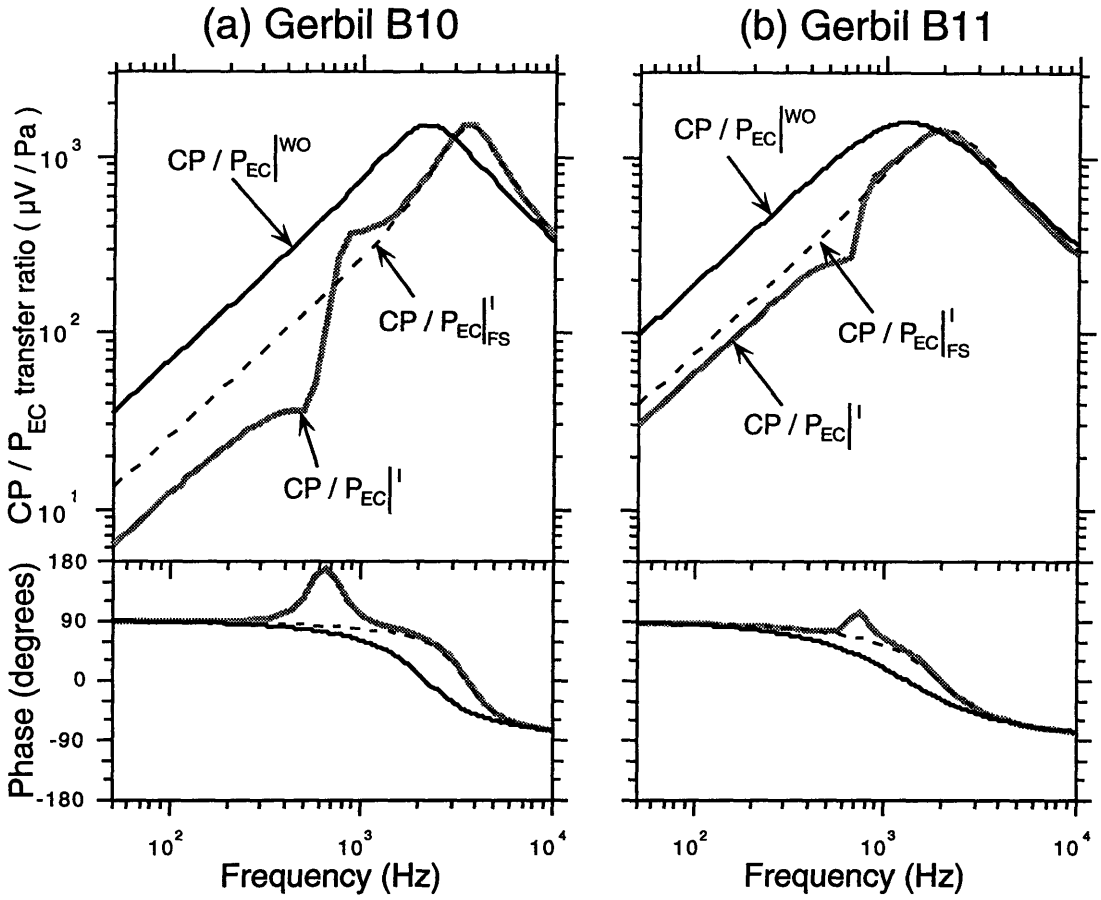

Figure 4-16: Predictions of the effects of middle-ear cavity and tympanic membrane manipulations on the middle ear transfer functions ($\frac{CP}{P_{EC}}$) of gerbils B10 and B11. The predictions are based on the circuit model shown in Figure 4-3, where cochlear potential is assumed to be directly proportional to volume velocity entering the *pars tensa*-ossicular-cochlear complex. The magnitudes of all transfer functions were scaled such that their numerical values are comparable to that of the measured transfer function (Figure 4-14).

$|\mathbf{Y_{PF}}|$ is comparable to both $|\mathbf{Y_{CAV}}|$ and $|\mathbf{Y_{TOC}}|$, which causes a further reduction in the transfer function magnitude.

In our experimental setup, the volume velocity entering the middle ear was held constant (the earphone acted as a volume velocity source when driven by a constant applied voltage). In this scenario, the middle-ear model predicts that the *pars flaccida* acts as a current divider, irrespective of the middle ear condition (Figure 4-17). Thus, at frequencies where the admittance of the *flaccida* is significant, volume velocity entering the cochlea is proportionally reduced according to this current divider principle. Consequently, with or without the middle ear cavity, the changes in cochlear potential production between ears with normal tympanic membrane and ears with *pars flaccida* stiffened are the same (Figure 4-18). From our results in the last section, we would expect:

$$\Delta\widehat{C}P\Big|_U^I = \Delta\widehat{C}P\Big|_U^{WO} = \Delta\widehat{Y}\Big|^{WO} = \Delta\widehat{P}_{EC}\Big|_U^{WO} = 20\log\left|\frac{\mathbf{Y_{TOC}}+\mathbf{Y_{PF}}}{\mathbf{Y_{TOC}}}\right| \qquad (4.19)$$

The subscript U indicates that the predicted quantity is calculated with the assumption that the ear is excited by a constant current source (which is approximately equal to the quantity calculated from experimental measurements obtained with constant voltage applied to the earphone). With the middle ear cavity intact, $\Delta\widehat{Y}\Big|^I$ and $\Delta\widehat{P}_{EC}\Big|_U^I$ differ from those observed in ears with middle ears widely opened. Quantitatively, it can be shown from the model that:

$$\Delta\widehat{Y}\Big|^I = \Delta\widehat{P}_{EC}\Big|_U^I = 20\log\left|\frac{(\mathbf{Y_{PF}}+\mathbf{Y_{TOC}})(\mathbf{Y_{CAV}}+\mathbf{Y_{TOC}})}{(\mathbf{Y_{PF}}+\mathbf{Y_{CAV}}+\mathbf{Y_{TOC}})\mathbf{Y_{TOC}}}\right| \qquad (4.20)$$

At frequencies where $|\mathbf{Y_{PF}}| \ll |\mathbf{Y_{TOC}}+\mathbf{Y_{CAV}}|$ (*i.e.* $f > 2$ kHz), Equation 4.20 reduces

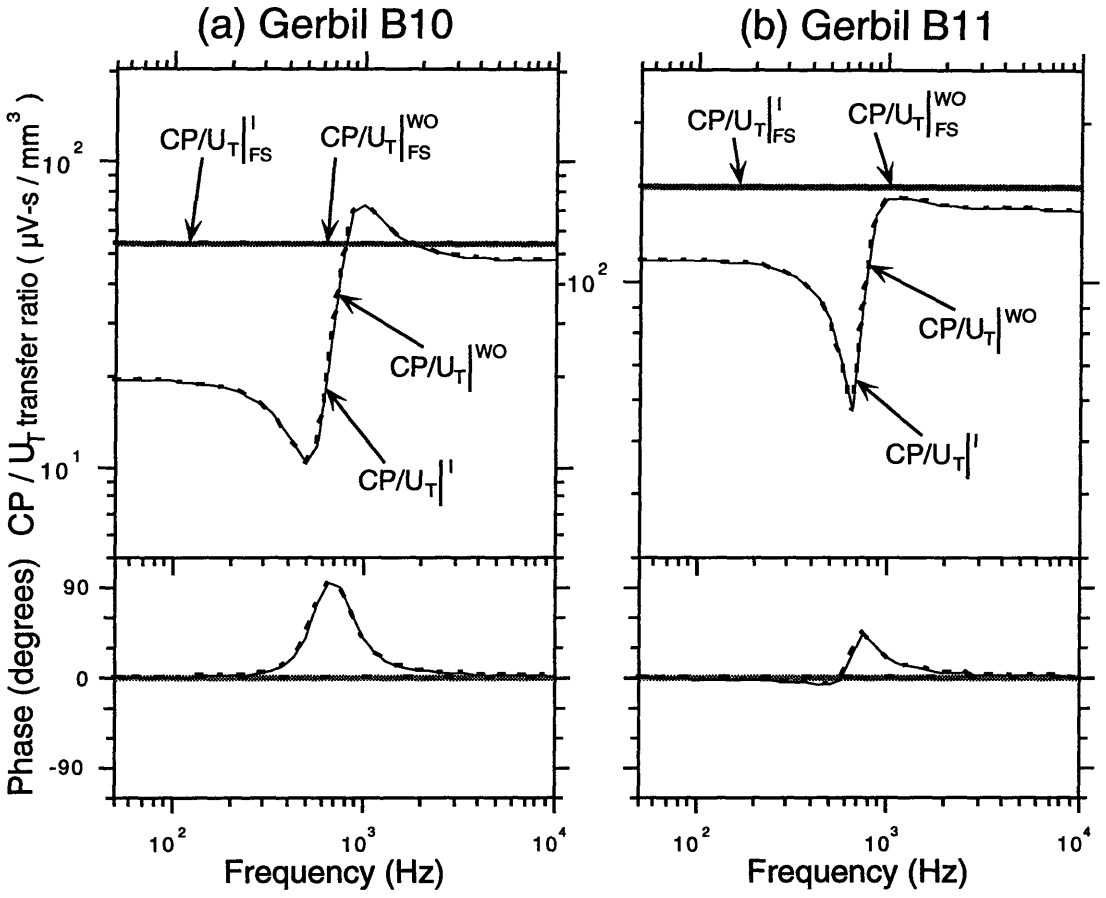

Figure 4-17: Predictions of the effects of middle-ear cavity and tympanic membrane manipulations on the transfer function ($\frac{\mathbf{CP}}{\mathbf{U_T}}$) of gerbils B10 and B11. The predictions are based on the circuit model shown in Figure 4-3, where cochlear potential is assumed to be directly proportional to volume velocity entering the *pars tensa*-ossicular-cochlear complex. The magnitudes of all transfer functions were scaled such that their numerical values are comparable to that of the measured transfer functions (Figure 4-15).

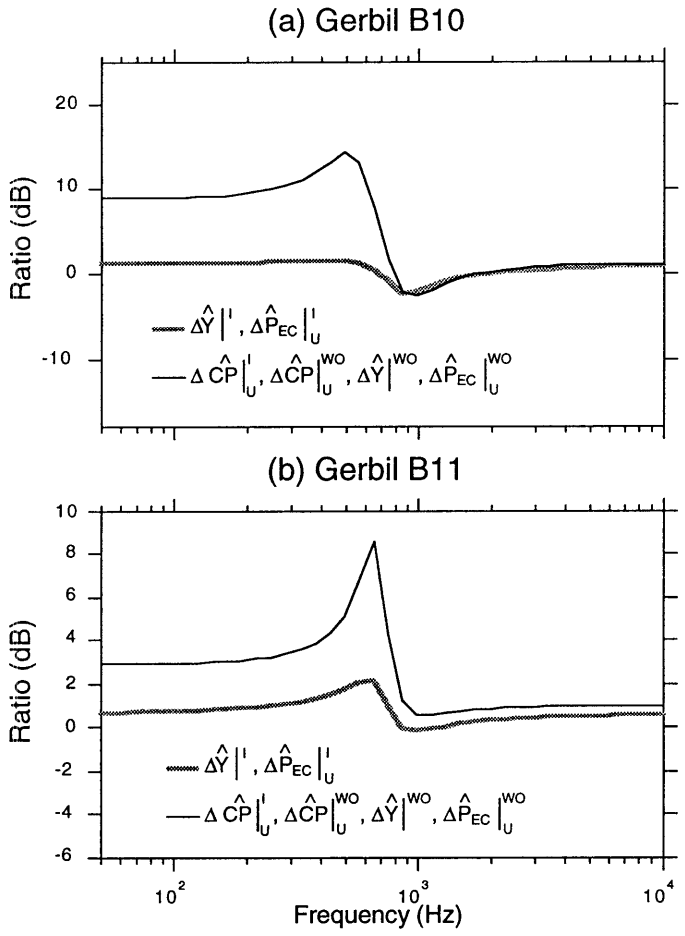

Figure 4-18: Predictions of the role of the middle-ear cavity on the effects of stiffening *pars flaccida*. This figure shows the predicted $\Delta Y, \Delta CP, and \Delta P_{EC}$ for ears with middle ear intact and ears with middle ear widely opened. The parameters used for the prediction calculations were obtained from acoustic measurements in gerbil B10 and B11. The theoretical calculations are based on the circuit model shown in Figure 4-3, and do not take into account the loading effects of the source internal admittance, thereby making the assumption that $|\mathbf{Y}_{gerbil\ ear}| \gg |\mathbf{Y}_{internal}|$.

to Equation 4.19, indicating their insensitivity to the cavity condition. At lower frequencies, where $|\mathbf{Y_{PF}}|$ is significant, closing the cavity decreases both $\Delta Y|^I$ and $\Delta P_{EC}|_U^I$. The model therefore predicts that in ears with middle ear intact, the presence of *pars flaccida* causes very little change in middle-ear input admittance and ear-canal sound pressure level under our experimental condition. This is true because the presence of the middle-ear cavity desensitizes the dependence of input admittance and ear-canal sound pressure level on the *pars flaccida*. This argument holds true even at low frequencies where the admittance of *pars flaccida* is significant (as shown in Figure 4-18). However, the presence of *pars flaccida* does affect the middle-ear transmission process. With a constant volume velocity source, the presence of *pars flaccida* decreases the volume velocity entering the *pars tensa*-ossicular pathway according to the current divider principle. This shunt path mechanism is independent of the middle ear condition.

In general, however, the environmental stimulus is considered to be a constant sound pressure source, not a constant current source. Under this condition, the mechanism of how *pars flaccida* affects the middle-ear transmission process is different than the shunt path mechanism discussed in the previous paragraph. Under this condition, both our model and our data suggest that the presence of *pars flaccida* has only a small effect on middle-ear sound transmission when the bulla wall is widely opened (see Figure 3-20). When the middle-ear cavity is intact, the presence of *pars flaccida* serves to reduce the pressure across the tympanic membrane at low frequencies (Figure 4-10), thereby lowering the driving force on the *pars tensa*. This has the effect of reducing the acoustic transmission to the inner ear, thus correspondingly reduces the hearing sensitivity. The amount of reduction in hearing sensitivity due to the presence of *pars flaccida*, however, depends on whether the stimulus is considered a constant pressure source or a constant

current source. Using the pressure source assumption, the circuit model predicts that the reduction in cochlear potential generation (which represents the volume velocity entering the inner ear) due to the presence of *pars flaccida* is:

$$\Delta\hat{C}P\Big|_P^I = 20\log\left|\frac{\mathbf{Y_{TOC}} + \mathbf{Y_{PF}} + \mathbf{Y_{CAV}}}{\mathbf{Y_{TOC}} + \mathbf{Y_{CAV}}}\right| \tag{4.21}$$

Correspondingly, a constant pressure source forces $\mathbf{P_{EC}}$ to be the same in all ears regardless of the condition of the *pars flaccida.* Therefore $\Delta\hat{P}_{EC}|_P^I = 0$. Comparing Equation 4.21 with Equation 4.19 shows that $\Delta\hat{C}P\Big|^I$ is reduced when the stimulus is assumed to be acting as a constant pressure source, indicating that the effect of *pars flaccida* on middle-ear sound transmission is smaller when the ear is exposed to environmental stimulus. Figure 4-19 compares the two $\Delta\hat{C}P\Big|^I$ across the entire frequency spectrum.

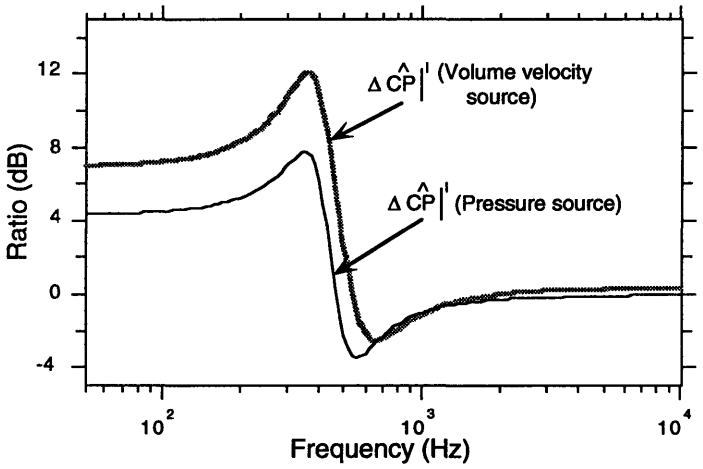

Figure 4-19: Effect of using different types of stimulus sources on $\Delta\hat{C}P\Big|^I$. The predictions shown in this figure were calculated using the model parameters of Table 4.3. At frequencies above 600 Hz, the difference between the two curves is small. At lower frequencies, the reduction of volume velocity entering the inner ear is approximately 3 dB larger when the ear is excited by a volume velocity source.

Chapter 5

Summary

Results from our acoustic and physiological measurements show that the sound transmission effect of gerbil *pars flaccida* can be accurately modeled by an RLC circuit. Below its resonance frequency ($\approx$ 300-800 Hz), *pars flaccida* is compliance dominated. Its admittance magnitude in this frequency range is similar to that of the middle-ear cavity and the *pars tensa*. Above this high-admittance resonance, the *pars flaccida* is primarily mass dominated. In this frequency range, its admittance magnitude is significantly lower than both the middle-ear cavity and the *pars tensa*-ossicular-cochlear complex.

Our pressure ratio measurements support the common assumption that the middle-ear cavity acts in series with the main ossicular transmission pathway. Our cochlear potential measurements further illustrate that over most frequency ranges, the movement of the *pars flaccida* portion of the tympanic membrane is independent of the *pars tensa*. These results are consistent with a middle-ear model having the *pars flaccida* in parallel with the combined input admittances of the *pars tensa*, ossicles, and cochlea. This parallel combination could then be connected in series to the admittance of the middle-ear cavity in accordance with the traditional middle-ear model. In one of our two cochlear

potential measurements, significant deviation from this general model was observed in the 300-600 Hz range, where cochlear potential generation was unexpectedly suppressed at low sound intensities. The cause of this deviation is unclear and requires further investigations.

Results in this study thus provide evidence that over most frequency ranges, the movement of the *pars flaccida* does not participate directly in eliciting ossicular motion. However, the presence of *pars flaccida* provides a shunt path for the acoustic volume velocity to enter the middle ear cavity. At low frequencies, where the admittance of *pars flaccida* is comparable to that of the *pars tensa*, the increase in middle-ear pressure due to this extra shunt path reduces the pressure difference across the tympanic membrane (by as much as 3-10 dB in gerbil), thereby lowering the driving force and input to the inner ear. The presence of *pars flaccida* therefore reduces low frequency hearing sensitivity.

Appendix A

Summary of the experimental measurements

Date	Animal/ Weight	Ear	Description
10/27/94	A1 67 g	L	Healthy ear. Practice the acoustic and cochlear potential measurements using the high frequency source. Learn the gerbil anatomy.
12/22/94	A2 47.3 g	L	Healthy ear. Both hfs and lfs were used. All measurements were made with the chirp stimulus. Measured the input admittances, cochlear potentials, and middle-ear pressures with the tympanic membrane undisturbed, *pars flaccida* stiffened, and *pars flaccida* removed. All measurements were repeated in both the middle ear intact and bulla hole open configurations.
1/5/95	B1 49.6 g	L	Healthy ear. Only the lfs was used. All measurements were made with the chirp stimulus. The round window niche and the surrounding areas were filled with fluids, possibly resulted from a punctured round window membrane. Measured the input admittances, cochlear potentials, and middle-ear pressures with the tympanic membrane undisturbed, *pars flaccida* stiffened, and *pars flaccida* removed. All measurements were repeated in the middle ear intact, bulla hole open, and middle ear

			widely opened configurations.
1/12/95	B2 59.0 g	L	Healthy ear. Only the lfs was used. All measurements were made with the chirp stimulus. With the middle ear widely opened, we measured the input admittances, cochlear potentials, and middle-ear pressures in two different cases — with the tympanic membrane undisturbed, and with *pars flaccida* stiffened. Only the tympanic membrane intact measurements were made in the hole open and middle ear intact configurations. Measured the ear canal volume.
1/18/95	B3 51 g	L	Healthy ear. Only the lfs was used. All measurements were made with the chirp stimulus. With the middle ear widely opened, we measured the input admittances, cochlear potentials, and middle-ear pressures in three different cases — with the tympanic membrane undisturbed, with the *pars flaccida* stiffened, and with the *pars flaccida* removed. Only the tympanic membrane intact measurements were made in the hole open and middle ear intact configurations. Measured the ear canal volume.
3/1/95	B4 53 g	L	Healthy ear. Both hfs and lfs were used. All measurements were made with the chirp stimulus. Measured the input admittances, cochlear potentials, and middle-ear pressures with the tympanic membrane undisturbed, *pars flaccida* stiffened, and *pars flaccida* removed. All measurements were repeated in both the middle ear intact and bulla hole open configurations. Measured the ear canal volume.
3/6/95	B5 65 g	L	Healthy ear. Only the hfs was used. All measurements were made with the chirp stimulus. With the middle ear widely opened, we measured the input admittances, cochlear potentials, and middle-ear pressures in three different cases — with the tympanic membrane undisturbed, with the *pars flaccida* stiffened, and with the *pars flaccida* removed. Only the tympanic membrane intact measurements were made in the hole open and middle ear intact configurations. Measured the ear canal volume.
3/14/95	B7 66 g	L	Healthy ear. Both the lfs and hfs were used. All measurements were made with the chirp stimulus. The middle ear was widely opened. Measured the input admittances, cochlear potentials, and middle-ear pressures with the tympanic membrane undisturbed, *pars flaccida* stiffened, and *pars flaccida* removed. Most measurements appear leaky. Measured the ear canal volume.

3/14/95	B7 66 g	R	Healthy ear. Both the lfs and hfs were used. All measurements were made with the chirp stimulus. Measurements were made with the middle ear intact and with the bulla hole open. Measured the input admittances, cochlear potentials, and middle-ear pressures with the tympanic membrane undisturbed, *pars flaccida* stiffened, and *pars flaccida* removed. Measured the ear canal volume.
3/20/95	B8 57 g	L	Healthy ear. Both the lfs and hfs were used. All measurements were made with the chirp stimulus. The middle ear was widely opened. Measured the input admittances, cochlear potentials, and middle-ear pressures with the tympanic membrane undisturbed, *pars flaccida* stiffened, and *pars flaccida* removed. Measured the ear canal volume.
3/20/95	B8 57 g	R	Healthy ear. Both the lfs and hfs were used. All measurements were made with the chirp stimulus. Measurements were made with the middle ear intact and with the bulla hole open. Measured the input admittances, cochlear potentials, and middle-ear pressures with the tympanic membrane undisturbed, *pars flaccida* stiffened, and *pars flaccida* removed. Measured the ear canal volume.
3/22/95	B9 54 g	L	Healthy ear. Both the lfs and hfs were used. All measurements were made with the chirp stimulus. The middle ear was widely opened. Measured the input admittances, cochlear potentials, and middle-ear pressures with the tympanic membrane undisturbed, *pars flaccida* stiffened, and *pars flaccida* removed. Measured the ear canal volume.
3/22/95	B9 54 g	R	Healthy ear. Both the lfs and hfs were used. All measurements were made with the chirp stimulus. Measurements were made with the middle ear intact and with the bulla hole open. Measured the input admittances, cochlear potentials, and middle-ear pressures with the tympanic membrane undisturbed, *pars flaccida* stiffened, and *pars flaccida* removed. Measured the ear canal volume.
4/24/95	B10 60 g	L	Healthy ear. Only the lfs was used. All measurements were made according to the tone-sweep protocol. The middle ear was widely opened. Measured the ear-canal pressures and cochlear potentials with the tympanic

			membrane undisturbed and with the *pars flaccida* stiffened. Measured the ear canal volume.
5/4/95	B11 59 g	L	Healthy ear. Only the lfs was used. All measurements were made according to the tone-sweep protocol. The middle ear was widely opened. Measured the ear-canal pressures and cochlear potentials with the tympanic membrane undisturbed and with the *pars flaccida* stiffened. Measured the ear canal volume.

Appendix B

Source accuracy charts

This appendix contains the accuracy charts of the low and high frequency sources used in this thesis. For each source, four different voltage levels were used to drive the earphone. The voltage levels indicated in the following charts refer to the amplitudes of the linear chirp signals. Four different gray scale levels are used to represent the degrees of accuracy attainable by the sound source. For instances, the darkest gray scale level delineate the regions where an unknown admittance can be measured to within 1 dB in magnitude *and* 5° in phase; while the lightest gray scale level represent regions where the errors are either greater than 4 dB in magnitude *or* 15° in phase. These results were calculated from 7 sets of measurements over a four month period. Each measurement set consisted of measurements in 5–6 known acoustic loads whose admittance spanned a wide range (see Figure 2-10. The errors were determined by comparing the mean of these measurements with the theoretical admittances discussed in Chapter 2. See Section 2.2.4 for the interpretations and discussions on these accuracy charts.

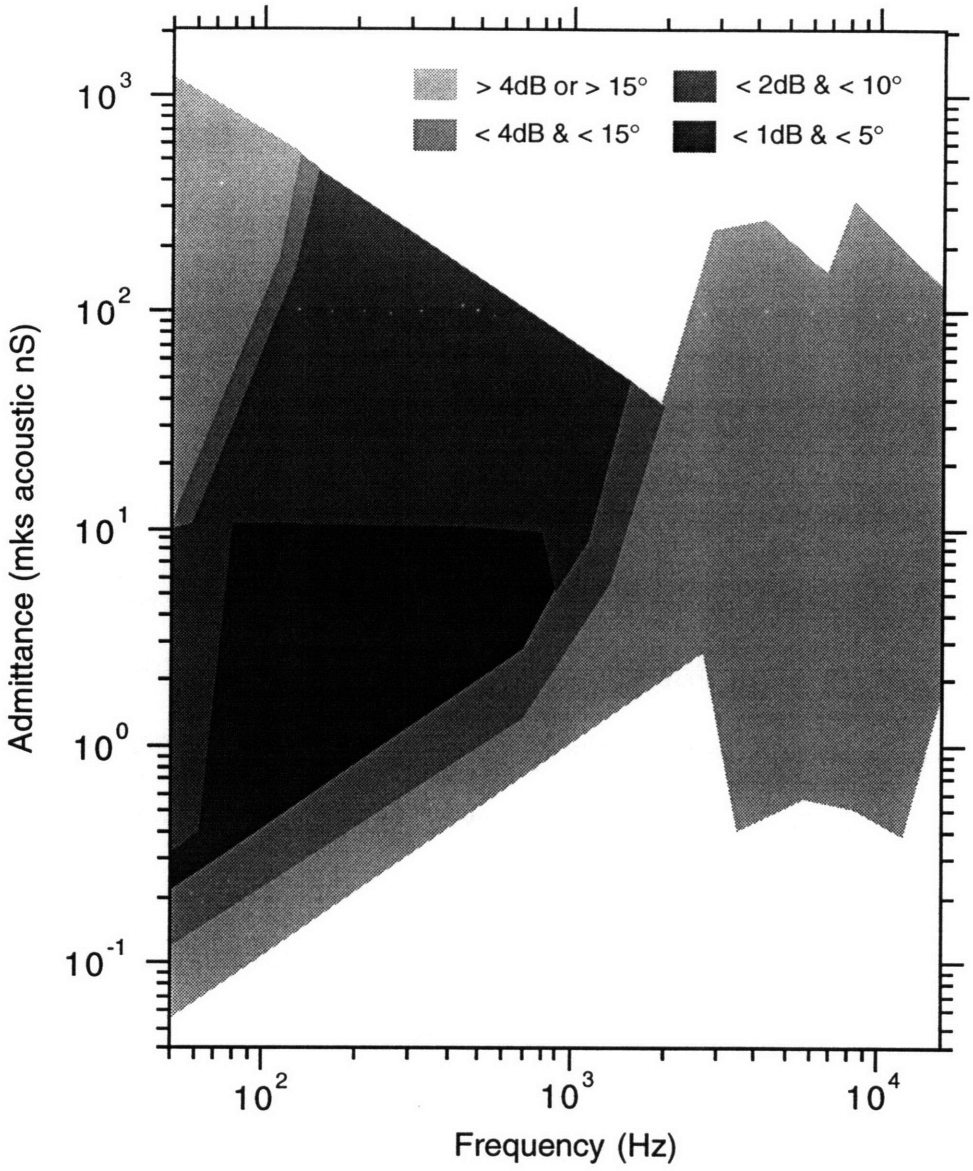

Figure B-1: Source accuracy chart for the low frequency source (driver voltage = 0.32 V). Four gray scale levels are used to represent the maximum accuracy attainable at the specified range of admittance magnitude and frequency. For example, the darkest gray level represents the range over which the source can measure an admittance to within 1 dB in magnitude and 5° in phase. Only the admittance range spanned by the reference loads is included in this chart. The actual accuracy domain can therefore be larger than what is shown.

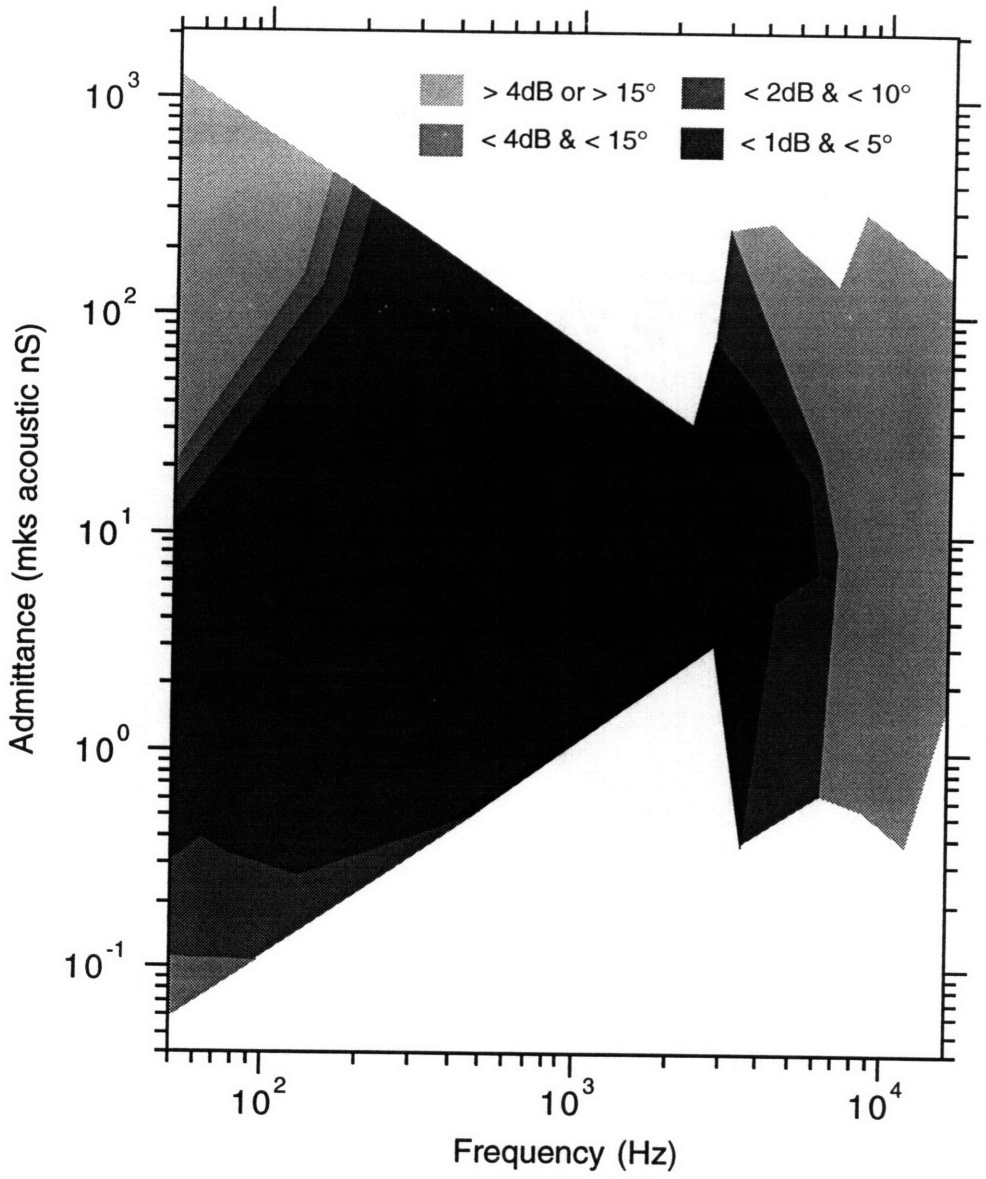

Figure B-2: Source accuracy chart for the low frequency source (driver voltage = 0.1 V). Four gray scale levels are used to represent the maximum accuracy attainable at the specified range of admittance magnitude and frequency. For example, the darkest gray level represents the range over which the source can measure an admittance to within 1 dB in magnitude and 5° in phase. Only the admittance range spanned by the reference loads is included in this chart. The actual accuracy domain can therefore be larger than what is shown.

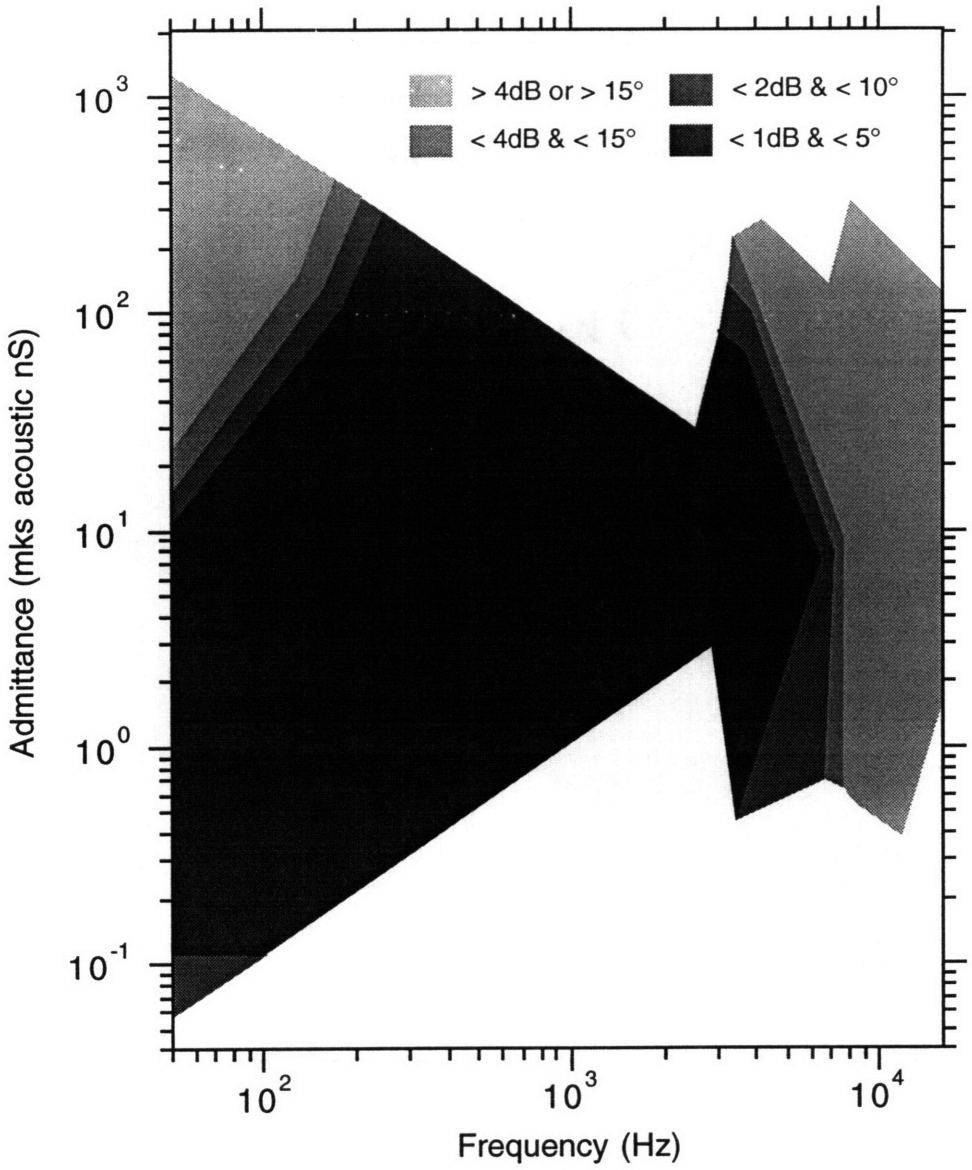

Figure B-3: Source accuracy chart for the low frequency source (driver voltage = 0.032 V). Four gray scale levels are used to represent the maximum accuracy attainable at the specified range of admittance magnitude and frequency. For example, the darkest gray level represents the range over which the source can measure an admittance to within 1 dB in magnitude and 5° in phase. Only the admittance range spanned by the reference loads is included in this chart. The actual accuracy domain can therefore be larger than what is shown.

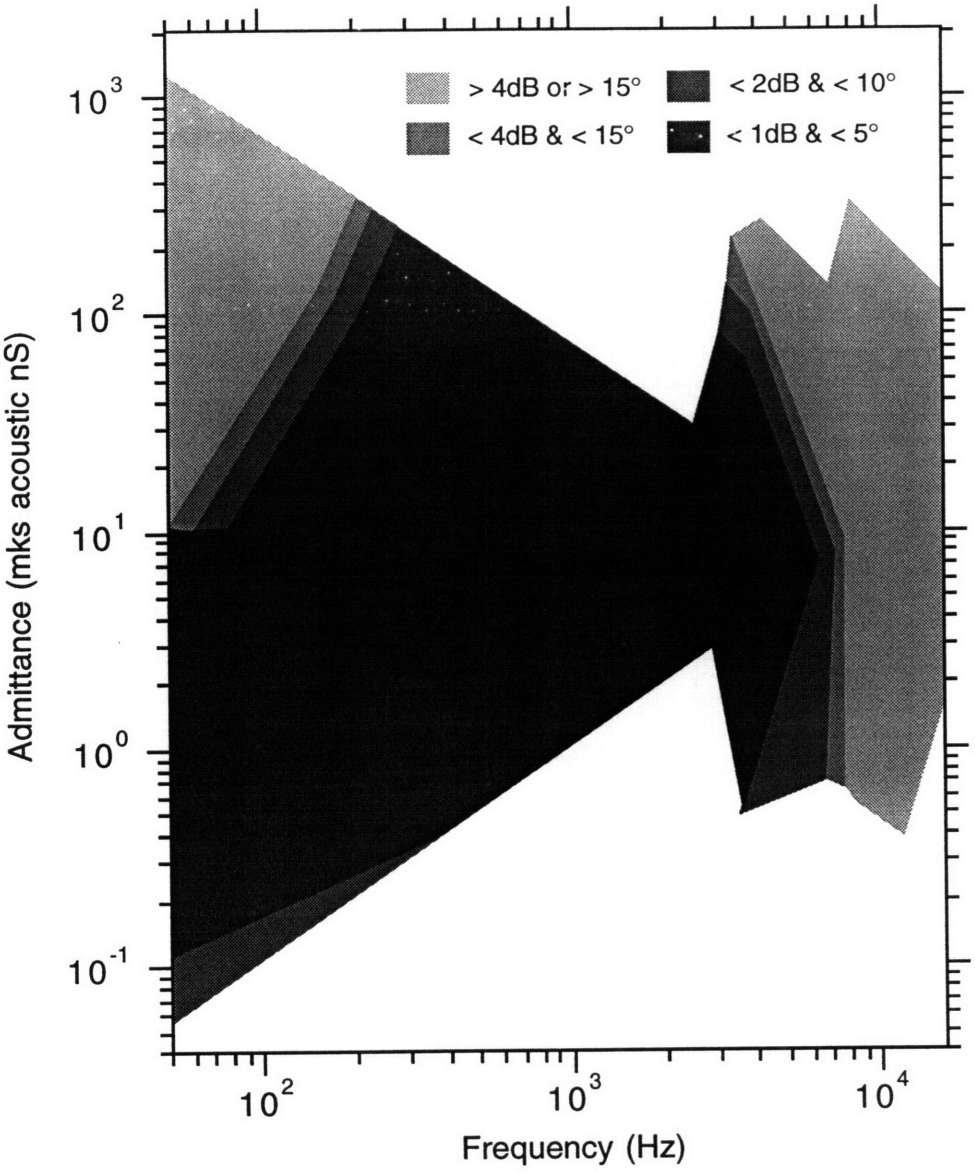

Figure B-4: Source accuracy chart for the low frequency source (driver voltage = 0.01 V). Four gray scale levels are used to represent the maximum accuracy attainable at the specified range of admittance magnitude and frequency. For example, the darkest gray level represents the range over which the source can measure an admittance to within 1 dB in magnitude and 5° in phase. Only the admittance range spanned by the reference loads is included in this chart. The actual accuracy domain can therefore be larger than what is shown.

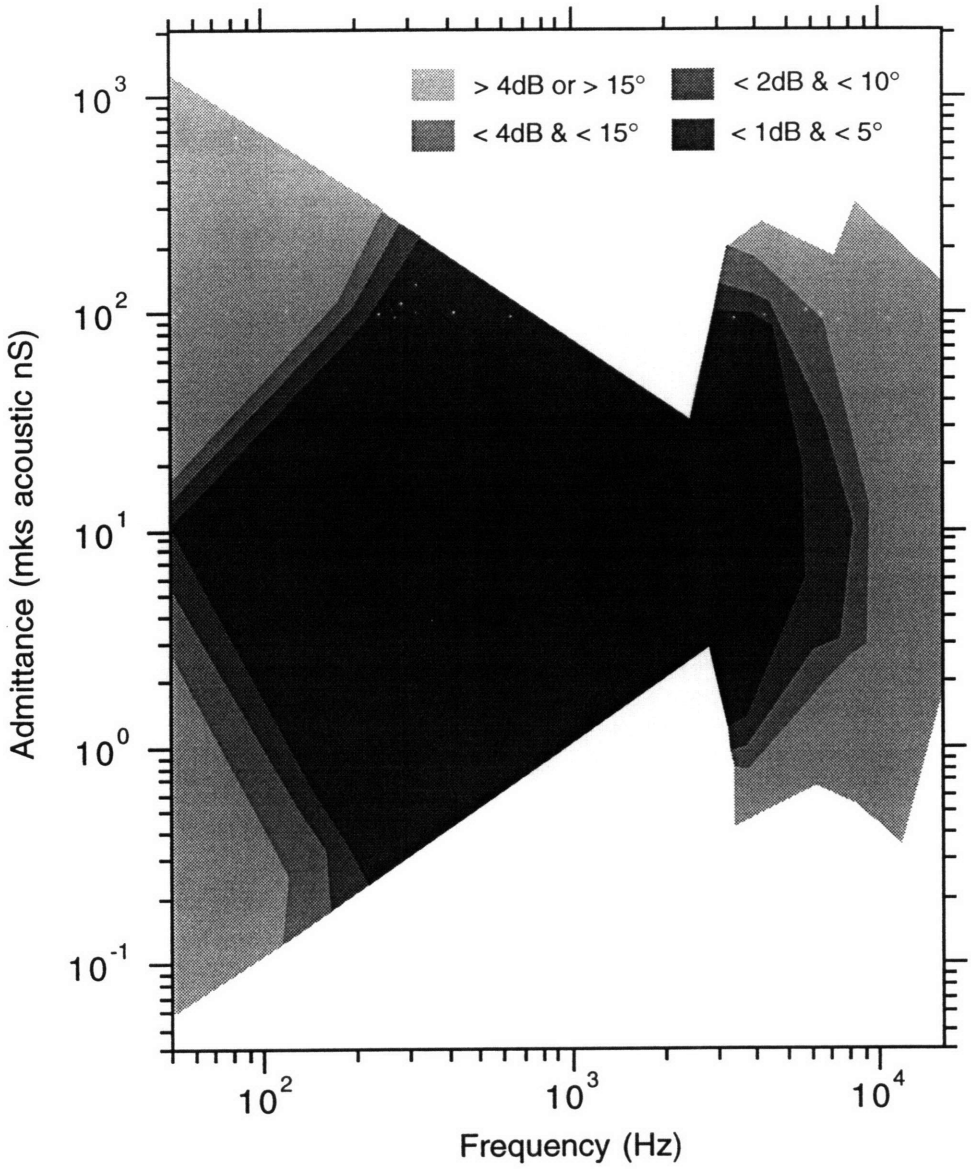

Figure B-5: Source accuracy chart for the high frequency source (driver voltage = 0.032 V). Four gray scale levels are used to represent the maximum accuracy attainable at the specified range of admittance magnitude and frequency. For example, the darkest gray level represents the range over which the source can measure an admittance to within 1 dB in magnitude and 5° in phase. Only the admittance range spanned by the reference loads is included in this chart. The actual accuracy domain can therefore be larger than what is shown.

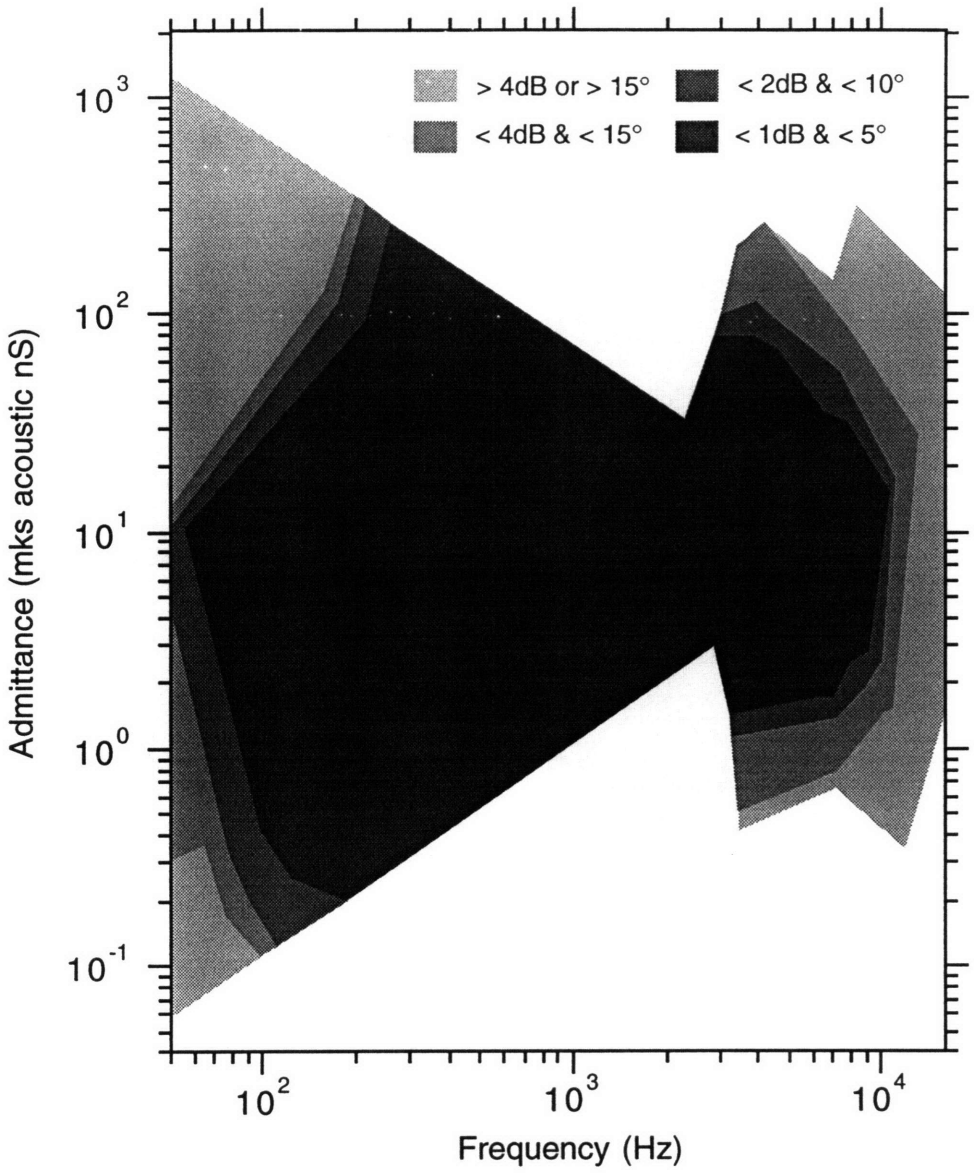

Figure B-6: Source accuracy chart for the high frequency source (driver voltage = 0.01 V). Four gray scale levels are used to represent the maximum accuracy attainable at the specified range of admittance magnitude and frequency. For example, the darkest gray level represents the range over which the source can measure an admittance to within 1 dB in magnitude and 5° in phase. Only the admittance range spanned by the reference loads is included in this chart. The actual accuracy domain can therefore be larger than what is shown.

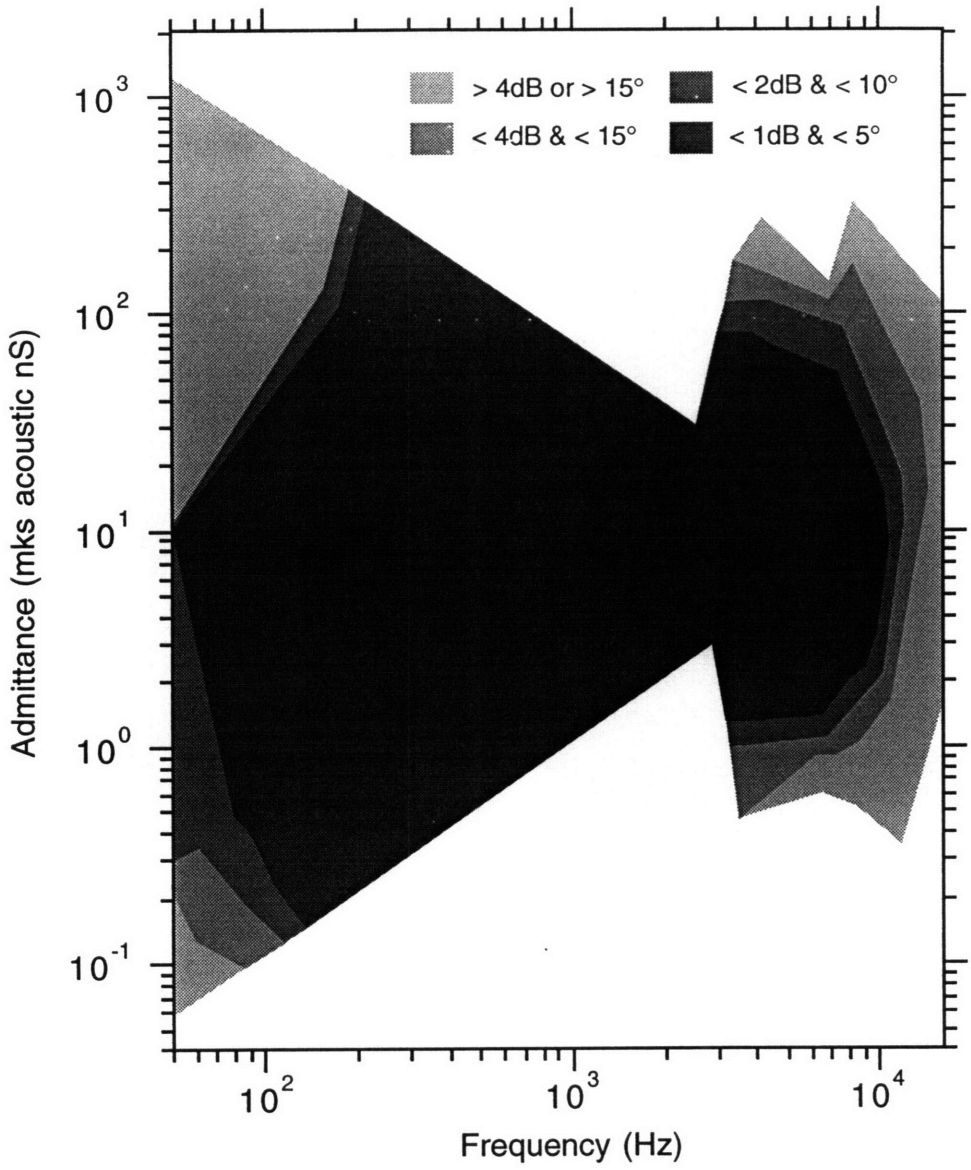

Figure B-7: Source accuracy chart for the high frequency source (driver voltage = 0.0032 V). Four gray scale levels are used to represent the maximum accuracy attainable at the specified range of admittance magnitude and frequency. For example, the darkest gray level represents the range over which the source can measure an admittance to within 1 dB in magnitude and 5° in phase. Only the admittance range spanned by the reference loads is included in this chart. The actual accuracy domain can therefore be larger than what is shown.

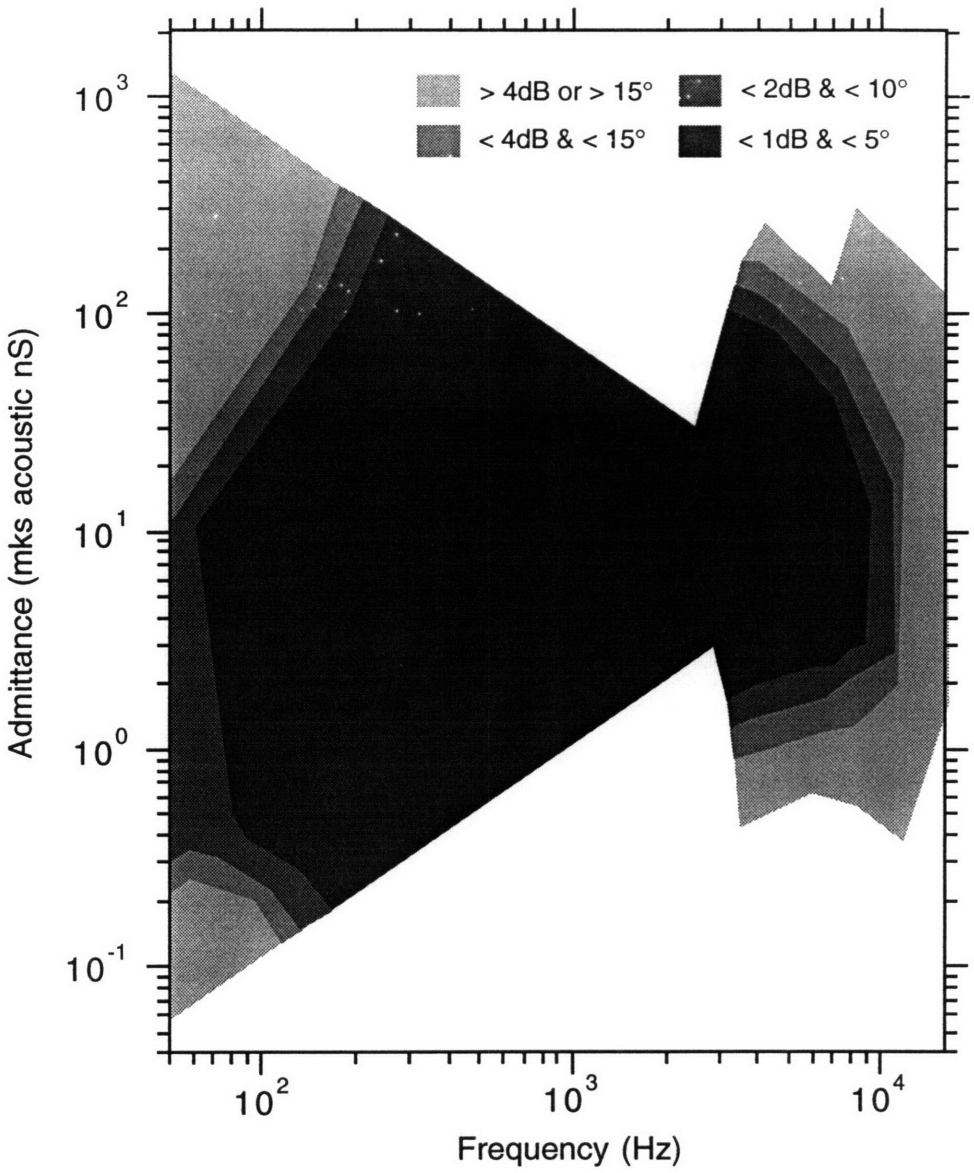

Figure B-8: Source accuracy chart for the high frequency source (driver voltage = 0.001 V). Four gray scale levels are used to represent the maximum accuracy attainable at the specified range of admittance magnitude and frequency. For example, the darkest gray level represents the range over which the source can measure an admittance to within 1 dB in magnitude and 5° in phase. Only the admittance range spanned by the reference loads is included in this chart. The actual accuracy domain can therefore be larger than what is shown.

Appendix C

Other admittance and pressure measurements

This appendix contains all the input admittance and pressure ratio measurements obtained in this study, but are not discussed in the thesis. Most of these measurements were made in the earlier part of the study, where the effects of membranal drying on acoustic measurements were not fully recognized. Consequently, care was not taken to prevent the drying of the tympanic membrane, and the results are less consistent than the measurements obtained in the later experiments. The frequency ranges of the measurements shown in this appendix were chosen in accordance with the discussion presented in Section 3.1: measurements made with the lfs alone were limited to frequencies below 6 kHz, and hfs measurements below 200 Hz were truncated. The largest frequency range was obtained from measurements made with both sources, which extend from 50 Hz to 10 kHz.

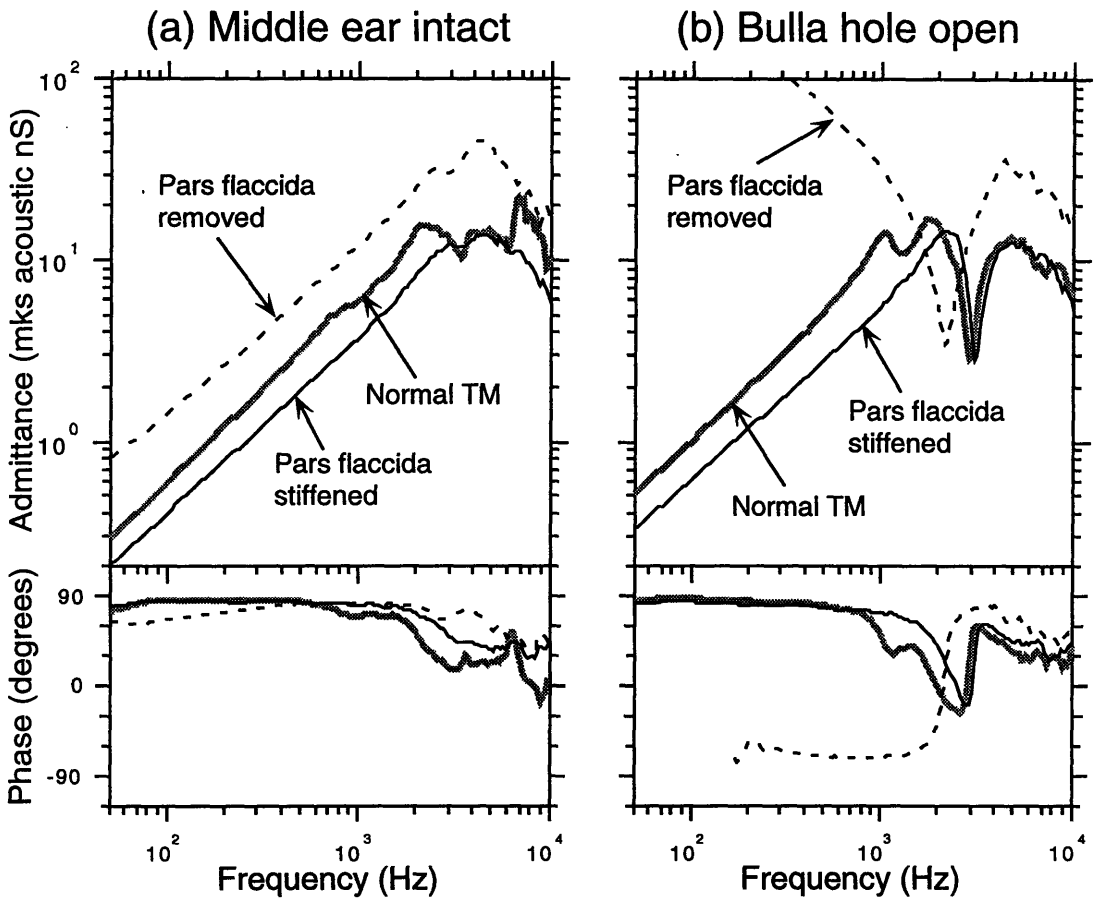

Figure C-1: The middle-ear input admittances measured in the left ear of gerbil A2. (a) Measurements made in the intact middle-ear, and (b) measurements made with the bulla hole open. Three measurements are shown in this figure: 1) with a normal and undisturbed tympanic membrane, 2) with the *pars flaccida* stiffened, and 3) with the *pars flaccida* removed.

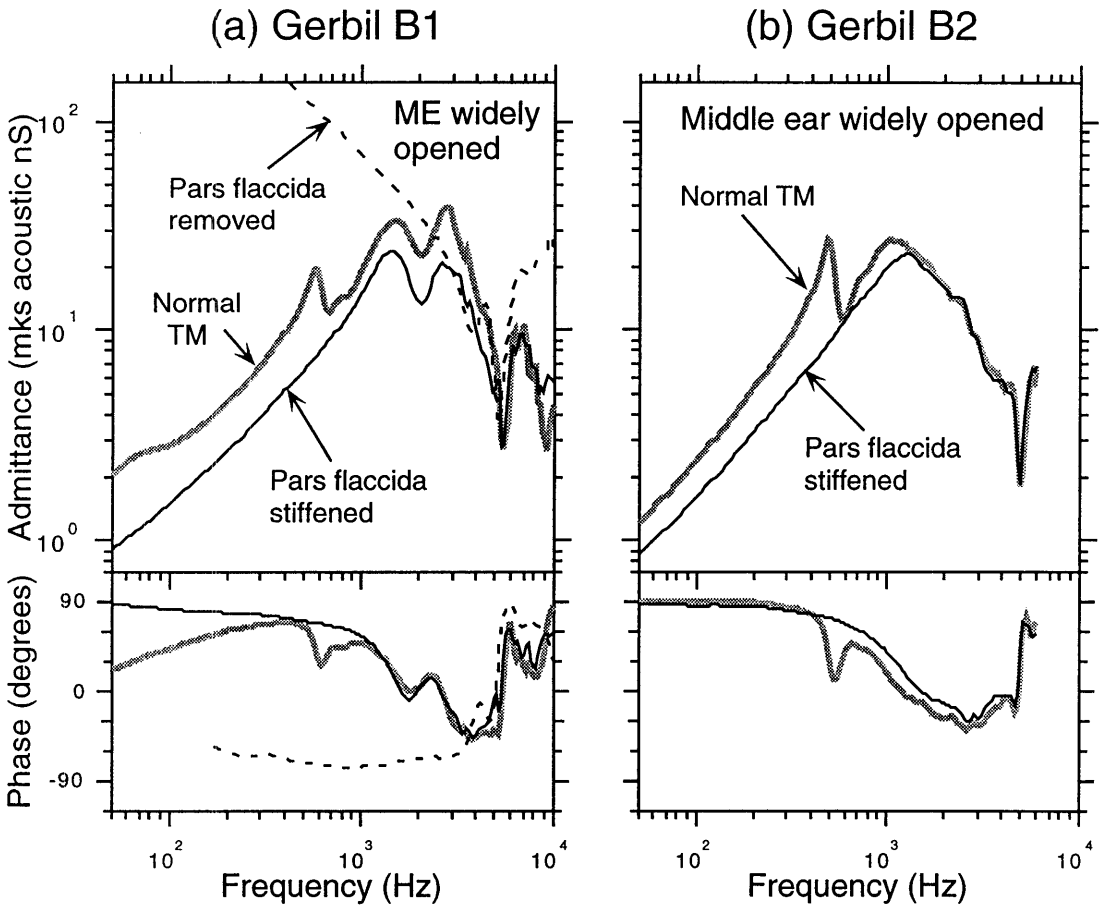

Figure C-2: The middle-ear input admittances measured in the left ears of gerbils B1 and B2—middle ears widely opened. For gerbil B1, three measurements are shown in this figure: 1) with a normal and undisturbed tympanic membrane, 2) with the *pars flaccida* stiffened, and 3) with the *pars flaccida* removed. For gerbil B2, only the first two measurements were obtained.

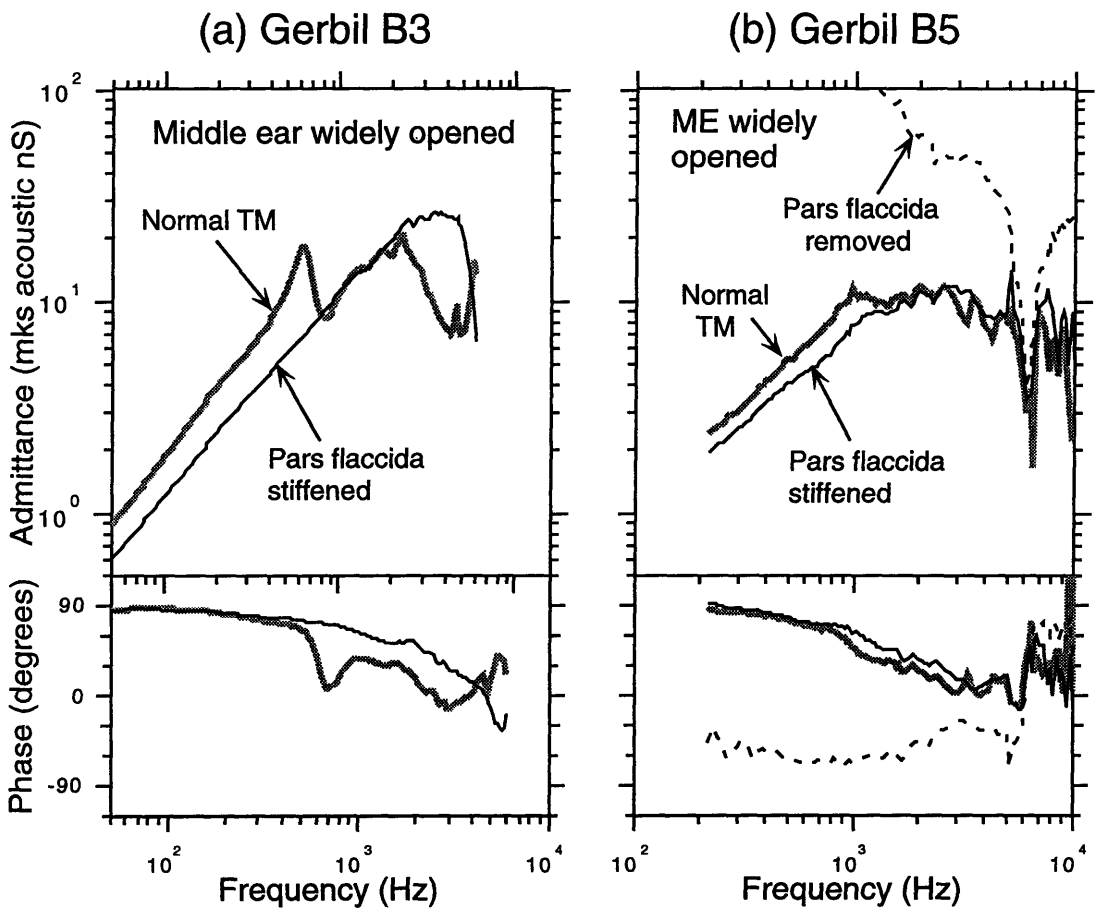

Figure C-3: The middle-ear input admittances measured in the left ears of gerbils B3 and B5—middle ears widely opened. For gerbil B5, three measurements are shown in this figure: 1) with a normal and undisturbed tympanic membrane, 2) with the *pars flaccida* stiffened, and 3) with the *pars flaccida* removed. For gerbil B3, only the first two measurements were obtained.

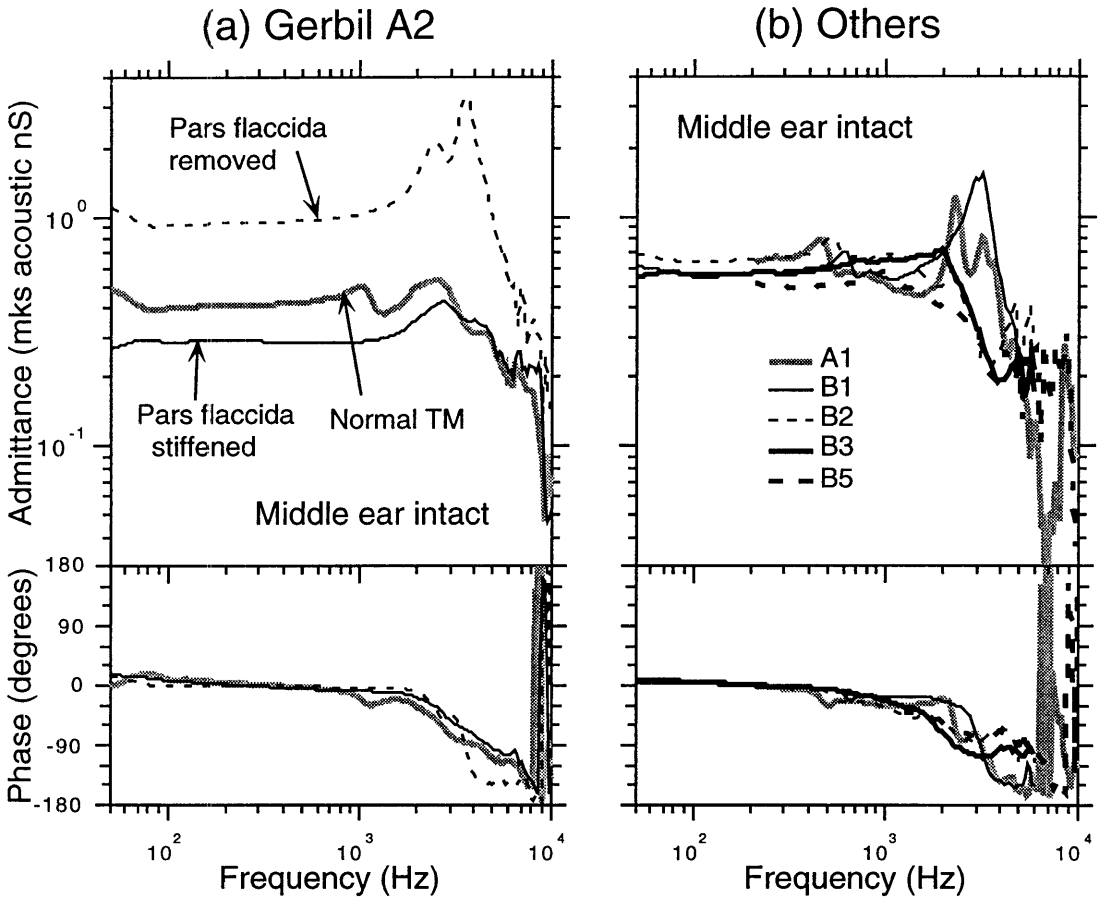

Figure C-4: Middle-ear cavity to ear-canal pressure ratio measurements. (a) Measurements made in the left ear of gerbil A2. The pressure ratios were measured under three different conditions: 1) with the tympanic membrane intact and undisturbed, 2) with the *pars flaccida* stiffened, and 3) with the *pars flaccida* removed. (b) Measurements made in five different gerbils. All measurements were made in ears with normal tympanic membrane.

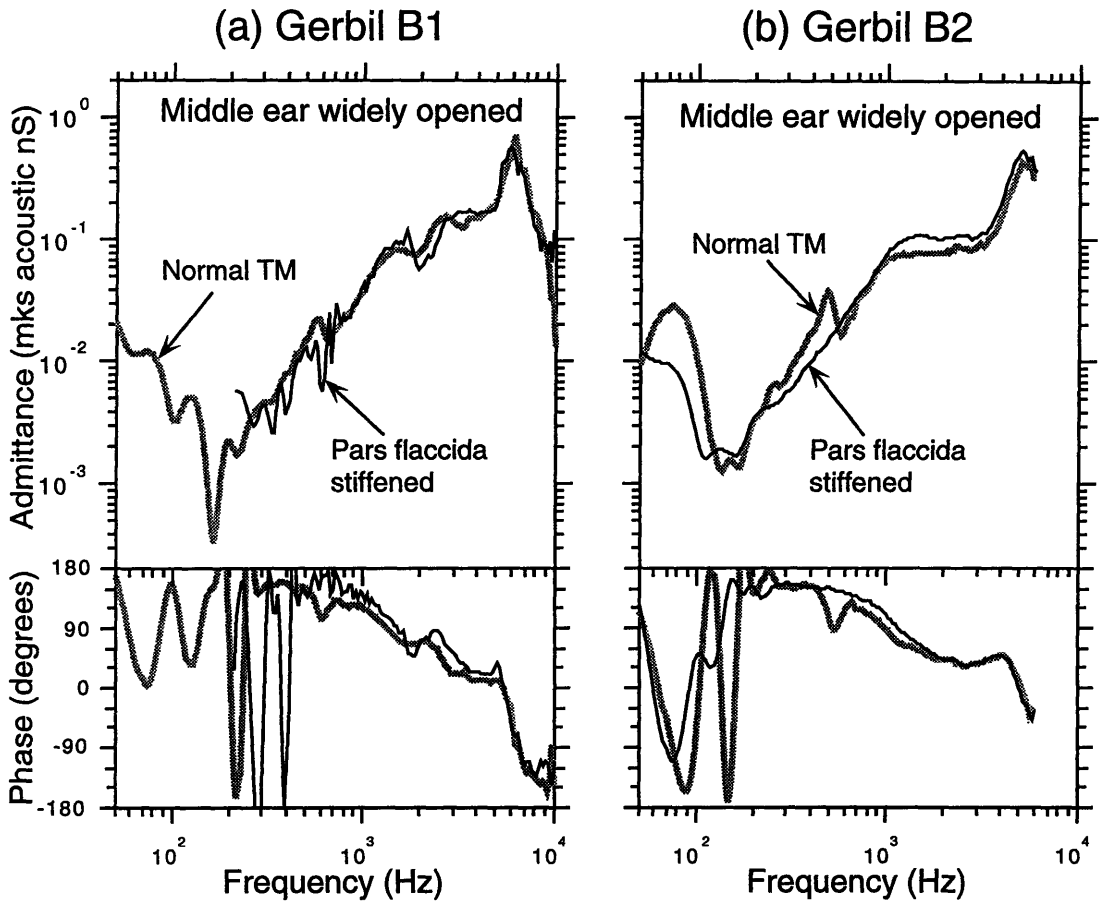

Figure C-5: Middle-ear cavity to ear-canal pressure ratios measured in the left ears of gerbils B1 and B2—middle ears widely opened. The pressure ratios were measured under two conditions: 1) with the tympanic membrane intact and undisturbed, and 2) with the *pars flaccida* stiffened.

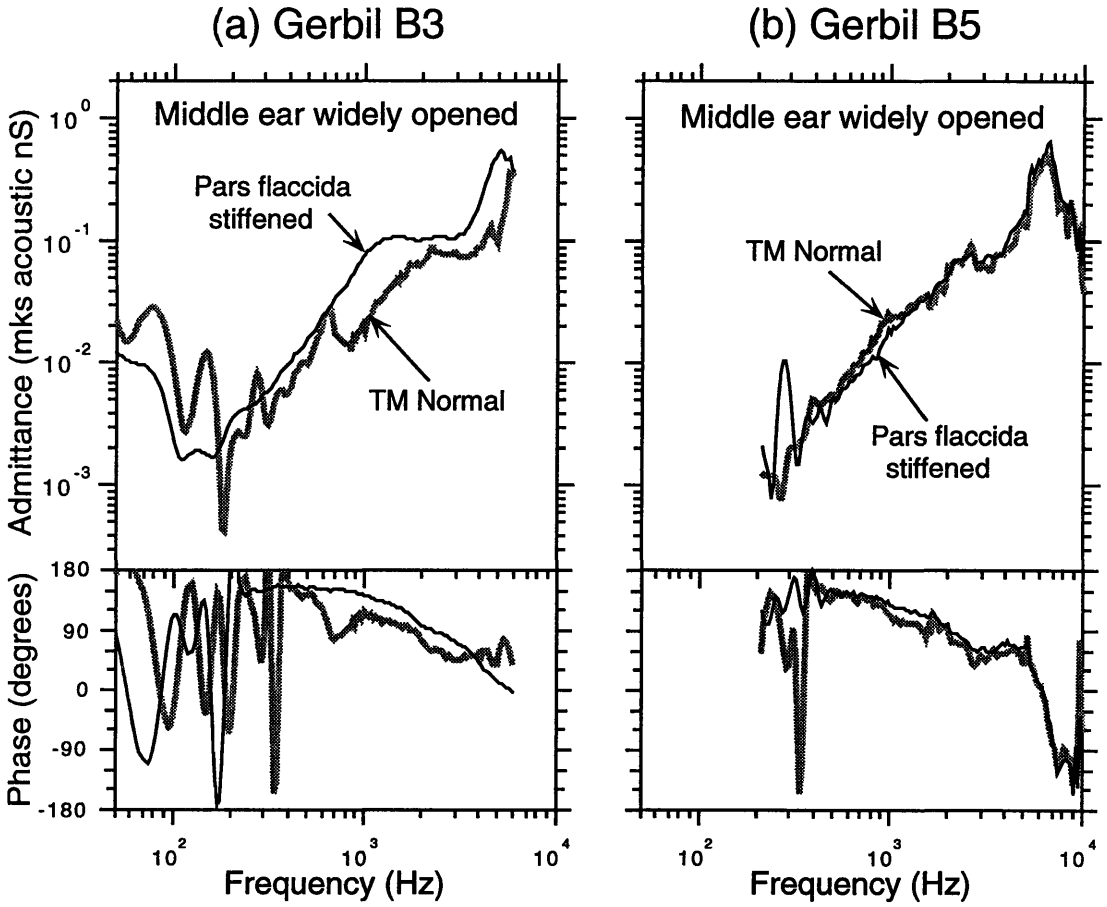

Figure C-6: Middle-ear cavity to ear-canal pressure ratios measured in the left ears of gerbils B3 and B5—middle ears widely opened. The pressure ratios were measured under two conditions: 1) with the tympanic membrane intact and undisturbed, and 2) with the *pars flaccida* stiffened.

Appendix D

List of symbols

Most acoustic variables used in this thesis are expressed in the complex frequency domain. They are printed in **bold**.

c	propagation velocity of sound (m/sec)
C^A	acoustic compliance (m^3/Pa)
C_{CAV}	acoustic compliance of the middle-ear cavity (m^3/Pa)
C_{PF}	acoustic compliance of the *pars flaccida* (m^3/Pa)
C_{TOC}	acoustic compliance of the *pars tensa*-ossicular-cochlear complex (m^3/Pa)
$\mathbf{CP}$	cochlear potential $(volt)$
ΔCP	ratio of pre- and post-stiffened cochlear potentials: $20\log\left\lvert\frac{\mathbf{CP}\rvert_{\mathbf{FS}}}{\mathbf{CP}}\right\rvert$ (dB)
ΔP_{EC}	ratio of pre- and post-stiffened ear-canal sound pressure levels: $20\log\left\lvert\frac{\mathbf{P}\rvert_{\mathbf{FS}}}{\mathbf{P}}\right\rvert$ (dB)
ΔY	ratio of pre- and post-stiffened middle-ear input admittances: $20\log\left\lvert\frac{\mathbf{Y}}{\mathbf{Y}\rvert_{\mathbf{FS}}}\right\rvert$ (dB)
η	viscosity coefficient $(N-sec/m^2)$
$\mathbf{F}[k]$	discrete frequency spectrum of the chirp stimulus
$i(t)$	current in time domain (Amp)
j	imaginary number $\sqrt{-1}$

$\mathbf{k_{pt}}$	complex proportionality constant of probe-tube microphone $(volt/Pa)$
$\mathbf{k_s}$	complex proportionality constant of source microphone $(volt/Pa)$
λ	wavelength of sound (m)
L	inductance $(Henry)$
L^A	acoustic mass (kg/m^4)
L_{HOLE}	acoustic mass of the bulla hole (kg/m^4)
L_K	Karal inertance $(Henry)$
L_{PF}	acoustic mass of the *pars flaccida* (kg/m^4)
L_{TOC}	acoustic mass of the *pars tensa*-ossicular-cochlear complex (kg/m^4)
$\mathbf{m}$	normalization constant
ω	radian frequency, $2\pi f$ $(1/sec)$
ν	kinematic velocity of air (m^2/s)
$\mathbf{P}$	sound pressure level $(Pa, N/m^2)$
$p(t)$	sound pressure level — time domain $(Pa, N/m^2)$
$\mathbf{P_{EC}}$	sound pressure level in ear canal $(Pa, N/m^2)$
$\mathbf{P_L}$	sound pressure level in acoustic load $(Pa, N/m^2)$
$\mathbf{P_{MEC}}$	sound pressure level in the middle-ear cavity $(Pa, N/m^2)$
ρ_o	density of air at STP $(1.19kg/m^3)$
R^A	acoustic resistance $(Pa - sec/m^5)$
R_{HOLE}	acoustic resistance of the bulla hole $(Pa - sec/m^5)$
R_{PF}	acoustic resistance of the *pars flaccida* $(Pa - sec/m^5)$
R_{TOC}	acoustic resistance of the *pars tensa*-ossicular-cochlear complex $(Pa - sec/m^5)$
$\mathbf{U}$	volume velocity (m^3/sec)
$\mathbf{U_{PF}}$	volume velocity entering the *pars flaccida* $(volt - m^3/Pa - sec)$

$\mathbf{U_{PT}}$	volume velocity entering the *pars tensa* $(volt - m^3/Pa - sec)$
$\mathbf{U_S}$	source volume velocity $(volt - m^3/Pa - sec)$
$\mathbf{U_T}$	volume velocity of the entire tympanic membrane $(volt - m^3/Pa - sec)$
$v(t)$	voltage in time domain $(Volt)$
$\mathbf{Y_{CAV}}$	acoustic admittance of middle-ear cavity $(S, m^3/Pa - sec)$
$\mathbf{Y^{HO}}$	middle-ear input admittance—bulla hole open $(S, m^3/Pa - sec)$
$\mathbf{Y^{HO}_{AR}}$	middle-ear input admittance—middle ear widely open and *pars flaccida*'s dental shield removed $(S, m^3/Pa - sec)$
$\mathbf{Y^{HO}_{FS}}$	middle-ear input admittance—bulla hole open and *pars flaccida* stiffened $(S, m^3/Pa - sec)$
$\mathbf{Y^{I}}$	middle-ear input admittance—bulla wall intact $(S, m^3/Pa - sec)$
$\mathbf{Y^{I}_{FS}}$	middle-ear input admittance—bulla wall intact and *pars flaccida* stiffened $(S, m^3/Pa - sec)$
$\mathbf{Y^{I}_{FR}}$	middle-ear input admittance—bulla wall intact and *pars flaccida* removed $(S, m^3/Pa - sec)$
$\mathbf{Y_L}$	admittance of acoustic load $(S, m^3/Pa - sec)$
$\mathbf{Y_{PF}}$	acoustic admittance of the *pars flaccida* $(S, m^3/Pa - sec)$
$\mathbf{Y_S}$	internal source admittance $(S, m^3/Pa - sec)$
$\mathbf{Y_{SC}}$	input admittance of the stapes and cochlea $(S, m^3/Pa - sec)$
$\mathbf{Y_T}$	total input admittance of the gerbil middle ear $(S, m^3/Pa - sec)$
$\mathbf{Y_{TOC}}$	input admittance of the *pars tensa*-ossicular-cochlear complex $(S, m^3/Pa - sec)$
$\mathbf{Y^{WO}}$	middle-ear input admittance—middle ear widely open $(S, m^3/Pa - sec)$
$\mathbf{Y^{WO}_{FS}}$	middle-ear input admittance—middle ear widely open and *pars flaccida* stiffened $(S, m^3/Pa - sec)$
$\mathbf{Z}$	acoustic impedance (acoustic $\Omega, Pa - sec/m^3$)

Bibliography

Beranek, L. L. (1954). *Acoustics.* McGraw-Hill, New York.

Cohen, Y. E., Doan, D. E., Rubin, D. M., and Saunders, J. C. (1993). "Middle-ear development V: Development of umbo sensitivity in the gerbil," *Am. J. Otolaryngol* **14**(3):191–198.

Dallos, P. (1970). "Low-frequency auditory characteristics: Species dependence," *J. Acoust. Soc. Am.* **48**(2):489–499.

Dallos, P., Cheatham, M., and Ferraro, J. (1974). "Cochlear mechanics, nonlinearities, and cochlear potentials," *J. Acoust. Soc. Am.* **55**(3):597–605.

Dear, S. P. (1987). *Impedance and sound transmission in the auditory periphery of the chinchilla.* Ph.D. thesis, U of Pennsylvania.

Dennis, J. and Woods, D. (1987). "New computing environments: Microcomputers in large-scale computing," in Wouk, A., editor, *SIAM*, pages 116–122.

Desoer, C. and Kuh, E. (1969). *Basic Circuit Theory.* McGraw-Hill Inc., New York.

Diependaal, R., de Boer, E., and Viergever, M. A. (1987). "Cochlear power flux as an indicator of mechanical activity," *J. Acoust. Soc. Am.* **82**:917–926.

Egolf, D. (1977). "Mathematical modeling of a probe-tube microphone," *J. Acoust. Soc. Am.* **61**:200–205.

Fletcher, N. H. (1992). *Acoustic Systems in Biology.* Oxford University Press, New York.

Guinan, J. and Peake, W. T. (1967). "Middle-ear characteristics of anesthetized cats," *J. Acoust. Soc. Am.* **41**:1237–1261.

Harada, Y. (1983). *Atlas of the ear by scanning electron microscopy.* MTP Press, London.

Hellström, S. and Stenfors, L.-E. (1983). "The pressure equilibrating function of pars flaccida in middle ear mechanics," *Acta. Physiol. Scand.* **118**:337–341.

Hutchings, M. (1987). "The gerbil as an animal model of otitis media with effusion," *J. Physiol. (London)* **396**.

Karal, F. C. (1953). "The analogous acoustical impedance for discontinuities and constrictions of circular cross section," *J. Acoust. Soc. Am.* **25**(2):327–334.

Khanna, S. M. and Tonndorf, J. (1972). "Tympanic membrane vibrations in cats studied by time-averaged holography," *J. Acoust. Soc. Am.* **51**(6):1904–1920.

Kohllöffel, L. (1984). "Notes on the comparative mechanics of hearing. iii. On Shrapnell's membrane," *Hearing Research* **13**:83–88.

Kringlebotn, M. (1988). "Network model for the human middle ear," *Scand. Audiol.* **17**:75–85.

Lay, D. (1972). "The anatomy, physiology, functional significance and evolution of specialized hearing organs of gerbilline rodents," *J. Morph.* **138**:41–120.

Lynch, III, T. J. (1981). *Signal processing by the cat middle ear: Admittance and transmission, measurements and models.* Ph.D. thesis, MIT.

Lynch, III, T. J., Nedzelnitsky, V., and Peake, W. T. (1982). "Input impedance of the cochlea in cat," *J. Acoust. Soc. Am.* **72**(1):108–130.

Lynch, III, T. J., Peake, W. T., and Rosowski, J. J. (1994). "Measurements of the acoustic input impedance of cat ears: 10 hz to 20 khz," *J. Acoust. Soc. Am.* **96**:2184–2209.

Møller, A. R. (1961). "Network model of the middle ear," *J. Acoust. Soc. Am.* **33**(2):168–176.

Møller, A. R. (1963). "Transfer function of the middle ear," *J. Acoust. Soc. Am.* **35**(10):1526–1534.

Møller, A. R. (1965). "An experimental study of the acoustic impedance of the middle ear and its transmission properties," *Acta oto-laryng.* **60**:129–149.

Nedzelnitsky, V. (1980). "Sound pressures in the basal turn of the cat cochlea," *J. Acoust. Soc. Am.* **68**(6):1676–1689.

Neely, S. T. and Kim, D. O. (1986). "A model for active elements in cochlear biomechanics," *J. Acoust. Soc. Am.* **79**(5):1472–1480.

Nelder, J. and Mead, R. (1964). "A simplex method for function minimization," *Computer Journal* **7**:308–313.

Nilsson, J. W. (1990). *Electric Circuits.* Addison-Wesley, Reading, Massachusetts.

Pang, X. D. and Peake, W. T. (1985). "How do contractions of the stapedius muscle alter the acoustic properties of the ear," in Allen, J. B., Hall, J. L., Hubbard, A., Neely, S. T., and Tubis, A., editors, *Peripheral Auditory Mechanisms*, pages 36–43. Springer-Verlag.

Pickles, J. O. (1988). *An Introduction to the Physiology of Hearing.* Academic Press, 2 edition.

Ravicz, M. E. (1990). Acoustic impedance of the gerbil ear. Master's thesis, Boston University.

Ravicz, M. E., Rosowski, J. J., and Voight, H. F. (1990). "Acoustic impedance measurements in the gerbil ear," *J. Acoust. Soc. Am. Suppl 1* **87**:S101.

Ravicz, M. E., Rosowski, J. J., and Voigt, H. F. (1992). "Sound-power collection by the auditory periphery of the mongolian gerbil *meriones unguiculatus.* i: Middle-ear input impedance," *J. Acoust. Soc. Am.* **92**(1):157–177.

Rosowski, J. J. (1991). "The effects of external- and middle ear filtering on auditory threshold and noise-induced hearing loss," *J. Acoust. Soc. Am.* **90**(1):124–135.

Rosowski, J. J., Carney, L. H., Lynch, T. J., and Peake, W. T. (1986). "The effectiveness of external and middle ears in coupling acoustic power into the cochlea," in Allen, J. B., Hall, J. L., Hubbard, A., Neely, S. T., and Tubis, A., editors, *Peripheral Auditory Mechanisms*, pages 3–12. Springer-Verlag.

Rosowski, J. J., Davis, P. J., Merchant, S. N., Donahue, K. M., and Coltrera, M. D. (1990). "Cadaver middle ears as models for living ears: Comparisons of middle ear input impedance," *Ann Otol Rhinol Laryngol* **99**(5):403–412.

Rosowski, J. J. and Merchant, S. N. (1995). "Mechanical and acoustic analysis of middle ear reconstruction," *Am. J. Otolaryngol* **16**(4):486–497.

Rosowski, J. J., Peake, W. T., and Lynch, T. J. (1984). "Acoustic input-admittance of the alligator-lizard ear: Nonlinear features," *Hearing Research* **16**:205–223.

Ryan, A. (1976). "Hearing sensitivity of the mongolian gerbil, *meriones unguiculatis*," *J. Acoust. Soc. Am.* **54**:1222–1226.

Schmiedt, R. and Zwislocki, J. (1977). "Comparison of sound-transmission and cochlear-microphonic characteristics in mongolian gerbil and guinea pig," *J. Acoust. Soc. Am.* **61**(1):133–149.

Shaw, E. A. G. (1974). "The external ear," in Keidel, W. D. and Neff, W. D., editors, *Handbook of sensory physiology: Vol V/1: Auditory System*, volume 5, chapter 1, pages 455–490. Springer-Verlag, New York.

Stenfors, L.-E., Salén, B., and Windblad, B. (1979). "The role of the pars flaccida in the mechanics of the middle ear," *Acta oto-laryng.* **88**:395–400.

Tonndorf, J. and Khanna, S. M. (1970). "The role of the tympanic membrane in middle ear transmission," *J. for Oto-Rhino-Laryngology and its related specialties* **79**:743–753.

von Unge, M., Bagger-Sjóback, D., and Borg, E. (1991). "Mechanoacoustic properties of the tympanic membrane: A study on isolated mongolian gerbil temporal bones," *Am. J. Otology* **12**:407–419.

Zuercher, J. C., Carlson, E. V., and Killion, M. C. (1988). "Small acoustic tubes: New approximations including isothermal and viscous effects," *J. Acoust. Soc. Am.* **83**(4):1653–1660.

Zwicker, E. (1986). "A hardware cochlear nonlinear preprocessing model with active feedback," *J. Acoust. Soc. Am.* **80**:146–153.

Zwislocki, J. (1962). "Analysis of the middle-ear function. Part 1: Input impedance," *J. Acoust. Soc. Am.* **34**:1514–1523.

Zwislocki, J. (1963). "Analysis of the middle-ear function. Part II: Guinea-pig ear," *J. Acoust. Soc. Am.* **35**:1034–1040.